



UNIVERSITÀ DEGLI STUDI DI PADOVA

DIPARTIMENTO DI FISICA

DOTTORATO DI RICERCA IN FISICA

CICLO XX

**Numerical study of magnetic topology
and test particle transport in the
Reversed Field Pinch and in the Tokamak**

Coordinatore: Ch.mo Prof. Attilio Stella

Supervisor: Ch.mo Prof. Piero Martin

Dott. Lionello Marrelli

Dottorando: Dott. Marco Gobbin

30 gennaio 2008

To Freedom

Preface

Thermonuclear fusion represents a promising chance to generate energy without the emission of carbon dioxide and the production of long living radioactive scores. Moreover, the raw materials used as fuel in the fusion reactions, deuterium and tritium, are easily available on Earth. This motivates the efforts on the controlled thermonuclear fusion research.

In order to reach thermonuclear fusion, the fuel needs to be heated to very high temperatures, therefore it becomes a *plasma*. The plasma can be confined by magnetic fields of toroidal topology. The most studied configurations are the Tokamak, the Reversed Field Pinch (RFP) and the Stellarator. An overview on nuclear fusion and plasma physics is given in [Chapter 1](#).

In this Thesis we shall analyze particle transport phenomena, in experiments which belong to the Tokamak and RFP classes, by numerical simulations with the Hamiltonian code ORBIT. We will describe at first the numerical tools that we developed to perform the simulations. [Chapter 2](#) will deal with the description of the magnetic field coordinates used in the simulation code. [Chapter 3](#) will describe the guiding center equations of the ORBIT code, by highlighting the recent generalization to straight field line coordinates. The tools have been applied to investigate a series of RFP and tokamak experiments. In particular, [Chapter 4 and 6](#) are devoted to RFP results in a recently discovered regime, the Quasi Single Helicity (QSH). In this scenario the particle transport is reduced and the plasma assumes an helical non axi-symmetric geometry. The magnetic topology of QSH states has been reconstructed and analyzed by ORBIT in discharges with different plasma currents and equilibrium parameters in the experiments RFX-mod

(Padova, Italy) and MST (Madison, USA).

The QSH state is the preliminary step to reach the Single Helicity (SH) regime where only one mode is non-zero. In [Chapter 5](#), an estimate of the diffusion coefficients for thermal particles in a theoretical SH state has been performed. Special numerical algorithms have been developed in order to study the particle transport in a non-axisymmetric geometry. The results have been compared with experimental values obtained in standard plasmas with many magnetic perturbations (non QSH or SH) and with previous axisymmetric simulations.

There is an other possibility for the RFP experiments to avoid the negative consequences on transport of the magnetic perturbations: the Pulsed Poloidal Current Drive (PPCD) technique, presented in [Chapter 6](#) for the MST experiment. PPCD allows for a global reduction of the instabilities to very low values. The topology and the confinement properties of the PPCD plasma in MST are discussed, especially when a QSH state appears. In the same Chapter we also show that, during QSH, electrons can be accelerated on the magnetic surfaces to very high energy (few hundreds of keV). This is a further proof of the formation of conserved helical flux surfaces during QSH regimes.

The beneficial effects of the QSH hold also for non-thermal ions. In fact, high energetic ions can be injected in fusion plasmas as additional heating. Experiments have shown that, in the RFP, these fast ions can be confined for longer time than the thermal particles. We explain this behavior with the formation of a QSH regime in the fast ion phase space ([Chapter 6](#)).

On the contrary of RFP, in Tokamak experiments it has been observed that fast ions (about 100keV) are rapidly lost from the system, especially when a magnetic perturbation is present. This phenomenon is discussed in terms of orbit stochasticity in the fast ion phase space generated by the interaction of the magnetic perturbation and the high energy particle drifts. The study has been executed for the experiment Asdex-UPGRADE (Garching, Germany) where a Fast Ion Loss Detector (FILD) with high time resolution is active. Numerical simulations by ORBIT used to interpret the experimental data are reported in [Chapter 7](#).

Finally, in [Chapter 8](#) we give an analytical explanation of the completely different behavior of fast ions in Tokamak and RFP in terms of the particles guiding center high energy drifts due to the curvature and non-uniformity of the magnetic field. This theory is also used to predict the confinement of fast ions in the experiment RFX-mod.

Prefazione

La fusione termonucleare rappresenta una promettente possibilità per generare energia evitando l'emissione di anidride carbonica e la produzione di scorie radioattive con lungo tempo di decadimento. Inoltre, le materie prime utilizzate come combustibili per le reazioni di fusione, deuterio e trizio, sono facilmente reperibili sulla Terra. Queste caratteristiche positive spingono a continuare la ricerca sulla fusione termonucleare controllata.

Le condizioni necessarie perché avvengano le reazioni di fusione richiedono che i combustibili siano portati a temperature molto elevate: la materia si trova quindi allo stato di *plasma*. I campi magnetici possono controllare e confinare il plasma in dispositivi di forma toroidale. Le configurazioni toroidali più diffuse sono il Tokamak, il Reversed Field Pinch (RFP) e lo Stellarator. Un richiamo generale sulla fusione e sulla fisica del plasma è riportato nel Capitolo 1.

In questa Tesi analizzeremo i fenomeni di trasporto di particelle in esperimenti Tokamak ed RFP con l'ausilio del codice hamiltoniano ORBIT. Descriveremo inizialmente gli strumenti numerici sviluppati per eseguire le simulazioni. Il Capitolo 2 presenterà una descrizione delle coordinate di campo magnetico utilizzate nel codice. Il Capitolo 3 sarà invece dedicato alle equazioni del moto implementate in ORBIT per il centro guida delle particelle, evidenziando la recente generalizzazione alle *coordinate con linee di campo dritte*. Questi nuovi strumenti numerici sono stati applicati per analizzare una serie di esperimenti tokamak ed RFP. In particolare, i Capitoli 4 e 6 sono dedicati ai risultati ottenuti negli RFP in un regime avanzato recentemente scoperto: la Quasi Singola Elicità (Quasi Single Helicity, QSH). In

questo caso il trasporto di particelle è ridotto ed il plasma assume una forma elicoidale non assial-simmetrica. La topologia magnetica della QSH è stata ricostruita e analizzata con ORBIT, in scariche con diverse correnti di plasma e parametri di equilibrio, negli esperimenti RFX-mod (Padova, Italia) e MST (Madison, USA).

Lo stato QSH è il passo preliminare per raggiungere il regime a Singola Elicità (SH) in cui un solo modo è diverso da zero. Nel Capitolo 5 è stata eseguita una stima dei coefficienti di diffusione per particelle termiche in un teorico stato SH. Per fare questo sono stati sviluppati appositi algoritmi, necessari per lo studio di trasporto in contesti non assial-simmetrici. I risultati sono stati confrontati con i dati sperimentali in scariche standard, quindi non SH o QSH, e con precedenti simulazioni in geometrie assial-simmetriche.

Esiste un altro metodo per ridurre le perturbazioni magnetiche nel plasma: la tecnica Pulsed Poloidal Current Drive o PPCD, illustrata nel Capitolo 6 per l'esperimento MST. La topologia magnetica e le proprietà di confinamento durante scariche di questo tipo, in particolare di stati QSH, sono state oggetto di studio durante l'attività di dottorato. Nello stesso Capitolo mostriamo anche che, durante gli stati QSH, appaiono elettroni che possono essere accelerati fino ad energie molto elevate (centinaia di keV). Questo è legato alla formazione di superfici elicoidali conservate durante i regimi QSH.

Gli effetti benefici della QSH riguardano anche ioni non termici. Infatti, ioni ad alta energia possono essere iniettati nei plasmi da fusione come riscaldamento addizionale. Gli esperimenti hanno mostrato come negli RFP questi ioni possono essere confinati per tempi molto più lunghi delle particelle termiche. Questo comportamento è spiegato, alla fine del Capitolo 6, con la comparsa di uno stato QSH nello spazio delle fasi degli ioni veloci.

Al contrario del RFP, negli esperimenti Tokamak è stato osservato che ioni ad alta energia (circa 100keV) sono persi in tempi molto rapidi, specialmente quando sono presenti delle instabilità magnetiche. Questo fenomeno è stato interpretato come conseguenza dell'iterazione tra la perturbazione magnetica ed il moto degli ioni energetici. Lo studio è stato condotto per l'esperimento ASDEX-Upgrade o AUG (Garching, Germania) dove è attivo un detector per le rivelazioni di ioni veloci con un alta risoluzione temporale (FILD, Fast Ion Loss Detector). I risultati delle simulazioni numeriche di ORBIT, eseguite per lo studio dei dati sperimentali di AUG, sono riportati nel Capitolo 7.

Infine, nel Capitolo 8, presentiamo una spiegazione analitica del diverso comportamento degli ioni energetici in Tokamak ed RFP in termini del moto di centro guida delle particelle in campi magnetici curvi e non uniformi. Questa teoria è stata utilizzata per fare delle previsioni sulle proprietà di confinamento degli ioni veloci nell'esperimento RFX-mod.

Contents

| | | |
|----------|--|-----------|
| 1 | Toroidally magnetic confined plasmas | 1 |
| 1.1 | Energy: the aftermath | 1 |
| 1.1.1 | Energy sources and the environmental problem | 2 |
| 1.1.2 | Alternative to Fossil Fuels | 6 |
| 1.2 | Thermonuclear Fusion | 8 |
| 1.2.1 | Fusion reactions and burning criteria | 9 |
| 1.2.2 | From the Sun to ITER | 12 |
| 1.3 | Plasma and its properties | 16 |
| 1.4 | Magnetic plasma confinement | 19 |
| 1.4.1 | MHD Equations | 20 |
| 1.4.2 | MHD Instabilities | 22 |
| 1.4.3 | Tokamak and RFP | 24 |
| 1.5 | Single Particle Motion and Drift Effects | 27 |
| 1.6 | Particle and heat transport in fusion plasma | 31 |
| 1.7 | Additional heating | 33 |
| 1.7.1 | NBI | 34 |
| 1.7.2 | Electromagnetic Wave Heating | 35 |
| 1.8 | Motivation and Aim of the work | 35 |
| 2 | Equilibrium Magnetic Field | 37 |
| 2.1 | Flux coordinates | 37 |
| 2.2 | Derivation of flux coordinates for cylindrical equilibria | 41 |

| | | |
|----------|---|-----------|
| 2.2.1 | The Grad-Shafranov equation | 43 |
| 2.3 | RFP Equilibrium | 46 |
| 2.3.1 | The BFM model | 47 |
| 2.3.2 | The $\mu&p$ model | 48 |
| 2.3.3 | First order: cylindrical equilibrium | 50 |
| 2.3.4 | Second order: the Shafranov shift Δ | 51 |
| 2.3.5 | Algorithm for RFPs equilibria: a summary | 51 |
| 2.4 | Circular Tokamak Equilibrium | 53 |
| 2.5 | Numerical Equilibria: the VMEC code | 54 |
| 2.5.1 | VMEC and ASDEX-Upgrade equilibrium | 56 |
| 3 | Hamiltonian Formulation | 61 |
| 3.1 | Lagrangian Formulation | 61 |
| 3.2 | Hamiltonian Formulation | 65 |
| 3.3 | Motion equations in axi-symmetric configurations and straight field line coordinates | 67 |
| 3.4 | Ripple effect in ORBIT | 68 |
| 3.4.1 | Ripple for Asdex-Upgrade | 70 |
| 3.5 | Helical Magnetic Perturbations | 71 |
| 3.6 | Time-dependent perturbations | 73 |
| 3.7 | Classification of particle orbits | 75 |
| 3.7.1 | Passing Particles | 76 |
| 3.7.2 | Trapped particles | 79 |
| 3.8 | Collisions | 82 |
| 3.8.1 | Collisions for thermal test particles | 83 |
| 3.8.2 | Slowing Down of fast particles | 84 |
| 3.8.3 | Classical and pitch angle scattering | 86 |
| 4 | The RFP configuration and the RFX-mod experiment | 89 |
| 4.1 | Physics of RFP configuration | 89 |
| 4.1.1 | Resistive Diffusion: the dynamo effect | 90 |
| 4.1.2 | Magnetic perturbations and dynamo | 92 |
| 4.2 | RFP experiments | 93 |
| 4.2.1 | RFX-mod components | 94 |
| 4.2.2 | Discharge setting up | 96 |
| 4.2.3 | Clean Mode Control | 98 |
| 4.3 | Diagnostics in RFP experiments | 98 |
| 4.4 | Magnetic perturbations by ORBIT | 100 |
| 4.4.1 | Magnetic perturbations in cylindrical approximation | 101 |
| 4.4.2 | Magnetic perturbations in toroidal geometry | 105 |

| | | |
|----------|---|------------|
| 4.5 | Experimental evidences of QSH regimes in RFX-mod | 107 |
| 4.5.1 | QSH examples | 108 |
| 4.5.2 | Magnetic Topology reconstructions during QSH | 109 |
| 4.5.3 | Stickiness around magnetic islands | 114 |
| 4.5.4 | Test particle transport studies | 115 |
| 4.5.5 | QSH in high plasma current regimes | 117 |
| 5 | Thermal particle transport in Single Helicity regimes | 123 |
| 5.1 | Single Helicity | 123 |
| 5.1.1 | The wire model of the RFP dynamo | 124 |
| 5.1.2 | MH-SH transition | 126 |
| 5.1.3 | Electrostatic nature of the dynamo | 127 |
| 5.1.4 | Numerical study of transport in helical states: a summary | 128 |
| 5.2 | Equilibrium and Perturbations | 128 |
| 5.3 | Perturbed flux ψ^M computation | 130 |
| 5.4 | Helical surface reconstruction | 133 |
| 5.4.1 | The polygon definition | 133 |
| 5.4.2 | Triangulation and 2D interpolation | 135 |
| 5.4.3 | Linear 3D interpolation | 137 |
| 5.5 | Calculations of ion and electron diffusion coefficients | 137 |
| 5.6 | Results: diffusion coefficients | 140 |
| 5.6.1 | Comparison with previous studies | 144 |
| 6 | QSH regimes and fast ions in MST | 147 |
| 6.1 | QSH regimes in the MST experiment | 147 |
| 6.1.1 | The Pulsed Poloidal Current Drive technique | 149 |
| 6.1.2 | Magnetic topology in PPCD shots | 150 |
| 6.1.3 | Standard QSH in MST | 153 |
| 6.1.4 | Loss Times in QSH regimes | 154 |
| 6.2 | F=0 shot and Runaway electrons | 156 |
| 6.2.1 | The inductive electric field in ORBIT | 158 |
| 6.2.2 | Numerical transport simulations by ORBIT | 161 |
| 6.3 | Fast ions from NBI in MST: experiment and simulation by ORBIT | 163 |
| 6.3.1 | Experimental results | 164 |
| 6.3.2 | Fast ion phase space | 165 |
| 6.3.3 | Thermal and fast ion loss times | 168 |
| 6.3.4 | Fast ion in QSH regime | 169 |

| | | |
|----------|---|------------|
| 7 | Fast Ions in ASDEX-Upgrade | 171 |
| 7.1 | The experiment ASDEX-Upgrade | 171 |
| 7.1.1 | The NBI system in ASDEX | 172 |
| 7.1.2 | The FILD detector | 174 |
| 7.1.3 | Neoclassical Tearing Modes | 175 |
| 7.2 | Fast Ion Losses: experimental evidences | 177 |
| 7.3 | Orbits stochasticity as mechanism for losses | 180 |
| 7.4 | Results of the transport simulation by ORBIT | 184 |
| 7.5 | A D-shaped version of ASDEX in straight field line coordinates | 189 |
| 7.5.1 | Phase space properties | 190 |
| 7.5.2 | The initial fast ion distribution in the D-shaped geometry | 191 |
| 7.5.3 | Transport numerical simulations with a fixed mode . . | 191 |
| 7.6 | Effect of the ripple implementation | 196 |
| 7.7 | Sensitivity of the losses amount on the radial perturbation profile | 197 |
| 7.8 | Steady-state with rotating modes | 201 |
| 8 | Fast ions in Tokamak and RFP | 205 |
| 8.1 | An analytic approach: the kinetic safety factor | 205 |
| 8.2 | The kinetic safety factor in a Tokamak | 209 |
| 8.3 | The kinetic safety factor in a RFP | 210 |
| 8.3.1 | A simple model of the toroidal drift | 212 |
| 8.3.2 | Application to fast ions in RFX-mod | 214 |
| | Conclusions | 217 |
| A | Flux Coordinates | 221 |
| A.1 | Reciprocal sets of vectors | 221 |
| A.1.1 | Metric Coefficients and their properties | 226 |
| A.1.2 | The Jacobian | 227 |
| A.1.3 | Differential elements | 227 |
| A.2 | Magnetic Field Structure | 228 |
| A.3 | The Elementary Toroidal Coordinates | 229 |
| A.4 | Flux Coordinates | 230 |
| A.5 | Straight Field Line Coordinates | 233 |
| A.5.1 | The vector potential. | 236 |
| A.6 | General Current Representation | 237 |
| A.7 | Boozer Coordinates | 240 |
| | Bibliography | 243 |
| | Acknowledgements | 249 |

CHAPTER 1

Toroidally magnetic confined plasmas

In this Chapter, we will first introduce the controlled thermonuclear fusion as an alternative energy source for the future. In particular, we will dedicate this introductory Chapter to magnetic fusion, which can be obtained in toroidal magnetically confined plasmas at sufficiently high temperatures and densities. We will then focus on toroidal plasmas and their instabilities, in particular in two important toroidal configurations, i.e. the tokamak and the reversed-field pinch (RFP). Also a description of single particle motion in external magnetic fields will be given, for a better understanding of the results presented in the following Chapters. Finally, additional heating systems for fusion plasma, such as Neutral Beam Injection and Radio Frequency, will be briefly introduced.

1.1 Energy: the aftermath

Energy is one of the building blocks of modern society. Energy is needed to create goods from natural resources and to provide many services. Economic development and improved standards of life are complex processes that share a common denominator: the availability of an adequate and reliable supply of energy.

The modernization of the West from a rural society to an affluent urban one was made possible through the employment of a modern technology

based on a multitude of scientific advances. Political events, beginning with an oil embargo in 1973 and continuing through the Iranian revolution of 1979 and the Persian Gulf War of 1991, made many people aware of how crucial energy is to the everyday functioning of our society. Long gasoline lines and cold winters with natural gas shortages in the 1970s are still unhappy memories for some people. The energy crises of the 1970s were almost forgotten in the 1980s; however that decade brought an increased awareness of our environment. Concern about global warming, acid rain and radioactive waste are still very much with us today and each of these topics is related to our use of energy. In the next 25 years if the world will continue to use the actual main energy sources, i.e. oil and carbon, we shall input the atmosphere the same amount of carbon dioxide (CO_2) we have produced since the beginning of the industrial revolution [1] [2].

Moreover, it has been calculated that in the next 40 years, with the actual trends, the global use of electricity will increase by the 160%. We are thus at a crucial point in the history of energy and technology, since we need in the imminent future energy sources both clean and available in large amounts, if we want to preserve our standard of life and ensure it to the emerging countries of Asia and Africa.

In the following of this Chapter we present a brief overview on these items focusing in particular on the energy produced by fusion reactions which could allow to obtain large amounts of CO_2 -free energy in the future. A great effort has been spent in the last 50 years to achieve this important goal and there are good possibilities that fusion will become a reality before the half of this century. The technology and the physics involved in this project are complex and have been representing a great challenge for physicist and engineers of past and present generations. In this Thesis we wish to give also our small contribution to the possibility of using fusion as an energy source, by focusing on particular aspects of the physics of magnetically confined plasma.

1.1.1 Energy sources and the environmental problem

The energy accompanies the evolution of mankind from its origin. From the solar energy to that geothermal one, from millenia the man tries to bridle them, to transform them, to render them available in order to construct his own development. Up to the XVII century energy was not a problem as we intend it today. When work was needed, to plow a field or to construct a palace, humans and animals gave the necessary energy to accomplish it; technology and science allowed also for using wind - in navigation - and the energy of falling water - in grinding wheat - but they were natural ways of making easier or eliminating muscles work. With industrial revolution, first

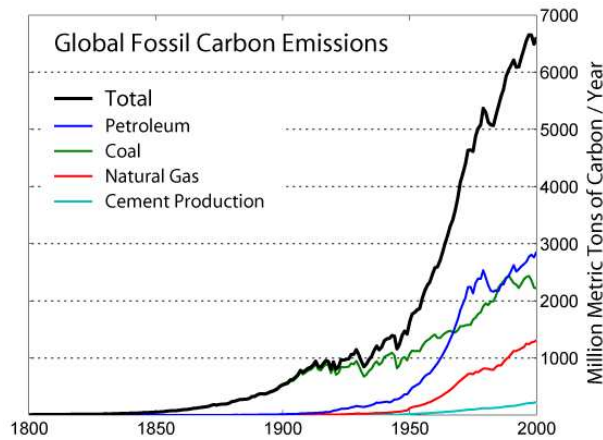


Figure 1.1: Annual carbon dioxide emission broken down into various fuel types during the years 1800 – 2000 expressed in million metric tons of carbon. In the graph the increasing rate at which fossil fuels are being consumed is shown. Data taken from [3].

in England and slowly almost everywhere on Earth, things changed dramatically. With steam power, and then with electricity and combustion engines, it was possible to do everything was done before with chemical energy coming from muscles and even more, but with the big price of using energy from hydrocarbons.

Still today, more than 90% of energy resources used in the world come from the fossil fuels - coal, oil and natural gas. Fossil fuels were formed from vegetation and animal residues during the Carboniferous through the Permian eras which extended 380 to 245 million years ago. As the plants and animal life died, they were buried under mud which gradually hardened into rock. The rotting plants and decayed animal were squashed between heavy layers of the rock and heated by the earth. By exposure to high temperatures and extreme pressures in the Earth's crust, over hundreds of millions of years they changed into coal, oil and natural gas deposits. Actually, to be technically correct, fossil fuels, come from the sun since without its light and heat, nothing would grow. Except for coal, the supply of these fuels at present rate might not last much longer than the lifetimes of the people now living. The fuel most commonly used, oil, appears to be in the shortest supply worldwide, but continues to be that commodity on which we rely most heavily. Indeed, dependence on oil, especially for transportation, leaves many countries quite vulnerable to a major economic disaster in the event of an oil shortage or interruption in supply.

The consumption of fossil fuels can be measured by estimating the tons of carbon dioxide that have been released into the atmosphere in the last

decades. An example of such analysis is presented in Fig. 1.1 where data take into account the different origins. The main message from this figure is that, since the industrial revolution, consumption of the hydrocarbons is increasing almost exponentially, and with the countries that now enter in the great economical competition things are not likely to get better. An obvious second conclusion from this plot is that world energy needs are increasing. Every day we use more than 80 million barrels of oil and close to 9 billion cubic meter of natural gas, which are no renewable sources, unless we wait geological eras for them building up again. Reserves are thus limited and are diminishing.

The geophysicist M. King Hubbert created a model of known reserves, and predicted in a paper [4] he presented in 1956 at a meeting of the American Petroleum Institute, that oil production in the continental United States would have peaked between 1965 and 1970; and that world production would peak in 2000. U.S. oil production peaked in 1971, and even if world production did not peak in 2000, new estimates predicts a peak not much further. The Association for the Study of Peak Oil and Gas (ASPO), based on current information about known oil reserves, estimates of future discovery, growing oil demand, and available technology, predicts that world oil production will peak around the year 2010. Even if other estimations are more optimistic, and new technology discoveries would allow in the future for easier extraction from places where now is difficult (or too expensive) to extract, the problem of finite resources remains open.

Fossil fuels present also an other negative aspect, beyond their limited and non-uniform distribution over the Earth. In fact, energy is produced during their combustion; during this process, large amounts of carbon dioxide are

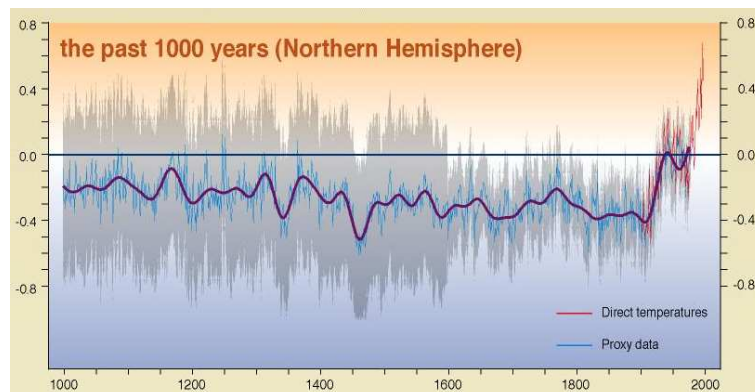


Figure 1.2: Evolution of average Earth temperature in the northern hemisphere in the last 1000 years.

released in the atmosphere. In the last 20 years there have been indications that the consumption of fossil fuels will have detrimental effects on our climate as a result of the accumulation of CO_2 in the atmosphere. The result of higher concentration of carbon dioxide is the strengthening of the greenhouse effect, which results mainly in the raise of temperature shown in Fig.1.2. An evident increase, that coincides with good approximation with the beginning of our industrial revolution, is clear. The connection with increasing emissions of combustion residual shown in Fig. 1.2 is quite straightforward, and the correlation between the two data is very strong [5]. Numerical models show that without increase in annual fossil consumption between now and the year 2100, we should expect an average temperature rise of approximately $1^\circ C$ by 2100. A faster rate of growth would lead to a temperature rise amounting approximately to $3.5^\circ C$ by the year 2100. Anyway it is only with great difficulty that the climatic effects of CO_2 can be distinguished from natural fluctuations in the yearly average temperature. There is a lack of agreement also on the quantitative validity of the models that relate CO_2 emissions to the temperature rise in the world's climate. There is further disagreement about the possible significance of a $3.5^\circ C$ rise in average temperature. Perhaps the most valid model for assessing the significance of an average temperature rise is in the Earth itself. In fact, between 4000 and 8000 years ago, the world was generally several degrees warmer than it is now: Europe, Alaska and many part of Africa were considerably wetter than they are now, and the central United States and the high northern latitudes were drier.

In addition to the problem of CO_2 concentration in the atmosphere, many of the known reserves of coal and oil contain large amounts (several percent) of sulfur. The combustion of this sulfur-laden fuel has large scale detrimental environmental effects. In the combustion process, the sulfur combines with oxygen to form sulfur dioxide, which is vented with the stack gases in the atmosphere. The sulfur dioxide reacts with water vapor to form acids which are detrimental to fish and plant life. Many species of game fish are sensitive to the acidity of the water in which they live. When the water becomes acid through acid rainfall, the fish can no longer survive. Acid rain tends also to acidify soil, thus retarding the growth of trees that are incapable of coping with the changed environment, such as some pines. Finally also monuments and buildings can be damaged and oxidized by the sulfur dioxide released during the rainfall. The effects of acid rain have been the subject of international conferences and the problems of acid rain has made it necessary either to install expensive scrubbers to remove sulfur before combustion occurs, or to develop atmospheric fluidized bed combustion technology to remove sulfur during the combustion process. Anyway, up to now many factories still

continue to use fossil fuels without removing the sulfur, especially in the emerging countries like China.

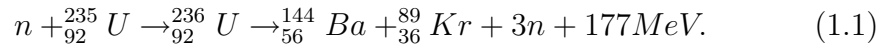
Regardless of the role of CO_2 in the global warming and its consequences, that we don't really know and about which many opinions still coexist, we have necessary and sufficient reasons to greatly restrict and/or cease to burn fossil fuels before known reserves are exhausted.

1.1.2 Alternative to Fossil Fuels

Many alternative energy sources have been suggested and even implemented on a small scale. These include wind power, tidal power, geothermal power, combustion of wood and biomass, hydroelectric power and solar energy. These alternative or renewable energy sources are not too promising as long term energy options, certainly not for the energy requirements implied by projections of our level of consumption. Many of these alternate energy sources are restricted to particular geological or geographic sites (tidal, geothermal, hydroelectric) and/or tend to be least available when most needed (solar energy at night or in the winter), and/or cannot be turned on and off at will to meet the power demand curve of an electric utility. Even if they are increasing in importance due to technological breakthroughs, up to now they cover less than the 10%, the most coming from hydroelectric (7%). These alternate energy sources will be useful only to supplement a source of primary power that can be turned off and on at will and that produces electrical power at an acceptable price for industry and the electric utilities.

The other important source of energy used so far to fulfill world energy needs is the nuclear power. As we will see, this definition lacks of precision, since it usually refers only to one of the two nuclear reactions that can be used to generate energy, the nuclear fission. In this process the nucleus of an atom splits into two or more smaller nuclei and usually some by-product particles, emitting energy in the form of gamma and other radiation. In order to obtain an exothermic reaction, the nucleus has to be heavier than Iron (and its isotopes), that is the most tightly bound element, i.e. the one with higher binding energy per nucleon (see Fig.1.4). For elements with mass number lower than iron the opposite reaction (fusion of light nuclei in a heavier one) can generate energy; this issue will be addressed in the next pages. In order to obtain energy from fission in the easiest way and with the higher production, usually the nuclear fuel (as it is called the father nucleus) is an isotope of Uranium, ^{235}U . The nuclear reaction can be activated with low energy neutrons ($\cong 1eV$), and yields fragments of intermediate mass (with average atomic masses near 100) and an average of 2.4 neutrons. These free neutrons released by each fission event can trigger yet more events, which

in turn release more neutrons and cause more fissions (the so-called *chain reaction*). An example of one of the many reactions in the ^{235}U fission process is:



Converting heat produced by reactions into kinetic energy by means of a steam turbine, and then into electricity using a generator, is the standard simplified use of energy developed by nuclear fission. Up to now nuclear power provides about 20% of the world's electricity. But the use of Uranium fission to generate electricity is still controversial because of the problem of storing radioactive waste for indefinite periods, the potential for possibly severe radioactive contamination by accident or sabotage, and the possibility that its use could lead in some countries to the proliferation of nuclear weapons. In addition many detractors claim nuclear power is an uneconomic, unsound energy source, especially compared to renewable energy. Moreover, Uranium is again a non-renewable resource and, at the present rate of use, there are 50 years left of low-cost known Uranium reserves.

Nuclear fission can be thus an alternate energy source in the next decades which may allow for a reduction of CO_2 from fossil fuels combustion. Anyway since the reserves of Uranium are limited, it is necessary to consider other solutions. As stated previously fission is not the only way to extract the nuclear energy from atom. The inverse process, fusion, has interesting and positive features both relative to the environment preservation and to the

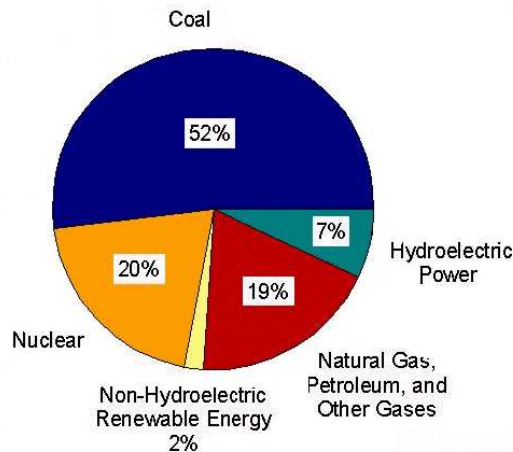


Figure 1.3: World Energy Use by type in 2000 to generate electricity. More than half of the electricity is still generated by fossil fuels, especially coal. Among the renewable energies only the hydroelectric power has a significant production, while the others (geothermal, biomass, solar, etc) are under the 2%.

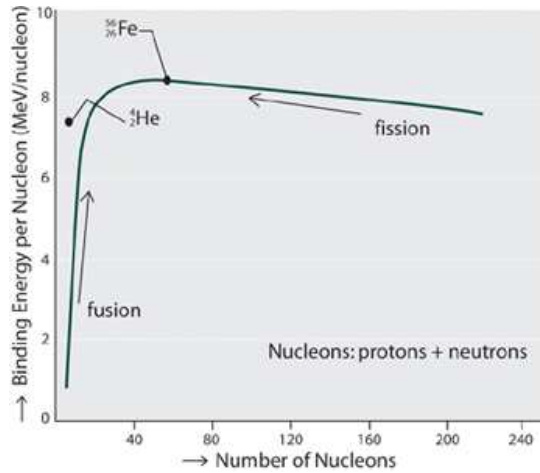


Figure 1.4: Bounding energy for nucleon as function of the atomic mass number. Elements on the left of Iron increase their bounding energy by fusing together and thus becoming more stable. On the contrary, elements with higher atomic mass than Iron tend to split in smaller atomic mass elements but with an increased bounding energy. In both the cases a final more stable state is reached.

availability of energy. We present in the next Section an overview on the physics which controls fusion reactions and the steps performed during the last 50 years towards its realization on Earth.

1.2 Thermonuclear Fusion

Thermonuclear fusion is referred to as the nuclear reaction among two light nuclei that fuse into a heavier one, releasing other reaction products like neutrons. This is a widespread phenomenon in nature. It is well known, for example, that fusion reactions provide a huge source of energy to stars and other astrophysical settings.

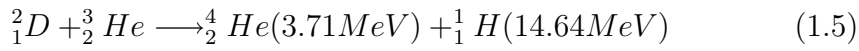
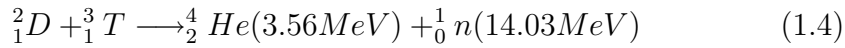
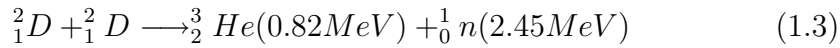
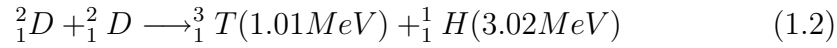
Two light nuclei can fuse together if they are brought sufficiently close for the short-range attractive nuclear force to overcome by quantum tunnelling the Coulomb repulsion among them. This is possible if the two reactants collide with high enough kinetic energy. For a significant fraction of fusion reactions to occur, matter has thus to be brought to high densities and temperatures for a sufficiently long time. In such conditions, matter is in the *plasma* state, a quasi-neutral ensemble of ions and electrons [6].

Two methods seem up to now to be rather promising to realize fusion conditions in the laboratory, i.e. the so called *magnetic confinement* and *inertial confinement* fusion.

- **Magnetic confinement** fusion [7], which will be the main focus of this Thesis, uses strong magnetic fields to confine matter in the plasma state.
- In **inertial confinement** [8] fusion experiments, on the other hand, small volumes of solid matter are brought to sufficiently high temperatures and densities by firing high power lasers from many different directions. This compresses and heats the matter, and brings it to critical conditions.

1.2.1 Fusion reactions and burning criteria

Some examples of fusion reactions are reported in the following:



The most favorable reaction in conditions attainable in laboratory is that reported in Eq. (1.4). As shown in Fig. 1.5, the cross-section of the D-T fusion reaction peaks in fact at a relatively low energy, $E \simeq 100keV$.

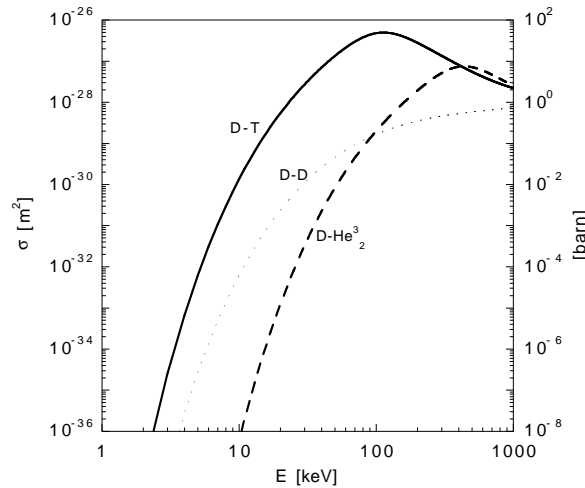
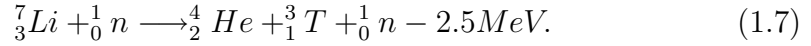
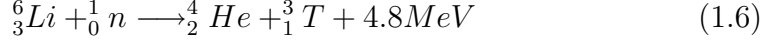


Figure 1.5: Cross-sections of the $D - T$, $D - D$, and $D - {}^3_2He$ fusion reactions as a function of the relative kinetic energy of the reactants.

Deuterium resources on Earth are practically endless, 0.0015% of hydrogen atoms in water being Deuterium, even though extraction methods are not yet affordable. Tritium is a hydrogen isotope which is not present in nature due to its radioactive half-life of 12.3 years. Tritium can be obtained from the two following reactions with Lithium:



The assembly of a Lithium blanket on the vacuum vessel of fusion reactors is estimated to provide the necessary Tritium source for an unlimited period of time, based on the present Lithium resources. Compared to fossil fuel power plant, there is no production of greenhouse gases, since the main natural product of the fusion reaction is Helium, which is completely harmless to life and does not contribute to global warming. Compared to nuclear fission power, the problems of accidents and radioactive waste is much less prominent, since the fuel contained in the reaction chamber is only enough to sustain the reaction for about a minute, whereas a fission reactor contains about a year's supply of fuel; moreover the half-time of Tritium prevents unlimited build-up and longterm contamination. In addition, in a fusion reactor, there is no risk of uncontrolled runaway of the reaction due to accidents.

For the energy balance of a fusion reactor to be positive, the energy produced by fusion reactions has to exceed that required to create and sustain the plasma itself. One form of energy loss for a D-T plasma with electron density n ($n_{D,T} = n/2$) and temperature T is bremsstrahlung radiation [6]. The power lost per unit volume due to bremsstrahlung emission is $P_b = bn^2T^{1/2}$, where b is a function of the effective charge $Z_{eff} = n^{-1} \sum_i n_i Z_i^2$ in a multi-species plasma. In addition, power losses due to confinement degradation, e.g. through collisional and turbulent transport phenomena, have to be considered in the power balance. A simple estimate of the energy losses due to mechanisms different from bremsstrahlung can be made as $P_t = 3nT/\tau_E$, by introducing the characteristic *energy confinement time* τ_E and the heating power P_t .

The power generated by fusion reactions can be written as $P_n = W_{DT}n^2 \langle \sigma v \rangle_T / 4$, where $W_{DT} = 17.59\text{MeV}$ is the energy released after a single D-T fusion reaction, and $\langle \sigma v \rangle_T$ is the product of the reaction cross-section and the relative velocity of the reactants averaged over a Maxwellian velocity distribution. Note that this last term is a function of temperature. Let us assume that the reaction power P_n balances the energy losses with an efficiency η . The self-sustainment condition is thus:

$$P_b + P_t \leq \eta(P_b + P_t + P_n), \quad (1.8)$$

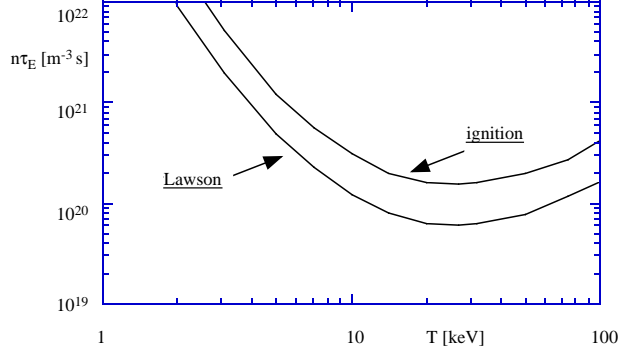


Figure 1.6: The minimum $n\tau_E$ curves for which the Lawson's and ignition criteria are satisfied. The Lawson's curve refers to an efficiency $\eta = 30\%$.

which can be rewritten as:

$$n\tau_E \geq 3T \left(\frac{\eta}{1-\eta} \frac{W_{DT}}{4} \langle \sigma v \rangle_T - bT^2 \right)^{-1}. \quad (1.9)$$

This last expression is also known as *Lawson's criterion* [9]. The right end side of Eq. (1.9) depends only on temperature, hence the product $n\tau_E$ where the equality is satisfied can be plotted as a function of T . In Fig. 1.6, the curve with efficiency $\eta = 30\%$ is reported, which has a minimum at $T \simeq 20\text{keV}$. Eq. (1.9) evaluated at this temperature becomes:

$$n\tau_E \geq 0.6 \cdot 10^{20} \text{m}^{-3} \text{s}. \quad (1.10)$$

The best reactor scenario is one in which the α particles (${}^4_2\text{He}$ nuclei) produced by fusion reactions are confined by the magnetic field, and replace all the energy losses by transferring their energy to the plasma, whereas neutrons escape the plasma volume and their energy is converted to electric energy. In this case the Lawson's criterion must be modified, it is called *ignition criterion* and is written as:

$$P_b + P_t \leq P_\alpha, \quad (1.11)$$

which can be expressed as:

$$n\tau_E \geq 3T \left(\frac{W_\alpha}{4} \langle \sigma v \rangle_T - bT^2 \right)^{-1}, \quad (1.12)$$

where $W_\alpha = W_{DT}/5$ is the energy of a single α particle after a fusion reaction. The $n\tau_E$ curve that corresponds to the equality is shown in Fig. 1.6. As the

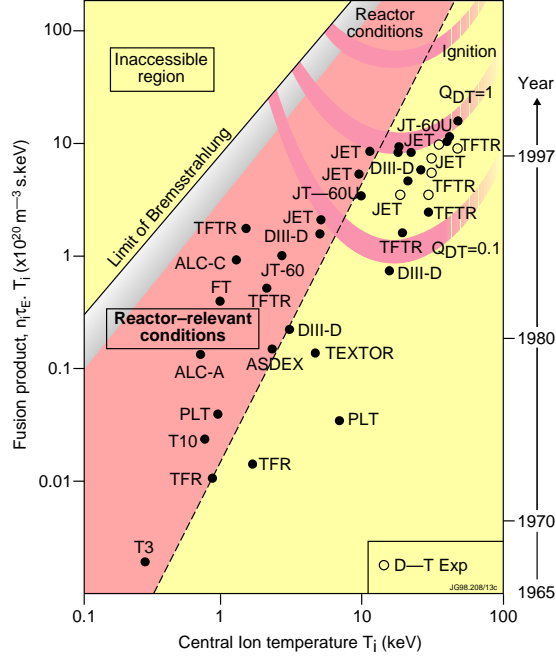


Figure 1.7: Values of the fusion triple product $n\tau_E T_i$ obtained in $D-T$ tokamak experiments as a function of the central ion temperature T_i .

Lawson's criterion curve, the ignition curve has a minimum at $T \simeq 20\text{keV}$, and the requirement for ignition at this temperature is:

$$n\tau_E \geq 1.5 \cdot 10^{20} \text{m}^{-3} \text{s}. \quad (1.13)$$

This last result can also be written through the so called *triple product*:

$$n\tau_E T \geq 3 \cdot 10^{21} \text{m}^{-3} \text{skeV}. \quad (1.14)$$

For temperatures $T \sim 20\text{keV}$ and electron densities $n \sim 10^{20}\text{m}^{-3}$, which are fixed in laboratory experiments by physical and technological constraints, the energy confinement time τ_E must be greater than 1s , as it is clear from Fig. 1.7.

1.2.2 From the Sun to ITER

Conditions approaching ignition have been achieved only in recent years in different tokamak experiments, after few decades of interesting theoretical studies and experiments. The scientific study of fusion energy had its origin in the astrophysical subdiscipline of stellar structure, the study of the origin,

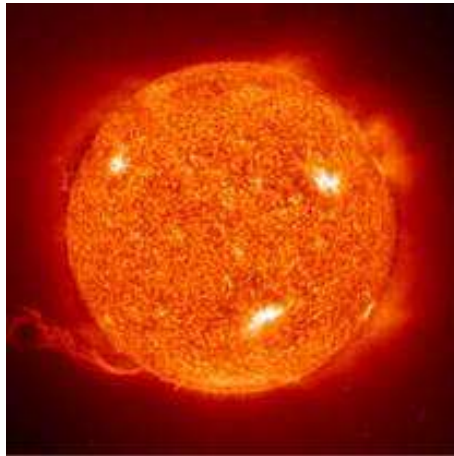


Figure 1.8: Fusion is the engine of the Sun. The first studies on fusion reactions and their cross sections had started in astrophysics and cosmology.

evolution, and fate of the Sun and the stars. It was not until the early 1930's that enough data became available about the cross sections and energy release of fusion reactions to formulate specific models for stellar fusion reactions. By 1940, informations were available to describe the major features of the conversion of hydrogen into Helium by the majority of the stars, including the Sun. By 1960, the discipline of stellar structure had advanced so that the life history of nearly all types of stars could be correctly described. A self-consistent model was available which described the origin of the heavy elements in the supernova explosions and predicted correctly the relative isotopic abundance of the naturally occurring elements.

Beyond the provision of basic cross section data, however the discipline of stellar structure had relatively little influence on the development of controlled fusion energy. Unlike magnetically-contained plasmas, the interior of stars is in thermodynamic equilibrium. Thus, the powerful theoretical tools of classical thermodynamics can be used to specify the properties and the behavior of stellar interiors. Stars also differ from magnetically-confined plasmas as the containment is provided by their deep gravitational potential wells. Unfortunately, it takes an amount of matter somewhat larger than the planet Jupiter to provide gravitational confinement!

Experimental research on magnetic fusion began shortly after 1950 in England, the URSS and the United States. In these countries fusion research was classified from its inception until 1958. During this classified phase, the fusion program in the Unites States was known as Project Sherwood. Many of the current mainline and alternate approaches to magnetic fusion, includ-

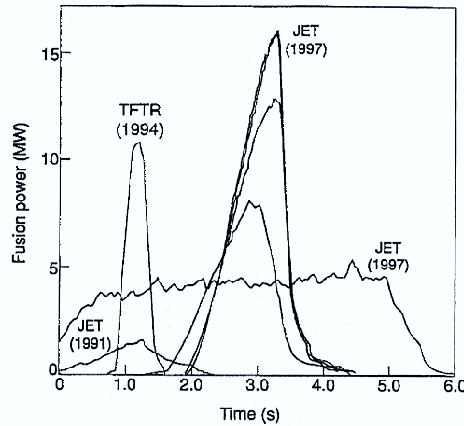


Figure 1.9: Waveforms of the fusion power produced in $D - T$ discharges in the JET and TFTR tokamak experiments [10],[11].

ing the stellarator, the magnetic mirror and various pinch configurations, had their origins during this period. By 1958 the original reasons for classifying fusion research were no longer persuasive, and all countries engaged in magnetic fusion research agreed to declassify their programs at the Second United Nations Conference on the Peaceful Uses of Atomic Energy held in Geneva, Switzerland in late 1958.

During most of the first 20 years of controlled fusion research, the confinement time achieved experimentally in toroidal devices was far below the durations theoretically predicted. In the first years of fusion research, progress in confinement was quite rapid. About 1955, however, the confinement time saturated at the much shorter Bohm or *anomalous* value and remained there for approximately ten years.

In 1965, Russian scientist under the leadership of Lev Artsimovitch were the first to report particle containment times significantly in excess of the Bohm value from their Tokamak, a toroidal containment device which featured a strong toroidal magnetic field combined with magnetic field generated by a large current flowing in the plasma. After 1968, progress both in URSS and the United States was quite rapid, and by 1970 several researches using other devices reported containment times sufficiently long that a new power producing fusion reactor appeared feasible.

The physical processes responsible for Bohm or anomalous diffusion during the era from 1955 through 1965 remain poorly understood. The success of the tokamak in rising above this level of containment can be termed a breakthrough and is largely responsible for the current optimism in fusion research. Because of this initial success, the tokamak magnetic-containment

concept became the dominant approach in the fusion programs of all major industrialized countries. Examples of D-T discharges from the European tokamak experiment JET and the American tokamak TFTR, where record high fusion power was produced for the first time, are shown in Fig. 1.9. Anyway others configurations like the Reversed Field Pinch (RFP) and the Stellarators are still studied as possible alternatives to the Tokamak and to understand basic plasma physics problems.

The large experimental database obtained in the last decade in tokamaks and other toroidal configurations, and the improving capability of numerical simulations have provided the international community the physics basis for the design of a burning plasma experiment based on the tokamak concept, which is called International Thermonuclear Experimental Reactor (ITER) [12, 13]. The designed parameters of the ITER machine are a major radius of the torus $R_0 = 6.2m$, minor radius $a = 2m$, maximum magnetic field $B = 5.3T$ and plasma current $I_p = 15MA$. ITER is predicted to produce inductively driven D-T burning plasmas. The discharge duration is designed to be several hundred seconds, which can be regarded as a stationary condition on the time scales characteristic of the plasma processes. A ratio of fusion power to auxiliary heating power $Q = Q_{fus}/Q_{aux} \geq 10$ is expected for ITER, at a nominal fusion power output of about $500MW$. All of these parameters have been predicted for plasmas with density $n \simeq 10^{20}m^{-3}$ and core electron and ion temperatures $T_e \simeq 8.8keV$ and $T_i \simeq 8keV$, respectively. ITER is designed to work also in a steady-state operation with less power gain $Q \geq 5$, by using a large fraction of non-inductive current drive.

ITER would offer the possibility of studying several reactor relevant scientific and technological issues, which are beyond the present experimental capabilities. In particular, regimes in which the α particles contribute significantly to the plasma pressure are very interesting. In these conditions a class of plasma instabilities is predicted to be driven by the α particles, which can only in part be studied in the present tokamaks. The study of plasma instabilities and their control is only one aspect of the research in burning scenarios. A variety of technological issues could also be studied in ITER, like for example the test of advanced materials facing very large heat and particle fluxes, the test of concepts for a Tritium breeding module, and many others. For example the interaction of the plasma with a divertor plate will be studied in ITER [14]. The divertor has the important function to exhaust the flow of energy from charged particles produced in the fusion reactions and to remove Helium and other impurities resulting from the reactions, and from interaction of plasma particles with the material walls.

The auxiliary systems needed to achieve the conditions expected in ITER are an external heating and current drive capability of about $73MW$ and

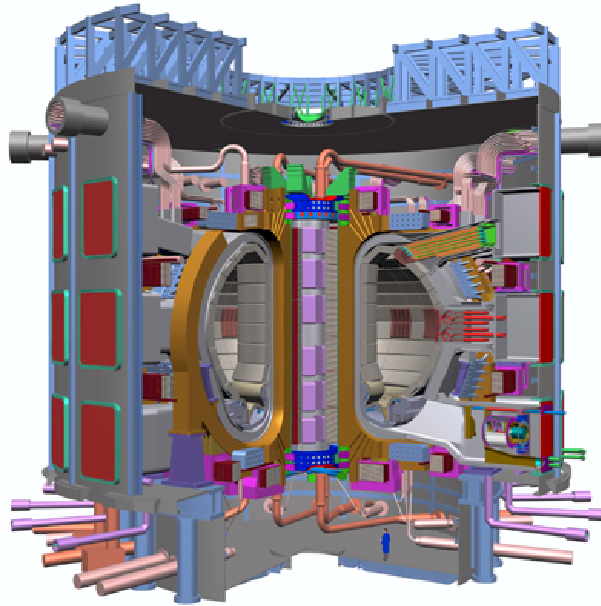


Figure 1.10: Schematic of the International Thermonuclear Experimental Reactor (ITER) design.

several advanced diagnostics for both analysis and plasma control. All of these requirements are expected to solve many of the scientific and engineering issues concerning a burning plasma, and could allow us to make a significant next step towards the demonstration of a tokamak power-plant.

1.3 Plasma and its properties

As introduced in the previous sections, at the high temperatures required to obtain nuclear fusion reactions, matter is not anymore in the ordinary state we can see everyday in our life, but becomes an ensemble which contains enough charged particles for its dynamics to be dominated by electromagnetic forces. In practice quite modest degrees of ionization are sufficient for a gas to exhibit electromagnetic properties. Even at 0.1% ionization a gas already has an electrical conductivity almost half the maximum possible, which is reached at about 1% of ionization.

Perhaps the most notable feature of a plasma is its ability to maintain a state of charge neutrality. The combination of low electron inertia and strong electrostatic field, which arises from even the slightest charge imbalance, results in a rapid flow of electrons to re-establish neutrality. The first point to note, on this issue, concerns the nature of the electrostatic field. Although at

first sight it might appear that the Coulomb force due to any given particle extends over the whole volume of the plasma, this is in fact not the case. Debye, in the context of electrolytic theory, was the first to point out that the field due to any charge imbalance is shielded so that its influence is effectively restricted to within a finite range [6].

For example we may suppose that an additional ion with charge Ze is introduced at the point P in an otherwise neutral plasma. The effect will be to attract electrons towards P and repel ions away from P so that the ion is surrounded by a neutralizing *cloud*. Ignoring ion motion and assuming that the number density of the electron cloud n_c is given by a Boltzmann distribution $n_c = n_e \exp(e\phi/k_B T_e)$, where T_e is the electron temperature, we solve the Poisson's equation for the electrostatic potential ϕ in the plasma. The final potential as function of r , the distance from P , is given by:

$$\phi(r) = \frac{Ze}{4\pi\epsilon_0 r} \exp(-r/\lambda_D) \quad (1.15)$$

where

$$\lambda_D = \frac{\epsilon k_B T_e^{1/2}}{n_e e^2} \quad (1.16)$$

is called the Debye shielding length. Beyond a Debye sphere, a sphere of radius λ_D centered at P , the plasma remains effectively neutral. By the same argument λ_D is also a measure of the penetration depth of external electrostatic field, i.e. of the thickness of the boundary sheet over which charge neutrality may not be maintained.

The plausibility of the argument used to establish Eq.1.15 requires that a large number of electrons is present within the Debye sphere, i.e. $n_e \lambda_D^3 \gg 1$. The inverse of this number is proportional to the ratio of potential energy to kinetic energy and plays a key role in the development of formal plasma theory. Broadly speaking, the more particles there are in the Debye sphere the less likely it is that there will be a significant resultant force on any given particle due to *collisions*. The quantity $(n_e \lambda_D^3)^{-1}$ is therefore a measure of the dominance of collective interactions over collisions [15].

The most fundamental of these collective interactions are the *plasma oscillations* set up in response to a charge imbalance. The strong electrostatic fields which drive the electrons to re-establish neutrality cause oscillations about the equilibrium position at a characteristic frequency, the *plasma frequency* ω_p . Since the imbalance occurs over a distance λ_D and the electrons speed is typically $v_e = (k_B T_e / m_e)^{1/2}$ we may express the electron plasma frequency by:

$$\omega_{pe} = \frac{v_e}{\lambda_D} = \left(\frac{n_e e^2}{m_e \epsilon_0} \right)^{1/2}. \quad (1.17)$$

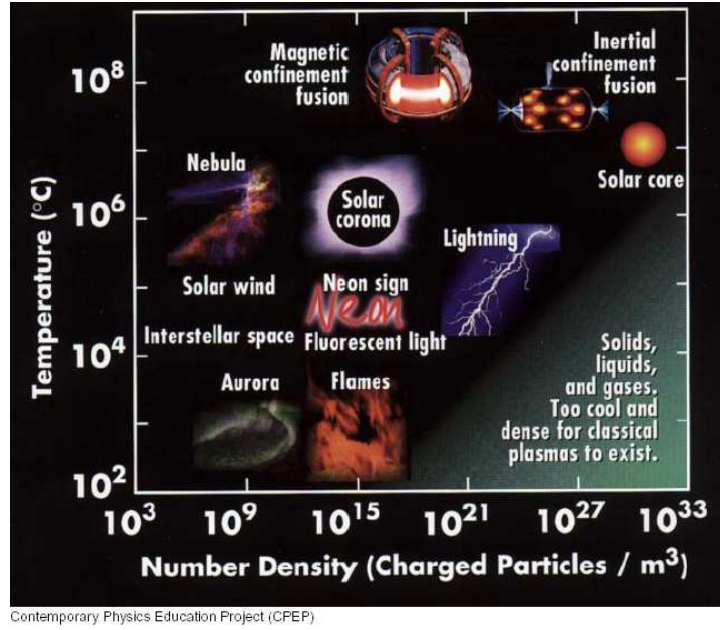


Figure 1.11: Landmarks in the plasma universe.

Note that any applied fields with frequency less than the electron plasma frequency are prevented from penetrating the plasma by the more rapid electrons response which neutralize the field. Thus a plasma is not transparent to electromagnetic radiation of frequency $\omega < \omega_{pe}$. The corresponding frequency for ions, the ion plasma frequency, is defined by:

$$\omega_{pi} = \left(\frac{n_i (Ze)^2}{m_i \epsilon_0} \right)^{1/2}. \quad (1.18)$$

where Z denotes the charge state.

We have seen that the effective range of an electric field, and hence of a collision, is the Debye Length λ_D . Thus, any particle interacts at any instant with the large number of particles in its Debye sphere. Plasma collisions are therefore many body interactions. We will discuss the different type of collisions and their effects in section 3.8. We report here only the important result for electrons collisions with ions of charge Ze ; the electron-ion collision time $\tau_{ei} = \nu_{ei}^{-1}$ is given by [6]:

$$\tau_{ei} = \frac{2\pi\epsilon_0^2 m_e^{1/2} (k_B T_e)^{3/2}}{Z^2 n_i e^4 \ln(4\pi n \lambda_D^3)}. \quad (1.19)$$

Strictly related to the collision frequency is the resistivity η of the plasma

which has the following expression:

$$\eta = \frac{m_i}{n_e e^2 \tau_{ei}}. \quad (1.20)$$

Typical value for a hydrogen plasma with $T_e = 1keV$ is $\eta = 2 \times 10^{-8} \Omega m$, the same resistivity of copper.

Fig. 1.11 shows a diagram of different plasmas as function of density and temperature which are the main parameters defining the Debye length and the plasma frequency for a given plasma. We see that plasma spans an enormous ranges in scale length, density of particles and temperatures. Fusion plasmas, the ones we are interestd in, are characterized by density of $\approx 10^{19} - 10^{20} m^{-3}$ and temperatures of $1 - 10keV$.

1.4 Magnetic plasma confinement

Several magnetic field geometries have been investigated for many years in fusion research to seek the best conditions for plasma confinement. Examples are magnetic mirrors, linear and toroidal configurations, and many others. Among them the toroidal geometry has given up to now the best confinement performances. This section will be dedicated to a brief introduction to the principles of magnetic plasma confinement in toroidal devices, and in particular in the so called tokamak and reversed-field pinch (RFP) configurations.

We define in Fig.1.12 the toroidal coordinates (r, θ, ϕ) : r is called radial coordinate, θ and ϕ are the poloidal and toroidal angles, respectively. By R_0 and a we indicate the major and minor radius of the torus, respectively.

Magnetic field lines in toroidal experiments have both a poloidal component B_θ , which is mainly generated by an externally driven toroidal plasma

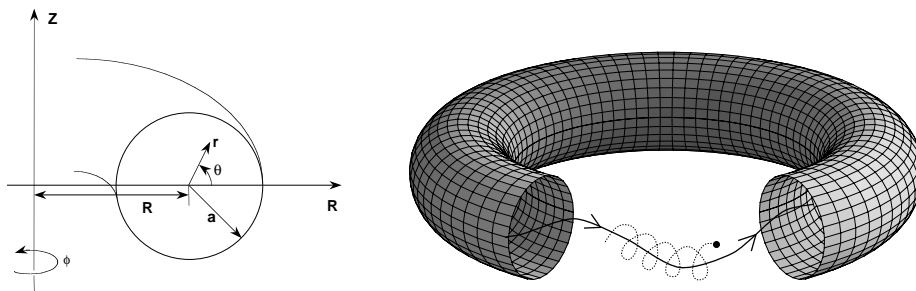


Figure 1.12: The system of toroidal (r, θ, ϕ) and cylindrical coordinates (R, ϕ, Z) (on the left). A scheme showing the principle of toroidal confinement (on the right): a charged particle orbits around a helical magnetic field line and is thus confined within the toroidal device.

current j_ϕ , and a toroidal component B_ϕ , which in some configurations is only in part produced by currents flowing in external conductors. The plasma itself can produce a large fraction of current through dynamo effects, which will be discussed more deeply in Chapter 4. Magnetic field lines are thus helices, which wound around the torus lying over toroidal surfaces called *magnetic surfaces*. Helical magnetic field lines are described by the so called *safety factor* q , which is defined as a function of radius as follows:

$$q(r) = \frac{rB_\phi(r)}{R_0B_\theta(r)}. \quad (1.21)$$

The inverse of this quantity represents the number of poloidal turns done by a helical field line per one toroidal turn. The name safety factor comes from the fact that this quantity is crucial to determine several features of the plasma instabilities.

1.4.1 MHD Equations

A large variety of plasma properties, like for instance the magnetic equilibria used to confine thermonuclear plasmas and several instabilities associated with them, can be described using a fluid model called *resistive magnetohydrodynamics (MHD)* [16], which will be briefly introduced in the following.

Let us consider here for simplicity a hydrogen plasma, but it would be possible to extend the present description also to multiple species plasmas. In the two-fluid MHD, where the two fluids are that of ions and that of electrons, the mass and momentum continuity equations can be written as follows:

$$\frac{\partial \rho_\alpha}{\partial t} + \nabla \cdot (\rho_\alpha \mathbf{u}_\alpha) = 0, \quad (1.22)$$

$$\rho_\alpha \left(\frac{\partial \mathbf{u}_\alpha}{\partial t} + \mathbf{u}_\alpha \cdot \nabla \mathbf{u}_\alpha \right) = \sigma_\alpha \mathbf{E} + \mathbf{j} \times \mathbf{B} - \nabla p_\alpha + \mathbf{R}_{\alpha\beta}, \quad (1.23)$$

where $\alpha, \beta = i, e$ (i.e. ions or electrons), $\rho_\alpha = m_\alpha n_\alpha$ is the mass density, and $\sigma_\alpha = \pm en_\alpha$ is the charge density of the single species. No particle or momentum sources are considered here for simplicity. The electromagnetic quantities \mathbf{E} , \mathbf{B} , and \mathbf{j} have the usual meaning. The first two terms in the right hand side of Eq. 1.23 represent the electromagnetic forces, $-\nabla p_\alpha$ is the kinetic pressure force, which is in general a tensor quantity, and $\mathbf{R}_{\alpha\beta}$ is the rate at which momentum is gained or lost by species α due to collisions with species β . Note in particular that the following relation holds: $\mathbf{R}_{\alpha\beta} = -\mathbf{R}_{\beta\alpha}$.

A plasma can be described as a single fluid by introducing the following variables: the mass density $\rho = \rho_i + \rho_e$, the kinetic pressure $p = p_i + p_e$, the mass fluid velocity $\mathbf{u} = (\rho_i \mathbf{u}_i + \rho_e \mathbf{u}_e) / \rho$, and the charge density $\sigma = e(n_i - n_e)$. By using these relations and combining the two-fluid Eqs. 1.22 and 1.23, it is simple to derive the following fluid equations (we follow here the derivation reported in [6]):

$$\frac{\partial \rho}{\partial t} + \nabla \cdot (\rho \mathbf{u}) = 0, \quad (1.24)$$

$$\rho \left(\frac{\partial \mathbf{u}}{\partial t} + \mathbf{u} \cdot \nabla \mathbf{u} \right) = \sigma \mathbf{E} + \mathbf{j} \times \mathbf{B} - \nabla p, \quad (1.25)$$

$$\mathbf{E} + \mathbf{u} \times \mathbf{B} = \eta \mathbf{j} + \frac{\mathbf{j} \times \mathbf{B} - \nabla p_e}{ne}. \quad (1.26)$$

Eq. 1.24 is the mass continuity equation, Eq. 1.25 is the momentum continuity equation, also called single-fluid equation of motion, and Eq. 1.26 is the generalized Ohm's law, which is not strictly a single-fluid equation due to the presence of the ∇p_e term.

The generalized Ohm's law is derived from the electron equation of motion under the often verified assumption of negligible electron inertia, and by writing the e-i collision term as follows: $\mathbf{R}_{ei} = m_e n_e \langle \nu_{ei} \rangle (\mathbf{u}_i - \mathbf{u}_e) = \eta n e \mathbf{j}$. Here the simple expression $\langle \nu_{ei} \rangle = \eta n_e e^2 / m_e$ for the e-i collision frequency averaged over a Maxwellian distribution is used, η being the plasma resistivity. In a plasma, the fluid motion across a magnetic field induces the electric field $\mathbf{u} \times \mathbf{B}$. The last two terms in the right-hand side of Eq. (1.26) arise due to the Hall and the diamagnetic effects, respectively.

What it is usually referred to as *resistive MHD model* can be derived by the fluid equations 1.24, 1.25 and 1.26 under the following two approximations: (i) charge quasi-neutrality, $n_i \simeq n_e$, which permits one to drop the term $\sigma \mathbf{E}$ in Eq. 1.25; and (ii) small ion Larmor radius compared with the scale-length of the fluid motion, which causes the Hall and diamagnetic terms in Ohm's law to be negligible with respect to the other terms.

We must add to this system of equations the Maxwell equations, in which the displacement current $\epsilon_0 \mu_0 \partial \mathbf{E} / \partial t$ can be neglected in most cases of interest, and a closure for the heat flux tensor. To this purpose, an equation of state for pressure is often used of the form $p \propto n^\gamma$. The exponent γ can be chosen depending on the phenomena to be modelled. For example, $\gamma = 1$ represents isothermal compression and $\gamma = 5/3$ adiabatic compression. The resistive MHD model is thus constituted by a set of single-fluid equations,

which can be summarized as follows:

$$\begin{aligned}
\frac{\partial \rho}{\partial t} + \nabla \cdot (\rho \mathbf{u}) &= 0 & \nabla \times \mathbf{B} &= \mu_0 \mathbf{j} & (1.27) \\
\rho \left(\frac{\partial \mathbf{u}}{\partial t} + \mathbf{u} \cdot \nabla \mathbf{u} \right) &= \mathbf{j} \times \mathbf{B} - \nabla p & \nabla \cdot \mathbf{B} &= 0 \\
\mathbf{E} + \mathbf{u} \times \mathbf{B} &= \eta \mathbf{j} & \nabla \times \mathbf{E} &= -\frac{\partial \mathbf{B}}{\partial t}
\end{aligned}$$

By combining Faraday's law with Ohm's law, it is simple to derive the following equation, which describes the coupled dynamics of the magnetic and fluid velocity fields in the resistive MHD framework:

$$\frac{\partial \mathbf{B}}{\partial t} = \nabla \times (\mathbf{u} \times \mathbf{B}) + \frac{\eta}{\mu_0} \nabla^2 \mathbf{B}, \quad (1.28)$$

The first term on the right-hand side in Eq. (1.28) describes convection of the magnetic field with the plasma, and its amplification or reduction due to compressive motion perpendicular to the magnetic field. Starting from this equation, it is possible to show that, in the *ideal* MHD limit, i.e. in the case where the resistivity η is negligible, the magnetic field lines move like if it were *frozen* to the plasma. The second term describes instead resistive diffusion of the field across the plasma.

A figure of merit for magnetic confinement is the so called β parameter, a dimensionless number introduced to estimate how much plasma pressure is balanced by the magnetic field pressure:

$$\beta = \frac{p}{B^2/2\mu_0}. \quad (1.29)$$

The toroidal or the poloidal magnetic field separately can be used in the above definition, and in this case the β parameter is called poloidal β_θ or toroidal β_ϕ respectively.

1.4.2 MHD Instabilities

The MHD equations introduced in 1.4.1 predict that under certain conditions a small perturbation in a fluid quantity, like for example the density, the fluid velocity, or the magnetic field, can grow unstable in time. These phenomena are called MHD instabilities [17], and are very important in determining the dynamics of many natural and laboratory plasmas. They can be present also in toroidal fusion devices, where they influence in many ways the global plasma properties, and can deteriorate the plasma confinement performances.

A perturbation $\tilde{\mathbf{A}}$ of a quantity \mathbf{A} in a toroidal plasma can be Fourier analyzed as follows:

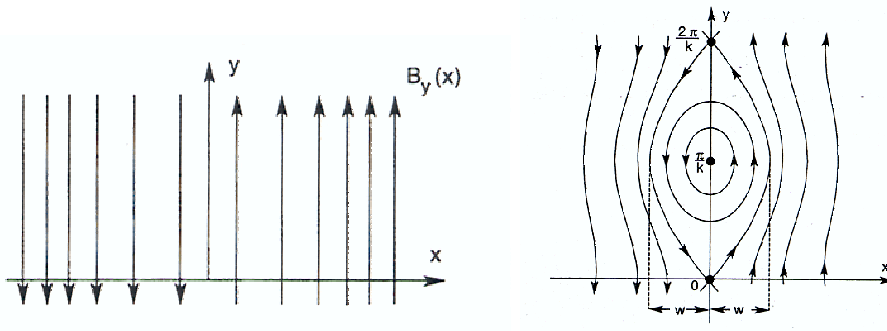


Figure 1.13: A sheared magnetic field in the x-y plane, plus a strong perpendicular z-component (left); the resultant magnetic field lines, after bending and reconnection due to the tearing instability (right). A magnetic island forms in this magnetic configuration, whose separatrix divides two regions with different field line topology.

$$\tilde{\mathbf{A}}(\mathbf{r}) = \sum_{\mathbf{k}} \tilde{\mathbf{A}}_{\mathbf{k}}(r) e^{i(\mathbf{k} \cdot \mathbf{r} - \omega t)} = \sum_{\mathbf{k}} \tilde{\mathbf{A}}_{\mathbf{k}}(r) e^{i(m\theta + n\phi - \omega t)}, \quad (1.30)$$

where $\mathbf{k} = (k_r, k_\theta, k_\phi) = (k_r, m/r, n/R_0)$ is the wavevector in toroidal coordinates, and m and n are the *poloidal* and *toroidal mode number*, respectively. Each couple (m, n) represents a helical perturbation, or mode. The angular frequency ω is in general a complex quantity, $\omega = \omega_R + i\omega_I$, of which the real part describes the propagation velocity, while the imaginary part represents an exponential growth, if $\omega_I > 0$, or damping of the perturbation amplitude, if $\omega_I < 0$.

A helical magnetic perturbation with wavevector \mathbf{k} can become unstable if it fulfills the resonance condition $\mathbf{k} \cdot \mathbf{B} = 0$, where $\mathbf{B} = (0, B_\theta, B_\phi)$ is the equilibrium magnetic field. In fact, a perturbation with $\mathbf{k} \cdot \mathbf{B} \neq 0$ would bend the mean magnetic field, and it would be thus energetically unfavored. The above resonance condition can be rewritten as follows:

$$\mathbf{k} \cdot \mathbf{B} = \frac{m}{r} B_\theta + \frac{n}{R_0} B_\phi = 0 \quad \longrightarrow \quad q(r) = \frac{r}{R_0} \frac{B_\phi(r)}{B_\theta(r)} = -\frac{m}{n}. \quad (1.31)$$

This shows that helical instabilities can grow only at radial positions where the safety factor assumes rational values. For this reason, these positions are called *rational* or *resonant radii*, and will be described later on for the tokamak and the RFP toroidal configurations.

Like in neutral fluids, a plasma instability can be driven, for example, by a thermal gradient. Under certain conditions, this can provide the neces-

sary free-energy for a whatever small perturbation to grow unstable. But also many other driving terms can be present in plasmas. An important example is given by the so called *tearing mode* [6, 17, 18] which is driven unstable by a gradient in the current density parallel to the magnetic field. The name of this instability comes from the fact that the magnetic field lines tear and reconnect during its evolution. This is represented in Fig. 1.13, where a sheared magnetic field is shown, which has also a strong magnetic field perpendicular to the x-y plane. Such a magnetic configuration is produced by a current profile with a gradient localized where the B_y component changes its sign. It is possible to show that, when this gradient is sufficiently high, a tearing instability is triggered, which causes the magnetic field lines to bend and reconnect, as represented in the figure. The resulting magnetic configuration is characterized by the formation of a so called *magnetic island*. In toroidal plasmas, such islands have a helical structure. In the following Chapters, we will show that tearing modes play an important role in toroidal plasma dynamics, and particularly in the RFP.

1.4.3 Tokamak and RFP

Several toroidal configurations have been investigated in fusion research, which are characterized by different magnetic field and safety factor profiles, instability behavior, and maximum attainable β values at comparable input power. We will focus here on two such configurations, i.e. the tokamak [19] and the RFP [20].

The tokamak and the RFP are similar under many aspects. In particular, they both belong to the class of *toroidal pinch* devices, in which a toroidal current is inductively driven by an external circuit, and generates a poloidal magnetic field that confines and compresses the plasma [16]. In both cases, the toroidal magnetic field is in part generated by external coils. Differences are given in the following, both in the basic physics processes underlying their dynamics and in more technical aspects.

Tokamak. This configuration is characterized by a relatively strong toroidal magnetic field B_ϕ and a much weaker poloidal magnetic field $B_\theta \sim 10^{-1}B_\phi$, as shown in Fig. 1.14. The toroidal magnetic field can reach values up to $8T$ in high-field machines, like for example FTU in Rome (Italy). Given these magnetic profiles, the tokamak safety factor usually increases monotonically with the radial coordinate r , with typical values greater or close to unity in the core, as represented in Fig. 1.15. For stability requirements, tokamak operation is preferable at $q > 1$, which is called *Kruskal-Shafranov limit*. When a rational surface $q = 1$ is present in the plasma, a strong ($m = 1, n =$

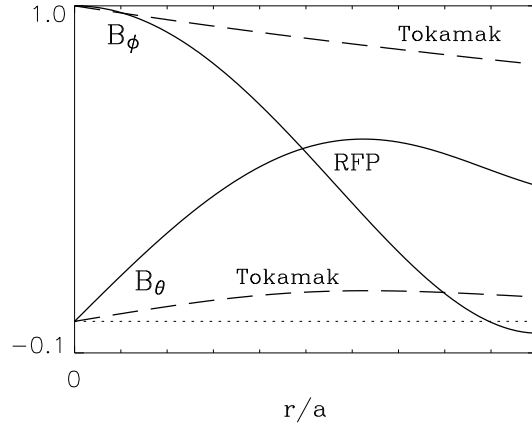


Figure 1.14: Typical radial profiles of the toroidal B_ϕ and poloidal B_θ components of the equilibrium magnetic field in a tokamak (dashed lines) and a RFP (continuous lines). The profiles are normalized to the value of B_ϕ in the plasma center at $r/a = 0$.

1) kink instability can grow unstable. This is usually characterized by a strong sawtooth dynamics, which causes severe confinement losses, and in some cases it can abruptly terminate the discharge. Other kinds of safety factor profiles have been studied in advanced tokamak operation, like for examples non-monotonic dependencies, which use magnetic and flow shear to stabilize the plasma instabilities and achieve enhanced confinement conditions [19].

The Kruskal-Shafranov limit takes to a limitation on the maximum achievable plasma current and related Ohmic heating in tokamaks, so that additional complex heating methods, like for example neutral beam or radio-frequency heating, are needed to reach thermonuclear conditions.

Reversed-field pinch. Differently from the tokamak, the toroidal and poloidal components of the magnetic field in the RFP are relatively weak and of comparable magnitude, $B_\phi \sim B_\theta$, as shown in Fig. 1.14. This implies that a simpler technology is required to generate the magnetic fields.

The name RFP comes from the fact that the toroidal magnetic field reverses its sign near the plasma edge. As a consequence, the safety factor profile also changes its sign at the same radius, as shown in Fig. 1.15. The RFP is thus an intrinsically low safety factor device. For this reason, a broad spectrum of ($m = 1, n \lesssim 2R_0/a$) magnetic modes is resonant throughout the plasma radius, and several ($m = 0, n \geq 1$) modes are resonant at the reversal radius. This has many consequences on the dynamics of this configuration

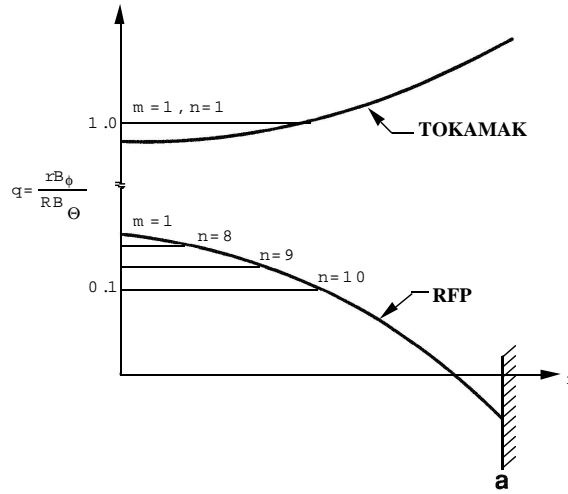


Figure 1.15: Safety factor profiles for a tokamak and a RFP. Horizontal lines indicate the $(m = 1, n)$ rational radii.

and on its transport properties, as we will see in section 1.6.

Low safety factor operation in the RFP does not bring to dangerous disruptive behavior. This is due to the combined action of a high level of magnetic shear (which characterizes this configuration and has a strong stabilizing function on the magnetic modes) and of a conducting shell (which passively reacts against growing magnetic perturbations).

For all the above reasons, the plasma current in the RFP is not limited by the Kruskal-Shafranov limit, as it happens in tokamaks. As an effect, the RFP can operate at plasma currents about ten times larger than in tokamaks with the same toroidal field, and it can reach $\beta \sim 10\%$ through Ohmic heating only.

Here we introduce for future reference two dimensionless parameters that are often used to describe pinch equilibria like the tokamak and the RFP. These are the so called *pinch parameter* Θ and the *reversal parameter* F , and are defined as follows:

$$\Theta = \frac{B_\theta(a)}{\langle B_\phi \rangle} \quad F = \frac{B_\phi(a)}{\langle B_\phi \rangle}, \quad (1.32)$$

where $\langle \dots \rangle$ indicates an average over a poloidal cross-section. In terms of these quantities, the tokamak is typically a low- Θ device with $F > 0$, while the RFP is a relatively high- Θ configuration, with $F < 0$.

Stellarator. A further toroidal configuration which could give interesting re-

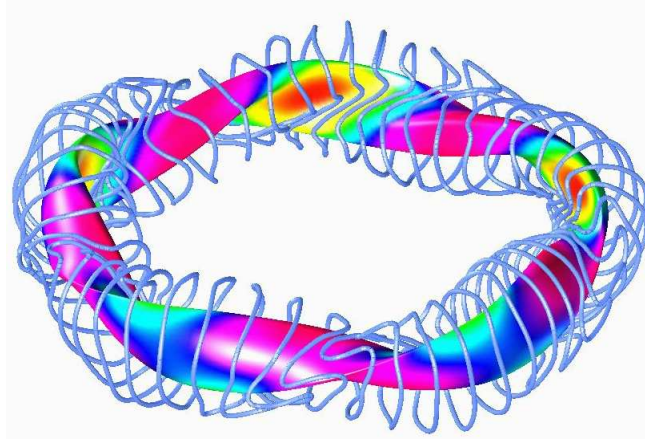


Figure 1.16: Stellarator configuration of the experiment W7-X. The colors correspond to different values of the magnetic field strength. Note the helically deformed plasma produced by the complex 3-D shaped coils.

sults in the development of a fusion reactor in the future is the Stellarator. Here we only mention its main features since we will not deal with this configuration in the work described in the Thesis.

In a stellarator, the screw-like twisting of field lines around the torus center is generated by external coils and it does not need a direct-axis flow component in the plasma, like in the Tokamak or in the RFP. The stellarator can therefore operate in steady state.

For a fusion power plant, the stellarators could provide a technically simpler solution than Tokamaks but this asserts an experimental verification. A picture of a stellarator configuration is shown in Fig. 1.16 which shows the W7-X experiment [21] [22] of the Max Planck Institute for Plasma Physics.

1.5 Single Particle Motion and Drift Effects

The behavior of the plasma in an electromagnetic field is determined by the motion of each particle in the field produced by all its neighbors combined with the externally applied ones. Given the number of particles involved, such an approach cannot be used to predict a plasma behavior in fusion plasmas; this explains the success of the MHD model explained in the previous section in studying the plasma physics in fusion devices. Anyway in the limit of strong magnetic field and low plasma density, interactions with other particles can be neglected: therefore the motion of a single particle depends on the

externally applied fields only. This is the so-called *single particle approach* which represents a considerable simplification.

In presence of both \mathbf{B} and \mathbf{E} fields, the equation of motion for a particle is determined by the sum of the electric force $q\mathbf{E}$ and the so-called Lorenz force, which acts perpendicular to both particle velocity \mathbf{v} and magnetic field:

$$m\dot{\mathbf{v}} = q(\mathbf{E} + \mathbf{v} \times \mathbf{B}). \quad (1.33)$$

The general solution of this equation can easily be numerical, as it will be done throughout this Thesis. It may be useful to consider some simple cases where an analytic solution can be given.

Gyro-motion

When there is no electric field, Eq.1.33 reduces to $m\dot{\mathbf{v}} = q(\mathbf{v} \times \mathbf{B})$ if \mathbf{B} is uniform. Taking as a reference the direction of the magnetic field $\hat{\mathbf{b}} \equiv \mathbf{B}/B$, we can decompose the particle motion into a parallel motion, in which the particle moves with constant v_{\parallel} velocity, and a motion which lies on the plane perpendicular to \mathbf{B} . For the latter, we can write two equations for the two components that define the perpendicular plane, i.e:

$$\dot{v}_x = qv_y B/m \quad (1.34a)$$

$$\dot{v}_y = -qv_x B/m \quad (1.34b)$$

It's easily demonstrated that Eqs.1.34 describe a gyration about the field line, characterized by the frequency:

$$\omega_c \equiv \frac{|q|B}{m}$$

which is called cyclotron frequency, or gyrofrequency. The direction of rotation is opposite for electrons and ions, while the radius of the motion around field lines (called Larmor radius or gyro-radius) is defined as:

$$r_L \equiv \frac{v_{\perp}}{\omega_c} = \frac{v_{\perp}m}{|q|B} \quad (1.35)$$

where $v_{\perp} = (v_x^2 + v_y^2)^{1/2}$; note that, for equal particle perpendicular energy $W_{\perp} = mv_{\perp}^2/2$, ion gyro-orbit is much larger than electron one, since the ratio of the two gyro-radii is proportional to the square-root of the ratio of their masses, i.e. $\sqrt{1837} \approx 43$.

As the gyrating particle moves along a line of force in a uniform field, it will follow a helical path, but the center of gyration (called guiding center or gyrocenter) will remain on the field line, and will give a measure of

particle's average location during a gyro-orbit. However, when magnetic field is not homogeneous, or in presence of non vanishing electric field, particle will undergo drift motions, which can be expressed as motions of gyrocenter superimposed to the helical path of the particle.

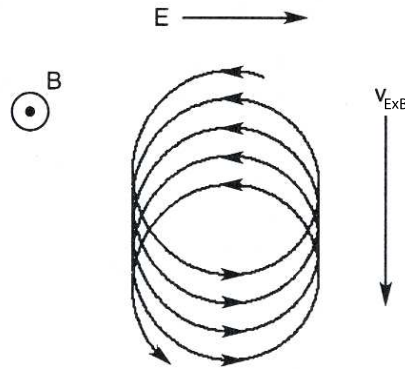


Figure 1.17: Example of $\mathbf{E} \times \mathbf{B}$ drift motion of a charged particle, when uniform electric and magnetic field are present.

$\mathbf{E} \times \mathbf{B}$ drift

When an electric field is added to the picture, two different effects arise. In the parallel direction the particle will undergo the acceleration due to qE_{\parallel} force. The component of \mathbf{E} perpendicular to magnetic field will instead superimpose to the helical particle motion a drift at constant velocity in a direction perpendicular both to magnetic field and to \mathbf{E}_{\perp} . The drift velocity, called $\mathbf{E} \times \mathbf{B}$ drift, can be expressed as:

$$\mathbf{v}_{\mathbf{E} \times \mathbf{B}} = \frac{(\mathbf{E} \times \mathbf{B})}{B^2}. \quad (1.36)$$

To understand the mechanism which results in this drift, consider a negatively charged particle rotating about a line of force in a magnetic field, directed upward and perpendicular to the plane of the page, as indicated in Fig.1.17. If an electric field is applied, in the direction shown, i.e. from the left toward the right of the page, the negative electron will now be accelerated during the bottom part of its gyro-orbit, while decelerated during the other part. The resulting of these accelerations and decelerations is the variation of Larmor radius (that depends on v_{\perp} value) that will be larger on the side where particle is gaining kinetic energy, and shorter on other side. This will give rise to the drift, as illustrated in Fig.1.17.

Note that this drift is independent of the mass and of the initial velocity of the particle; moreover it is independent of the sign of the charge. This means that the whole plasma drifts together across electric and magnetic field with the same velocity.

∇B and curvature drifts

Other kind of drifts are generated by inhomogeneities of magnetic field, i.e. gradients both perpendicular and parallel to \mathbf{B} , and curved magnetic fields. We will not enter into details of demonstrations, that can be found in literature (see e.g. [6]); let us only underline that such drifts are particularly important in studying toroidal magnetic configurations, since both gradients and curved field lines are present.

Choosing the gradient to be perpendicular to magnetic field \mathbf{B} , the related guiding-center drift can be written as:

$$\mathbf{v}_{grad} = \frac{W_{\perp}}{q} \frac{\mathbf{B} \times \nabla B}{B^3} \quad (1.37)$$

The drift is directed both perpendicularly to \mathbf{B} and ∇B , and is dependent on the sign of the charge. This leads in the plasma to a charge separation (electrons and ions drift in opposite directions), which turns into net volumetric electric field.

When magnetic field lines are not straight, another kind of drift arises, called curvature drift. It can be expressed as:

$$\mathbf{v}_{curv} = \frac{2W_{\parallel}}{qB^2} \mathbf{B} \times \left[(\hat{\mathbf{b}} \cdot \nabla) \hat{\mathbf{b}} \right]. \quad (1.38)$$

The measure of the field lines curvature is the term $(\hat{\mathbf{b}} \cdot \nabla) \hat{\mathbf{b}}$, that represents the spatial derivative along the \mathbf{B} direction of the unit vector $\hat{\mathbf{b}}$.

Parallel gradients and magnetic mirrors

Defining the magnetic moment, μ , of a gyrating particle as:¹

$$\mu = \frac{mv_{\perp}^2}{2B} = \frac{W_{\perp}}{B} \quad (1.39)$$

one can demonstrate that it is a constant of particle motion. This invariance of μ implies that when a particle undergoes a (parallel) gradient of magnetic

¹The definition is not misleading, since μ is indeed equal to IA , the current represented by the moving charged particle times the area of the loop it circumnavigate.

field, moving into regions of higher magnetic field strength, its perpendicular velocity v_{\perp} increases; since particle's energy is also constant, this translates into a correspondent v_{\parallel} decrease.

This means that parallel gradients affect particle's parallel velocity according to:

$$\frac{mv_{\parallel}^2}{2} = W - \mu B \quad (1.40)$$

being $W = W_{\perp} + W_{\parallel}$ the total kinetic energy. Eq.1.40 is the basis for understanding the basic principle of one of the early magnetic traps for confining charged particles, called magnetic mirror. A particle moving from a weak-field region to a high-field one will experience an increasing B , and hence will decrease its parallel velocity. If the field is high enough, there will be a point where v_{\parallel} becomes zero, and the particle is reflected back toward weak-field regions. The fact that a particle is or not trapped depends on the ratio of parallel velocity vs. total velocity, that can be expressed as the so-called particle pitch, $\lambda = v_{\parallel}/v$; for example, particles with $\lambda = 1$ will not be trapped, since they have zero magnetic moment and don't experience any deceleration approaching the high-field region.

An example of a trapped particle orbit which is particularly important in toroidal magnetic confinement and which is directly related to parallel motion gradients is the *banana orbit*. Similarly to the case of the magnetic mirror, if a particle possesses sufficiently large parallel velocity, it circulates continually round the torus in poloidal direction (it is hence a *passing particle*). When the velocity is lower, the particle is trapped on the outer part of the torus, since it experiences a magnetic mirror as a result of the poloidal variation of the magnetic field (the toroidal component of the magnetic field decreases in fact as $1/R$). We will discuss in details trapped and passing particles in toroidal fusion experiments in Chapter 3.

1.6 Particle and heat transport in fusion plasma

Particle and heat transport are very important topics in discussing fusion experiments. In fact these are the most relevant mechanisms which negatively affect the confinement properties of the plasma. The quantity which describes heat transport in a physical system is the thermal diffusivity χ . In axisymmetric systems it is related with the vector heat flux \mathbf{Q} by the Fick relation:

$$\mathbf{Q} = -\chi(r)n(r)\nabla T(r) \quad (1.41)$$

where $n(r)$ is the density profile and $\nabla T(r)$ the temperature gradient.

Generally, ions and electrons in plasmas have different properties concerning thermal transport, thus usually an ion χ_i and an electron diffusivity χ_e are defined. The presence of a magnetic field in the plasma introduces a further a-symmetry in the energy transport parallel or orthogonal to the magnetic field. This is why it's useful to distinguish between the diffusivity parallel to the magnetic field χ_{\parallel} and the perpendicular one χ_{\perp} . Similarly, we can define a particle diffusion coefficient D which has different values if related to ions or electrons and to parallel or perpendicular transport with respect to the magnetic field.

In an ideal and stable plasma the thermal diffusivity is determined by Coulomb collisions. In this case it's possible to understand the thermal transport mechanism by a simple diffusive model. We consider a plasma without a magnetic field. The situation is similar to a neutral gas scenario: the particles move on a straight line till they collide with other particles. During the collisions energy is exchanged. The distance covered between two collisions is the mean free path λ . It can be shown that the thermal diffusivity is given by:

$$\chi \cong \nu \lambda^2 \cong \frac{v_t^2}{\nu} \quad (1.42)$$

where $v_t = \sqrt{T/m}$ is the thermal velocity of particle with mass m and temperature T and ν is the collision frequency for unit of time, proportional to $T^{-3/2}$ (see section 1.3).

When a magnetic field is present the motion of the particles must be split in two directions: along and perpendicular to the magnetic field. Along the magnetic field the particles continue to move freely and they exchange energy as if the magnetic field were not present. The thermal parallel diffusivity χ_{\parallel} is still given by Eq. 1.42. To obtain the contribution to the parallel thermal transport for ions and electrons it's necessary to substitute in relation 1.42 the corresponding quantities for the two species. The relation between $\chi_{e\parallel}$ and $\chi_{i\parallel}$ is thus given by:

$$\chi_{e\parallel} \cong \left(\frac{M_i}{m_e} \right)^{1/2} \chi_{i\parallel}. \quad (1.43)$$

Because $M_i \gg m_e$ the thermal transport along the magnetic field is mainly due to electrons. Its main effect is to make the temperature uniform on the magnetic flux surfaces, where the magnetic field lines lie. In a closed configuration, like the toroidal one, there are no net energy losses parallel to \mathbf{B} .

Consider now the perpendicular transport. Without collisions the particles orbit around the same magnetic field line for an indefinite time. The radius of the orbit is the Larmor Radius r_L defined in the previous paragraph. Due to the presence of collisions, the centers of the particle orbits shift perpendicularly to the magnetic field of a quantity of order r_L . In this case the thermal diffusivity is thus given by:

$$\chi_{\perp} \cong \nu r_L^2. \quad (1.44)$$

Ions have a bigger Larmor radius with respect to electrons and they give an important contribute to perpendicular thermal transport. It's interesting to compare the diffusivity $\chi_{i\perp}$ with $\chi_{e\parallel}$:

$$\frac{\chi_{e\parallel}}{\chi_{i\parallel}} \propto \left(\frac{M_i}{m_e}\right)^{1/2} \cong 40. \quad (1.45)$$

The conclusion from this model is that the main contribution to the energy transport in a plasma is in the direction parallel to the magnetic field. The transport perpendicular to the magnetic field is smaller and reduces with the increasing temperature [6].

Unfortunately experimental results show that the thermal transport in fusion plasmas is not as described by collisional models, but the thermal diffusivity perpendicular to the magnetic field is much bigger than the predicted classical values. In fact, the electron thermal transport measured in the experiments is important also for the perpendicular directions and is responsible of the heat fluxes to the edge. These energy losses may cause a remarkable degradation of the confinement. This kind of transport, not due to collisions, is usually called *anomalous transport* and is originated by a mechanism of turbulent diffusion, caused by the electrostatic or magnetic fluctuations in the plasma. These fluctuations are intrinsic to the RFP configuration as it will be described in Chapter 4.

1.7 Additional heating

The heating due to the ohmic effect of the plasma current is not enough to reach the temperatures required to trigger the fusion reactions in tokamaks. To compensate the dissipations of energy, due to thermal transport and to radiation emission, and to increase the core plasma temperature, in many experiments several additional heating are used. These have been included also in the ITER project and they will be absolutely necessary in future reactors.

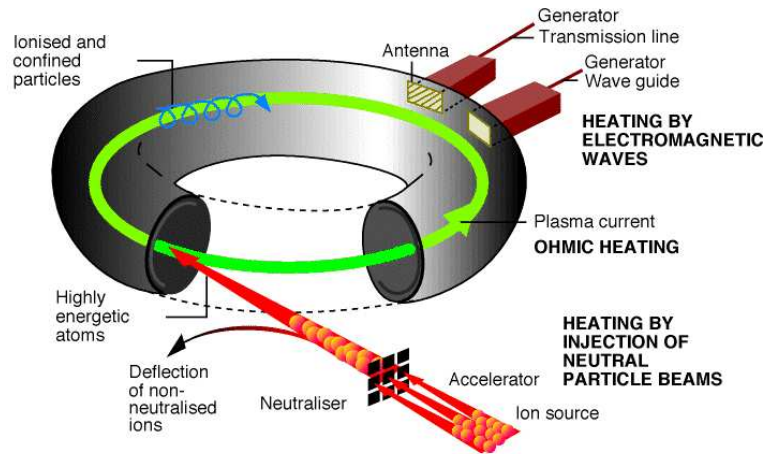


Figure 1.18: Additional heating in a fusion plasma.

There are two additional heating systems which are broadly used in most of the fusion experiments: the Neutral Beam Injection (NBI) system and the Electromagnetic Wave Heating. A short overview of their main features is here reported, while a more detailed description of the NBI system in the experiment ASDEX-Upgrade is postponed to Chapter 7.

1.7.1 NBI

The NBI heating consists of injecting a beam of neutral fuel atoms at high energy into the plasma. In plasma the beam atoms are ionized through ionization by electrons (dominant only at low electron temperatures of $1keV$), charge exchange (dominant process below $90keV$ for Deuterium beam), and ionization by ions (dominant process above $90keV$ for Deuterium beam). In total, these different processes lead to an approximately exponential decay of the beam neutral density along its path.

The energetic neutral atoms are created by extracting positive ions from suitable ions sources, accelerating the ions to high energies, and finally neutralizing the energetic ions by collisions with a gas target in the so-called neutralizer. However, not only hydrogen or Deuterium ions are created in the ion source, but also the hydrogen or Deuterium molecular ions H_2^+ and H_3^+ or D_2^+ and D_3^+ respectively. Hence, the final neutral beam consists not only of neutral atoms with the full acceleration energy, but also of neutral atoms with one half and one third of the acceleration energy. After passing through a magnet, which reflects the non neutralized ions, the neutral atoms are injected into the plasma through the duct between the beam lines and the torus vessel.

1.7.2 Electromagnetic Wave Heating

As an auxiliary heating system, Radio Frequency (RF) electromagnetic waves have been used successfully in several fusion devices. Since the RF heating feasibility and efficiency substantially depend on the capability of the wave to propagate inside the plasma and on the wave-particle interaction mechanism, not all RF frequencies are viable. In general there are three main ranges of frequencies: ion cyclotron frequency (30-80MHz), lower hybrid frequency (several GHz), and electron cyclotron frequency (several tens of GHz). The RF power is transferred from the generator to the plasma chamber through specially dimensioned low loss transmission lines and is coupled to the plasma by means of antennas, the dimensions and design of which depend on the frequency and on the polarization of the wave to be launched. The antenna couples to a wave that can propagate in the plasma such that all the incoming wave power is launched into the plasma. There are two mechanisms through which the externally launched waves lose energy inside the plasma. The first is by energy transfer to another propagative wave, this process is called mode-conversion. The second one is through direct energy absorption by particles in resonance with the waves. In the latter case, as a consequence of the interaction with the waves, the particle distribution function deviates from a Maxwellian.

1.8 Motivation and Aim of the work

The actual limitations to obtain an higher confinement time are mainly due to the anomalous particles and heat transport from the core to the edge. Anyway, both in Tokamak and RFP configurations, there have been evidences of improved regimes which have shown a reduction of this negative transport. In the RFP, for example, there are regimes in which an important fraction of the plasma presents conserved helical surfaces. Within this region the thermal particles are confined for a longer time than the rest of the plasma. In this Thesis we analyze the magnetic topology of these states, their main properties in terms of increased confinement, and we perform an estimate of the particle diffusion coefficients inside the helical states by numerical transport simulations.

As we have seen above, particles can be injected by NBI in the plasma or heated by RF. The result is a population of high-energy particles which have a different dynamic and confinement properties in the Tokamak and the RFP configuration. It is important to underline that in next fusion experiments or reactors this class of particles should be well-confined since their loss may

reduce the confinement time and damage seriously the vessel because of their high energy. Part of this Thesis will be dedicated to study the motion of fast ions in RFP and Tokamak and how they are affected by the magnetic instabilities of the plasma. In particular we shall highlight their properties in the two configurations and an analytical explanation will be suggested to understand their different behavior.

The main issue of this Thesis is thus to study the transport of thermal and fast particles in the Tokamak and in the RFP advanced regimes and their interactions with the magnetic instabilities of the plasma. Since we deal with extremely complex systems, numerical simulations by computer codes are required. Chapters 2 and 3 will be dedicated to explain how our particular code, ORBIT, works.

CHAPTER 2

Equilibrium Magnetic Field

The numerical study of transport phenomena is described by simple equations in flux coordinates. In particular, straight field line coordinates will be used in the formulation of the evolution equations of test particle guiding center that will be obtained in the next Chapter. Appendix A offers an introduction to flux coordinates with a notation consistent with this Thesis.

Flux coordinates are based on equilibrium magnetic fields. We give here, in sections 2.1 – 2.2, a brief summary and the basic notions which have been used to obtain the magnetic equilibria for the experiments analyzed in this Thesis. In particular, we considered: a Reversed Field Pinch configuration (section 2.3), a circular Tokamak in high aspect ratio approximation (section 2.4) and a D-shaped Tokamak device (section 2.5). We describe then how the equilibria are treated in order to be used by the ORBIT code that will be the object of Chapter 3.

2.1 Flux coordinates

A point in a toroidal system is determined by three coordinates : a poloidal angle θ , a toroidal angle ϕ and a radial coordinate. The choice of the radial coordinate is arbitrary as it can be any quantity which is constant along a magnetic field surface. In the following we shall use the poloidal flux ψ_p i.e. the flux enclosed by the poloidal magnetic field within that surface but

normalized to 2π . An analogous definition holds also for the toroidal flux ψ . The quantities introduced in the following sections are adimensional. In particular, μ_0 is assumed to be equal to 1, the magnetic fields are normalized to the axis field B_0 , the lengths to the major radius R_0 , the currents to $R_0 B_0$, the magnetic fluxes to $2\pi R_0 B_0$.

In general flux coordinates (ψ_p, θ, ϕ) , for a generic non axi-symmetric equilibrium, the *contravariant* representation of the magnetic field is:

$$\mathbf{B} = \nabla\psi \times \nabla\theta + \nabla\phi \times \nabla\psi_p + \nabla\psi_p \times \nabla\tilde{\nu} \quad (2.1)$$

where $\tilde{\nu}$ is a function of all coordinates θ, ϕ and ψ_p ; the contravariant basis vectors $\nabla\phi, \nabla\psi_p$ and $\nabla\theta$ are defined in the appendix A. It can be proven that $\tilde{\nu}$ must be a periodic function in θ and ϕ . Eq. 2.1 derives from a Clebsh form representation of the magnetic field:

$$\mathbf{B} = \nabla\psi_p \times \nabla\nu \quad (2.2)$$

where ν is a constant function on the magnetic surfaces:

$$\nu = \left(\frac{d\psi}{d\psi_p} \theta - \phi \right) + \tilde{\nu}(\psi_p, \theta, \phi) \quad (2.3)$$

which is related to the vector potential \mathbf{A} of the magnetic field.

The *covariant* representation of the magnetic field $\mathbf{B} = B_{\psi_p} \nabla\psi_p + B_\theta \nabla\theta + B_\zeta \nabla\zeta$ is given by:

$$\mathbf{B} = \delta(\theta, \psi_p, \phi) \nabla\psi_p + g(\theta, \psi_p, \phi) \nabla\phi + I(\theta, \psi_p, \phi) \nabla\theta. \quad (2.4)$$

where $B_\zeta = g$ is the covariant toroidal magnetic field component, $B_\theta = I$ the poloidal component of the magnetic field and $B_{\psi_p} = \delta$ the radial component. These equations, together with their relation with currents flowing in and outside the plasma, are derived in appendix A. Generally, functions I, g, δ depend on all the flux coordinates (ψ_p, θ, ϕ) but in straight field line coordinates, for an axi-symmetric configuration, a significant simplification occurs, as shown in the following.

Axi-symmetry

Since in this Thesis we shall always deal with axi-symmetric magnetic equilibria we suppose hereafter that $\partial_\phi = 0$ for \mathbf{B} . This assumption implies that also the function $\tilde{\nu}$ depends only on θ and ψ_p . Moreover, in axi-symmetric conditions the covariant toroidal magnetic field component $B_\zeta = g$ is a function of ψ_p only. Thus the covariant magnetic field representation simplifies to:

$$\mathbf{B} = \delta(\theta, \psi_p) \nabla\psi_p + g(\psi_p) \nabla\phi + I(\theta, \psi_p) \nabla\theta. \quad (2.5)$$

while in the contravariant form Eq. 2.1 the $\tilde{\nu}(\psi_p, \theta)$ function only depends on (ψ_p, θ) .

Straight Field Line

The field representation is further simplified in straight field line coordinates (described in A.5). The Hamiltonian equations will be derived for this kind of coordinates in Chapter 3, therefore a change of variable is required. Consider equation 2.3 on a given flux surface: by definition $\nu(\psi_p) = \text{constant}$. In straight field line coordinates, $\tilde{\nu}(\theta, \psi_p)$ is identically zero everywhere. In fact, if this condition holds, the magnetic field lines coordinates are derived from Eq. 2.3:

$$\phi = \frac{d\psi}{d\psi_p}(\psi_p)\theta + \nu(\psi_p) \quad (2.6)$$

which is a straight line in the (θ, ϕ) plane.

If $\tilde{\nu}$ is not identically zero then it can be proven that the new toroidal variable ζ can be chosen to obtain a straight field line coordinate system (θ, ζ, ψ_p) by the position:

$$\zeta = \phi - \tilde{\nu}. \quad (2.7)$$

Let us note that this is not the unique way of obtaining straight field lines. It would have been possible, in fact, to choose a new poloidal coordinate θ' , as can be found in the literature.

The representation of axisymmetric fields in straight field lines is further simplified as follows. The contravariant magnetic field can be written as:

$$\mathbf{B} = \nabla\psi \times \nabla\theta + \nabla\zeta \times \nabla\psi_p \quad (2.8)$$

and the covariant magnetic field is given by:

$$\mathbf{B} = \delta(\theta, \psi_p)\nabla\psi_p + g(\psi_p)\nabla\zeta + I(\theta, \psi_p)\nabla\theta. \quad (2.9)$$

An important property of straight field line coordinates is that the quantity $d\psi/d\psi_p$ gives directly the safety factor q :

$$q(\psi_p) = \frac{\mathbf{B} \cdot \nabla\zeta}{\mathbf{B} \cdot \nabla\theta} = \frac{d\psi}{d\psi_p}. \quad (2.10)$$

We can use q and the Jacobian of the transformation J to write the explicit contravariant components of the magnetic field $\mathbf{B} = B^{\psi_p}\mathbf{e}_{\psi_p} + B^\theta\mathbf{e}_\theta + B^\zeta\mathbf{e}_\zeta$, which will be useful in the next sections for the equilibrium reconstruction:

$$B^{\psi_p} = 0 \quad B^\theta = \frac{1}{J} \quad B^\zeta = \frac{q}{J}. \quad (2.11)$$

The component B^θ has the same value also for general axi-symmetric flux coordinates. On the other hand, the toroidal component B^ϕ is generally different from B^ζ since it depends on the function $\tilde{\nu}$. A general relation can be found between these components and q . Let us suppose that the function $\tilde{\nu}$ is known, and that (ψ_p, θ, ζ) is a straight field line system while (ψ_p, θ, ϕ) is a generic axi-symmetric coordinate system. It is then possible to compute the safety factor q from Eq. 2.10 and 2.7 as follows:

$$q(\psi_p) = \frac{\mathbf{B} \cdot \nabla \zeta}{\mathbf{B} \cdot \nabla \theta} = \frac{\mathbf{B} \cdot (\nabla \phi - \partial_\theta \tilde{\nu} \nabla \theta)}{B^\theta}. \quad (2.12)$$

where the right-hand side does not depend on the θ coordinate. Using the expression for field contravariant components 2.11, we obtain a differential equation that can be used to compute the $\tilde{\nu}$ function:

$$q = \frac{B^\phi - (\partial_\theta \tilde{\nu}) B^\theta}{B^\theta} = \frac{g \frac{1}{X^2} - \frac{1}{J} \partial_\theta \tilde{\nu}}{\frac{1}{J}}, \quad (2.13)$$

and finally:

$$\partial_\theta \tilde{\nu} = \frac{gJ}{X^2} - q. \quad (2.14)$$

This is a general relation for any Jacobian J that is used to convert a generic axi-symmetric coordinate system to a straight field lines one.

Boozer

Straight field line constraint does not uniquely identify a coordinate system: in fact there is still one free parameter which can be chosen, i.e. the Jacobian of the transformation. Boozer coordinates are obtained by setting the Jacobian J to be proportional to the inverse of the square magnetic field. We recall the basic properties of Boozer coordinates because they were used in guiding center codes before the generalization of the Hamiltonian formulation to straight field lines [23]. The properties of such coordinates are explained with details in Appendix A. We give here the final expression of the magnetic field in Boozer coordinates, with the axi-symmetry condition. The contravariant magnetic field is given by:

$$\mathbf{B} = \nabla \psi \times \nabla \theta + \nabla \zeta \times \nabla \psi_p \quad (2.15)$$

while the covariant magnetic field components g, I depend on ψ_p only:

$$\mathbf{B} = \delta(\theta, \psi_p) \nabla \psi_p + g(\psi_p) \nabla \zeta + I(\psi_p) \nabla \theta. \quad (2.16)$$

The Jacobian has the following form:

$$J = \frac{qg + I}{B^2}. \quad (2.17)$$

In Boozer coordinates the quantities g and I have a direct physical interpretation. In fact, $2\pi I(\psi_p)$ is the total toroidal current enclosed by the magnetic surface labelled with ψ_p and $2\pi g(\psi_p)$ is the total poloidal current outside ψ_p . Note that the function $\tilde{\nu}$ which relates ϕ and ζ can be computed by Eq. 2.14 by inserting the Boozer Jacobian. In this thesis we shall apply Boozer coordinates to RFP devices, such as RFX-mod and MST and to a circular approximation of the tokamak Asdex-Upgrade.

2.2 Derivation of flux coordinates for cylindrical equilibria

In general, the computation of a generic equilibrium magnetic field requires a code that numerically solves the MHD equations $\nabla p = \mathbf{J} \times \mathbf{B}$ and $\nabla \times \mathbf{B} = \mu_0 \mathbf{J}$, which together form the *Grad-Shafranov* equation, with the constraints given by experimental measurements. Under simplified conditions (i.e. a circular geometry, large aspect ratio, low plasma pressure) it is possible to derive approximate analytical expressions. In particular, as it will be shown in the next Chapter, the integration of the motion equations for the test particles requires the computation of the covariant components of the magnetic field (I, g) and of its square value B^2 on the flux coordinates grid (ψ_p, θ) .

Before deriving such approximate expressions in a RFP and in a circular cross section Tokamak, we need to briefly recall the properties of the Grad-Shafranov equation expressed in general toroidal coordinates. We will show how to derive an approximate flux coordinate system given a cylindrical equilibrium.

Several geometric reference coordinate systems and the transformations between them must be studied. Let us summarize them in this section, full details are given in the Appendix A.

Cylindrical Coordinate System

The well-known Cylindrical coordinate system is represented by the following transformation $(x, y, z) \rightarrow (r, \theta, z)$:

$$x = r \cos \theta \quad y = r \sin \theta \quad (2.18)$$

while the third coordinate z is unchanged. The Jacobian of the transformation is $J = r$. The calculation of the contravariant and covariant basis follows the general procedure described at the beginning of appendix A. We find for the covariant basis:

$$\mathbf{e}_r = \cos\theta\mathbf{e}_x + \sin\theta\mathbf{e}_z + \mathbf{e}_z \quad \mathbf{e}_\theta = -r\sin\theta\mathbf{e}_x + r\cos\theta\mathbf{e}_z + \mathbf{e}_z \quad (2.19)$$

which can be normalized to unity to obtain a triad (i.e. a local orthonormal basis, see also Appendix A):

$$\mathbf{e}_{\hat{r}} = \mathbf{e}_r \quad \mathbf{e}_{\hat{\theta}} = \mathbf{e}_\theta/r \quad \mathbf{e}_{\hat{z}} = \mathbf{e}_z. \quad (2.20)$$

From the Jacobian and the covariant basis it's straightforward to define also the contravariant basis and the corresponding triad:

$$\mathbf{e}^r = \mathbf{e}_r \quad \mathbf{e}^\theta = \mathbf{e}_\theta/r^2 \quad \mathbf{e}^z = \mathbf{e}_z; \quad (2.21)$$

$$\mathbf{e}^{\hat{r}} = \mathbf{e}^r \quad \mathbf{e}^{\hat{\theta}} = \mathbf{e}^\theta/r \quad \mathbf{e}^{\hat{z}} = \mathbf{e}_z. \quad (2.22)$$

Toroidal Coordinate System

The transformation for the toroidal elementary coordinate system $(x, y, z) \longrightarrow (r, \theta, \phi)$ is defined by:

$$x(r, \theta, \phi) = (1 + r\cos\theta)\cos\phi \quad (2.23)$$

$$y(r, \theta, \phi) = (1 + r\cos\theta)\sin\phi, \quad (2.24)$$

$$z(r, \theta, \phi) = r\sin\theta \quad (2.25)$$

where (x, y, z) are the usual Cartesian coordinates and (r, θ, ϕ) are the radius on a poloidal section, the geometric poloidal angle and the geometric toroidal angle respectively. The Jacobian is: $J = -r(1 + r\cos\theta)$. The coordinates (r, θ) have the same meaning of those in the cylindrical system; they are both defined on a poloidal cross section at a constant value of z for the cylinder and of ϕ for the torus. The covariant basis vector are:

$$\mathbf{e}_r = \cos\phi\cos\theta\mathbf{e}_x + \cos\theta\sin\phi\mathbf{e}_y + \sin\theta\mathbf{e}_z \quad (2.26)$$

$$\mathbf{e}_\theta = -r\cos\phi\sin\theta\mathbf{e}_x - r\sin\phi\sin\theta\mathbf{e}_y + r\cos\theta\mathbf{e}_z \quad (2.27)$$

$$\mathbf{e}_\phi = -(r\cos\theta + 1)\sin\phi\mathbf{e}_x + \cos\phi(1 + r\cos\theta)\mathbf{e}_y. \quad (2.28)$$

These vectors need a normalization to become a triad:

$$\mathbf{e}_{\hat{r}} = \mathbf{e}_r, \quad \mathbf{e}_{\hat{\theta}} = \mathbf{e}_\theta/r \quad \mathbf{e}_{\hat{\phi}} = \mathbf{e}_\phi/\sqrt{x^2 + y^2}. \quad (2.29)$$

Now we can find the reciprocal contravariant basis by computing the Jacobian and the cross product of the basis vectors already found:

$$\nabla r = \mathbf{e}^r = \mathbf{e}_r \quad \nabla \theta = \mathbf{e}^\theta = \mathbf{e}_\theta / r^2 \quad \nabla \phi = \mathbf{e}^\phi = \mathbf{e}_\phi / (x^2 + y^2) \quad (2.30)$$

and the respective triad:

$$\mathbf{e}^{\hat{r}} = \nabla r \quad \mathbf{e}^{\hat{\theta}} = r \nabla \theta \quad \mathbf{e}^{\hat{\phi}} = \nabla \phi \sqrt{x^2 + y^2}. \quad (2.31)$$

Toroidal Cartesian Coordinates

It is convenient to define another set of geometric coordinates which are useful while describing toroidal magnetic systems. We refer to them as *toroidal Cartesian coordinates* and their relations with the toroidal and Cartesian coordinates are given by:

$$X = \sqrt{x^2 + y^2} = 1 + r \cos \theta \quad (2.32)$$

$$Z = z = r \sin \theta \quad (2.33)$$

$$\phi = \phi. \quad (2.34)$$

We shall derive the triad basis vector for these coordinates and the Jacobian in the following paragraph, while considering the toroidal effect for circular cross section experiments.

2.2.1 The Grad-Shafranov equation

Consider now the force balance equation $\nabla p = \mathbf{j} \times \mathbf{B}$ in axi-symmetric general flux coordinates (ψ_p, θ, ϕ) where ϕ is the geometric toroidal angle:

$$J(j^\theta B^\phi - j^\phi B^\theta) = \frac{dp}{d\psi_p}. \quad (2.35)$$

The contravariant poloidal component of the magnetic field is $B^\theta = 1/J$ (Eq.2.11). The component B^ϕ along the geometric toroidal angle ϕ is given by the following relation :

$$B^\phi = \mathbf{B} \cdot \mathbf{e}^\phi = \mathbf{B} \cdot \mathbf{e}_\phi \frac{1}{x^2 + y^2} = \frac{g}{X^2} \quad (2.36)$$

obtained from Eq.2.31 and Eq.2.32.

To calculate j^ϕ consider that:

$$\mathbf{j} \cdot \nabla \phi = (\nabla \times \mathbf{B}) \cdot \nabla \phi = \nabla \cdot [(\nabla \phi \cdot \nabla \zeta) \nabla \psi_p] \quad (2.37)$$

where we have used the contravariant form of the magnetic field Eq. 2.1 and the definition of ζ (Eq. 2.7). Since $\nabla\phi \cdot \nabla\zeta = 1/X^2$, from Eq.2.30 and Eq.2.32, we finally have:

$$j^\phi = \nabla \cdot \left(\frac{\nabla\psi_p}{X^2} \right). \quad (2.38)$$

The covariant representation for the magnetic field (Eq.2.9) is used to compute j^θ :

$$j^\theta = \mathbf{j} \cdot \nabla\theta = \nabla \cdot (\mathbf{B} \times \nabla\theta) = -\nabla B_\phi / J = -\frac{1}{J} \frac{dg}{d\psi_p}. \quad (2.39)$$

where, we recall, g is only ψ_p -dependent since the configuration is axi-symmetric. By substitution in Eq. 2.35 we obtain:

$$\nabla \cdot \left(\frac{\nabla\psi_p}{X^2} \right) + \frac{dp}{d\psi_p} + \frac{g}{X^2} \frac{dg}{d\psi_p} = 0 \quad (2.40)$$

which is the well known Grad Shafranov equation. This equation can be solved in an approximate way under some simplifying assumptions. We shall derive a series of relations that will be used to define a flux coordinate system, provided that a cylindrical equilibrium is known. In particular Eq. 2.40 can be solved perturbatively in the inverse aspect ratio $\epsilon = a/R$ with the boundary condition given by a circular conducting wall. To lowest order the equilibrium constant ψ_p surfaces are concentric circles. To the second order the equilibrium surfaces consist of shifted circles [24], and to third order they have elliptical and triangular distortion [25]. We shall solve the Grad-Shafranov equation only to the second order in ϵ in the toroidal system (r, θ, ϕ) .

We assume that the flux surfaces consist of shifted circles and verify that a solution of the Grad-Shafranov equation is obtained. Given the usual normalizations $R_0 = 1$ and the axis field $B_0 = 1$, we write:

$$X(r, \theta) = 1 + r\cos(\theta) - \Delta(r) \quad Z(r, \theta) = r\sin(\theta) \quad (2.41)$$

which are exactly the toroidal Cartesian coordinates defined above (Eqs. 2.32-2.33) shifted by a quantity $\Delta(r)$ which derives from the solution of the Grad-Shafranov equation. The covariant basis vector of the transformation $(X, Z, \phi) \rightarrow (r, \theta, \phi)$ are:

$$\nabla r = \frac{\cos\theta}{1 - \Delta'\cos\theta} \mathbf{e}_{\hat{X}} + \frac{\sin\theta}{(1 - \Delta'\cos\theta)} \mathbf{e}_{\hat{Z}} \quad (2.42)$$

$$\nabla\theta = \frac{-\sin\theta}{r(1 - \Delta'\cos\theta)} \mathbf{e}_{\hat{X}} + \frac{\cos\theta - \Delta'}{r(1 - \Delta'\cos\theta)} \mathbf{e}_{\hat{Z}} \quad (2.43)$$

$$\nabla\phi = \frac{1}{X}\mathbf{e}_{\hat{\phi}}. \quad (2.44)$$

with the Jacobian J :

$$J^{-1} = \frac{1}{rX(1 - \Delta'(r)\cos\theta)}. \quad (2.45)$$

Expressions 2.42-2.45 are useful to express the first term of the Grad-Shafranov equation in the toroidal system (r, θ, ϕ) . In fact, the divergence of a vector A is generally given by:

$$\nabla \cdot \mathbf{A} = \frac{1}{J} \frac{\partial(JA^i)}{\partial u^i} \quad (2.46)$$

with $A^i = \mathbf{A} \cdot \mathbf{e}^i$. Thus we obtain:

$$\nabla \cdot \left(\frac{\nabla\psi_p}{X^2} \right) = \frac{1}{J} \frac{\partial}{\partial\theta} \left(\frac{J\nabla\theta \cdot \nabla\psi_p}{X^2} \right) + \frac{1}{J} \frac{\partial}{\partial r} \left(\frac{J\nabla r \cdot \nabla\psi_p}{X^2} \right). \quad (2.47)$$

The next step is to substitute the expressions for $\nabla r, \nabla\theta$ given by Eqs. 2.42-2.44 and to define a function λ which relates ψ_p and r :

$$\nabla\psi_p = \lambda\nabla r. \quad (2.48)$$

The expression for λ depends on the toroidal configuration considered and it's supposed to be known. Eq. 2.48 allows to completely define the transformation from (X, Z, ϕ) to (ψ_p, θ, ϕ) which is characterized by the new Jacobian:

$$J^{-1} = \frac{\lambda}{rX(1 - \Delta'\cos\theta)}. \quad (2.49)$$

Eq. 2.47 is finally implemented in the Grad-Shafranov equation 2.40. We report here its final expression in (r, θ, ϕ) :

$$\frac{\lambda}{r}(\lambda r)' + p' + gg' + \cos\theta \left(\Delta''(r) + \Delta' \left[\frac{2(r\lambda)'}{r\lambda} - \frac{1}{r} \right] - \frac{2(r\lambda)'}{\lambda} - 1 - \frac{2rgg'}{\lambda^2} \right) = 0 \quad (2.50)$$

where the primes mean derivatives respect to r . We can clearly see that this equation is composed by two parts: the first θ -independent and the second made of terms which multiply $\cos\theta$.

At lowest order the equation reduces to the radial pressure balance equation for a generic cylindrical screw pinch.

$$\frac{\lambda}{r}(\lambda r)' + p' + gg' = 0 \quad (2.51)$$

where the coordinates (r, θ) can now be assumed cylindrical. The solution of Eq. 2.51, i.e. the profile of the toroidal field covariant component g , is obtained as follows:

$$g(r^*) = 1 - \int_0^{r^*} 2(p(r)') + \frac{\lambda(r)}{r}(r\lambda(r)')dr. \quad (2.52)$$

Once the function λ and the pressure profile p are given, this equation can be solved numerically.

The second order effects are included by setting to zero the members of Eq. 2.50 which multiply $\cos \theta$:

$$\Delta''(r) + \Delta' \left[\frac{2(r\lambda)'}{r\lambda} - \frac{1}{r} \right] - \frac{2(r\lambda)'}{\lambda} - 1 - \frac{2rgg'}{\lambda^2} = 0 \quad (2.53)$$

which determines the function Δ and thus the physical location of the flux surfaces in terms of the functions g, λ defining the first order equilibrium. The solution of this equation gives the dependence of $\Delta \propto r^2$ [26].

In summary, the solution of the Grad-Shafranov equation allows to define on a grid of (r, θ) the two function $X(r, \theta)$ and $Z(r, \theta)$, the Shafranov shift $\Delta(r)$ and the covariant toroidal magnetic field component $g(r)$. The knowledge of λ , that depends on the cylindrical equilibrium, defines a flux coordinate system where X, Z, g can be transformed into functions of (ψ_p, θ) . Axi-symmetry means that there are no function depending on ϕ or ζ . Since in the code ORBIT the Boozer coordinates are implemented, it is necessary also to compute the function $\tilde{\nu}$ which relates ϕ and ζ by Eq. 2.14 with the Boozer Jacobian J .

In this section we have not specified the function λ necessary to compute $g(\psi_p)$ by integrating Eq. 2.52. Moreover, B^2 and I are not given. Their derivations are different in the Tokamak and in the RFP: these will be shown in the next two sections.

2.3 RFP Equilibrium

The derivation of the equilibrium for the RFP configuration is split in three different steps. First, from the experimental values of the toroidal and poloidal magnetic measured fields at the vessel we compute their radial profiles with the assumption of a cylindrical geometry. Then the poloidal and toroidal fluxes are computed together with the g and I function in first order cylindrical approximation. Finally the second order effect are introduced with the Shafranov shift Δ and with the definition of the square magnetic field B^2 .

2.3.1 The BFM model

The magnetic field radial profiles are obtained by assuming the theory proposed by J.B. Taylor [27] to describe the RFP. Taylor theory predicts that in a zero-pressure plasma (thus with $\mathbf{j} \times \mathbf{B} = 0$) with a resistivity η , surrounded by a perfectly conducting wall and in which the total helicity $K = \int_V \mathbf{A} \cdot \mathbf{B} dV$ is conserved, states of minimum energy are given by the force-free condition:

$$\nabla \times \mathbf{B} = \mu \mathbf{B} \quad (2.54)$$

where $\mu = \mu_0 \frac{\mathbf{j} \cdot \mathbf{B}}{B^2}$ is a constant which is fixed by minimizing the energy of the system with the constrain of the conserved total helicity. We solve this equation in a cylindrical geometry by projecting it on the contravariant basis triad 2.22. The final solution for the magnetic field components is:

$$B^{\hat{z}} = B_0 J_0(\mu r), \quad (2.55)$$

$$B^{\hat{\theta}} = B_0 J_1(\mu r), \quad (2.56)$$

$$B^{\hat{r}} = 0 \quad (2.57)$$

where J_0 and J_1 are Bessel Functions (Bessel Function Model, BFM) and B_0 is the on-axis field. $B^{\hat{i}} = \mathbf{B} \cdot \mathbf{e}^{\hat{i}}$ is the i -th component of the magnetic field as measured by a local observer. The quantity μ can be related with the F and θ pinch parameters already introduced in Chapter 1:

$$F = \frac{\mu a J_0(\mu a)}{2 J_1(\mu a)}, \quad (2.58)$$

$$\Theta = \frac{\mu a}{2}. \quad (2.59)$$

It is possible to see that $F < 0$ if $\Theta > 1.2$. On the other hand, when $\Theta > 1.56$ the lowest energy state is no longer described by Eq. 2.58 but it is helically symmetric, for discrete values of the parameter μ .

By means of Eqs. 2.58-2.59 fully relaxed states can be described by a continuous curve on the $F - \Theta$ plane. We can see in Fig. 2.1 that the experimental points agree only partially with the theoretical curve, due to two main reasons:

- The presence of non vanishing pressure gradients implies the existence of a perpendicular component of the current density that enters in the equilibrium modifying the field: a completely force-free equilibrium is not achievable in the experiment.

- A resistivity gradient enhances the dissipation in the outer region of the plasma; $\mu = j_{\parallel}/B$ is not constant anymore but decreases to zero at the edge.

Several numerical models have been proposed to include these two aspects. The most used are the Modified Polynomial Function Model (MBFM)[28] and the $\mu&p$ model. The MBFM is based on a polynomial decomposition of the field as function of F and Θ . In the following we shall use the $\mu&p$ model, so a brief description is worth to be given in the next section.

2.3.2 The $\mu&p$ model

From the force balance equation $\nabla p = \mathbf{j} \times \mathbf{B}$ we can easily get by using Eq. 2.54:

$$\nabla \times \mathbf{B} = \frac{\mathbf{B} \times \nabla p}{B^2} + \mu \mathbf{B} \quad (2.60)$$

where $\mu(r) = j_{\parallel}/B$ is a function of the radius r which depends on the current parallel profile. With this notation it is sufficient to provide the profiles of $\mu(r)$ and of the pressure $p(r)$. It has been found that experimental distributions are well described by radial profiles of μ of the form:

$$\mu(r) = \frac{2\Theta_0}{a}(1 - (r/a)^\alpha). \quad (2.61)$$

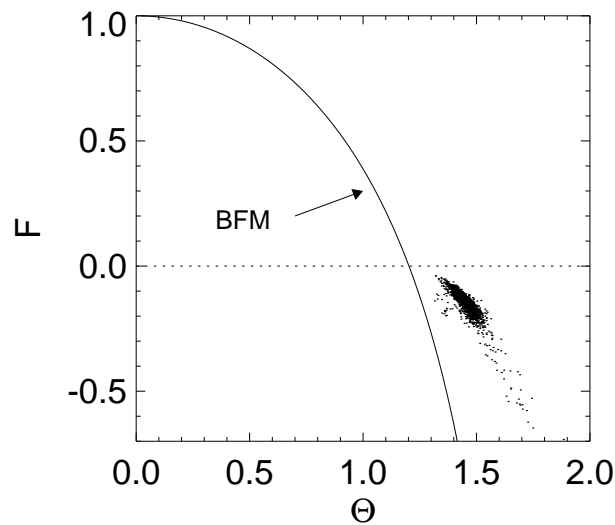


Figure 2.1: Theoretical BFM curve and experimental points.

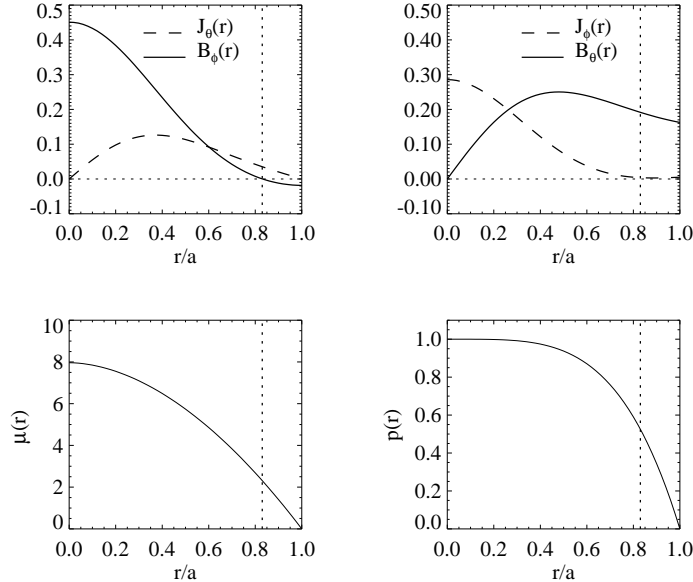


Figure 2.2: Example of reconstruction of an equilibrium RFP magnetic fields and currents with the μ and pressure profiles displayed in the bottom part of the figure.

Note that the parameter Θ_0 corresponds to the on-axis value of the safety factor q by $q(0) = a/(R_0\Theta_0)$. For given $\mu(r)$ and $p(r)$ profiles, with 2 fixed values of Θ_0 and $\beta_0 = \beta(0)$ (usually 0.1), the components of the field are determined by numerically solving the differential equations 2.60 system in a cylindrical geometry respect to the contravariant triad basis vectors (Eq. 2.22):

$$\frac{\partial B^{\hat{z}}}{\partial r} = -2\Theta_0\mu B^{\hat{\theta}} - \beta_0 \frac{B^{\hat{z}}}{B^2} \frac{\partial p}{\partial r}, \quad (2.62)$$

$$\frac{\partial(rB^{\hat{\theta}})}{\partial r} = 2\Theta_0\mu B^{\hat{z}} - \beta_0 r \frac{B^{\hat{\theta}}}{B^2} \frac{\partial p}{\partial r}. \quad (2.63)$$

Note again that the field components must be given normalized to the field on-axis B_0 and as function of the normalized radius r/R_0 . With this formalism μ, p and β_0 are also normalized to their on-axis values.

Usually the RFP equilibria can be reproduced varying α in the range $2 < \alpha < 6$ and Θ_0 in the range $1.4 < \Theta_0 < 2$. Once the field components are computed by solving equations 2.62-2.63 also the current components parallel and perpendicular to the magnetic field can be calculated by the Maxwell equation $\nabla \times \mathbf{B} = \mu_0 \mathbf{J}$. An example of the magnetic field and current reconstruction by the μ & p model is given in Fig. 2.2.

2.3.3 First order: cylindrical equilibrium

Once we know the radial profiles of the magnetic fields is straightforward to find also the poloidal and toroidal fluxes. In fact in a cylindrical geometry approximation we have that:

$$\psi_p = \int_0^r B^{\hat{\theta}} dr \rightarrow \frac{\partial \psi_p}{\partial r} = B^{\hat{\theta}}(r) \quad (2.64)$$

and

$$\psi = \int_0^r B^{\hat{z}} r dr \rightarrow \frac{\partial \psi}{\partial r} = r B^{\hat{z}}(r). \quad (2.65)$$

We remind that fluxes are normalized to $2\pi R_0 B_0$. But $\partial \psi_p / \partial r$ is just the definition of λ given in Eq. 2.48 which is thus equal simply to $B^{\hat{\theta}}(r)$. In particular, note that:

$$B^{\hat{\theta}} = \lambda(r) = \mathbf{B} \cdot \mathbf{e}^{\hat{\theta}} = \mathbf{B} \cdot \mathbf{e}_{\theta} / r = B_{\theta} / r \quad (2.66)$$

$$B^{\hat{z}} = \mathbf{B} \cdot \mathbf{e}^{\hat{z}} = \mathbf{B} \cdot \mathbf{e}^z = \mathbf{B} \cdot \mathbf{e}_z = B_z \quad (2.67)$$

where the relations between the cylindrical basis 2.20-2.22 have been used. We assume now that the quantities B_{θ} and B_z are the toroidal Boozer covariant components of the magnetic field, respectively $I(r)$ and $g(r)$. By the λ function they can be written in terms of only the poloidal flux ψ_p as required to fulfill the Boozer constraint. Thus from relations 2.66 – 2.67 we obtain:

$$\lambda(r) = B_{\theta} / r = I / r \quad (2.68)$$

$$B_z = B_{\phi} = g. \quad (2.69)$$

The cylindrical q profile is given by:

$$q = \frac{d\psi}{d\psi_p} = \frac{r B^{\hat{\phi}}}{B^{\hat{\theta}}} = \frac{r g}{\lambda}. \quad (2.70)$$

Equations 2.69 and 2.68 are valid also for a cylindrical tokamak provided that the appropriate λ and g are used. From the set of equations of this paragraph we find the relations to compute q and I ; g is calculated from λ by Eq. 2.52. We are going to introduce now the second order effects taking into account the Shafranov shift Δ .

2.3.4 Second order: the Shafranov shift Δ .

The second order effects are introduced by taking into account the correct expression of X given by Eq. 2.41. This means that the X function is not identically equal to 1, $X \neq 1$, and that a differential shift $\Delta(r)$ of the magnetic surfaces must be introduced.

The total amplitude of the square magnetic field is found by the dot product of the covariant and contravariant components. In fact:

$$B^2 = B_\theta B^\theta + B_\phi B^\phi = \frac{B_\theta}{J} + B_\phi \frac{g}{X^2} \quad (2.71)$$

where Eqs. 2.11 and 2.36 have been used. We also have that:

$$B_\theta = \mathbf{B} \cdot \mathbf{e}_\theta = r^2 B^\theta = \frac{r^2}{J} \quad (2.72)$$

from Eqs. 2.26-2.30. Substituting the expression for J at the second order approximation (Eq.2.49) and $B_\phi = g(\psi_p)$ (which holds for all axi-symmetric configurations) we obtain:

$$B^2 = \frac{g^2}{X^2} + \frac{\lambda^2}{X^2(1 - \Delta' \cos\theta)^2}. \quad (2.73)$$

The term g/X in this expression is of second order, since the toroidicity is taken into account by assuming Eq. 2.41 and not $X = 1$ as we would do for the cylindrical case. The second term on the right hand side has a denominator $X^2(1 - \Delta' \cos\theta)$ which takes to a third order for the global square magnetic field B^2 . This is necessary in RFP configurations since, if we stop at the second order in ϵ , the poloidal magnetic field is $\lambda(r)$. But this is too crude an approximation at the edge of the RFP where $g = 0$ and the toroidal field vanishes.

Finally, the functional dependence of $\Delta(r)$ is assumed too be parabolic with the edge displacement Δ_0 experimentally measured:

$$\Delta(r) = (r/a)^2 \Delta_0 \quad (2.74)$$

where r is normalized to R_0 . Eq. 2.74 takes to a linear dependence of Δ' on r as predicted by analytical computations (see [26] for example).

2.3.5 Algorithm for RFPs equilibria: a summary

A summary is given here about the several steps that must be performed to implement the equilibrium functions for reversed field pinch configurations.

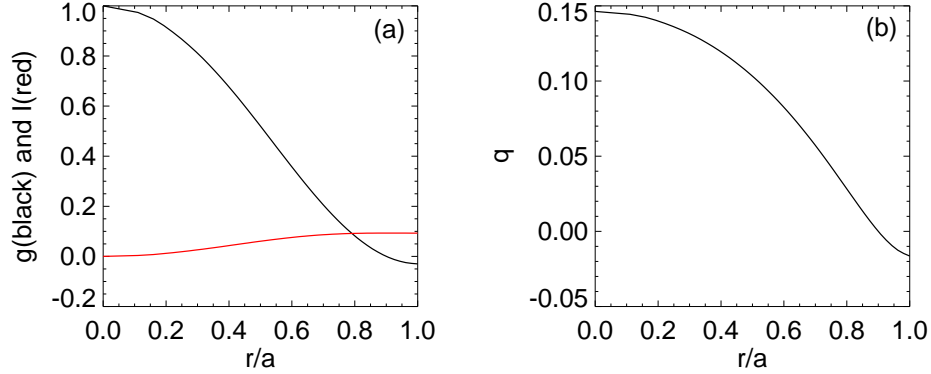


Figure 2.3: (a) Profiles of the g and I for a discharge in the RFX-mod experiment. (b) The safety factor q relative to profiles in (a).

The first step is to define analytically the function λ by computing the equilibrium fields by theoretical model such for example the $\mu&p$ for the RFP configuration in a cylindrical geometry. Once the fields are known they can be used to build the λ function which is given by the poloidal magnetic field $B^{\hat{\theta}}$.

Integration of λ from zero to the minor radius values gives the poloidal flux at wall p_w . Then a bi-dimensional grid in ψ_p and θ needs to be determined where all quantities will be numerically evaluated. Since the cylindrical equilibrium is defined as a function of the radius, a relation between radius and poloidal flux needs to be derived. We use Eq. 2.48: $\nabla\psi_p = \lambda(r)\nabla r$ which gives, once integrated, the following implicit relation:

$$r(\psi_p) = \int_0^{\psi_p} \frac{1}{\lambda(r(\psi'_p))} d\psi'_p. \quad (2.75)$$

Note that when $r \rightarrow 0$ also $\lambda \rightarrow 0$. From a numerical point of view is convenient to define a function $\Lambda(r) = \lambda(r)/r$ such that $\Lambda(r) \rightarrow c \neq 0$ for $r \rightarrow 0$; therefore the desired relation can be obtained by recursively solving:

$$r(\psi_p) = \left[\int_0^{\psi_p} \frac{2}{\Lambda(r(\psi'_p))} d\psi'_p \right]^{\frac{1}{2}} \quad (2.76)$$

The steps that follow are straightforward:

- computation of the poloidal field as a function of the flux, $\lambda(\psi_p) = \lambda(r(\psi_p))$;

- determination of $g(\psi_p)$ (covariant component of the toroidal field) function by the Grad-Shafranov equation solution. This can be done also with a non zero pressure profile p , but usually we shall consider for RFP the approximation $p = 0$ in solving the Grad-Shafranov equation.
- $I(\psi_p) = r(\psi_p)\lambda(\psi_p)$ (covariant component of the poloidal field)
- Shafranov shifted cylindrical coordinates are given by: $X(\psi_p, \theta) = 1 + r(\psi_p)\cos(\theta) - \Delta(r(\psi_p))$, $Z(\psi_p, \theta) = r(\psi_p)\sin\theta$;
- field strength taking into account the toroidal effects to the third order:

$$B^2 = \frac{g^2}{X^2} + \frac{\lambda^2}{X^2(1 - \Delta'\cos\theta)^2}; \quad (2.77)$$

- Jacobian imposed equal to: $J = (gq + I)/B^2$ by which we may compute the correct $\tilde{\nu}$ function with the straight field line condition at the desired order in ϵ ;
- the parabolic $\Delta(r)$ function is adjusted by matching the experimentally measured shift of the plasma column;
- the relation between the poloidal coordinate angle θ of the shifted system and the geometric poloidal angle Θ is given by: by $\theta = \Theta + r\sin(\Theta)$;

An example of the final equilibrium g and I profiles for the experiment RFX-mod in Padua are shown in Fig. 2.3-(a) with a black and a red line respectively. They are normalized to the product B_0R_0 with B_0 the field on axis. In the same figure the radial profile of the RFP safety factor q obtained by Eq. 2.70 is shown.

2.4 Circular Tokamak Equilibrium

The derivation of the circular Tokamak equilibrium is similar to the RFP. The only difference is the definition of the function λ and the expression for the square magnetic field B^2 .

For a cylindrical Tokamak, with the usual normalization $2\pi R_0 B_0 = 1$, the toroidal flux is given by $\psi = r^2/2$ (see [26]) and thus:

$$\lambda = \frac{d\psi_p}{d\psi} \frac{d\psi}{dr} = \frac{r}{q} \quad (2.78)$$

Usually the safety factor q is known from the experimental data and allows to compute λ by Eq. 2.78 and g by 2.52. From λ , with the same procedure

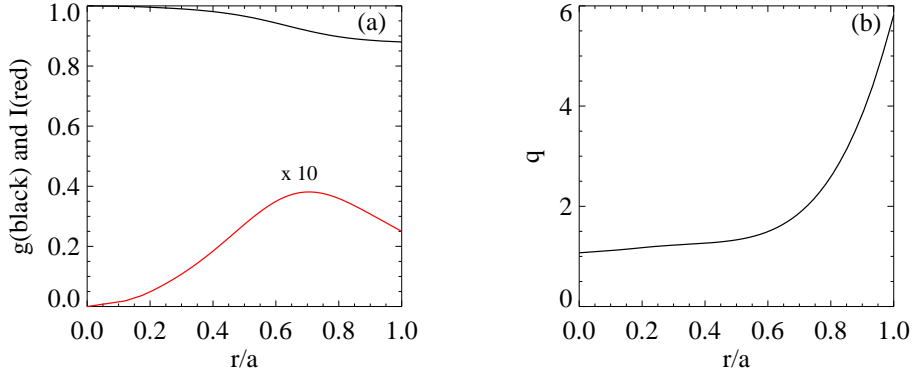


Figure 2.4: (a) Profiles of the g and I for a discharge in the tokamak ASDEX-Upgrade experiment. (b) The safety factor q relative to profiles in (a).

used for the RFP, a grid in the poloidal flux ψ_p is defined. After computing the relation $r(\psi_p)$ also the other quantities X, Z can be defined on the grid of the flux coordinates as for the RFP case. The same holds for the Jacobian J .

In the tokamak, as the magnetic field is dominated by the toroidal component at every radius, we can take only the second order for the toroidal field and the first order for the poloidal part which is usually ten times smaller; the expression for B^2 is thus:

$$B^2 = \frac{g^2}{X^2} + \frac{I^2}{r^2} \quad (2.79)$$

where, as we have shown, $\lambda = I/r$ is first order in ϵ .

In Chapter 7 we shall deal with a circular Boozer equilibrium for the Tokamak. The experimental safety factor q will be used to compute λ by the formula $\lambda = r/q$. Once we know λ and we calculate g from the Grad-Shafranov equation, at the first order, all the other quantities are easily derived. Fig. 2.4 shows, similarly to Fig. 2.3, the I and g functions, together with the q profile for a circular tokamak with the parameters of magnetic field and current of the experiment ASDEX-Upgrade.

2.5 Numerical Equilibria: the VMEC code

Approximate toroidal equilibrium obtained in the last two sections are not well suited for low aspect ratio tokamaks. Moreover, the cross section of several experiments is D-shaped. In such cases, equilibria are computed thought

numerical integration of the Grad Shafranov equation. The RFP and Tokamak equilibrium described in the last two sections are an approximation which allows to use the code ORBIT with Boozer coordinates. The numerical equilibrium has to be converted in coordinates suitable for the Hamiltonian equations as in ORBIT. We describe here the determination and the conversion of equilibria computed by *VMEC* [29].

In *VMEC*, equilibria are found numerically by fixing the value of the flux variable ϱ at the edge of the plasma and prescribing the functions $q(\varrho)$ and $p(\varrho)$, usually known by experimental data or assumed by theoretical considerations.

Since *VMEC* uses generic flux coordinates (ϱ, θ, ζ) , we recall here the magnetic field expression in Clebsh form :

$$\mathbf{B} = \nabla\varrho \times \nabla\nu \quad (2.80)$$

with

$$\nu = \dot{\psi}\theta - \dot{\psi}_p\zeta + \tilde{\nu}. \quad (2.81)$$

The dot means derivation in the flux label coordinates ϱ . Consider the cylindrical coordinate system (X, Z, ϕ) with Z the vertical axis and ϕ the geometric toroidal angle. The relation with the coordinates (ϱ, θ, ϕ) is given by the metric tensor:

$$ds^2 = (dX)^2 + (dZ)^2 + X^2d\phi^2 \quad (2.82)$$

with $dX = \partial_\varrho X d\varrho + \partial_\theta X d\theta$ and $dZ = \partial_\varrho Z d\varrho + \partial_\theta Z d\theta$; as we are considering an axi-symmetric device, no derivations with respect to ζ or ϕ appear.

Equation 2.82 can be rewritten symbolically as:

$$ds^2 = g_{\alpha\beta}d\alpha d\beta \quad (2.83)$$

where

$$g_{\alpha\beta} = \partial_\alpha X \partial_\beta X + \partial_\alpha Z \partial_\beta Z + \delta_{\alpha\phi} \delta_{\beta\phi} X^2. \quad (2.84)$$

The square of the magnetic field, using the properties of the metric tensor can be written as:

$$B^2 = (B^\theta)^2 g_{\theta\theta} + 2B^\theta B^\zeta g_{\zeta\theta} g_{\zeta\theta} + (B^\zeta)^2 g_{\zeta\zeta}. \quad (2.85)$$

Note that the last expression requires an explicit expression for the contravariant components B^ζ, B^θ as function of the Jacobian and of $\tilde{\nu}$. In fact from the definition of ν in Eq.2.81 and its properties, reported with equations A.62 in Appendix A, we have that:

$$B^\zeta = \frac{1}{J} \frac{\partial \nu}{\partial \theta} = \frac{1}{J} (\partial_\varrho \psi + \partial_\zeta \tilde{\nu}) \quad (2.86)$$

and

$$B^\theta = -\frac{1}{J} \frac{\partial \nu}{\partial \zeta} = \frac{1}{J} (\partial_\varrho \psi_p - \partial_\theta \tilde{\nu}) \quad (2.87)$$

where ϱ is still a generic flux coordinate.

Functions $X(\varrho, \theta, \phi)$, $Z(\varrho, \theta, \phi)$ and $\tilde{\nu}(\varrho, \theta, \phi)$ are defined in *VMEC* using Fourier expansion:

$$X = \sum X_{mn}(\varrho) \cos(m\theta - n\phi) \quad (2.88)$$

$$Z = \sum Z_{mn}(\varrho) \sin(m\theta - n\phi) \quad (2.89)$$

$$\tilde{\nu} = \sum \tilde{\nu}_{mn}(\varrho) \sin(m\theta - n\phi) \quad (2.90)$$

and are then iterated upon and adjusted to minimize the energy $\int (B^2/2 + p)dV$ subject to the constraint that the plasma edge (ρ_E) is fixed in space, i.e. for $\rho = \rho_E$ the surface described by $X(\rho_E, \theta, \zeta)$, $Z(\rho_E, \theta, \zeta)$ is fixed. The minimization of the energy with respect to the variation of the flux surface ρ guarantees that the obtained configuration satisfies $\mathbf{j} \times \mathbf{B} = \nabla p$. The *VMEC* code thus computes the Fourier components X_{mn} , Z_{mn} , $\tilde{\nu}_{mn}$ which are necessary to obtain X , Z , $\tilde{\nu}$. From $\tilde{\nu}$ it's easy to compute the contravariant component of the magnetic field and by the metric tensor also the covariant ones as shown in the Appendix A. The detailed algorithm for the Asdex-Upgrade case is described in the next section.

2.5.1 VMEC and ASDEX-Upgrade equilibrium

In Asdex-Upgrade, a variant of VMEC, i.e. the VMEC-NEMEC code, is adopted. This code uses the left-handed curvilinear coordinates (s, θ, ζ) where $s = \psi/\psi_E$ is the normalized toroidal flux corresponding to the flux surface label ρ , θ is the poloidal coordinate ($0 \leq \theta \leq 2\pi$), and ζ the toroidal coordinate ($0 \leq \zeta \leq 2\pi$). The relations of (s, θ, ζ) with the toroidal Cartesian coordinates (X, ϕ, Z) are given by:

$$X = \sum_{m=0, n=-n_b}^{m_b, n_b} x_{m,n}^c(s) \cos(m\theta - n\zeta N_p) + x_{m,n}^s(s) \sin(m\theta - n\zeta N_p); \quad (2.91)$$

$$Z = \sum_{m=0, n=-n_b}^{m_b, n_b} z_{m,n}^c(s) \cos(m\theta - n\zeta N_p) + z_{m,n}^s(s) \sin(m\theta - n\zeta N_p); \quad (2.92)$$

$$\phi = \zeta; \quad (2.93)$$

with $r_{m,n}^c(s), r_{m,n}^s(s), z_{m,n}^c(s), z_{m,n}^s(s)$ being the Fourier coefficients of a flux surface with normalized toroidal flux s , N_p is the number of periods, $0 \leq m \leq m_b$ are the poloidal mode numbers and $-n_b \leq n \leq n_b$ are the toroidal mode numbers. In ASDEX-Upgrade the equilibrium is axisymmetric and not depending on ζ thus equations 2.91 and 2.92 simply become ($N_p = 0$):

$$X = \sum_{m=0}^{m_b} x_m^c(s) \cos(m\theta) + x_m^s(s) \sin(m\theta); \quad (2.94)$$

$$Z = \sum_{m=0}^{m_b} z_m^c(s) \cos(m\theta) + z_m^s(s) \sin(m\theta). \quad (2.95)$$

The contravariant components of the magnetic field is:

$$B^\theta = \sum_{m=0}^{m_b} b_m^{\theta,c}(s) \cos(m\theta) + b_m^{\theta,s}(s) \sin(m\theta); \quad (2.96)$$

$$B^\zeta = \sum_{m=0}^{m_b} b_m^{\zeta,c}(s) \cos(m\theta) + b_m^{\zeta,s}(s) \sin(m\theta); \quad (2.97)$$

$$B^s = 0, \quad (2.98)$$

with the Fourier coefficients $b_m^{\theta,c}(s), b_m^{\theta,s}(s), b_m^{\zeta,c}(s), b_m^{\zeta,s}(s)$, while the covariant components of the magnetic field are given by:

$$B^\theta = I = \sum_{m=0}^{m_b} b_{\theta,c}^m(s) \cos(m\theta) + b_{\theta,s}^m(s) \sin(m\theta); \quad (2.99)$$

$$B_\zeta = g = \sum_{m=0}^{m_b} b_{\zeta,c}^m(s) \cos(m\theta) + b_{\zeta,s}^m(s) \sin(m\theta); \quad (2.100)$$

$$B_s = \delta = \sum_{m=0}^{m_b} b_{s,c}^m(s) \cos(m\theta) + b_{s,s}^m(s) \sin(m\theta). \quad (2.101)$$

with the Fourier coefficients $b_{\theta,c}^m(s), b_{\theta,s}^m(s), b_{\zeta,c}^m(s), b_{\zeta,s}^m(s), b_{s,s}^m(s), b_{s,c}^m(s)$.

By using these series expansions for the fields and the geometry, the Fourier components are computed by minimizing the total energy of the plasma confined in a toroidal domain and the plasma pressure $p(s)$ and $q(s)$ profile as function of the flux coordinate s . The output of VMEC are thus the Fourier components of the geometry and of the magnetic field from which it's easy to reconstruct, by summing up the terms, the profiles of $X(s, \theta), Z(s, \theta), B(s, \theta), g(s, \theta), I(s, \theta)$. Once the equilibrium is obtained, all

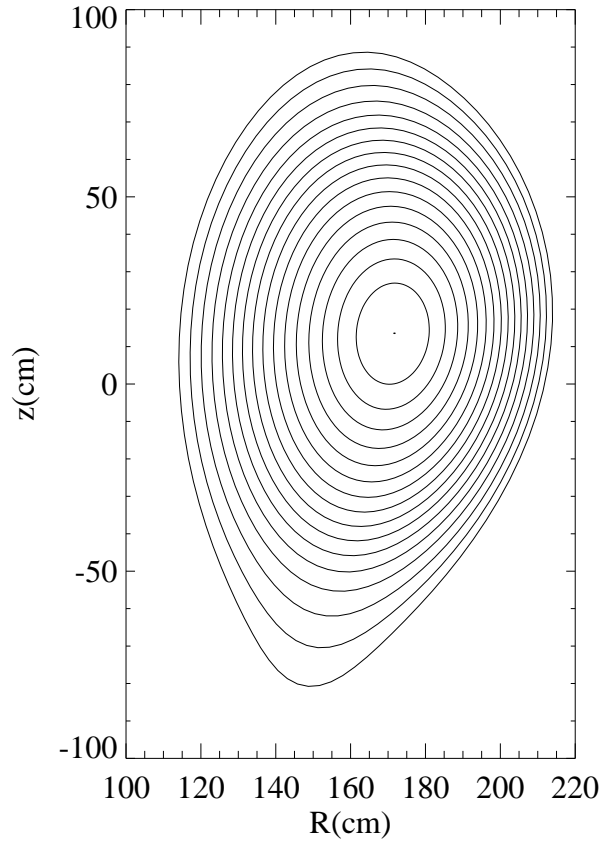


Figure 2.5: Examples of the magnetic surfaces inside the separatrix for the ASDEX-Upgrade equilibrium by VMEC.

the quantities need to be normalized according to the ORBIT conventions. Moreover the functions must be evaluated on a grid in poloidal flux ψ_p and θ , therefore a change of variable is required. The relation between s and ψ_p is obtained by using $q(s) = \frac{d\psi}{d\psi_p}$ to construct the function $\psi_p = \psi_p(s)$, since we know the value of s at the edge (s_E). The toroidal flux ψ is given by the relation:

$$\psi = s_E s / (2\pi R_0 B_0), \quad (2.102)$$

with the normalization factor $2\pi R_0 B_0$ necessary for the input in ORBIT. By integration we thus find:

$$\psi_p = \int \frac{d\psi}{q} = \int_0^s \frac{s_E}{2q(s')\pi R_0 B_0} ds'. \quad (2.103)$$

The values of ψ_p we have found are not equally spaced, but equation 2.103

can be used to calculate the poloidal flux at the edge (ψ_w). We can thus construct a new variable ψ_p^{lin} linearly increasing from 0 to ψ_w . Now all the quantities which are function of $s(\psi_p)$ and θ must be computed for the values of the new grid (ψ_p^{lin}, θ). For a generic function $K(s(\psi_p), \theta)$ we can compute its values on the new grid and have $K'(\psi_p^{lin}, \theta)$. This is performed for all the quantities which are needed in ORBIT with the correct normalization. In the following we shall call ψ_p the poloidal flux equally spaced (instead of ψ_p^{lin}) and we assume that all the quantities have been splined on the new grid. We give here a brief summary of the final procedures for implementing the equilibrium in ORBIT.

- the magnetic field is computed by using the covariant and contravariant component of the field with the relation:

$$B(\psi_p, \theta) = (B^\zeta B_\zeta + B^\theta B_\theta)^{\frac{1}{2}} \quad (2.104)$$

and normalizing it to value of the magnetic field on axis B_0 .

- the current profile $g(\psi_p)$ and $I(\psi_p, \theta)$ in ORBIT are given by:

$$g = \frac{B_\zeta}{B_0 R_0}, I = \frac{B_\theta}{B_0 R_0} \quad (2.105)$$

Note that g is a function of the poloidal flux only because the system is axi-symmetric (see appendix A).

- X, Z must be normalized to the major radius R_0 .
- toroidal flux for ORBIT is given by: $\psi(\psi_p) = \int_0^{\psi_p} q(\psi'_p) d\psi'_p$.
- $B_{\psi_p} = \delta$ must be normalized to B_0 .
- also the function $\tilde{\nu}$ must be implemented in the code if straight field lines coordinates are used. Since the ORBIT convention is different from the one of VMEC ($\nu_{ORBIT} = \theta - \zeta/q + \tilde{\nu}_{ORBIT}$) we have that:

$$\tilde{\nu}_{ORBIT}(\psi_p, \theta) = \tilde{\nu}_{VMEC}(\psi_p, \theta)q(\psi_p). \quad (2.106)$$

The function $\tilde{\nu}$ does not appear in the motion equations but must be implemented when performing Poincaré plots if we want the correct representation on a poloidal cross section. In fact it is the link between the geometrical ϕ and the straight field line ζ . Poloidal Poincaré must be performed at a constant ϕ . In fact, the interpolation of Poincaré performed at constant ζ surfaces, which are not simple planes, may lead to wrong conclusions.

CHAPTER 3

Hamiltonian Formulation

We derive in this Chapter the Lagrangian (section 2.1) and Hamiltonian (section 2.2) formulation of the guiding center motion equations in the equilibrium magnetic field. The particular case of axi-symmetry and straight field line coordinates is presented in section 2.3, which reports the motion equations implemented in the ORBIT code. Deviations from the equilibrium, such as the ripple effects and the helical magnetic perturbations are discussed in sections 2.4, 2.5 and 2.6. A classification of particle orbits follows in section 2.6. Finally, section 2.7 is dedicated to the interactions between the test particles and the plasma background, i.e. the collision mechanisms.

3.1 Lagrangian Formulation

The motion of charged particles in electromagnetic field is one of the oldest problems of plasma physics. It is characterized by different time scales: the rapid rotation and the slower dynamic of the guiding center motion. We are usually interested in the long time scales, i.e. in the evolution of the guiding center. It is therefore more efficient to separate the time scales and average the fast gyro motion scale. This is defined as the drift approximation. In order to integrate particle trajectories, an expansion of the equations of motion in the gyro radius must be made, and the rapid gyro phase motion averaged over, leaving equations for the guiding center dynamic. The Larmor radius

of charged particles in a reactor plasma is small compared to the plasma dimensions and to the curvature radius of the magnetic field. Thus charged particle motion is well described using the drift approximation.

The guiding center motion is determined by the mass, charge and energy of the particle and the field strength. These four quantities, however, enter in the equations in one combination only: the gyro radius. We consider as unit of time the inverse of the on-axis cyclotron frequency ω_c^{-1} and the units of distance given by the major radius R_0 ; thus, the basic unit of energy becomes $m\omega_c R_0^2$. Particle motion both along and across the magnetic field lines is of the order of the gyro radius $\rho = v/B$ but to leading order the cross field motion is the gyro motion, and cross field drift is of order ρ^2 .

Consider first the Lagrangian for a particle in an electromagnetic field:

$$L = [\mathbf{A}(\mathbf{x}, t) + \mathbf{v}] \cdot \frac{d\mathbf{x}}{dt} - H(\mathbf{x}, t) \quad (3.1)$$

where $\mathbf{B} = \nabla \times \mathbf{A}$ and H is the Hamiltonian function: $H = \mathbf{v}^2/2 + \Phi(\mathbf{x}, t)$, being Φ the electric field potential. Casting the Lagrangian in the form $L = \sum_i P_i \frac{dq_i}{dt} - H$ the canonical momentum \mathbf{P} for a charged particle in a electromagnetic field is given by $\mathbf{P} = \mathbf{v} + \mathbf{A}$. In order to separate time scales, the velocity is expressed as the sum of two components. One is parallel to the magnetic field and the other is perpendicular:

$$\mathbf{v} = v_{\parallel} \mathbf{b} + w \mathbf{c} \quad (3.2)$$

with $\mathbf{b} = \mathbf{B}/B$, $\mathbf{c} = -\sin\xi \mathbf{e}_1 - \cos\xi \mathbf{e}_2$ with \mathbf{e}_1 and \mathbf{e}_2 unit vectors orthogonal to \mathbf{B} and to each other satisfying $\mathbf{e}_1 \times \mathbf{e}_2 = \mathbf{b}$, ξ the gyro phase, and w the magnitude of the perpendicular velocity \mathbf{v}_{\perp} . The particle guiding center \mathbf{X} can be defined through the position:

$$\mathbf{x} = \mathbf{X} + \frac{w \mathbf{a}}{B(\mathbf{X})} \quad (3.3)$$

with $\mathbf{a} = \cos\xi \mathbf{e}_1 - \sin\xi \mathbf{e}_2$ so that $\mathbf{c} \times \mathbf{a} = \mathbf{b}$ and the magnetic field is evaluated at the guiding center \mathbf{X} . The Lagrangian thus becomes:

$$L = [\mathbf{A}(\mathbf{x}, t) + v_{\parallel} \mathbf{b} + w \mathbf{c}] \cdot \left[\frac{d\mathbf{X}}{dt} + \frac{d}{dt} \left(\frac{w \mathbf{a}}{B} \right) \right] - H. \quad (3.4)$$

The expression for the Lagrangian can be simplified in the guiding center approximation, i.e. with the following assumptions: ω is a small parameter; the spatial variation of \mathbf{B} occurs on scales much longer than a gyro radius; the time variations of \mathbf{B} occurs on scales much slower than the gyration frequency $d\xi/dt$. By substituting the first order expansion of the vector potential:

$$\mathbf{A}(x, t) \simeq \mathbf{A}(\mathbf{X}, t) + \frac{w \mathbf{a}}{B} \cdot \nabla \mathbf{A}(\mathbf{X}, t) \quad (3.5)$$

into the Lagrangian, we obtain:

$$\begin{aligned}
L = & [\mathbf{A} + v_{\parallel} \mathbf{b} + w \mathbf{c}] \cdot \frac{d\mathbf{X}}{dt} + v_{\parallel} \mathbf{b} \cdot \frac{d}{dt} \left(\frac{w \mathbf{a}}{B} \right) + \\
& w \mathbf{c} \cdot \frac{d}{dt} \left(\frac{w \mathbf{a}}{B} \right) + \left(\frac{w \mathbf{a}}{B} \cdot \nabla \right) \mathbf{A} \cdot \frac{d}{dt} \left(\frac{w \mathbf{a}}{B} \right) + \\
& \mathbf{A} \cdot \frac{d}{dt} \left(\frac{w \mathbf{a}}{B} \right) + \left(\frac{w \mathbf{a}}{B} \cdot \nabla \right) \mathbf{A} \cdot \frac{d\mathbf{X}}{dt} - H.
\end{aligned} \tag{3.6}$$

In this expression the vector potential is evaluated at the guiding center (\mathbf{X}, t) . After some straightforward but tedious computations and substituting the relation $\frac{d\mathbf{A}}{dt} = \frac{d\mathbf{A}}{dt} \cdot \nabla \mathbf{A} + \frac{\partial \mathbf{A}}{\partial t}$, the expression for the Lagrangian, approximated to the second order in ω is finally obtained:

$$L = [\mathbf{A} + v_{\parallel} \mathbf{b}] \cdot \frac{d\mathbf{X}}{dt} + \frac{w^2 d\xi/dt}{2B} - H(v_{\parallel}, w, \mathbf{X}, t). \tag{3.7}$$

where the Hamiltonian H is evaluated at the guiding center. From this equation it appears that $w^2/2B \equiv \mu$ is a constant of motion and that $d\xi/dt$ is constant too. This expression is absolutely general: it does not depend on the existence of magnetic surfaces, or on any other condition on \mathbf{B} .

Equation 3.7 can be cast as follows:

$$L = (\mathbf{A} + \rho_{\parallel} \mathbf{B}) \cdot \mathbf{v} + \mu \frac{d\xi}{dt} - H \tag{3.8}$$

with \mathbf{v} guiding center velocity, $\rho_{\parallel} = v_{\parallel}/B$ the normalized parallel velocity, μ the magnetic moment and ξ the gyrophase. The Hamiltonian is rewritten as:

$$H = \rho_{\parallel}^2 B^2/2 + \mu B + \Phi. \tag{3.9}$$

We now choose general magnetic flux coordinates ϱ, θ, ϕ and express the \mathbf{A} and \mathbf{B} vectors in contravariant representation. This will allow to obtain the dynamical equations for the evolution of the particle's coordinates.

In Chapter 2 we have seen that the magnetic field can be written as

$$\mathbf{B} = \nabla \psi_p \times \nabla \nu \tag{3.10}$$

with $\nu = \frac{d\psi}{d\psi_p} \theta - \phi + \tilde{\nu}$. Substituting this in Eq. 3.10 we obtain:

$$\begin{aligned}
\mathbf{B} = & \nabla \psi_p \times \nabla \left(\frac{d\psi}{d\psi_p} \theta - \phi + \tilde{\nu} \right) = \\
& \frac{d\psi}{d\psi_p} \nabla \psi_p \times \nabla \theta - \nabla \psi_p \times \nabla \phi + \nabla \psi_p \times \nabla \tilde{\nu} = \\
& \left(\frac{d\psi}{d\psi_p} + \frac{\partial \tilde{\nu}}{\partial \theta} \right) \nabla \psi_p \times \nabla \theta + \left(1 - \frac{\partial \tilde{\nu}}{\partial \phi} \right) \nabla \phi \times \nabla \psi_p
\end{aligned} \tag{3.11}$$

where the following relations have been used: $\nabla\psi_p \times \frac{d^2\psi}{d\psi_p^2}\nabla\psi_p = 0$, $\nabla\psi_p \times \frac{\partial\tilde{\nu}}{\partial\psi_p}\nabla\psi_p = 0$ and $\nabla\tilde{\nu} = \frac{\partial\tilde{\nu}}{\partial\phi}\nabla\phi + \frac{\partial\tilde{\nu}}{\partial\theta}\nabla\theta + \frac{\partial\tilde{\nu}}{\partial\psi_p}\nabla\psi_p$.

An alternative way to derive Eq.3.11 is to consider:

$$\mathbf{B} = \nabla \times (\psi\nabla\theta - \psi_p\nabla\phi - \tilde{\nu}\nabla\psi_p) \quad (3.12)$$

This immediately gives the vector potential $\mathbf{A} = \psi\nabla\theta - \psi_p\nabla\phi - \tilde{\nu}\nabla\psi_p$. Insert now this expression for \mathbf{A} in Eq. 3.8. The product $\mathbf{B} \cdot \mathbf{v}$ is performed by casting \mathbf{B} in its covariant form: $\delta\nabla\psi_p + g\nabla\phi + I\nabla\theta$ and the guiding center velocity in its contravariant form: $\mathbf{v} = \dot{\psi}_p\mathbf{e}_{\psi_p} + \dot{\theta}\mathbf{e}_\theta + \dot{\phi}\mathbf{e}_\phi$. Using the properties of the reciprocal basis of vectors (see A.1), $\nabla x^i \cdot \mathbf{e}_j = \delta_i^j$, where δ_i^j is the Kronecker symbol, we obtain for the Lagrangian:

$$L = (\psi + \rho_{||}I)\dot{\theta} + (\rho_{||}g - \psi_p)\dot{\phi} + \mu\dot{\xi} + \delta\rho_{||}\dot{\psi}_p - \tilde{\nu}\dot{\psi}_p - H. \quad (3.13)$$

The equation of motion in Lagrange formulation are given by:

$$\frac{d}{dt} \frac{\partial L}{\partial \dot{x}_k} - \frac{\partial L}{\partial x_k} = 0 \quad (3.14)$$

with $x_k = \psi_p, \theta, \phi, \rho_{||}$. Inserting Eq. 3.13 into 3.14 the coupled equations are obtained. They can be written in matrix form as:

$$\begin{pmatrix} 0 & \delta & I & g \\ -\delta & 0 & F & C \\ -I & -F & 0 & 0 \\ -g & -C & 0 & 0 \end{pmatrix} \cdot \begin{pmatrix} \dot{\rho}_{||} \\ \dot{\psi}_p \\ \dot{\theta} \\ \dot{\phi} \end{pmatrix} = \begin{pmatrix} \partial_{\rho_{||}}H \\ \partial_{\psi_p}H \\ \partial_\theta H \\ \partial_\phi H \end{pmatrix} \quad (3.15)$$

where we have defined C and F as:

$$\begin{aligned} C &= -1 + \rho_{||}(\partial_{\psi_p}g - \partial_\phi\delta) + \partial_\phi\tilde{\nu} \\ F &= g + \rho_{||}(\partial_{\psi_p}I - \partial_\theta\delta) + \partial_\theta\tilde{\nu} \end{aligned} \quad (3.16)$$

and used the general condition from Eq.A.109: $\partial_\theta g = \partial_\phi I$. By inverting the system in 3.15, an explicit expression for time derivatives, i.e. the equations of motion, are obtained:

$$\begin{pmatrix} \dot{\rho}_{||} \\ \dot{\psi}_p \\ \dot{\theta} \\ \dot{\phi} \end{pmatrix} = \frac{1}{D} \begin{pmatrix} 0 & 0 & C & F \\ 0 & 0 & -g & I \\ -C & g & 0 & -\delta \\ F & -I & \delta & 0 \end{pmatrix} \cdot \begin{pmatrix} \partial_{\rho_{||}}H \\ \partial_{\psi_p}H \\ \partial_\theta H \\ \partial_\phi H \end{pmatrix} \quad (3.17)$$

with determinant:

$$D = gq + I + \rho_{||}(g\partial_{\psi_p} - I\partial_{\psi_p}g - g\partial_\theta\delta + I\partial_\phi\delta) + g\partial_\theta\tilde{\nu} - I\partial_\phi\tilde{\nu}. \quad (3.18)$$

These equations are valid for a generic field as described in Eq. 3.10. Note that there are no derivatives of I or g with respect to ϕ and θ .

3.2 Hamiltonian Formulation

The Lagrangian formulation is not of practical use for computing particle trajectories. It is customary to write equations of motion in Hamiltonian formulation. In fact this allows an easier introduction of magnetic field perturbations. Moreover the conservation properties of the Hamiltonian can be used in the numerical algorithms to check for accuracy and to reduce the numerical errors. The first step for obtaining the Hamiltonian equations of motion is to identify the canonical variables. Consider again the Lagrangian 3.13; canonical variables are obtained by rewriting it in the form:

$$L = \sum_i P_i \dot{q}_i - H. \quad (3.19)$$

Let us change the toroidal coordinate ϕ with the new ϕ_c , as follows:

$$\phi = \phi_c + \phi_d \quad (3.20)$$

with $\phi_d = -\int_0^{\psi_p} d\psi_p \delta/g$ and write $\dot{\phi}_d = \dot{\theta} \partial_\theta \phi_d + \dot{\psi}_p \partial_{\psi_p} \phi_d + \dot{\phi} \partial_\phi \phi_d$. Now let's drop the exact derivatives:

$$\frac{d}{dt} \int_0^{\psi_p} \frac{\psi_p \delta}{g} d\psi_p, \quad (3.21)$$

$$\frac{d}{dt} \int_0^{\psi_p} \tilde{\nu} d\psi_p, \quad (3.22)$$

and rewrite the Lagrangian as a function of the new coordinate ϕ_c :

$$\begin{aligned} L = & (\psi + \rho_{||} I) \dot{\theta} + (\rho_{||} g - \psi_p) (\dot{\phi}_d + \dot{\phi}_c) + \dot{\psi}_p (\delta \rho_{||} - \tilde{\nu}) + \\ & + \mu \dot{\xi} - H + \frac{d}{dt} \int_0^{\psi_p} \frac{\psi_p \delta}{g} d\psi_p + \frac{d}{dt} \int_0^{\psi_p} \tilde{\nu} d\psi_p = \\ & (\psi + \rho_{||} I) \dot{\theta} + (\rho_{||} g - \psi_p) \dot{\phi}_c + (\rho_{||} g - \psi_p) + (\dot{\theta} \partial_\theta \phi_d + \dot{\psi}_p \partial_{\psi_p} \phi_d) + \\ & + \dot{\psi}_p (\delta \rho_{||} - \tilde{\nu}) + \mu \dot{\xi} - H + \frac{d}{dt} \int_0^{\psi_p} \frac{\psi_p \delta}{g} d\psi_p + \frac{d}{dt} \int_0^{\psi_p} \tilde{\nu} d\psi_p. \end{aligned} \quad (3.23)$$

By grouping the $\dot{\theta}, \dot{\phi}_c$ and $\dot{\phi}$ terms and with the following positions:

$$P_\phi = (\rho_{||} g - \psi_p) (1 + \partial_\phi \phi_d) + \partial_\phi \int_0^{\psi_p} \frac{\psi_p \delta}{g} d\psi_p + \partial_\phi \int_0^{\psi_p} \tilde{\nu} d\psi_p; \quad (3.24)$$

$$P_\theta = \psi + \rho_{||} I + (\rho_{||} g - \psi_p) \partial_\theta \phi_d + \partial_\theta \int_0^{\psi_p} \frac{\psi_p \delta}{g} d\psi_p + \partial_\theta \int_0^{\psi_p} \tilde{\nu} d\psi_p. \quad (3.25)$$

the Lagrangian can be rewritten as follows:

$$L = P_\theta \dot{\theta} + P_\phi \dot{\phi}_c + \mu \dot{\xi} - H. \quad (3.26)$$

By inspection, the canonical coordinates and the momenta are identified to be θ , ϕ_c and P_θ, P_ϕ . Therefore the Hamiltonian equations of motion are:

$$\dot{\theta} = \frac{\partial H}{\partial P_\theta}, \dot{P}_\theta = -\frac{\partial H}{\partial \theta} \quad (3.27)$$

$$\dot{\phi}_c = \frac{\partial H}{\partial P_\phi}, \dot{P}_\phi = -\frac{\partial H}{\partial \phi_c} \quad (3.28)$$

together with the evolution of the ϕ variable, which is linked to ϕ_c by Eq. 3.20. Equations of motion are given as function of $x_k = P_\phi, P_\theta, \phi_c, \theta$ but the Hamiltonian is expressed in terms of $y_k = \rho_{||}, \psi_p, \phi, \theta$. A change of variable is then required to get the equations of motion in explicit format. Partial derivatives for this change of variables are:

$$\left(\frac{\partial x_k}{\partial y_j} \right) = \begin{pmatrix} \partial_{\rho_{||}} P_\phi & \partial_{\psi_p} P_\phi & \partial_\phi P_\phi & \partial_\theta P_\phi \\ \partial_{\rho_{||}} P_\theta & \partial_{\psi_p} P_\theta & \partial_\phi P_\theta & \partial_\theta P_\theta \\ 0 & \partial_{\psi_p} \phi_d & 1 & \partial_\theta \phi_d \\ 0 & 0 & 0 & 1 \end{pmatrix} \quad (3.29)$$

and the inverse is:

$$M = \left(\frac{\partial y_k}{\partial x_j} \right). \quad (3.30)$$

The equations of motion can be written as:

$$\frac{dx_k}{dt} = S_{kj} \frac{\partial H}{\partial x_j} \quad (3.31)$$

with

$$S = \begin{pmatrix} 0 & 0 & -1 & 0 \\ 0 & 0 & 0 & -1 \\ 1 & 0 & 0 & 0 \\ 0 & 1 & 0 & 1 \end{pmatrix}. \quad (3.32)$$

By applying the change of variables $x_k \rightarrow y_k$ the equations of motion become:

$$\frac{dy_k}{dt} = (MSM^T)_{kj} \frac{\partial H}{\partial y_j}. \quad (3.33)$$

Once written in matrix form, the same equations as 3.15 are obtained. The advantage of such a derivation will appear in the next sections.

3.3 Motion equations in axi-symmetric configurations and straight field line coordinates

The system in Eq. 3.17 is simplified for an axisymmetric toroidal configuration. In fact, axisymmetry means that for all the equilibrium functions f we have $\partial_\phi f = 0$. A further simplification is obtained by using straight field line coordinates which imply that $\tilde{\nu} = 0$. This choice requires a change of the toroidal variable from ϕ to ζ as explained in section 2.1. Thus, the equations of guiding center particle motion with both these two assumptions (i.e. axisymmetry and straight field line coordinates) become:

$$\dot{\theta} = \frac{\rho_{\parallel} B^2}{D} (1 - \rho_{\parallel} \partial_{\psi_p} g) + \frac{g}{D} \left[(\mu + \rho_{\parallel}^2 B) \frac{\partial B}{\partial \psi_p} + \frac{\partial \Phi}{\partial \psi_p} \right] \quad (3.34)$$

$$\dot{\psi}_p = -\frac{g}{D} \left[(\mu + \rho_{\parallel}^2 B) \frac{\partial B}{\partial \theta} + \frac{\partial \Phi}{\partial \theta} \right] \quad (3.35)$$

$$\dot{\rho}_{\parallel} = -\frac{(1 - \rho_{\parallel}) \partial_{\psi_p} g}{D} \left[(\mu + \rho_{\parallel}^2 B) \frac{\partial B}{\partial \theta} \right] \quad (3.36)$$

$$\dot{\zeta} = \frac{\rho_{\parallel} B^2}{D} (q + \rho_{\parallel} [\partial_{\psi_p} I - \partial_\theta \delta]) - \frac{I}{D} \left[(\mu + \rho_{\parallel}^2 B) \frac{\partial B}{\partial \psi_p} + \frac{\partial \Phi}{\partial \psi_p} \right] + \frac{\delta}{D} \left[(\mu + \rho_{\parallel}^2 B) \frac{\partial B}{\partial \theta} + \frac{\partial \Phi}{\partial \theta} \right]. \quad (3.37)$$

These equations are valid also for Boozer coordinates but in this case I is a function of the poloidal flux only and does not depend on θ . Note also that the δ function appears in equations 3.34-3.35-3.36 only in the denominator D , i.e. it modifies the ψ_p, θ, ζ variables only through a renormalization of the time interval. Thus the projection of the orbit into the poloidal plane is independent of δ . But equation 3.37 has a term with δ of second order in ρ_{\parallel} , which means a change of the toroidal precession rate. The motion in physical space X, Z, ϕ is independent of the coordinate system, but these equations prove that neglecting the function δ in the equations modifies the toroidal drift.

We will show here that also the toroidal precession is independent of δ , so its omission produces only a redefinition of the guiding center. This takes to an alternative derivation of the canonical momenta and of the Hamilton

equations. To obtain the second order drift of a particle write the variation $\Delta\zeta$ calculated over one poloidal transit:

$$\Delta\zeta = \int \dot{\zeta} dt = \oint \frac{\dot{\zeta}}{\dot{\theta}} d\theta \quad (3.38)$$

and uses equations of motion 3.34 and 3.37 to first order in $\rho_{||}$:

$$\Delta\zeta = \oint d\theta (q + \rho_{||} [\partial_{\psi_p} I - \partial_{\theta} \delta + \partial_{\psi_p} g]) - \oint d\theta \frac{(\mu + \rho_{||}^2 B)}{\rho_{||} B^2} \left[(I + gq) \frac{\partial B}{\partial \psi_p} - \delta \frac{\partial B}{\partial \theta} \right]. \quad (3.39)$$

Energy conservation with $E = \rho_{||}^2 B^2 / 2 + \mu B$ gives, by differentiation, $(\mu + \rho_{||}^2 B) \partial_{\theta} B = -\rho_{||} B^2 \partial_{\theta} \rho_{||}$; by substitution in Eq.3.39, the terms in δ can be written as:

$$- \oint d\theta \partial_{\theta} [\delta \rho_{||}] = 0. \quad (3.40)$$

Thus, neglecting δ produces only a canonic change in the guiding center motion. Dropping the term in δ the Lagrangian has the following form:

$$L = (\psi + \rho_{||} I) \dot{\theta} + (\rho_{||} g - \psi_p) \dot{\zeta} + \mu \dot{\xi} - H \quad (3.41)$$

and the canonical momenta are immediately identified to be θ, ζ and P_{θ}, P_{ζ} with $P_{\theta} = \psi + \rho_{||} I$ and $P_{\zeta} = \rho_{||} g - \psi_p$. Equations of motion can be derived by the usual Hamilton equations.

3.4 Ripple effect in ORBIT

In the previous section equations of motion for an axi-symmetric equilibrium have been obtained. This allows to study particle's orbits in the equilibrium configuration. But usually, small deviations from axi-symmetry may have deep consequences on the particle's trajectory. First, we allow for a ϕ dependence of B , generated for example by the discrete coils system of the toroidal magnetic field, and also for a toroidal dependence of the electric potential Φ . The equations of motion are then:

$$\dot{\theta} = -C \frac{\rho_{||} B^2}{D} + \frac{g}{D} \left[(\mu + \rho_{||}^2 B) \frac{\partial B}{\partial \psi_p} + \frac{\partial \Phi}{\partial \psi_p} \right] - \frac{\delta}{D} \left[(\mu + \rho_{||}^2 B) \frac{\partial B}{\partial \phi} + \frac{\partial \Phi}{\partial \phi} \right] \quad (3.42)$$

$$\dot{\psi}_p = -\frac{g}{D} \left[(\mu + \rho_{||}^2 B) \frac{\partial B}{\partial \theta} + \frac{\partial \Phi}{\partial \theta} \right] + \frac{I}{D} \left[(\mu + \rho_{||}^2 B) \frac{\partial B}{\partial \phi} + \frac{\partial \Phi}{\partial \phi} \right] \quad (3.43)$$

$$\dot{\rho}_{\parallel} = \frac{C}{D} \left[(\mu + \rho_{\parallel}^2 B) \frac{\partial B}{\partial \theta} + \frac{\partial \Phi}{\partial \theta} \right] - \frac{K}{D} \left[(\mu + \rho_{\parallel}^2 B) \frac{\partial B}{\partial \psi_p} + \frac{\partial \Phi}{\partial \psi_p} \right] + \frac{F}{D} \left[(\mu + \rho_{\parallel}^2 B) \frac{\partial B}{\partial \phi} + \frac{\partial \Phi}{\partial \phi} \right] \quad (3.44)$$

$$\dot{\phi} = \frac{F \rho_{\parallel} B^2}{D} - \frac{I}{D} \left[(\mu + \rho_{\parallel}^2 B) \frac{\partial B}{\partial \psi_p} + \frac{\partial \Phi}{\partial \psi_p} \right] + \frac{\delta}{D} \left[(\mu + \rho_{\parallel}^2 B) \frac{\partial B}{\partial \theta} + \frac{\partial \Phi}{\partial \theta} \right] \quad (3.45)$$

where C, D, F have been defined in the paragraph 3.2. Equations 3.42-3.45 hold also for non-axisymmetric equilibria with generic flux coordinates. It's straightforward to obtain the corresponding equations in straight field line by the substitution $\phi \rightarrow \zeta$ which implies $\tilde{\nu} = 0$.

We discuss in this paragraph the effect of the deviation from axi-symmetry due to a discrete coils system. Consider an ideal situation with a toroidal device completely surrounded by circular coils. They produce, according to Ampere Law, a toroidal magnetic field of the form:

$$B_{\phi} = \frac{B_0 R_0}{R} \quad (3.46)$$

where R_0 is the major radius and B_0 is the field on axis. In real experiments the toroidal device has a finite number of coils. This affects the magnetic field which in this case has periodic variations in the toroidal direction, called *ripple*. The ripple R_p can be described by the following equation:

$$R_p = A(\psi_p, \theta) \sin(N\zeta) \quad (3.47)$$

where N is the number of the coils and A is a function of the coordinates (ψ_p, θ) which represents the local amplitude of the ripple and depends on the geometry of the device. Eq. 3.47 must be added to the magnetic field expression in the equations of motion.

We are usually given a map of the ripple as function of X, Z , i.e. a function $A(X, Z)$, produced by an other code. To be read by ORBIT this function must be splined on the ORBIT flux coordinates (ψ_p, θ) . This is straightforward to do because we know the functions $X(\psi_p, \theta)$ and $Z(\psi_p, \theta)$, and by a simple spline we can compute the function $A(\psi_p, \theta)$. Usually the ripple is represented using the logarithm of A and is normalized to the field on axis as all the other magnetic field and currents. For example, an amplitude of $\log(A)$ equal to -1 means at that point the magnetic field ripple amplitude is $1/10$ of the field on axis. The ripple effects are stronger near the low field side where coils have a greater distance between each other.

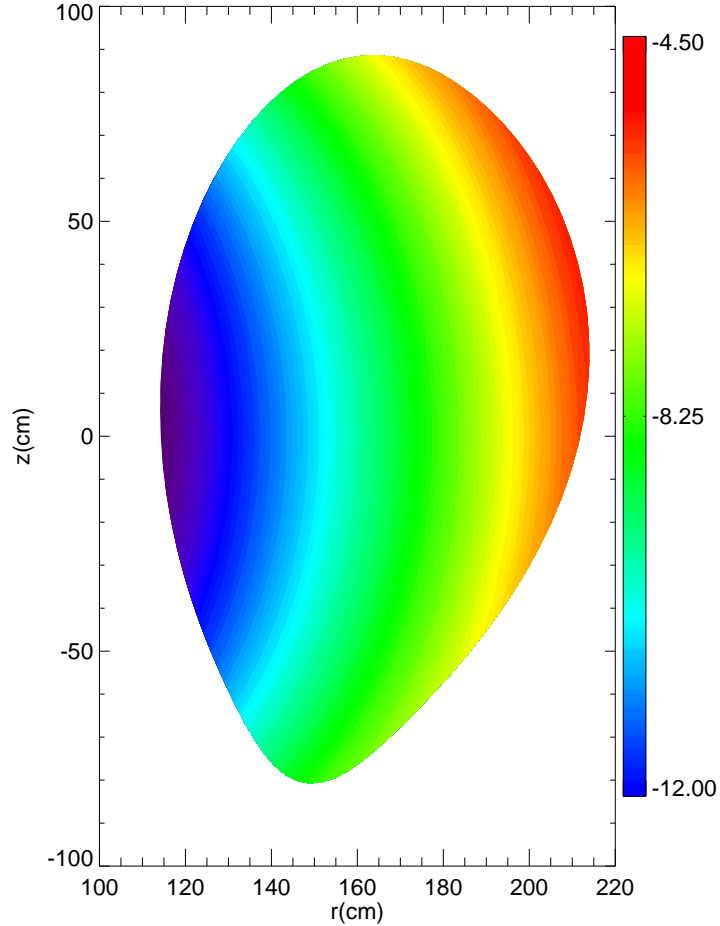


Figure 3.1: Ripple contour map for the function $\log(A)$ in ASDEX-Upgrade

3.4.1 Ripple for Asdex-Upgrade

In order to estimate losses due to ripple in ASDEX-Upgrade, an analytical approximation has been used. The most common and general form for A in many devices is the following:

$$A(\psi_p, \theta) = d_0 \frac{B(\psi_p)}{B_0} \exp(\tau(\psi_p, \theta)/w_{rip}) \quad (3.48)$$

where d_0 is a constant, B/B_0 the normalized magnetic field, and the quantities τ and w_{rip} are adjusted to fit the given numerical function A . In ASDEX-

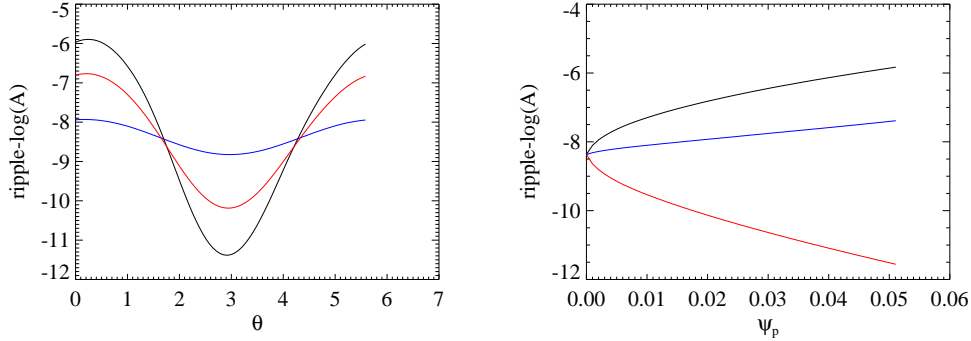


Figure 3.2: On the left hand side: ripple in Asdex for different values of the poloidal flux versus the poloidal angle θ . The black line refer to ripple near the the edge, the red one in the middle, and the blue close to the origin. Right hand side: ripple as function of the poloidal flux at three different poloidal angles from zero (black) to $\pi/2$ (red).

Upgrade the ripple effect is well described by the following functions:

$$\alpha_{rip} = -21.959 + 4.653Z(\psi_p, \theta)^2 + 1.747Z(\psi_p, \theta)^4 \quad (3.49)$$

$$\beta_{rip} = 7.891 - 1.07Z(\psi_p, \theta)^2 - 0.86Z(\psi_p, \theta)^4 \quad (3.50)$$

$$A(\psi_p, \theta) = \exp(\alpha_{rip} + \beta_{rip}X(\psi_p, \theta)) \quad (3.51)$$

and A is already normalized to the field on axis B_0 . The ripple function is shown in Fig.3.1. It's clear the great effect of the ripple on the LFS which is closer to the coils. More precisely this is observed in Fig. 3.2. On the left hand side ripple amplitude is shown vs the poloidal angle for different values of the poloidal flux. The ripple variation is higher in the external region and for θ close to zero. On the right hand side ripple versus poloidal flux for three different poloidal angles is plotted.

Ripple has a strong effect on particles with a velocity orthogonal to the magnetic field as we shall show in the following and is responsible for high energy particle losses. This issue is relevant for future reactors: if the ripple is too high, in fact, a significant fraction of α particles may be lost, seriously damaging the first wall.

3.5 Helical Magnetic Perturbations

An other class of deviations from axi-symmetry is represented by helical perturbations; the inclusion of their effect is less straightforward. In particular,

it is impossible to derive an Hamiltonian formulation for a general form of the perturbation. The Hamiltonian nature of the motion is preserved provided that fields perturbations of a restricted form are considered.

All tear and shear perturbations of \mathbf{B} are primarily orthogonal to the equilibrium \mathbf{B} . These perturbations can be described through:

$$\delta\mathbf{B} = \nabla \times \alpha\mathbf{B} \quad (3.52)$$

with α an arbitrary scalar function of ψ_p, θ, ζ . This form represents exactly the $\nabla\psi_p$ component of any perturbation, which is the component responsible for the presence of magnetic field lines orthogonal to the flux surfaces. It can be shown that if α has the form $\alpha = \alpha_{mn}\sin(m\theta - n\zeta)$ it produces a magnetic island at ψ_p with $q(\psi_p) = m/n$ of width:

$$\delta\psi_p = 4 \left(\frac{\alpha_{mn}}{s} \right)^{1/2} \quad (3.53)$$

where s is the local *shear* which is defined as:

$$s = \frac{q'(\psi_p)}{q(\psi_p)}. \quad (3.54)$$

The choice of the magnetic perturbations 3.52 allows to obtain the equations of motion by replacing \mathbf{A} with $\mathbf{A} + \alpha\mathbf{B}$; the following Lagrangian is obtained:

$$L = (\psi + \rho_{||}I + \alpha I)\dot{\theta} + (\rho_{||}g + \alpha g - \psi_p)\dot{\zeta} + \mu\dot{\zeta} + \delta(\rho_{||} + \alpha)\dot{\psi}_p - H \quad (3.55)$$

and with the Lagrangian equations given by the system:

$$\begin{pmatrix} 0 & \delta & I & g \\ -\delta & 0 & F & C \\ -I & -F & 0 & K \\ -g & -C & -K & 0 \end{pmatrix} \cdot \begin{pmatrix} \dot{\rho}_{||} \\ \dot{\psi}_p \\ \dot{\theta} \\ \dot{\zeta} \end{pmatrix} = \begin{pmatrix} \partial_{\rho_{||}} H \\ \partial_{\psi_p} H \\ \partial_{\theta} H \\ \partial_{\zeta} H \end{pmatrix} \quad (3.56)$$

where $C = -1 + (\rho_{||} + \alpha)(\partial_{\psi_p}g - \partial_{\zeta}\delta) + g\partial_{\psi_p}\alpha - \delta\partial_{\zeta}\alpha + \partial_{\zeta}\tilde{\nu}$, $K = g\partial_{\theta}\alpha - I\partial_{\zeta}\alpha$, $F = q + (\rho_{||} + \alpha)(\partial_{\psi_p}I - \partial_{\theta}\delta) + I\partial_{\psi_p}\alpha - \delta\partial_{\theta}\alpha + \partial_{\theta}\tilde{\nu}$ and we have used Eq. A.109. Inverting the system we have finally:

$$\begin{pmatrix} \dot{\rho}_{||} \\ \dot{\psi}_p \\ \dot{\theta} \\ \dot{\zeta} \end{pmatrix} = \frac{1}{D} \begin{pmatrix} 0 & -K & C & -F \\ K & 0 & -g & I \\ -C & g & 0 & -\delta \\ F & -I & \delta & 0 \end{pmatrix} \cdot \begin{pmatrix} \partial_{\rho_{||}} H \\ \partial_{\psi_p} H \\ \partial_{\theta} H \\ \partial_{\zeta} H \end{pmatrix} \quad (3.57)$$

with denominator:

$$D = gq + I + (\rho_{||} + \alpha)(g\partial_{\psi_p} - I\partial_{\psi_p}g - g\partial_{\theta}\delta + I\partial_{\zeta}\delta) + g\partial_{\theta}\tilde{\nu} - I\partial_{\zeta}\tilde{\nu}. \quad (3.58)$$

Equations of motion for axi-symmetric devices and with straight field line coordinates become:

$$\dot{\theta} = -C \frac{\rho_{\parallel} B^2}{D} + \frac{g}{D} \left[(\mu + \rho_{\parallel}^2 B) \frac{\partial B}{\partial \psi_p} + \frac{\partial \Phi}{\partial \psi_p} \right] - \frac{\delta}{D} \left[(\mu + \rho_{\parallel}^2 B) \frac{\partial B}{\partial \zeta} + \frac{\partial \Phi}{\partial \zeta} \right] \quad (3.59)$$

$$\dot{\psi}_p = K \frac{\rho_{\parallel} B^2}{D} - \frac{g}{D} \left[(\mu + \rho_{\parallel}^2 B) \frac{\partial B}{\partial \theta} + \frac{\partial \Phi}{\partial \theta} \right] + \frac{I}{D} \left[(\mu + \rho_{\parallel}^2 B) \frac{\partial B}{\partial \zeta} + \frac{\partial \Phi}{\partial \zeta} \right] \quad (3.60)$$

$$\begin{aligned} \dot{\rho}_{\parallel} = \frac{C}{D} \left[(\mu + \rho_{\parallel}^2 B) \frac{\partial B}{\partial \theta} + \frac{\partial \Phi}{\partial \theta} \right] - \frac{K}{D} \left[(\mu + \rho_{\parallel}^2 B) \frac{\partial B}{\partial \psi_p} + \frac{\partial \Phi}{\partial \psi_p} \right] + \\ - \frac{F}{D} \left[(\mu + \rho_{\parallel}^2 B) \frac{\partial B}{\partial \zeta} + \frac{\partial \Phi}{\partial \zeta} \right] \end{aligned} \quad (3.61)$$

$$\dot{\zeta} = \frac{F \rho_{\parallel} B^2}{D} - \frac{I}{D} \left[(\mu + \rho_{\parallel}^2 B) \frac{\partial B}{\partial \psi_p} + \frac{\partial \Phi}{\partial \psi_p} \right] + \frac{\delta}{D} \left[(\mu + \rho_{\parallel}^2 B) \frac{\partial B}{\partial \theta} + \frac{\partial \Phi}{\partial \theta} \right] \quad (3.62)$$

In the derivations of the previous equations we have assumed positively charged particles, so these are the equations for ions. The trajectories of electrons are slightly different. Aside from the different gyroradius and thus energy normalization, the normalization of time to the gyro frequency makes it necessary to change the sign of ρ_{\parallel} , and the overall sign of the time derivatives to obtain electron trajectories. This is equivalent to changing the sign of the electric potential and of the order ρ^2 drift terms.

3.6 Time-dependent perturbations

In fusion experiments magnetic instabilities like the tearing modes are often not stationary but rotate inside the plasma. The introduction of a time dependence for the function α is not straightforward when a test particle is moving in a background plasma. In fact, the variation of the magnetic perturbation induces an electric field, which is shorted out by electrons, on the guiding center time scales

Consider a time varying representation of the mode (m, n) of the form:

$$\alpha(\psi_p, \theta, \zeta, t) = \tilde{\alpha}(\psi_p) \sin(m\theta - n\zeta + \omega t). \quad (3.63)$$

This time variation of the magnetic field induces an electric potential perturbation Φ of the same form:

$$\Phi = \tilde{\Phi}(\psi_p) \sin(m\theta - n\zeta + \omega t). \quad (3.64)$$

as prescribed by the Maxwell equation: $\nabla \times \mathbf{E} = -\partial_t \mathbf{B}$ applied to the perturbation of magnetic field $\delta \mathbf{B}$ which has a potential vector $\delta \mathbf{A} = \alpha \mathbf{B} + \nabla \Phi$ ($\nabla \Phi$ is the gauge's choice). Using the relation $\delta \mathbf{b} = \nabla \times \alpha \mathbf{B}$, we finally have:

$$\mathbf{E} = -\frac{\partial(\alpha \mathbf{B})}{\partial t} - \nabla \Phi = \omega \tilde{\alpha}(\psi_p) \cos(m\theta - n\zeta + \omega t) \mathbf{B} - \nabla \Phi. \quad (3.65)$$

But the rapid mobility of electrons shorts out the parallel electric field E_{\parallel} on a very fast time scale, as shown in [26]. Thus:

$$E_{\parallel} = \omega \tilde{\alpha}(\psi_p) \cos(m\theta - n\zeta + \omega t) B - \mathbf{B} \cdot \nabla \Phi / B = 0 \quad (3.66)$$

which, with the notation in Eq. 3.64 and expressing $\mathbf{B} \cdot \nabla = (\partial_{\theta} + q\partial_{\zeta})/J$, becomes:

$$E_{\parallel} = \omega \tilde{\alpha}(\psi_p) B - \frac{nq - m}{JqB} \tilde{\Phi} = 0. \quad (3.67)$$

Finally, we substitute the expression of the square magnetic field in Boozer coordinates $B^2 = (gq + I)/J$ and we obtain the desired expression of $\tilde{\Phi}$:

$$\tilde{\Phi} = \omega \tilde{\alpha} \frac{gq + I}{nq - m} \quad (3.68)$$

where g is the covariant component of the toroidal magnetic field and I that of the poloidal magnetic field.

The field produced by electrons can be computed also for straight field line coordinates, but in the derivation we cannot use the Boozer constraint on the Jacobian. Thus, Eq. 3.67 in straight field lines is given by:

$$\tilde{\Phi} = \omega \tilde{\alpha} \frac{JB^2}{nq - m} \quad (3.69)$$

where J and $B^2 = B_{\zeta} B^{\zeta} + B_{\theta} B^{\theta}$ must be calculated from the metric tensors and the field components given as output from proper numerical codes (*VMEC* in our case). Expression 3.69 hides a problem since on the left hand side the term $\tilde{\Phi}$ is a function only of the poloidal flux ψ_p but on the right hand side generally $B^2 J$ may depend both on ψ_p and θ . For a correct solution B^2 and the Jacobian should be expressed in Fourier decomposition in $m\theta$ too. In the numerical simulations presented in Chapter 7 we have approximated JB^2 with its average value on the angle θ and inserted the result in Eq. 3.69; the final expression for $\tilde{\Phi}$ is:

$$\tilde{\Phi} = \omega \tilde{\alpha} \frac{\langle JB^2 \rangle_{\theta}}{nq - m} \quad (3.70)$$

where $\langle \dots \rangle_\theta$ represents the average over θ . This is a good approximation since JB^2 have small oscillations in θ around its mean value for every surface of constant poloidal flux ψ_p .

The potential 3.70 (or 3.68 for Boozer coordinates) is implemented in the ORBIT motion equations. It needs to be regularized at the position $q = m/n$, i.e. at the radial position of the magnetic island. This is performed by setting the potential inside the magnetic island equal to the value it assumes just outside the separatrix.

3.7 Classification of particle orbits

In this section we deal with the different topology for particle orbits in a axi-symmetric device ($\partial_\zeta = 0$). Many of the following considerations will be important to understand the calculations of Chapters 7-8, concerning high-energy ion motion in fusion devices.

In the absence of an electric field from the relation $P_\zeta = \rho_{||}g - \psi_p$ and the definition of the Hamiltonian H we find for the total energy particle the following expression:

$$E = \frac{[P_\zeta + \psi_p(P_\theta, P_\zeta)]^2 B^2}{2g} + \mu B. \quad (3.71)$$

We know that in a device where ζ is an ignorable coordinate, the momentum P_ζ is a constant of motion. This integral of the motion considerably simplifies the particle orbits. In this case, E is a function of P_θ and θ . But also $\rho_{||} = (2E - 2\mu B)^{1/2}/B$ is a function of ψ, θ , so $E = \text{constant}$ defines closed curves in the ψ, θ planes. Thus in the case of axisymmetry the particle motion is restricted to a two dimensional drift surface characterized by the values of E, μ , regardless of the shape of the flux surface cross section. Note that this is also true in the presence of electric and magnetic perturbations as long as they are independent of the ignorable coordinate ζ , but in the following of this section we shall consider only situations when these perturbations are absent. From the equations of motion in straight field lines and without perturbations we have:

$$\dot{\psi}_p = -\frac{g}{D}(\mu + \rho_{||}^2 B) \frac{\partial B}{\partial \theta} \quad (3.72)$$

which is second order in ρ and usually odd in θ since B increases in the direction of decreasing X . To first order in ρ the particles follow the field lines and to next order it drifts across the surfaces, with $\dot{\psi}_p < 0$ for $0 < \theta < \pi$ and $\dot{\psi}_p > 0$ for $-\pi < \theta < 0$, i.e. inward drift in the upper half of the torus and

outward drift in the lower half. As it moves around θ towards decreasing X it will normally encounter increasing field magnitude, and may encounter a point where $\rho_{\parallel} = 0$ (mirror point) because $B(\psi_p, \theta) = E/\mu$. We shall denote the bounce angle by θ_b . If such a point exists the particles is called trapped, otherwise it is called passing.

3.7.1 Passing Particles

We start in this paragraph to study passing particles and their properties. A new method to determine the mean surface displacement for passing particles is here presented. The drift across toroidal surfaces is given by conservation of toroidal momentum $P_{\zeta} = g(\psi_p)\rho_{\parallel}(\psi_p, \theta) - \psi_p$. Take ψ_p to be the reference flux surface, with the maximum excursion of the orbit given by $\psi_p + \sigma$ on the low field side (LFS) and $\psi_p - \sigma$ on the high field side (HFS). P_{ζ} evaluated at these two points is subtracted:

$$0 = P_{\zeta}(LFS) - P_{\zeta}(HFS) = g(\psi_p + \sigma)\rho_{\parallel}(\psi_p + \sigma, \theta) - g(\psi_p - \sigma)\rho_{\parallel}(\psi_p - \sigma, \theta) - 2\sigma. \quad (3.73)$$

By defining $M_{\theta}(\psi_p, \sigma)$ as the maximum over θ of $\rho_{\parallel}(\psi_p + \sigma, \theta)$ and $m_{\theta}(\psi_p, \sigma)$ as the minimum of $\rho_{\parallel}(\psi_p - \sigma, \theta)$ over θ , we find by iteration a rapidly convergent sequence for σ

$$2\sigma_{n+1} = g(\psi_p + \sigma_n)M_{\theta}(\psi_p, \sigma_n) - g(\psi_p - \sigma_n)m_{\theta}(\psi_p, \sigma_n) \quad (3.74)$$

with $\sigma_0 = 0$, and for low energies a single iteration is sufficient, i.e. σ can be ignored on the right hand side. We have assumed positive pitch, σ becomes negative for negative pitch. This equation is valid for arbitrary axisymmetric equilibria. Note that the shift depends on ρ_{\parallel} which is proportional to the energy of the particles. Orbits of passing particles with sufficiently high energy can be displayed and lost to the wall.

A simpler analytical expression can be derived for the shift σ in a simplified situation when the device has a circular section and in a low pressure configuration where the plasma diamagnetism is negligible and the dominant drifts experienced by the plasma are due to ∇B and curvature. These drift are due to toroidicity because of the $1/X$ dependence of B_{ϕ} and the centrifugal force. The drift velocity according to the expression in Chapter 1 (Eq. 1.37-1.38) is in the vertical direction (z) and is given for a far passing particles by:

$$v_z = \frac{\frac{v_{\perp}^2}{2} + v_{\parallel}^2}{R_0\omega_c} \mathbf{e}_z. \quad (3.75)$$

Note that the drift is in opposite directions for electrons and ions. As a result positive and negative charges collect at the top and the bottom of

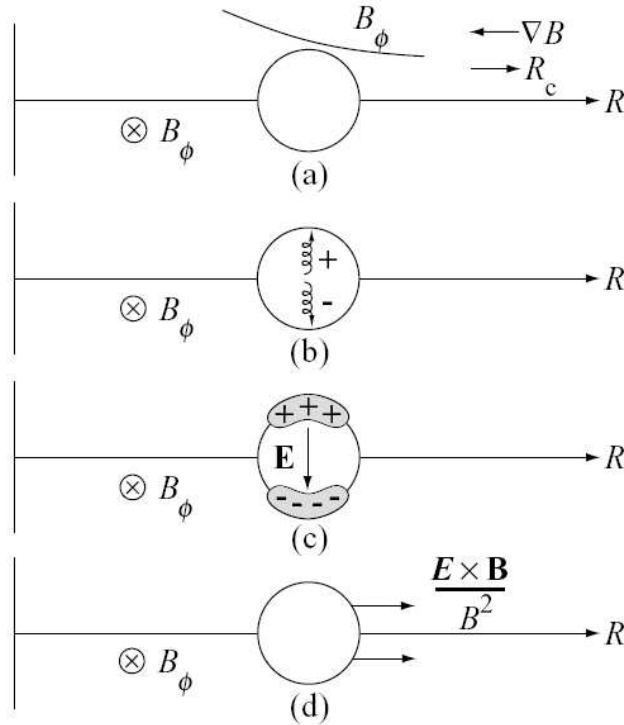


Figure 3.3: Lack of equilibrium in a system with purely toroidal field (a) geometry (b) guiding center drifts (c) induced electric field and (d) plasma moving outward with $\mathbf{E} \times \mathbf{B}/B^2$ drift velocity.

the plasma, respectively, as shown in Fig. 3.3-(b). These charges set up a z -directed electric field, which then propels the entire plasma outward along X with the $\mathbf{E} \times \mathbf{B}/B^2$ drift velocity; hence there is no toroidal equilibrium for the configuration with purely toroidal field.

Consider the situation now where a small poloidal field is superimposed on the toroidal field, as shown in fig 3.4. The magnetic field lines wrap slowly around the plasma on approximately helical trajectories. If $B_\theta \ll B_\phi$ the particles still experience the same up-down drift given by Eq. 3.75. One is then faced with the apparently paradoxical question of how a small poloidal field can lead to single-particle confinement for particles that have a constant vertical drift. The resolution is illustrated in Fig. 3.4. The dashed lines represent flux surfaces. To zero order, a particle's parallel motion simply follows a field line. Thus the projection of the particles's orbit on a poloidal cross section would coincide with the flux surface if there was no up-down drift. If the drift is now included, as the particle spirals from point 1 to point 2, it actually arrives at point 2' because of the upward drift. From point 2' to 3'

the drift off the surface continues to increase. However from point 3' to 4' the upward drift causes the particle to drift back toward the surface, eventually returning to its starting position. The point is that a constant upward drift correspond to motion away from the surface half the time and toward the surface the other half of the time; on average the net due to the drift cancels and the particles remain confined.

We estimate the drift in the case when the poloidal magnetic field is really small, so we can suppose that the poloidal rotation velocity is:

$$v_p = \frac{rd\theta}{dt} = \frac{B_\theta}{B_\phi}v_\phi \simeq \frac{B_\theta}{B_\phi}v_{||} \quad (3.76)$$

where we have used the relation $d\phi/d\theta = rB_\phi/RB_\theta$ and we have assumed that $v_{||} \simeq v_\phi$ being the poloidal field very small. In polar coordinates the total velocity along the radial coordinate (r) is the projection of the vertical drift v_z along \hat{r} . On the poloidal angle coordinate we have two contributes: the velocity $v_p = r\dot{\theta}$ and the projection of v_z on $\hat{\theta}$. We thus have from the ratio of the poloidal and radial components:

$$\frac{dr}{rd\theta} = \frac{v_z \sin\theta}{-v_z \cos(\theta) + v_p} \quad (3.77)$$

and integrating we have:

$$r(\theta)/r_0 = \int_{r_0}^r \frac{dr'}{r'} = \int_{\pi/2}^\theta \frac{v_z \sin\theta'}{-v_z \cos(\theta') + v_p} d\theta' \quad (3.78)$$

where we have assumed $r(\pi/2) = r_0$. The final orbit of the particle projected on the poloidal plane is:

$$\frac{r(\theta)}{r_0} = \left[1 - \frac{v_z}{v_p} \cos(\theta)\right]^{-1} \simeq 1 + \frac{v_z}{v_p} \cos(\theta). \quad (3.79)$$

We finally have obtained the displacement of the distorted circle in the direction of the major radius for a passing particle:

$$\sigma = r_0 v_z / v_p = r_0 \frac{v_z B_\theta}{v_{||} B_\phi} = \frac{(v_{||}^2 + \frac{1}{2}v_\perp^2)}{v_\perp v_{||}} q r_L \quad (3.80)$$

which for particles with $v_\perp = 0$ becomes:

$$\sigma = \frac{|v|q(r)}{\omega_c}. \quad (3.81)$$

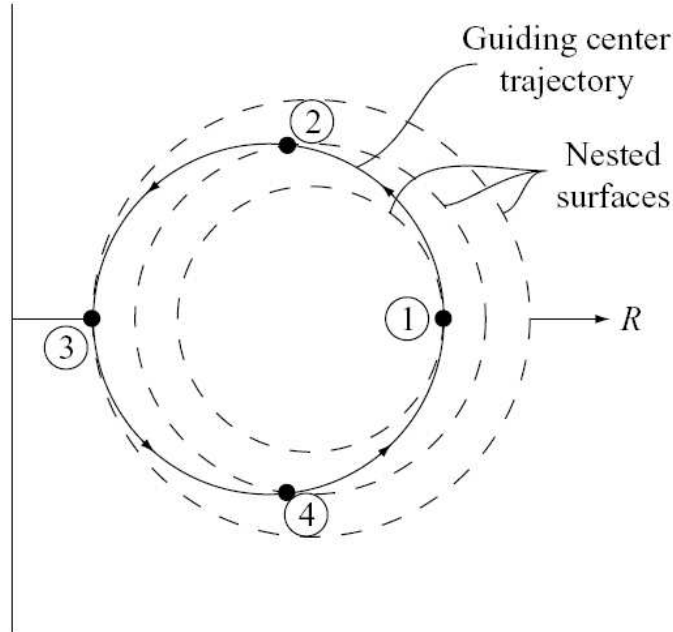


Figure 3.4: Single particle picture of toroidal confinement in the presence of a poloidal magnetic field: particle orbit including a uniform upward drift.

In the following we shall often use the displacement σ in units of poloidal flux. This also allows to generalize the previous equations to general shape devices. Once the function $\sigma(\psi_p)$ is known the orbit of a passing particle initially placed on the poloidal flux surface labelled by ψ_{p0} is given to the first order by:

$$\psi_p = \psi_p^0 + \sigma \cos\theta. \quad (3.82)$$

Note that low energy and thermal ions ($\leq 5keV$) have a shift σ often negligible compared with the standard dimensions of the fusion experiments, but fast ions generated by NBI or radio-frequency system may have very deformed orbits and may be lost from to the plasma.

3.7.2 Trapped particles

The invariance of the magnetic moment μ plays an important role in particle trajectories in magnetically confined plasmas. Charged particles can get trapped, changing their velocity direction due to magnetic mirrors. The mirror effect occurs when a particle guiding center moves toward a region with a stronger magnetic field as described in the first Chapter while discussing

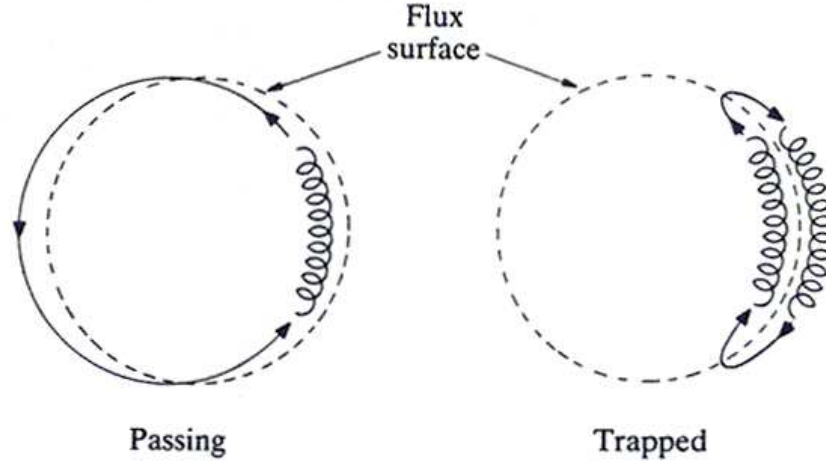


Figure 3.5: Diagram illustrating particle drift due to the non-uniformity of magnetic field when moving in poloidal direction over a magnetic flux surface in the case of a passing particle (on the left) and a trapped one (on the right).

the single orbit dynamic.

We report in Fig. 3.5 a comparison between a trapped and passing particle. The typical form of the trapped orbit is no more a circle (like for passing particles) but a *banana* shape, where the tips are the mirror points of the particle trajectory. The width of the banana represents the mean displacement from the original magnetic surface, where the particle was initially placed. We can give an estimation of the size of the drift orbit for trapped particles by using the conservation of P_ζ . In fact, neglecting variations of g along the orbit (a good approximation for Tokamak device) we obtain from the definition of P_ζ and its conservation:

$$\Delta P_\zeta = 0 \implies \Delta \psi_p = g \rho_{||}. \quad (3.83)$$

For a trapped particle $\rho_{||}$ is zero near the banana tip, thus the excursion of the orbit is:

$$\Delta \psi_p = g \rho_{||} = g \sqrt{\frac{(2E - 2\mu B)}{B^2}}. \quad (3.84)$$

Ignoring the excursion from a flux surface the bounce period for a trapped particle is given by:

$$T = \int dt = \oint \frac{d\theta}{\dot{\theta}} \cong \oint \frac{d\theta D}{\rho_{||} B^2}. \quad (3.85)$$

Note that the direction of the drift across the flux surfaces is dependent on the sign of ρ_{\parallel} . Thus particles with opposite velocities, initially at the same point at $\theta = 0$, describe different banana orbits. An ion moving toroidally in the direction of the plasma current (co-moving) begins its trajectory at the outermost point of the banana orbit, whereas a countermoving ion begins its trajectory at the innermost point. The opposite is true for electrons.

As we have shown for passing particles in the previous paragraph also for the trapped ones we can give an estimation of the drift size in terms of q and of the Larmor radius. In this case we obtain [15]:

$$(\Delta r)_{tr} = 2\left(\frac{2R}{r}\right)^{1/2}qr_L \quad (3.86)$$

from which we see that in Tokamak (where $q \gtrsim 1$) trapped particles orbits can be an order of magnitude bigger than a Larmor radius. On the contrary in the RFP configuration ($q \leq 0.2$) banana orbits are very small for thermal particles but still present. We discuss this topic in Chapter 5, dedicated to the RFP physics and in particular to the RFX-mod experiment.

Despite being trapped, high energy particles can escape from the plasma. Usually this effect is also stronger than for thermal particles. Furthermore, also small perturbations of the field leading to destruction of toroidal symmetry produce classes of trapped particles, and new loss mechanisms. We shall discuss them in the following Chapters when presenting the effect of the instabilities.

Finally, a further parameter which generates classes of trapped particles is the ripple. In fact, all banana orbits with bounce tips in the ripple domain are ultimately ripple trapped, due to the fact that near the lower banana tip, where the velocity parallel to the magnetic field is very small, the particle is drifting outwards toward larger ripple. The well potential depth generated by the ripple effect seen by the particle is increasing as the particle passes over it; if the toroidal phase is such that the well is attractive, the particle is trapped in this domain. A ripple trapped particle drifts downward at a rate given by $v_d = (r_L/R_0)^2 R_0 \omega_0$ with r_L the gyroradius, ω_0 the gyro frequency and R_0 the major radius. For example, with a ripple of the 5% at the plasma edge and a $\omega_0 = 3 \times 10^8/s$, 1keV proton has a drift velocity of $3 \times 10^2 m/s$, so that once a particle is ripple trapped in a loss orbit leading to the wall the loss process typically takes a fraction of ms [26].

The calculation of the shift Δr across the magnetic surfaces of the bounce point of the banana orbits caused by the ripple can be performed by integrating the cross surface drift with and without the ripple and taking the difference. For a deeply trapped particle with energy $E = v_{\parallel}^2/2 + \mu B$ but $v_{\parallel}^2 \ll E$ throughout the orbit we obtain, following [26], the final expression

for a cylindrical geometry:

$$\Delta r = \left(\frac{q}{r}\right)^{3/2} \left(\frac{\pi N}{\sin\theta_b}\right)^{1/2} r_L A \sin(N\phi_b - \pi/4) \quad (3.87)$$

with N the number of the toroidal coils, θ_b the new bounce angle, $\phi_b = q\theta_b$ and A the ripple amplitude introduced in section 3.4.

3.8 Collisions

The particle motion considered so far neglected the interaction with the background plasma. Under certain conditions this effect must be taken into account. Each charge particle, in fact, generates a Coulomb electric field which is felt by the other ions and electrons of the plasma. The motion of a particle in a stationary field generated by a central force is a classical problem and has been discussed with details in many works. We summarize in this section the main results presented by Trubnikov in [30]; in particular we shall discuss their application to the cases of interest studied in this Thesis.

A uniform plane flux of particles α is assumed to move through a quasi neutral plasma consisting of electrons and singly charged ions (field particles) distributed according to a Maxwellian distribution with temperature $T \sim T_e \sim T_i$. The particles in the flux can be electrons or ions of the same species as the background particles. We label with β a single species of the background and we consider its interaction with particles α . The statistical effect of the collisions is described by the following equations:

- **Slowing down:**

$$\frac{d\mathbf{v}_\alpha}{dt} = -\frac{\mathbf{v}_\alpha}{\tau_s^{\alpha/\beta}} \quad (3.88)$$

- **Transverse Diffusion:**

$$\frac{d}{dt}(\mathbf{v}_\alpha - \langle \mathbf{v}_\alpha \rangle)_\perp^2 = \frac{(v_\alpha)^2}{\tau_\perp^{\alpha/\beta}} \quad (3.89)$$

- **Parallel Diffusion:**

$$\frac{d}{dt}(\mathbf{v}_\alpha - \langle \mathbf{v}_\alpha \rangle)_\parallel^2 = \frac{(v_\alpha)^2}{\tau_\parallel^{\alpha/\beta}} \quad (3.90)$$

- **Energy Loss:**

$$\frac{d}{dt}\epsilon_\alpha = \frac{\epsilon_\alpha}{\tau_\epsilon^{\alpha/\beta}} \quad (3.91)$$

where \mathbf{v}_α is the velocity of the species α with mass m_α ; $v_\alpha = |\mathbf{v}_\alpha|$ and averages $\langle \dots \rangle$ are performed over an ensemble of test particles and a Maxwellian field particle distribution. By the symbol \perp and \parallel we label the components of the velocity perpendicular and parallel to the initial trajectory for the species α after the collision. The quantities $\tau_s^{\alpha/\beta}, \tau_d^{\alpha/\beta}, \tau_\epsilon^{\alpha/\beta}$ are the relaxation times whose expressions are:

$$\tau_s^{\alpha/\beta} = \frac{\tau_1^{\alpha/\beta}}{(1 + \frac{m_\alpha}{m_\beta})\mu} \quad \tau_d^{\alpha/\beta} = \frac{\tau_1^{\alpha/\beta}}{2(\mu + \mu' - \frac{\mu}{2x_\beta})} \quad \tau_\epsilon^{\alpha/\beta} = \frac{\tau_1^{\alpha/\beta}}{4\mu/x_\beta}$$

where the functions μ and μ' are defined as:

$$\mu = \mu(x_\beta) = \frac{2}{\sqrt{\pi}} \int_0^{x_\beta} e^{-t} \sqrt{t} dt \quad \mu' = \frac{2}{\pi} e^{-x_\beta} \sqrt{x_\beta}$$

with the following definitions:

$$x_\beta = \frac{m_\alpha \epsilon_\alpha}{m_\beta T_\beta} \quad \tau_1^{\alpha/\beta} = \frac{\sqrt{m_\alpha}}{\pi \sqrt{2} e_\alpha^2 e_\beta^2} \frac{\epsilon_\alpha^3 / 2}{\lambda_{\alpha/\beta} n_\beta}$$

where $\lambda_{\alpha/\beta}$ is the Coulomb logarithm and n_β, T_β are the particle density and temperature of the background species β respectively. If the background is composed of more species, equations 3.88-3.91 are still valid but with the substitution of the partial relaxation times $\tau^{\alpha/\beta}$ with the total τ^α which takes into account all of the β species. The relation between the total τ^α and the partial relaxation times $\tau^{\alpha/\beta}$ can be derived by the forementioned equations and for a plasma composed by ions and electrons we obtain:

$$\frac{1}{\tau^\alpha} = \sum_\beta \frac{1}{\tau^{\alpha/\beta}} = \frac{1}{\tau^{\alpha/e}} + \frac{1}{\tau^{\alpha/i}}. \quad (3.92)$$

For our studies it is sufficient to consider only four kind of collisions: electrons/ions, electrons/electrons, ions/ions, ions/electrons. Moreover we shall deal with two extreme situations only: collisions between test particles β and background particles α at the same energy and interaction of fast test particle α with a thermalized background β . In these situations the expression for the relaxation times is simpler. In the following we shall use often the inverse of the relaxation times ($\nu = 1/\tau$) to quantify the collisional effects.

3.8.1 Collisions for thermal test particles

If the test particles are in equilibrium with the plasma background (with $Z = 1, T_i \sim T_e, n = n_e = n_i$) the computation is simplified and there are just

two collision rates, one for the electrons (ν_e) and one for the ions (ν_i):

$$\nu_e = 2.9 \times 10^{-6} n \lambda T_e^{-3/2} \quad (3.93)$$

$$\nu_i = 4.8 \times 10^{-8} n \lambda T_e^{-3/2} (m_i/m_p)^{-1/2} \quad (3.94)$$

where m_i is the mass of the test ion and m_p the proton mass. Temperature are in eV , densities in cm^{-3} and the final frequencies in s^{-1} .

In the RFP experiments the range of variation for the density is between 10^{19} and $10^{20} m^{-3}$ and between $250eV$ and $1keV$ for the temperature. With these values and $\lambda \sim 17$, typical of fusion plasmas, we obtain:

$$\nu_e \sim 10^4 \div 10^5 \text{coll}/s, \quad (3.95)$$

$$\nu_i \sim 10^3 \div 10^4 \text{coll}/s. \quad (3.96)$$

In ORBIT, collision frequencies are usually normalized to the inverse of the transit time, i.e. the time required by a test particle at the magnetic axis to perform a toroidal turn (coll/tran). In the same range of temperature and densities, for electrons we have $0.1 \div 1 \text{coll}/\text{tran}$ while for the ions about $0.05 \div 0.5 \text{coll}/\text{tran}$. A typical mean value for the ion collision frequency in RFX-mod is $0.2 \text{coll}/\text{tran}$ and for electrons $0.3 \text{coll}/\text{tran}$.

3.8.2 Slowing Down of fast particles

The interaction of fast particle with a background is more complex. We shall focus our attention to the slowing down collisions, since these are implemented in ORBIT when non thermal test particles are considered.

We begin by studying a **fast ion** on a background of thermal electrons and ions with temperature T . We must split the problem into two parts since we need to calculate the collision frequency $\nu^{i/e}$ of the test ion with the electrons and $\nu^{i|i'}$ with the other background ions. We first suppose to be in a situation in which x_β is very greater than one. This means that $\epsilon_i \gg T$ for the collisions with ions and $\epsilon_i \gg (m_i/m_e)T$ with the electrons. In this approximation, $x_\beta \gg 1$, the collisions frequencies are simplified and have the following expressions for the ion-ion case:

$$\epsilon_i \gg T \rightarrow \nu_s^{i|i'} \simeq 9 \times 10^{-8} \left(\frac{m_p}{m_i} + \frac{m_p}{m_{i'}} \right) \frac{(m_i/m_p)^{1/2}}{\epsilon_i^{3/2}} n_{i'} Z^2 Z'^2 \lambda_{ii'} \quad (3.97)$$

where the quantities with the apex ' refers to the background ions and those without to the high energetic ions. Test ion energy ϵ_i and field temperature T are both in eV ; $\mu = m_i/m_p$ where m_p is the proton mass; Z is the ion

charge state, $n_{i'}$ the ion background density and $\lambda_{ii'} \sim 20$ is the Coulomb logarithmic for ion-ion interactions. The ion-electron case is simply related with the previous one by the formula:

$$\epsilon_i \gg \frac{m_i}{m_e} T \rightarrow \nu_s^{i|e} \simeq \frac{m_i}{m_e} \nu_s^{i|i'} \quad (3.98)$$

which shows that collisions of fast ions with electrons are those dominant by a factor $(m_i/m_e) \sim 2000$. Anyway, this is not a typical case since the condition $\epsilon_i \gg (m_i/m_e)T$ is not satisfied for fast ions produced by auxiliary heating in present day devices. In the case of NBI or RH, in fact, fast ions are characterized by energy of the order of hundreds of keV while the background T_e is of few keV . For example, a fast ion with energy $\epsilon_i = 100keV$ on a background with $T \sim 1keV$ has $x_\beta \sim 0.05$ which is smaller than one. On the contrary for the collisions with the ions of the background $x_\beta \sim 100$. For the collisions fast ions-electrons we have thus to consider the case when $x_\beta \ll 1$ which gives:

$$\epsilon_i \ll \frac{m_i}{m_e} T \rightarrow \nu_s^{i|e} \simeq 1.6 \times 10^{-9} \left(\frac{m_p}{m_i} \right)^{-1} T^{-3/2} n_e Z^2 \lambda_{ie} \quad (3.99)$$

where $\lambda_{ie} \sim 15 \div 18$ is the Coulomb logarithm for the ion-electron interaction.

We compute the collision frequencies $\nu^{i|e}$ and $\nu^{i|i'}$ for the cases analyzed in this Thesis. In AUG we shall consider fast ions with an energy of about $\epsilon_i \sim 100keV$ on a background with a temperature of few keV and density $n_e \simeq n_i \simeq 10^{19}$. We find the following values by applying Eqs. 3.97 and 3.98:

$$\text{Asdex-Upgrade:} \quad \nu_s^{i|e} \sim 1Hz \quad \nu_s^{i|i'} \sim 13Hz \quad (3.100)$$

from which we can conclude that, at the energy we are considering, the interaction of the fast ions with ions of the background is the dominant effect. When implementing the slowing down collisions in ORBIT the frequencies values must be normalized to the cyclotron frequency, which means for typical scenarios a value of $\nu_s^{i|i'}/\omega_c \sim 2 \cdot 10^{-7}$ (assuming $B \sim 2T$ on axis).

We shall also investigate the effect of fast ions from NBI in RFP configurations. In this case the beam energy is of $\epsilon_i \sim 20keV$ and interacts with a background with few hundreds of eV . We thus find:

$$\text{RFPs:} \quad \nu_s^{i|e} \sim 15Hz \quad \nu_s^{i|i'} \sim 50Hz \quad (3.101)$$

which means a global collision frequency for slowing down to be implemented in ORBIT of $\nu_s/\omega_c \sim 5e-07$, with the standard values of density ($n_e \simeq 10^{19}m^{-3}$), temperature ($T_e \simeq 300eV$) and magnetic field ($B \sim 0.8T$ on axis) considered.

The test particles can be also **fast electron** on a background of ions and electrons at the temperature T . We will consider this situation in the reversed field pinch experiment MST where the energy of fast electrons is of the order of hundreds of keV and $T \sim 300eV$. The condition $x_\beta \gg 1$ holds for the electron-electron collisions, since it means that $\epsilon_e \gg T$, but also for the electron-ion case because $\epsilon_e \gg (m_e/m_i)T$. Thus both the frequencies can be computed with the approximation $x_\beta \gg 1$ and we obtain:

$$\nu_s^{e|e} \simeq 7.7 \times 10^{-6} \epsilon_e^{-3/2} \quad (3.102)$$

$$\nu_s^{e|i} \simeq 3.9 \times 10^{-6} \epsilon_e^{-3/2} \quad (3.103)$$

where, as usual in this section, the test electrons energy ϵ is in eV and the final frequencies in Hz . Note that the two frequencies are rather near.

In ORBIT the initial frequency inserted is taken constant during the run even if the energy of the particles may change because of external fields or collisions. This approximation is not important on short time scales in comparison with the relaxation times, and we are often in this situation. On the contrary, on long time scales the effect of collisions can be underestimated or overestimated.

For example, in Asdex or RFPs devices, the energy of fast ions after few ms is decreased by slowing down and thus the collision frequency increases. Taking a constant frequency we are underestimating collisions on long times scale (tens of ms).

In the case of fast electrons in RFP they initially have a thermal velocity and thus the collision frequency we use for them is that given by Eq. 3.93. As a consequence of the acceleration due to the toroidal electric field their energy grows and the collision frequency decreases. In this case we are overestimating the collisions on long times scale.

3.8.3 Classical and pitch angle scattering

Slowing down is not the only collision mechanism implemented in ORBIT. Following a collision, in fact, a sudden change of the gyro center (*classical scattering*) occurs, together with a change of the pitch (*pitch angle scattering*), i.e. of the ratio between parallel and perpendicular velocity. These two collision mechanisms are thus related with transverse diffusion with a relaxation time τ_\perp .

- **Classical scattering:** when the collision between two particle occurs, their velocity vector undergoes a change which causes the guiding center to move from one collisionless orbit to an other. In this way particles can

migrate across the magnetic field by a *random walk process*. Clearly not only the guiding center position changes but also the Larmor radius. In ORBIT this type of collisions is modelled by radially displacing a test particle by a quantity proportional to the Larmor radius and to the collision frequency ν_{\perp} in a random direction (Eqs. 3.93-3.94 for thermal particles). We assume that the particles do not gain or lose energy in the perpendicular direction so that the Larmor radius is unchanged. The algorithm simulates the radial diffusion of an ensemble of test particles. It has been shown, in fact, that the final distribution of an ensemble of test particles initially placed at ψ_{p0} is distributed as a Maxwellian whose width is $(\nu_{\perp} n \tau)^{1/2} \Delta \psi_p$, where n is the number of integration steps, τ is the time step and $\Delta \psi_p$ corresponds to the flux step by a gyroradius. [31]. Therefore when a particle has travelled for a time $n \tau = 1/\nu_{\perp}$ it has been displaced, on average, by $\pm(\nu_{\perp} n \tau)^{1/2} \Delta \psi_p$.

- **Pitch angle scattering:** the pitch angle scattering is the fundamental collision mechanism in the Tokamak configurations where the banana orbits of trapped particles are radially larger than the gyroradius. It acts by changing the pitch angle of the test particles: after n steps a particle with initial pitch angle λ_0 has a final pitch of $\lambda = \lambda_0(1 - \nu_{\perp}(n\tau)) \pm [(1 - \lambda_0^2)\nu_{\perp}(n\tau)]^{1/2}$. By this mechanism an initially trapped particle can become trapped or vice-versa. This kind of collisions has been implemented also in Tokamak while considering the interaction between the fast ions and the background. The thermal approximation for ν_{\perp} is not anymore correct. The main contribution is given by the ions-ions collisions and it is estimated by using the $x_{\beta} \gg 1$ approximation:

$$\nu_{\perp}^{i|i'} \simeq 1.8 \times 10^{-7} n_{i'} Z^2 Z'^2 \lambda_{ii'} (m_i/m_p)^{-1/2} \epsilon_i^{-3/2}. \quad (3.104)$$

In Asdex with $100keV$ fast deuterons on a background of few keV we have:

$$\nu_{\perp}^{i|i'} \simeq 2\nu_s^{i|i'} \simeq 20Hz. \quad (3.105)$$

For deuterons in RFP we have the same relation with a different energy of the test particle ($20keV$) and of the background ($300eV$): $\nu_{\perp}^{i|i'} \simeq 100Hz$.

We summarize all the results for the collision frequencies we shall use in the following of this Thesis in the table 3.1. The total frequency of slowing down and of classical/pitch angle scattering are reported. When considering thermal ions and electrons as test particle in RFPs device we suppose that the

energy is constant and there is no a slowing down mechanism. On the contrary slowing down is taken into account for fast electrons in RFP configuration.

| | slowing down ν_s | scattering ν_{\perp} |
|--|----------------------|--------------------------|
| fast deuterons 100keV in AUG | $10 \div 15Hz$ | $20 - 30Hz$ |
| fast deuterons 20keV in RFPs | $50 \div 70Hz$ | $\sim 100Hz$ |
| thermal ions in RFP (300-800 eV) | / | $10^3 - 10^4Hz$ |
| thermal electrons in RFP (300-800 eV) | / | $10^4 \div 10^5Hz$ |

Table 3.1: Typical values of the collisions frequency used for the numerical simulation in the Thesis. For thermal electrons and ions only the pitch angle and classical scattering have been considered.

CHAPTER 4

The RFP configuration and the RFX-mod experiment

In this Chapter we present the main features of the Reversed Field Pinch configuration (section 4.1) and in particular we describe the experiment RFX-mod in Padua and its recent results (secs. 4.2–4.3). Section 4.4 explains how the magnetic perturbations are implemented in ORBIT for the RFP experiments analyzed in this Thesis, both in a cylindrical and toroidal geometry approximation. Finally, the last section is dedicated to the studies of magnetic topology and numerical particle transport performed with the ORBIT code for the RFX-mod experiment.

4.1 Physics of RFP configuration

As already presented in Chapter 1 of this Thesis, the name of the Reversed Field Pinch configuration is due to the properties of the toroidal magnetic field which reverses its direction in a region close to the wall. The term *pinch* addresses the phenomenon where a magnetic field line keeps the plasma away from the wall, increases the plasma density and heats the plasma by adiabatic compression; in the meantime the plasma is heated by the Joule effect too.

Studies on RFP began in 1958 at Harwell (England): during the experiments in the ZETA[32] toroidal device, a period of improved stability was

observed. In this period the plasma current was almost constant and several years later it was observed that the toroidal magnetic field at the wall was reversed in this phase of the discharge.

In the years 1958-1960 it was proposed that the application of a reversed toroidal magnetic field at the wall would provide a pinch stabilization and theoretical physicists made the first efforts to explain this phenomenon and its benefit on the instabilities $m = 0$ and $m = 1$. The first important theoretical contribution to the understanding of the Reversed Field Pinch configuration was given in 1974 by J.B. Taylor [27] at the International Atomic Energy Agency in Tokyo with an explanation of the experimental data of ZETA. Since then many progress have been performed in the knowledge of the RFP physics thanks to several experiments dedicated to this configuration. In the last years a great effort has been spent in studying a regime where a single mode dominates the global spectrum of the tearing instabilities; in this regime an improvement of the plasma confinement properties has been observed.

4.1.1 Resistive Diffusion: the dynamo effect

In Chapter 2 we have presented the BFM and the $\mu&p$ models which describe the equilibrium magnetic fields and currents but we neglected the time evolution. If we consider the RFP as a static conductor subject to resistive diffusion, the magnetic field evolution is given by:

$$\frac{\partial \mathbf{B}}{\partial t} = \eta \nabla^2 \mathbf{B} \quad (4.1)$$

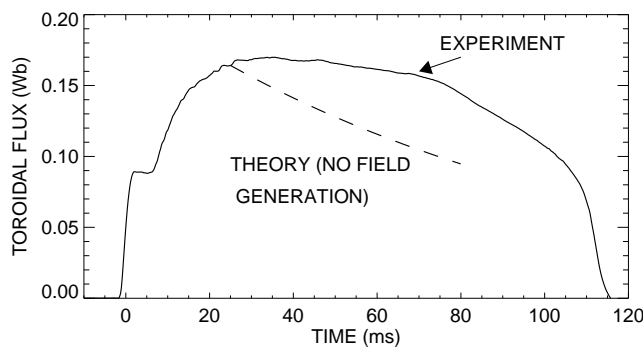


Figure 4.1: Toroidal flux as function of time during a typical RFX discharge. The dashed line represents the theoretical diffusion exponential decay, without field regeneration.

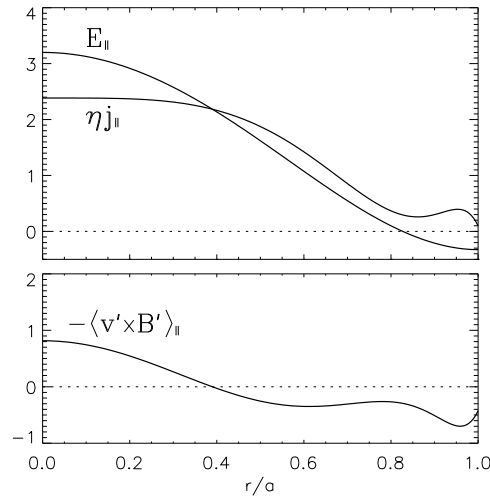


Figure 4.2: Mismatch between the applied electric field E_{\parallel} and the resistive counterpart. It is noted that $E_{\parallel} > \eta j_{\parallel}$ at the center while $E_{\parallel} < \eta j_{\parallel}$ at the edge. In the absence of fluctuations the field would be entirely Ohmic, $E_{\parallel} = \eta j_{\parallel}$.

that for the BFM model in cylindrical geometry, and with a constant resistivity η profile, has the solution:

$$B_{\phi} = B_0 J_0(\mu r) e^{-t/\tau}, \quad (4.2)$$

$$B_{\theta} = B_0 J_1(\mu r) e^{-t/\tau}. \quad (4.3)$$

with $\mu = j_{\parallel}/B$, J_0 and J_1 Bessel functions and $\tau = a^2/\eta$ where a is the minor radius. It is worth noting that the field decays keeping the same radial shape, so the stability properties of the configuration remain unchanged in time.

In any case it is experimentally proven that a RFP discharge lasts longer than the resistive diffusion time. In particular it has been observed that the reversed field configuration is maintained as long as the toroidal current lasts, as shown in Fig. 4.1. This indicates that the magnetic field continuously lost through resistive diffusion is regenerated by some mechanism, usually defined *dynamo*.

The dynamo mechanism is also necessary for the sustainment of the reversal of the toroidal magnetic field by a toroidal electric field, $E_{\phi} = \mathbf{E} \cdot \mathbf{e}_{\hat{\phi}}$, as those inductively applied in toroidal fusion plasma. Let us, in fact, consider the parallel component of the mean-field Ohm's law:

$$E_{\parallel} = \frac{\mathbf{E} \cdot \mathbf{B}}{B} = \frac{E_{\phi} B_{\phi}}{B} = \eta j_{\parallel}. \quad (4.4)$$

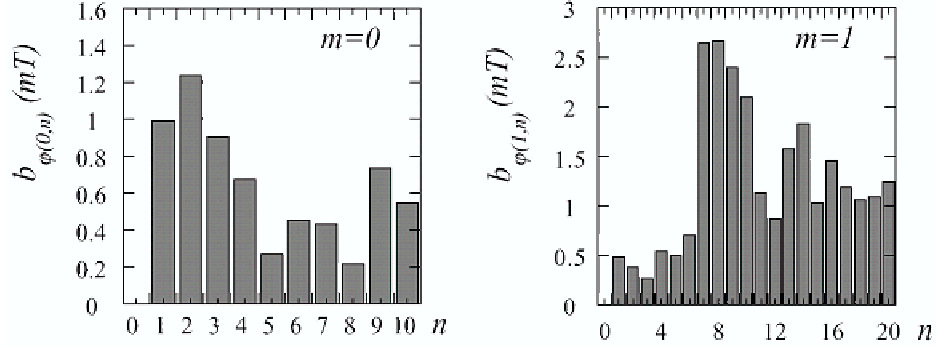


Figure 4.3: Typical toroidal mode number spectra of $(m = 0, n)$ and $(m = 1, n)$ modes in a standard RFX discharge.

Since E_ϕ and B are always positive throughout the radius, $E_{||}$ at each radial position is proportional to B_ϕ , which reverses its sign near the edge. On the other hand, the term $\eta j_{||}$ is always positive, which shows that other terms are needed to balance the Ohm's law. This mismatch is represented in Fig. 4.2-(a), which has been obtained with a MHD simulation: current is under-driven in the core, where the applied electric field is almost parallel to the magnetic field $E_{||} \simeq E_\phi$, while it is over-driven near the edge, where $E_{||} \simeq E_\theta$.

4.1.2 Magnetic perturbations and dynamo

The dynamo is linked to resonant magnetic instabilities, also dubbed *dynamo modes*. In fact, a broad spectrum of $m = 1$ resonant instabilities can be unstable due to the current gradients. An example of a toroidal mode number spectrum for $(m = 0, n)$ and $(m = 1, n)$ modes in a standard discharge from the RFX device is shown in Fig. 4.3. It is evident that the standard RFP operation is characterized by a broad spectrum of helical magnetic modes resonant throughout the plasma radius. For this reason, the standard RFP operation is also called *multiple helicity* (MH) regime. These instabilities are associated to velocity fluctuations. If we write the magnetic and velocity fields as a sum of a mean-field plus a fluctuation term, $\mathbf{B} = \mathbf{B}_0 + \tilde{\mathbf{b}}$ and $\mathbf{v} = \mathbf{v}_0 + \tilde{\mathbf{v}}$, a new mean electric field arises in the parallel Ohm's law, which is called dynamo electric field \mathbf{E}_d , and is given by the coherent interaction of the velocity and magnetic field fluctuations (Fig. 4.2-bottom):

$$E_{0||} + E_{d||} = E_{0||} + \langle \tilde{\mathbf{v}} \times \tilde{\mathbf{b}} \rangle_{||} = \eta j_{0||}. \quad (4.5)$$

If several modes are present, as in Multiple Helicity, plasma confinement is reduced. In fact, the spatial superposition of many different magnetic is-

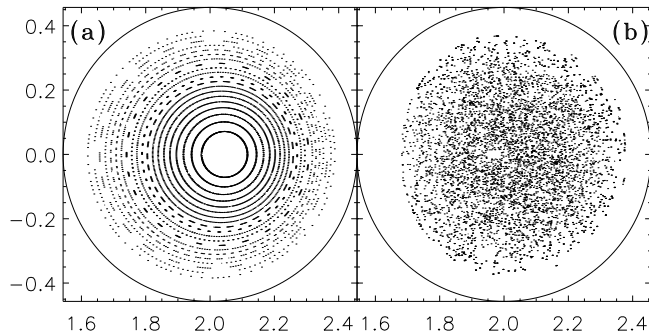


Figure 4.4: Poincaré plots of the magnetic field lines in a poloidal cross-section for a typical RFX discharge (a) without and (b) with the experimental spectrum of magnetic fluctuations. The magnetic field lines have been reconstructed by the guiding center code ORBIT.

lands associated with these resonant instabilities produces a chaotic magnetic field in the MH regime, as shown in Fig. 4.4, where field lines can wander chaotically from the hot plasma core to the colder edge. Since particles are transported along magnetic field lines much faster than in the direction perpendicular to them, this determines an anomalous source of radial thermal and particle transport, as shown by A.B. Rechester and M.N. Rosenbluth in [33].

Anomalous transport associated to dynamo fluctuations has severely limited the confinement performances of the RFP configuration for a long time. More recently, it has been found, both theoretically [34] and experimentally [35], that the configuration can exist even if a single mode is present. Thus, dedicated experiments with an active control of the dynamo modes (see section 4.2.1 and [36]) and with transitions to less turbulent scenarios, which are named Single Helicity (SH) or Quasi Single Helicity (QSH) regimes, have been performed in the last years. The QSH regime will be introduced in the last section of this Chapter and SH will be discussed with details in the next one where we shall show the strong reduction of particle transport in such a configuration with respect to the MH scenarios.

4.2 RFP experiments

The RFPs experiment currently in operation are:

- Extrap-T2R in Stockholm [37]; a small RFP device characterized by a high aspect ratio $R_0/a = 1.24m/0.183m \simeq 6.8$ and low plasma currents ($I_p = 100kA$).

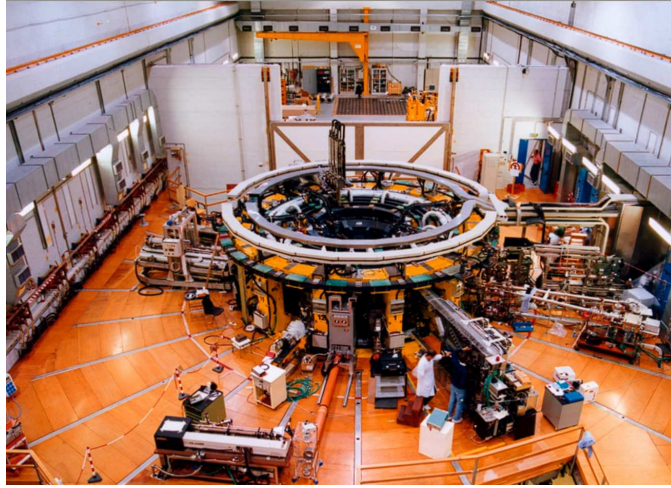


Figure 4.5: Photo showing RFX-mod experiment.

- Madison Symmetric Torus [38], MST (Madison, Wisconsin, USA); aspect ratio $R_0/a = 1.5m/0.52m \simeq 3$ and plasma currents up to $600kA$.
- Reversed Field eXperiment modified, RFX-mod [39] (Padova, Italy); the larger RFP device in the world, $R_0/a = 2m/0.459m \simeq 4.4$ with plasma currents up to $2MA$.

In this Thesis we shall consider data from the RFX-mod and MST experiments. In the following of this section a detailed overview on RFX-mod is given, while the description of MST is postponed to Chapter 6.

4.2.1 RFX-mod components

The RFX-mod device (see Fig.4.5) is an upgraded version of the RFX experiment [40]. A new power supply system and a set of 192 independently driven saddle coils has been added aimed at actively controlling the local radial perturbations at the edge.

The main technical components in RFX-mod are:

- **vacuum vessel:** the toroidal chamber containing the plasma. It is an all-welded, rigid structure made of INCONEL 625, with a major radius of 1995 mm and minor radius of 475 mm. It is bakeable up to 350° , in order to eliminate the impurities of the first wall.
- **first wall:** it's the inner side of the vacuum vessel, exposed to the plasma discharge. It is composed by 2016 graphite tiles that cover completely the inner part of the vacuum vessel (see Fig. 4.6). In RFX-mod

the shape of the tiles has been redesigned to minimize the emissivity due to plasma-wall interaction. Graphite has been chosen for its low atomic number Z .

- **stabilizing shell:** it has the main purpose of stabilizing MHD ideal instabilities. It is made of copper and it is $3mm$ thick, located at $1.11a$ where $a = 0.51$ is the minor radius. This shell is enclosed by a mechanical structure which bears the weight of the vacuum vessel and of the toroidal windings.
- **magnetizing coils:** they provide the time varying magnetic flux that induces the plasma current during the discharge. It is composed by 40 coils that can carry a maximum current of $50kA$ and produce a $15Wb$ maximum flux.
- **toroidal coils:** a set of 48 coils uniformly distributed along the toroidal direction, that surround the vessel and the shell. They are designed to generate the toroidal magnetic field needed to set-up and maintain the discharge (up to $0.7T$). The coils are series-connected in 12 groups of 4: each group is connected to an independently controlled power supply unit.
- **field shaping coils:** this set of poloidal coils is designed to generate a vertical field aimed at feedback controlling the position of the plasma column with respect to the vessel during the discharge.
- **virtual shell:** this new set of saddle coils is necessary in RFX-mod in order to control the instability arising on the shell time-scale. It is a set of 192 coils, distributed in 48 different toroidal positions and four

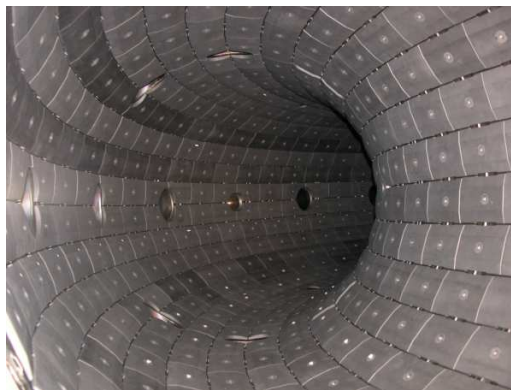


Figure 4.6: New graphite tiles in RFX-mod.

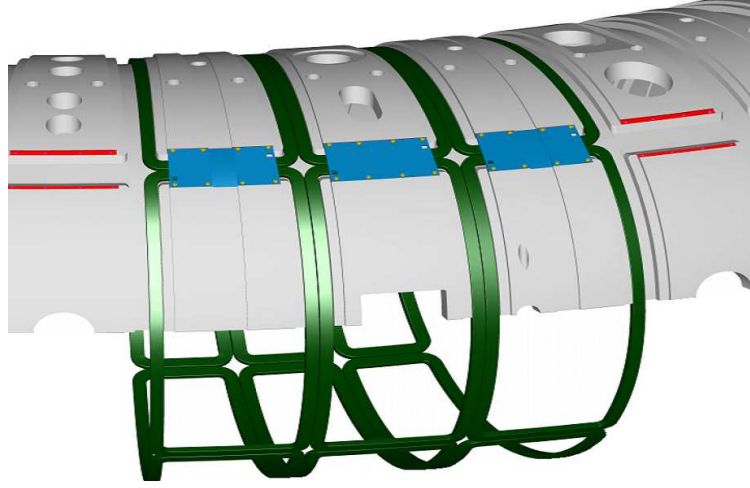


Figure 4.7: Saddle coils (green) which form the Virtual Shell in RFX-mod.

poloidal positions; they extend 90° poloidally and 7.5° toroidally, for a full surface coverage. The power supply units are digitally controlled by a set of dedicated CPUs that can process 192 sensor inputs and generate 192 reference outputs at a rate of $\approx 2.5 \div 3kHz$. The digital system allows for a great flexibility in the implementation of feedback algorithms. In Fig.4.7 you can see a scheme of the saddle coils disposition on a section of RFX-mod. An overview on the Intelligent Shell concept can be found in [41] and the main results in RFX-mod obtained with the VS application in [42].

4.2.2 Discharge setting up

The procedure to set up the discharge in RFX-mod starts when the magnetizing winding is charged and the camera is filled with hydrogen with a pressure of $2 - 5mbar$. A current also circulates in the toroidal coils, generating a toroidal magnetic field (*direct field*). Plasma breakdown is obtained by releasing the energy carried in the magnetizing coils by electrically connecting them to the ground trough a resistor (like a L-R circuit). The time varying magnetic field induces an electric field in the toroidal direction which ionizes the gas and creates the plasma current. The plasma current generates a poloidal field which tends to pinch the plasma inward. With an appropriate delay of a few ms, the current of the toroidal coils is reversed by connecting them to a capacitor bank through a feedback controlled inverter. When the

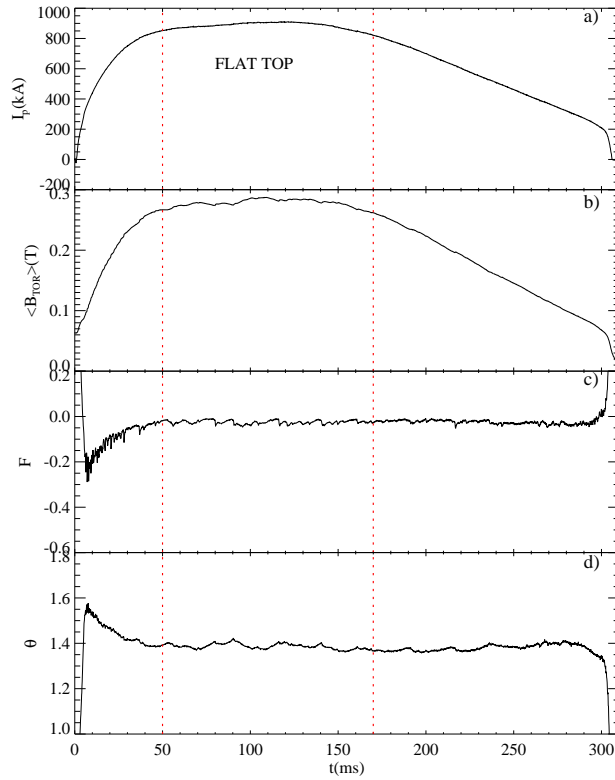


Figure 4.8: Example of discharge in RFX-mod, shot 21796. In (a) the current evolution during the discharge as function of time, while in (b) the average toroidal magnetic field is plotted. The time evolution of the main parameters F, θ which characterizes the RFP configuration are displayed in (c) and (d). The red dashed lines delimit the *flat top* phase of the discharge.

plasma current reaches the planned value, this is kept constant by varying linearly the current in the magnetizing coils by means of auxiliary power supply units. The discharge ends when the flux stored in the magnetizing windings is exhausted.

In Fig. 4.8-(a) the evolution of the current during a discharge is shown. In this case the maximum value was 800 kA . The phase of the discharge while the current is almost constant is generally called *flat top* (between the red dashed lines in Fig.4.8-(a)). In the last years also current up to 1500 kA have been reached. In (b) of the same figure the average toroidal magnetic field

is reported, while in (c) and (d) the F and θ parameters. Typical values in RFX-mod are in the range: $F \simeq -0.2 \div 0$ and $\theta \simeq 1.4 \div 1.6$.

4.2.3 Clean Mode Control

The Virtual Shell stabilizes MHD perturbations on longer periods compared to the shell time penetration constant. In fact, as we have shortly explained above, the virtual shell is composed by a grid of active coils counteracting in a feedback scheme the radial field measured by an identical grid of radial field sensors loop. In this way it is possible to keep to zero the flux measured by each sensor loop, as an ideal conducting wall would do. This scheme has been tested in RFX-mod with good results and has improved the confinement of the plasma and the reduction of the tearing modes amplitude.

After a brief period of initial operations with the VS it was realized that an intrinsic limitation did not allow for further improvements of the plasma performance. The origin of the problem is the aliasing of the sideband harmonics generated by the discrete coils system coupled with coils with the same periodicity. In fact in the VS scheme the current flowing in each control coil aims to cancel the flux measured by the underlying sensor loop. But the measured fluxes includes the aliased sidebands produced by the coils besides the harmonics related to the plasma instabilities. Therefore in general the perfect cancellation of the sensor fluxes does not correspond to the cancellation of the instability harmonics at the sensor radius. To overcome this systematic limitation, the aliased sidebands contribution (estimated from the coil currents) is subtracted from the measurements; the *cleaned* measurements are used as the feedback variable.

More details about this procedure are reported in [43] and [42]. In the following of this Chapter we shall refer to discharges where this correction has been implemented as *Clean Mode Control (CMC)* shot to distinguish them from the previous ones (only *Virtual Shell (VS)* Shot).

4.3 Diagnostics in RFP experiments

In RFX a full set of diagnostics is capable of measuring many physical quantities, in their temporal and spatial variations. A brief description of the most important ones follows:

- a complete set of *magnetic* diagnostics: 4 Rogowski coils which measure the plasma current; 8 toroidal and 6 poloidal voltage loop coils which provide information over loop voltage and toroidal flux; 196 $40 \times 36 \times 4$

mm bi-axial pick-up coils, distributed along 48 toroidal directions and 4 poloidal directions, which measure toroidal and poloidal components of magnetic fields; 48×4 saddle probes, measuring the radial component of the field, coupled to the active control coils;

- a *tomographic system* [44] which allows the reconstruction of total radiation losses and SXR radiation by means of 36 bolometric detectors (which measure total emission of the plasma) and 78 silicon detectors (which measure soft-X rays radiation). In this Thesis we shall often analyze SXR emissivity profiles obtained with this diagnostic on poloidal sections of the plasma. The reconstruction of the profiles is based on the technique developed in [45]. An example is given in Fig. 4.9 for a standard MH plasma of RFX-mod;
- a *Thomson scattering* diagnostic [46], which provides a 84-point radial profile of electronic temperature by analyzing the scattering properties of the plasma when a high power laser beam is injected; the repetition rate is of about 25 ms, for a maximum number of 10 pulses in a discharge;
- an *interferometer* [47], which measures the electronic density averaged along 13 lines of sight. The measurement is performed by detecting the

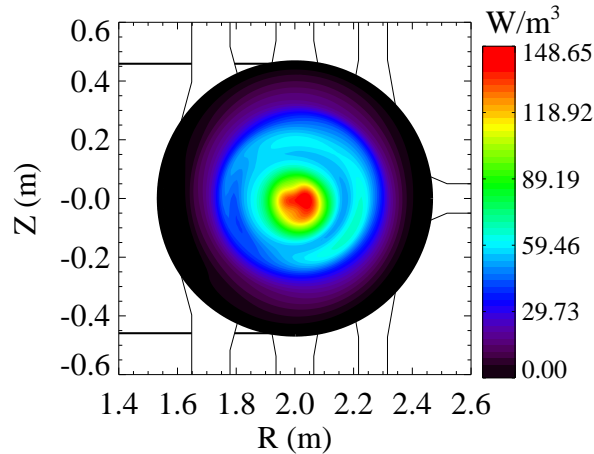


Figure 4.9: Example of the emissivity SXR profile reconstructed by the tomographic technique for a standard MH plasma in RFX-mod. The colors correspond to different values of the SXR emissivity (in W/m^3) as shown in the color bar.

phase variation induced in a CO_2 laser beam ($\lambda = 5.4\mu\text{m}$) that passes through the plasma;

- *spectroscopic* [48] diagnostics, which measure line intensities of radiation emitted by impurities, in order to calculate their influxes at the edge;
- an *integrated system of internal sensors* (ISIS) [49], which includes poloidal and toroidal arrays of 139 magnetic pick-up coils and 97 electrostatic (Langmuir) probes (used to measure and correlate fluctuations of electric and magnetic fields), and 8 calorimetric sensors;
- a *Soft-X Rays multifilter* diagnostic [50], used for measuring electronic temperature at the center of the plasma; it allows a higher time resolution with respect to the Thomson scattering, but with a lower spatial resolution; 4 chords with different filter thicknesses ($40\mu\text{m}$, $75\mu\text{m}$, $100\mu\text{m}$, $150\mu\text{m}$) are used, in order to measure temperature in a wider range of emission levels.

The data from all these diagnostics are collected during the discharge execution and are then analyzed and used as input to several numerical codes. In particular we are interested in the data from the magnetic coils. These are in fact necessary to reconstruct and study the magnetic topology of RFX-mod inside the plasma with ORBIT, by field line tracing.

4.4 Magnetic perturbations by ORBIT

The first step to perform field line tracing by ORBIT is the determination of the magnetic equilibrium and of the radial perturbation profiles. The reconstruction of the equilibrium in Boozer coordinates follows the procedure described in Chapter 2. Radial field perturbations are not measured, therefore a model needs to be used. A cylindrical and, more recently, a toroidal model has been used. We present in the following both these representations, underlining the main differences between the two approaches.

In both the schemes, cylindrical and toroidal, we consider only the tearing modes which are resonant, i.e. those with an helicity (m, n) such that for a given radius r the condition $q(r) = m/n$ is satisfied, where q is the already introduced safety factor. The function $q(r)$ is computed once the $\mu&p$ model has calculated the toroidal and poloidal component of the magnetic field by $q(r) = rB_\phi/(R_0B_\theta)$, as presented in Chapter 2. A typical profile for the absolute value of $q(r)$ in RFX-mod is reported in Fig. 4.10. The correct sign

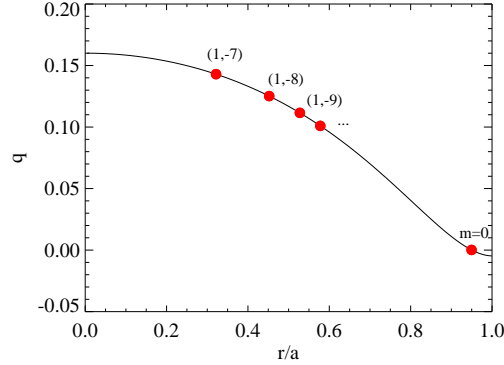


Figure 4.10: Typical safety factor profile in RFX-mod with the main resonances.

of q is negative with the conventions usually adopted: the toroidal current is taken positive in the direction of the toroidal magnetic field on axis, so that the poloidal magnetic field is in the negative direction. This is why in Fig. 4.10 the n -values of the resonant modes are negative inside the reversal. For other configurations, like in MST, the opposite convention is used and the modes resonant inside the reversal are positive, while the outer are negative. Plot of Fig. 4.10 shows that in RFX-mod the inner resonant modes are the $(1, -7)$ and $(1, -8)$. The position for the resonances $m = 0$ depends on the F parameter of the discharge, i.e. on the value of the toroidal magnetic field at the edge.

4.4.1 Magnetic perturbations in cylindrical approximation

The magnetic perturbations profiles in cylindrical geometry are computed by following the Newcomb approach [51], here briefly described. In ideal MHD the stability of a system can be determined by the energy principle - (see [16] for more details). This takes to an Euler - Lagrange equation of the form:

$$\frac{d^2\chi}{dr^2} + A\chi = 0 \quad (4.6)$$

where A is a complex function which depends on the radial profiles of the magnetic field components B^θ, B^ϕ , on the pressure profile and its radial derivative and on the helicity (m, n) of the considered mode [52]. Solving the differential equation 4.6 allows to obtain a final profile for $\chi(r)$ which is

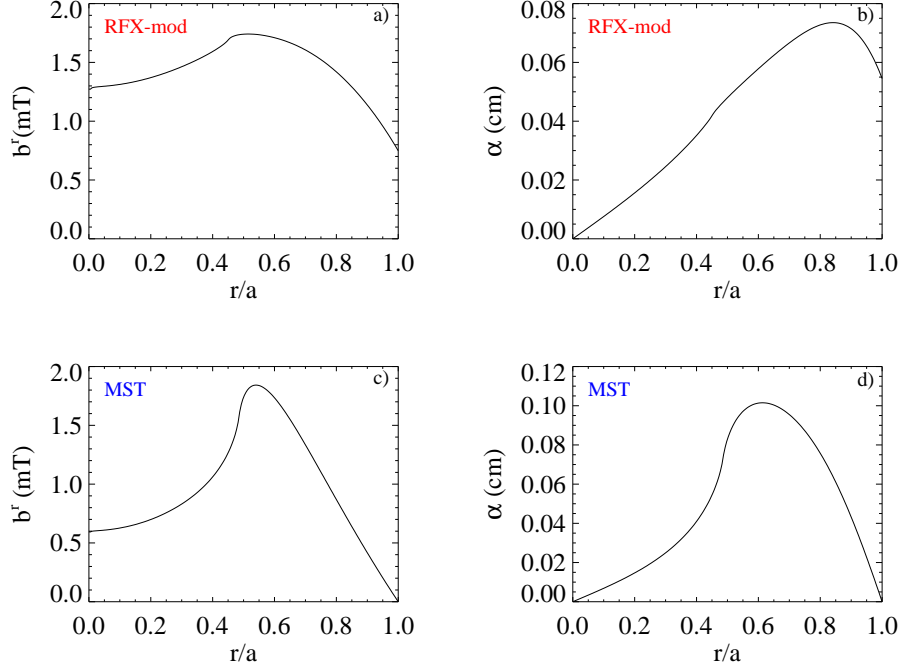


Figure 4.11: In (a) the radial b^r eigenfunction for the (1, 8) mode in cylindrical geometry in RFX-mod; in (b) the corresponding α . (c)-(d) The same of (a)-(b) for the mode (1, 8) in MST.

related to the radial magnetic field perturbation by:

$$b^{\hat{r}} = \frac{\chi(r)(m^2 + n^2 r^2 / R_0^2)^{1/2}}{r^{3/2}}. \quad (4.7)$$

Equation 4.6 is solved between the origin and the rational surface, and between the rational surface and the shell at $r = r_s$. At the rational surface only $\chi(r)$, and not its derivative, needs to be continuous. We will assume vanishing pressure, $p = 0$. In this approximation the term A of Eq. 4.6 has the following expression:

$$A = -\frac{m^2 + n^2 r^2}{r^2} - \mu^2 + \mu' \frac{mB_{\hat{z}} + nrB_{\hat{\theta}}}{mB_{\hat{\theta}} - nrB_{\hat{z}}} + \frac{2\mu mn}{m^2 + n^2 r^2} - \frac{m^4 + 10m^2 n^2 r^2 - 3n^4 r^4}{4r^2(m^2 + n^2 r^2)^2} \quad (4.8)$$

where the cylindrical covariant components have been used for the equilibrium magnetic field and $\mu = \mathbf{j} \cdot \mathbf{B} / B^2$.

The boundary conditions both for $b^{\hat{r}}$ and its first derivative must be set in order to fit the experimental values of the magnetic perturbations $b^{\hat{\phi}}, b^{\hat{\theta}}, b^{\hat{r}}$ at

the shell. The relation between these components are given by the divergence free of the magnetic field and imposing, by the Ampere Law, that no net radial current is present at $r = r_s$:

$$\nabla \cdot \mathbf{b} = 0, \quad (4.9)$$

$$(\nabla \times \mathbf{b})^r|_{r=r_s} = 0. \quad (4.10)$$

After expressing the perturbation of the magnetic field \mathbf{b} as:

$$\mathbf{b} = (b^{\hat{r}} e^{-i\delta_r}, b^{\hat{\theta}} e^{-i\delta_\theta}, b^{\hat{\phi}} e^{-i\delta_\phi}) e^{i(m\theta+n\phi)},$$

with $z = R_0\phi$, Eq. 4.9 in cylindrical geometry becomes:

$$\frac{1}{r} b^{\hat{r}} e^{-i\delta_r} + \frac{\partial b^{\hat{r}}}{\partial r} e^{-i\delta_r} + \frac{m}{r} b^{\hat{\theta}} e^{-i\delta_\theta + i\frac{\pi}{2}} + \frac{n}{R_0} b^{\hat{\phi}} e^{-i\delta_\phi + i\frac{\pi}{2}} = 0 \quad (4.11)$$

and from Eq. 4.10 we obtain:

$$\frac{b^{\hat{\phi}}}{b^{\hat{\theta}}} = \frac{nr}{mR_0} \quad (4.12)$$

$$\delta_\theta = \delta_\phi. \quad (4.13)$$

Substitute these last conditions in Eq. 4.11 and after few algebraic manipulations we have that:

$$\frac{\partial b^{\hat{r}}}{\partial r} = \frac{b^{\hat{\phi}} n}{R_0} \left(1 + \frac{m^2 R_0^2}{n^2 r^2} \right) - \frac{b^{\hat{r}}}{r}. \quad (4.14)$$

and the following relation for the phases needs to be satisfied:

$$\delta_r = \delta_\phi - \frac{\pi}{2}. \quad (4.15)$$

Inserting the expression of $b^{\hat{r}}$ and of its radial derivative calculated at the shell in Eq. 4.7, the value of χ at $r = r_s$ is given by:

$$\chi(r_s) = \frac{r_s^{3/2} b^{\hat{r}}(r_s)}{(m^2 + r_s^2 n^2 / R_0^2)^{1/2}} \quad (4.16)$$

while its derivative:

$$\frac{d\chi}{dr}(r_s) = \frac{3}{2} r_s^{1/2} b^{\hat{r}} \chi_c + \left(\frac{b^{\hat{\phi}} R_0}{\chi_c n r_s^{1/2}} \right) - r_s^{1/2} b^{\hat{r}} \chi_c - r_s^{5/2} b^{\hat{r}} \frac{n^2}{R_0^2} \chi_c^3 \quad (4.17)$$

with the position:

$$\chi_c = \left(\frac{1}{m^2 + n^2 r_s^2 / R_0^2} \right)^{1/2}. \quad (4.18)$$

Once the function χ is known at $r = r_s$, Eq. 4.6 can be numerically integrated and the final result substituted in Eq. 4.7.

As we have explained in Chapter 3, perturbations are implemented in ORBIT by using the function α which is related to the magnetic instabilities \mathbf{b} by:

$$\mathbf{b} = \nabla \times (\alpha \mathbf{B}_0). \quad (4.19)$$

We remind here that α can be written for each mode (m, n) as:

$$\alpha = |\alpha(r)| e^{i(n\zeta - m\theta)}. \quad (4.20)$$

In a cylindrical geometry Eq. 4.19 can be easily solved for the α profile; the relation between $b^{\hat{r}}$ and α is given by:

$$\alpha(r) = \frac{r b^{\hat{r}}}{m B^z + r n B^{\hat{\theta}}} \quad (4.21)$$

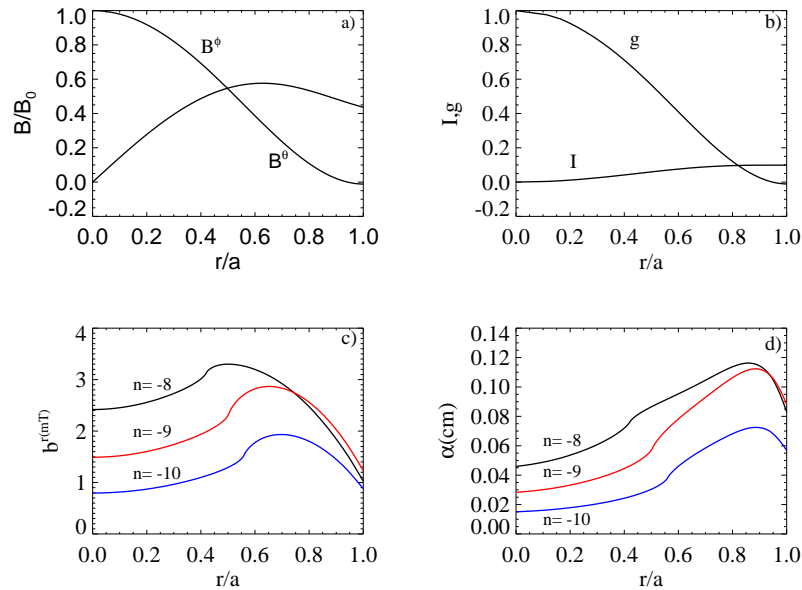


Figure 4.12: (a) Equilibrium magnetic field in RFX-mod normalized to B_0 . (b) Current profiles for RFX-mod. (c) Radial profiles for the eigenfunctions $m = 1, -10 \leq n \leq -8$ in toroidal geometry (d) Radial profiles for $\alpha(\psi_p)$ relative to the modes $m = 1, -10 \leq n \leq -8$ in toroidal geometry.

with (m, n) the helicity of the tearing mode considered, and $B^{\hat{\theta}}, B^{\hat{z}}$ the magnetic field components of the equilibrium computed by the $\mu&p$ model.

The cylindrical approximation is currently used for the MST device in Chapter 6, and it was the standard implementation of perturbations in the previous RFX experiment. In particular, condition 4.16 and 4.17 were simplified in these devices because the radial field at $r = r_s$ was experimentally forced to zero, due to the presence of a thick shell. In RFX-mod this condition is not long valid and the complete expressions reported above must be used for the boundary conditions with the measured values of the radial and toroidal field. Fig. 4.11 shows an example of the cylindrical modes reconstruction following the scheme just explained. In (a) and (b) the $b^{\hat{r}}$ profiles of tearing mode $(1, -8)$ and of its α are reported. The magnetic field perturbation does not go to zero at the edge; on the contrary, in the bottom of the figure, the same mode is reconstructed for the MST experiment, where $b^r(r_s) = 0$ and $\alpha(r_s) = 0$.

4.4.2 Magnetic perturbations in toroidal geometry

In the toroidal calculation of the α eigenfunctions we express equation 4.19 using the Boozer Jacobian of toroidal geometry. In this case the b^r perturbation is computed by the same Newcomb approach described in the previous section but with the real RFX-mod toroidal geometry and magnetic equilibrium, as explained in [53].

For the radial component of a perturbation with (m, n) helicity, and assuming: $\alpha = |\alpha(\psi_p)|e^{i(n\zeta - m\theta)}$, we obtain:

$$b^{\psi_p} = \frac{R_0}{J} \left[\frac{\partial(\alpha g)}{\partial\theta} - \frac{\partial(\alpha I)}{\partial\zeta} \right] = \frac{R_0 |\alpha| e^{i(n\zeta - m\theta - \frac{\pi}{2})} (mg + nI)}{J} \quad (4.22)$$

where $J = (I + gq)/B^2$ is the Boozer Jacobian and q is the usual safety factor.

Once b^r is known, by inverting Eq. 4.22, it's possible to express α in terms of it. Note that while expression 4.22 holds for the component of the perturbation \mathbf{b} along the coordinate ψ_p , we are usually given the radial component of \mathbf{b} (along ∇r). The relation between them is the following:

$$b^{\psi_p} = \mathbf{b} \cdot \nabla \psi_p = \mathbf{b} \cdot \frac{\partial \psi_p}{\partial r} \nabla r = b^r \frac{\partial \psi_p}{\partial r}. \quad (4.23)$$

Note that $\mathbf{e}^{\hat{r}} = \mathbf{e}^r = \nabla r$, thus $b^{\hat{r}} = b^r$. The absolute value of the $\alpha(\psi_p)$ profile is thus given by:

$$|\alpha(\psi_p)| = \frac{J |b^{\psi_p}|}{R_0 (gm + nI)} = \frac{\partial \psi_p}{\partial r} \frac{(I + gq)}{R_0 B^2} \frac{|b^r|}{gm + nI}. \quad (4.24)$$

Examples of the ($m = 1, n = -8, -9, -10$) b^r modes for the equilibrium field represented in 4.12-(a)-(b) are reported in Fig. 4.12-(c). The corresponding $\alpha(\psi_p)$ profiles, obtained by applying Eq. 4.24, are on the right-hand side (d). In Fig. 4.13(a)-(b) we have reported the averaged profiles of the modes ($m = 1, n = -7, -8$) from a cylindrical (black) and toroidal (red) reconstruction, both for b^r and α in CMC shots. The mode values in the toroidal reconstruction for α and b^r are slightly different than those cylindrical but have similar shapes and amplitudes values.

On the contrary, for the $m = 0$ modes, resonant near the edge where the toroidal magnetic field reverses its direction, the profiles are more different. This is clear in Fig.4.14 where a comparison between cylindrical and toroidal $m = 0$ eigenfunctions is reported. Otherwise we expected a stronger effect on the $m = 0$ modes due to the toroidicity, in particular for the $m = 0, n > 6$ modes. In fact, the toroidal geometry introduces a toroidal coupling $(1, 0)$ which, interacting with the tearing instability in the plasma ($m = 1, n < -6$) generates additional components for the ($m = 0, 2$ and $n > 6$) modes. This may affect the particle transport near the edge and will be the object of future

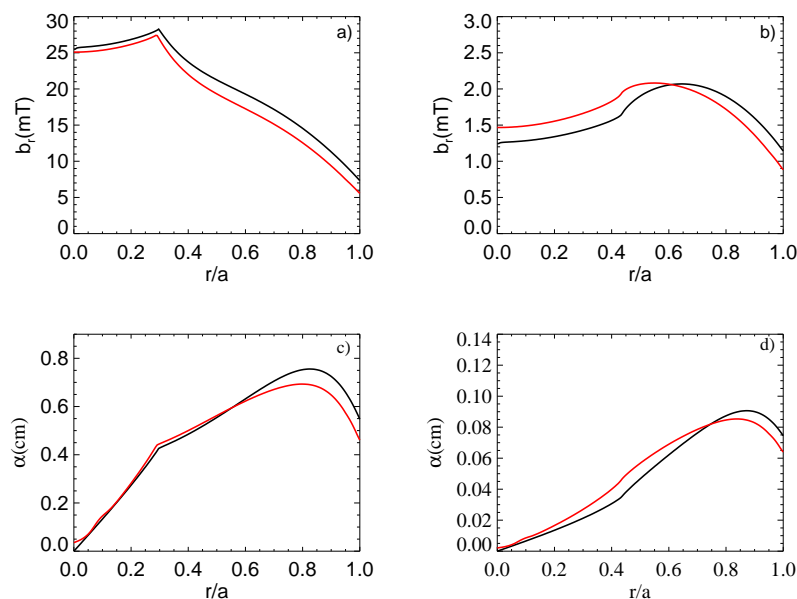


Figure 4.13: (a) Radial b^r eigenfunction for the $(1, -7)$ mode in cylindrical (black) and toroidal (red) reconstruction. (b) The same of (a) for the mode $(1, -8)$. (c) Cylindrical (black) and toroidal (red) reconstruction of α for the $(1, -8)$ modes. (d) The same of (c) for the $(1, -8)$ mode.

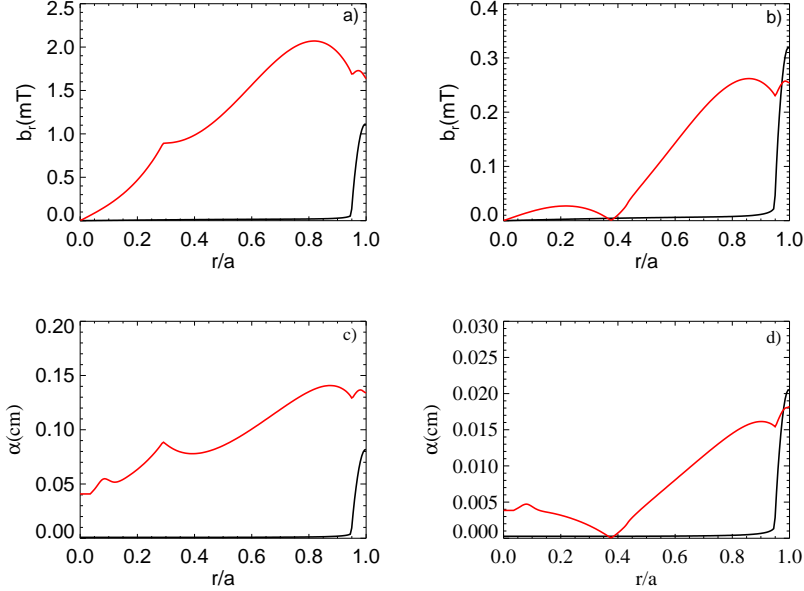


Figure 4.14: (a) Radial b^r eigenfunction for the (0, 7) mode in cylindrical (black) and toroidal (red) reconstruction. (b) The same of (a) for the mode (0, 8). (c) Cylindrical (black) and toroidal (red) reconstruction of α for the (0, 7) modes. (d) The same of (c) for the (0, 8) mode.

studies. The topology of the magnetic field is analyzed using the toroidal α eigenfunctions for several discharges, and in the next section a comparison with the experimental results from SXR tomography will be presented.

4.5 Experimental evidences of QSH regimes in RFX-mod

The study of the magnetic topology in RFX-mod is of particular interest in Quasi Single Helicity regimes when one tearing mode dominates the magnetic spectrum of the configuration. In these conditions a region of the plasma assumes an helical shape. The size of this structure depends on the ratio between the dominant and the secondary modes and it has been found to grow with the plasma current [54].

QSH is considered a key element toward the full realization of the theoretically predicted Single Helicity state (SH) where all the secondary modes are exactly zero and only the dominant is active. In this situation the whole

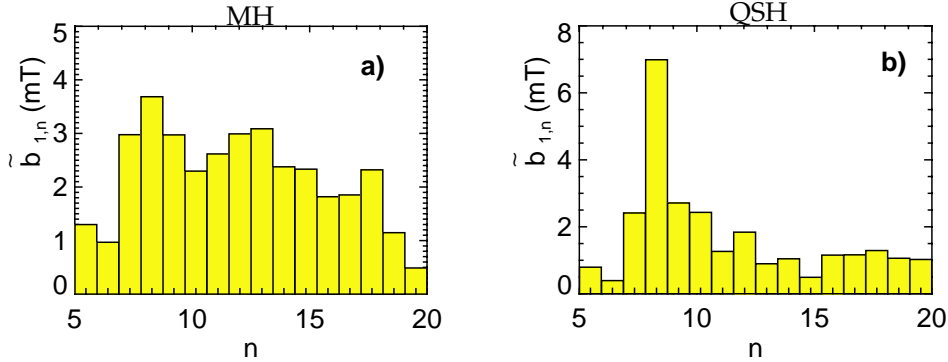


Figure 4.15: Example of an MH mode spectrum (a) and of a QSH one (b). The toroidal perturbation of magnetic field is plotted versus the toroidal mode number. In this case the QSH is generated by the mode (1,8).

plasma would be helically deformed, with a twist which depends on the (m, n) helicity of the dominant mode. A QSH mode spectrum is shown in Fig. 4.15-(b). While in the MH case, reported in (a) of the same figure, all the toroidal perturbations have comparable amplitudes, in (b) the mode (1,8) is more than the double of the other modes.

A more detailed explanation of the SH state will be presented in the next Chapter. Here we discuss the QSH regimes experimentally observed in RFX-mod with a particular attention to the magnetic topology reconstructed by ORBIT and to transport simulations dedicated to estimate the particles confinement properties in these configurations of the plasma.

4.5.1 QSH examples

In Fig. 4.16-(a)-(c)-(e)-(g) a typical discharge with a QSH regime is reported. The internal mode (1, -7) at about $50ms$ starts to grow, while all the others modes remain very low; this is clear in Fig. 4.16-(c) where the energy of the dominant mode and of the secondaries are displayed versus time.

Up to $150ms$ the mode (1, -7) has long periods during which its amplitude is high and constant, then it decays in the final phase of the discharge. Another class of QSH transitions is shown in Fig. 4.16-(b)-(d)-(f)-(h). The dominant mode never reaches a stationary amplitude but oscillates quasi-periodically: these are called intermittent QSH. It is useful to introduce a parameter which reflects the quality of the QSH state. This is the N_s num-

ber, defined as:

$$N_s = \frac{1}{\sum (W_{n,\phi} / \sum W_{n,\phi})^2} \quad (4.25)$$

where $W_{n,\phi}$ is the energy of the toroidal component of the $(1, n)$ mode. Thus, N_s measures the *width* of the modes spectrum and is equal to 1 for a Single Helicity state. This quantity is reported in Fig. 4.16-(e)-(f) for the quasi-stationary and intermittent QSH. In both cases, during the setting up phase of the plasma this parameter is typically high i.e. the plasma has a MH spectrum. When the mode $n = -7$ starts growing, the N_s parameter decreases to values close to one. The plasma core electron pressure is higher during the QSH periods, for a given density, and the synergistic interplay between the dominant and the secondary modes leads to high electron temperature T_e (data from multifilter are reported in Fig. 4.16-(i)-(l)).

In both quasi-stationary and intermittent QSH scenarios there are phases during which the secondary modes increase and a back-transition to MH is observed. This back transition is preceded by an increase of secondary modes and a decrease of kinetic pressure. An explanation of this behavior is still not available. It can be speculated that the presence of the dominant mode alters the current profile which consequently increases the saturation level of secondary modes. Also the value of the plasma current seems to play an important role on the probability of having long QSH periods during a discharge, as reported in [54].

By using the Virtual Shell, a significant reduction of the relative edge toroidal magnetic field fluctuation is recorded, and QSH regimes with low N_s are more accessible. The control on a single tearing mode of a selected helicity can be switched off and this instability can naturally grow. An other possibility consists in prescribing a non zero-reference value for one or more modes in the VS control. In both the situations the QSH state can be stimulated and helped actively.

4.5.2 Magnetic Topology reconstructions during QSH

In order to investigate the mechanism of QSH on set and termination, the time evolution of the magnetic topology has been studied for several experimental conditions. At first, we will show that an helical structure may occur even if the magnetic spectrum measured at the edge is not dominated by a single mode. This is similar to results in RFX (see [55] and [56]). RFX-mod tends to be characterized by larger islands.

In Fig. 4.17 we show a magnetic field reconstruction for a case in which the good confinement was obtained with an externally measured MH spectrum.

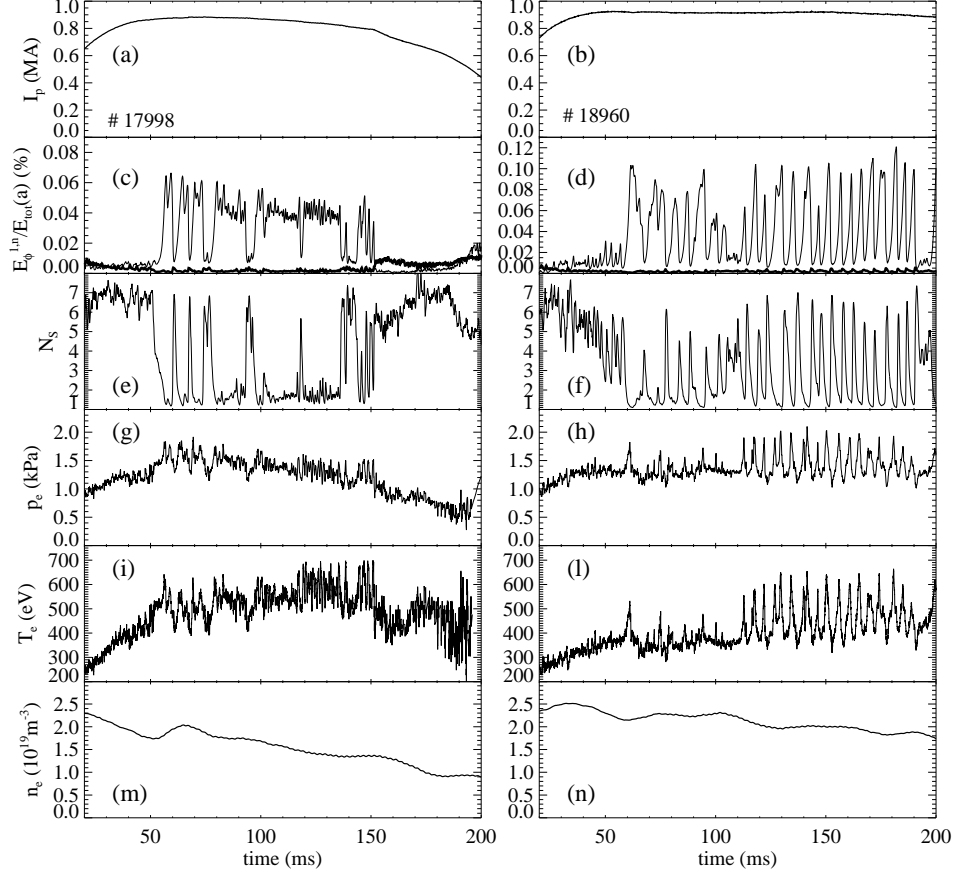


Figure 4.16: Time evolution of: (a) plasma current in MA, (c) magnetic energy density of the dominant mode (solid curve) and average energy density of secondary modes with $-8 > n > -15$ (dotted curve), both normalized to the energy density of the edge magnetic field, (e) N_s parameter, (g) electron pressure, (i) core electron temperature and (m) core electron density for a quasi-stationary QSH discharge. (b),(d),(f),(h),(l),(n) are the same quantities for a discharge with intermittent QSH.

It refers to a shot (#17453) with a plasma current of $I_p \simeq 600kA$. The period of the QSH state is limited in time between 83.5 and 85.5 ms. Details on the modes energy and the temperature profiles by Thomson scattering are shown in panels (a)-(b).

The dominant mode is the $(1, -7)$ which resonates very close to the center of the plasma. Despite its low value at the edge, the $n = -7$ eigenfunction reconstructed via the Newcomb equation, is significantly large in the core. In

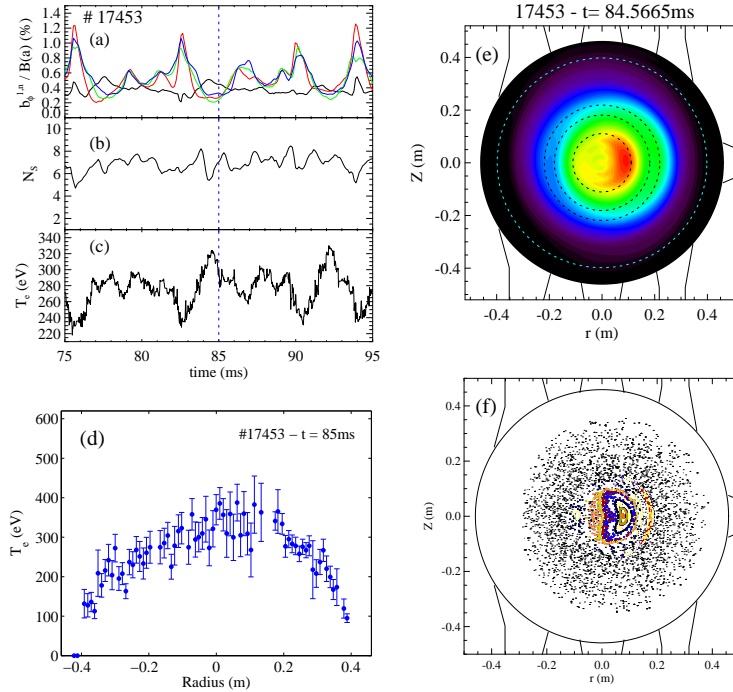


Figure 4.17: Time evolution of: (a) selected $m = 1$ amplitudes (black = -7 , red = -8 , green = -9 , blue = -10); (b) N_s parameter and (c) core electron temperature for the shot 17453. (d) Electron temperature profile at $t = 85ms$ for the same shot; (e) SXR emissivity distribution at $84.57ms$ (going from the inside to the outside, the dotted circumferences correspond to the resonant surfaces of the $m = 1, n = -7, -8, -9$ modes and of the reversal surface respectively) We do not report the color bar with the absolute value of emissivity since for our analysis we are interested only on the qualitative shapes of the structures which appear in the plasma. This holds for all the next tomographic reconstructions of the Thesis. The red zone corresponds to the most SXR emissive surfaces. (f) Magnetic field puncture plot at $t = 84.57ms$ by ORBIT. The colored points refer to conserved helical flux surfaces.

panel (c) SXR tomography shows a poloidal axisymmetry near the center. at the time $t = 84.6ms$.

The magnetic topology is computed by field line tracing with ORBIT. This is done by implementing the equilibrium and the perturbations in the code as described in Chapter 2 and in 4.4, for a given time during the discharge, and solving the guiding center motion equations of Chapter 3 for very low energy particles with a velocity parallel to the magnetic field. At low energies, drifts are negligible, and therefore particle trajectories closely

follow magnetic field lines. Intersections of their motion with a poloidal (or toroidal) plane are recorded to generate a Poincaré plot (poloidal or toroidal). For the shot #17453 at $t = 85ms$ the result is shown in Fig. 4.17-(f)

The magnetic structure corresponds to the asymmetry in the SXR and in the Thomson scattering measurements. It is worth noting that the magnetic field line reconstruction by ORBIT also shows a small $n = -8$ island, due to the low amplitude of the secondary magnetic perturbations. This island is so small that cannot be resolved by the SXR tomography and in fact it is not

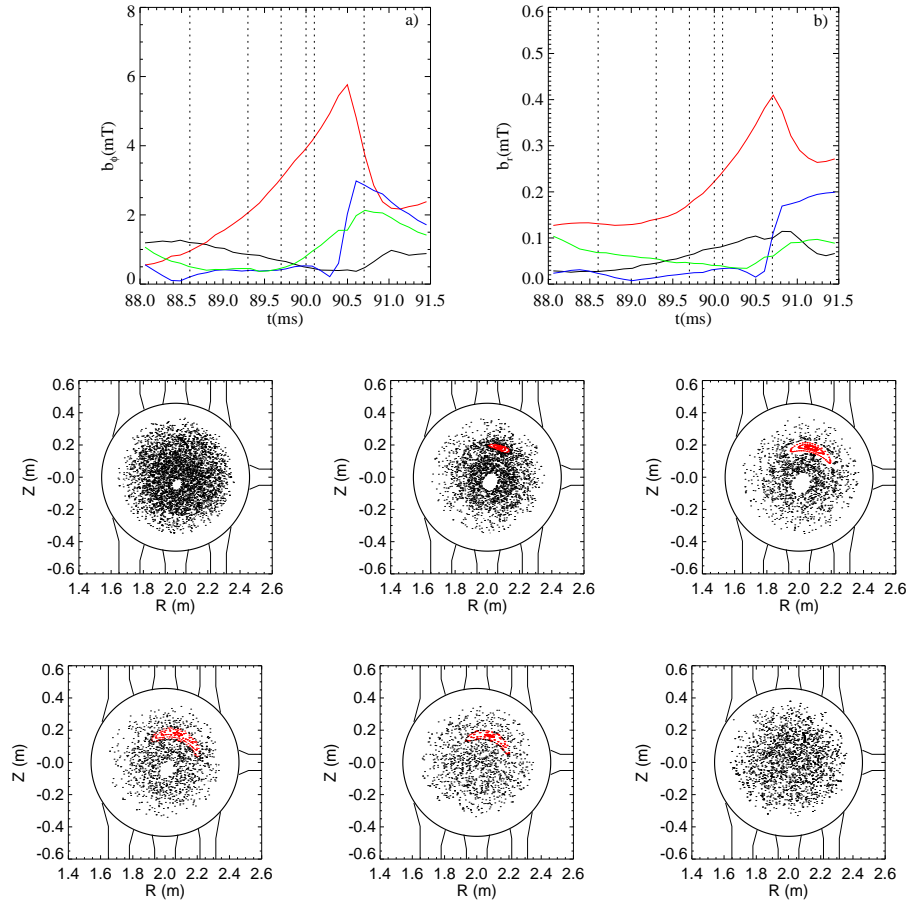


Figure 4.18: On the top: time evolution of the toroidal (a) and radial (b) components of the modes $n = -1, n = -7$ (red), -8 (blue), -9 (black), -10 (green) for the shot 17462. On the bottom: magnetic field topology at the times correspondent to the dashed lines in (a)-(b). Poincaré plots are in sequence of increasing time from the top left to the down right. Shot:17462.

visible in (c).

Another example of QSH magnetic topology is reported in figure 4.18. Reconstruction by ORBIT at several times during the shot #17462 shows the evolution of the magnetic topology during a MH-QSH transition. On the top the evolution of the $m = 1, n = -7$ (red), $n = -8$ (blue), $n = -9$ (black), $n = -10$ (green) modes is shown for the toroidal (a) and radial (b) components at the edge. At the times corresponding to the dashed black lines the reconstruction of the magnetic field has been performed. At the time $t = 88.6ms$ the $n = -7$ mode is still low and of the same order of the others instabilities. The corresponding Poincaré (first on the top-left), in fact, is that typical of a MH scenario. At $t = 89.3ms$ the mode starts growing and a small helical structure appears in the Poincaré (in red). The magnetic island becomes larger while the mode $n = -7$ continues to grow and the other modes remain at small values. From $t = 90ms$ also the secondary modes are not constant anymore but are increasing and the QSH state degenerates as displayed in the last two Poincaré on the bottom-right. At the last time considered the magnetic topology is again MH.

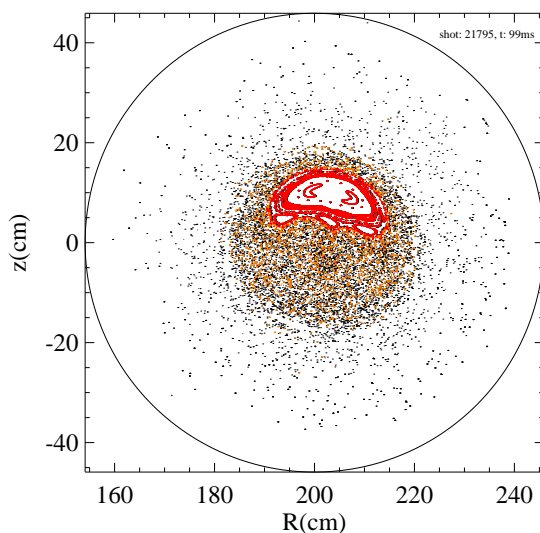


Figure 4.19: In this Poincaré three different magnetic field topologies are visible. The black points correspond to chaotic magnetic field lines; the red lines are the conserved surfaces of the magnetic island $(1, -7)$; the orange regions is dominated by the stickiness, an intermediate regime between chaos and order. Shot:21795,time:99ms.

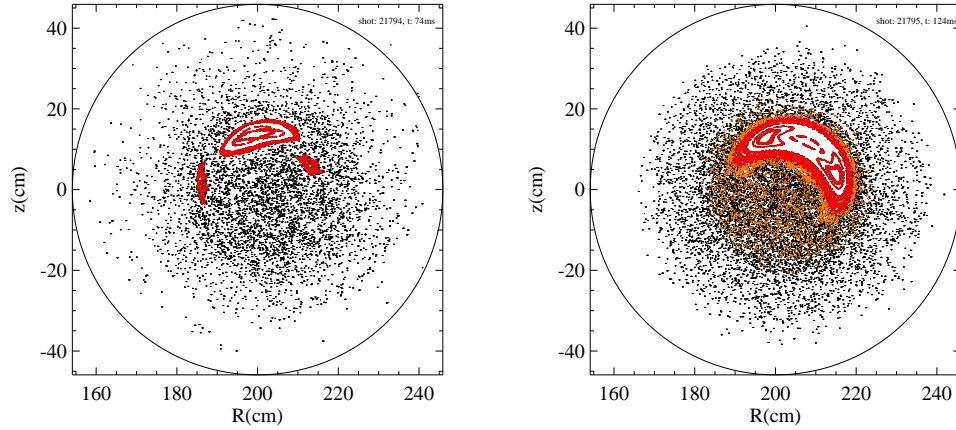


Figure 4.20: Left hand side: conserved magnetic flux surface for the island $(1, -7)$ in red (shot: 21794 at 74ms). Right hand side: conserved surfaces (red) and stickiness (orange) for a similar shot (21795 at 124ms).

These two examples illustrate the variety of structures that can occur in RFX-mod. In the former case, in fact, the magnetic structure is composed by conserved flux surfaces, surrounded by a region of weakly chaotic field (sticky region). The differences are due to the kind of equilibrium and to the magnetic perturbation spectrum: both these parameters depend on the experimental details such as the level of plasma current, the value of the reversal parameter F and the control algorithm used for controlling modes. Anyway, situations with large magnetic islands seem to be of the type shown in Fig. 4.17-(f) and represent the typical situation in RFX-mod, while the Poincaré of Fig. 4.18 were more standard in the old RFX configuration.

4.5.3 Stickiness around magnetic islands

We investigated further the issue of the weakly chaotic region surrounding the magnetic islands in RFX-mod. Another example is reported in Fig. 4.19 for a QSH during a shot (#21795) with a plasma current of about $800kA$. As far as magnetic topology is concerned, it can be seen that two class of field lines are present. A first class describes conserved flux surfaces (red points), while a second class is chaotic (orange points) but the lines remain in a bounded region around the conserved surfaces. This bounded chaos is usually dubbed *stickiness*.

When comparing the magnetic topology with thermal measurements, it is unclear whether the sticky region needs to be considered or not. There are, in fact, several cases in which no conserved flux surfaces exist but an helical sticky region remains. Such a comparison requires considering the particles drift with a technique described in the next sections. In fact, particles with an energy of $400 - 500 eV$, which is typical in these RFX-mod shots, are also subjected to drift effects and to collisions. This allows them to escape both from the conserved flux surfaces in red and from the stickiness region. Sticky regions have been recently identified and analysis is still on going. They seem to occur if the mode $(1, -7)$ has a very large amplitude and the other modes are relatively small in comparison. For example, in Fig. 4.20 two examples of magnetic field topology reconstruction are shown for two similar shots with a maximum plasma current of $I_p \simeq 900 kA$ and $F \simeq -0.03$. In the plot on the left, only a conserved structure $(1, -7)$ is present, even if close to the main island two secondary structures appear. In the Poincaré on the right, the high mode $(1, -7)$ produces a wider island surrounded by stickiness.

From the preliminary analysis it seems that the sticky region is formed for particular high values of the dominant mode, at the resonant surface. High current and shallow F (i.e. resonant surfaces near the axis) seem to be experimental conditions that favor such a growth of the dominant mode.

4.5.4 Test particle transport studies

The link between the magnetic topology and thermal content is rather complex, as particles may drift away from the magnetic flux surfaces. A rough estimate of the confinement properties in a prescribed region of the plasma, by computing the so-called *loss time*, is here given. An ensemble of ions or electrons is placed in the spatial region of which we want to test the confinement properties. When half of these particles arrives at a fixed loss surface the run is stopped and the run-time is recorded. In Fig. 4.21 it is reported an example of a toroidal Poincaré for the magnetic field of a plasma in QSH regime. Particles can be deposited inside the island surface, around it or in the chaotic regions. The loss surface is represented by a thick red line. Previous studies published in [56] have shown that particles in QSH (or SH) regimes are characterized by higher loss times with respect to MH regimes. Anyway this method couldn't allow to obtain an estimation of the diffusion coefficients of the particles inside the island. In fact the loss surface is axisymmetric; to study the diffusion properties in the magnetic island is then necessary to consider its helical geometry as it will be described in Chapter 5.

Despite the limitations, the loss time indicator allows to compare qualita-

tively the confinement properties of different magnetic topologies obtained in various experimental situations. For example it can be computed at different times during a shot. In order to do this, at each time the correct equilibrium with the proper modes must be implemented. As an example, a comparison of two similar shots with different control algorithms is shown in Fig. 4.22: one with the Clean Mode Control (red) and the other without (blue). In the example, the application of the CMC control algorithm results in a different magnetic spectrum. This is reported on the right hand side of Fig. 4.23 for the $m = 1$ radial perturbations measured at the shell, with the corresponding Poincaré; on the right hand side the same is shown for a standard VS shot. The correction of the sidebands, as explained in section 4.2.3, takes to a reduction of the amplitude of the modes and thus to an improved control of the tearing instabilities by the Virtual Shell, which reflects in a higher loss time.

Another application of the loss time is to test, at a given time of a shot, the loss time in several spatial regions of the plasma. Particles are deposited in the same equilibrium and with the same magnetic perturbations but in different positions. The result is a scan of the loss time along a radius at a fixed angle or, vice versa, at different poloidal angles for a given radius. By varying both these variables a final 2-D map of the loss time in the plasma can be plot. Example of these applications are given in the next section and in Chapter 6 for the MST device.

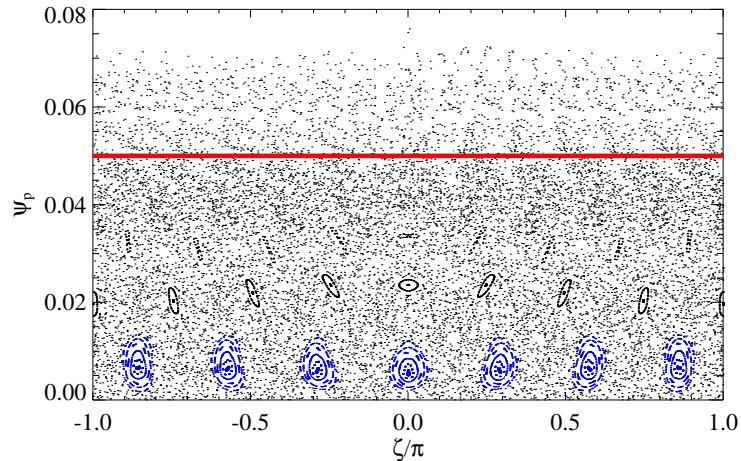


Figure 4.21: Toroidal Poincaré section for a QSH plasma in RFX-mod. Particles are deposited in a selected region and the time they take to reach the loss surface (red thick line) is recorded.

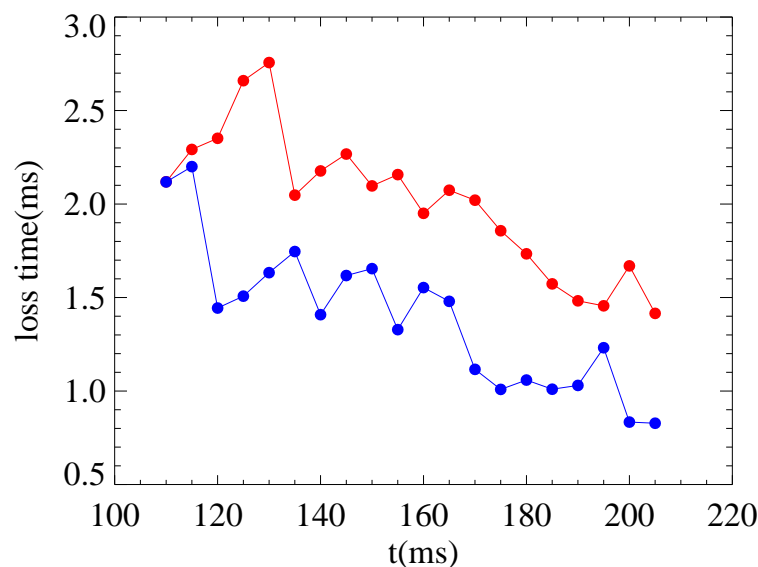


Figure 4.22: Loss time computed in two shots with the clean mode control (red, shot 21804) and without (blue, shot 21805). The correction of the sidebands has a good effect on the modes control by the Virtual Shell.

4.5.5 QSH in high plasma current regimes

In recent high current experiments a new phenomenology has been observed. Thermal structures bigger than the ones shown in previous experiments (at lower current), but with flat temperature inside, have been detected. This seems to be related to the level of the dominant mode.

The best performances in the RFX-mod device have been recently reached when the plasma current has been increased up to $1.5MA$. Quasi Single Helicity regimes are more often achieved with the dominant $(1, -7)$ mode. Large magnetic island appearing in the central region of the plasma during these shots can affect the whole equilibrium and improve the global confinement properties of the system.

An example of a high-current discharge (#22222) is reported in Fig. 4.24. The plasma current rises close to $1.3MA$ (panel (a)) and during the flat top phase an increasing of the mode $(1, -7)$ is clear in (b). In this period the other modes are low. The radial profiles of the electron temperature at the selected times t_1 and t_2 are reported in Fig. 4.24-(c)-(d). The profile at t_1 in (c) shows a mean temperature in the core close to $700eV$ but despite the magnetic

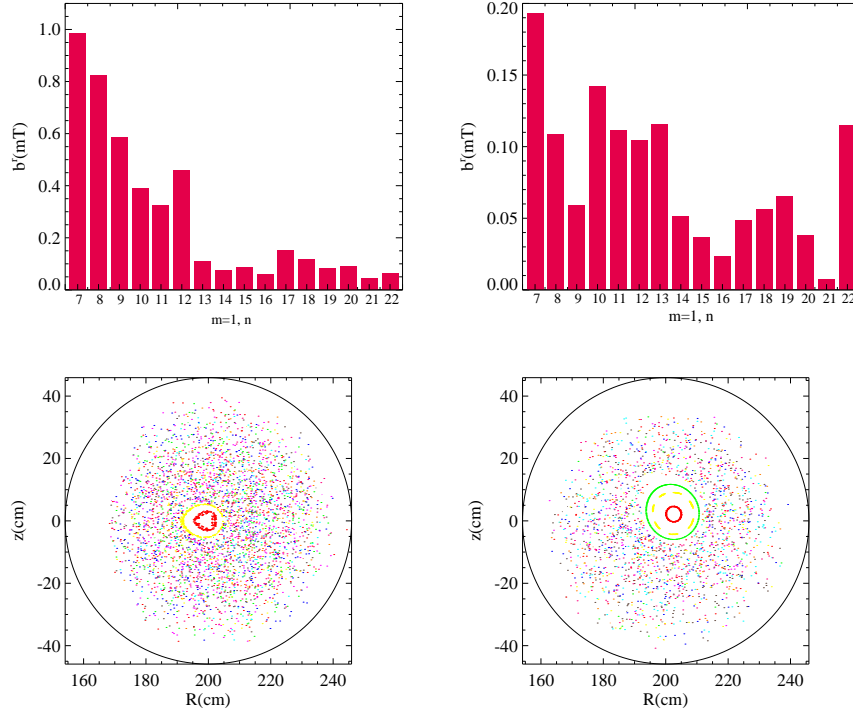


Figure 4.23: On the left hand side: $m = 1$ magnetic spectrum of the perturbations at the shell for the VS 21804 shot at $t = 125ms$ (top) and corresponding poloidal Poincaré (down). On the right hand side: $m = 1$ magnetic spectrum of the perturbations at the shell for the CMC 21805 shot at $t = 125ms$ (top) and corresponding poloidal Poincaré (down).

island no asymmetries are present, the profile is flat and constant in the central region. This is not a typical scenario in a QSH regime at low currents (i.e under $1MA$). As we have discussed above, in fact, the presence of a helical magnetic structure with conserved surfaces reduces the particle and energy transport and increases the temperature in the island. An asymmetry in the radial T_e profile with a peak corresponding to the island position is measured by the Thomson scattering diagnostic (see Fig. 4.17-(c), for example). In the same discharge an high peak in the temperature profile appears after few ms , at $t_2 = 98.98ms$ (Fig. 4.24-(d)). The regions close to this maximum have a lower temperature, but not less than $600eV$.

At the times of the different electron temperature profiles, Poincaré plots have been performed. We report both the plots of the Poincaré obtained only using the dominant perturbation (left hand side) and that with all the $m = 1$ spectrum (on the right) in Fig. 4.25. These reconstructions refer to

the time $t_1 = 74ms$. The Poincaré with the single mode $(1, -7)$ shows that the magnetic island extends over a large region of the plasma. On the right the Poincaré with all the $m = 1$ modes shows a region of stickiness and conserved surfaces which is still an important fraction of the plasma. Such a topology for the magnetic field could explain the flat electron temperature profiles just shown in Fig. 4.24-(c). In fact, if a large region of the plasma is dominated by stickiness or quasi-conserved helical surfaces, the particles and energy transport is reduced. This reflects in a global core increasing of the temperature.

The situation is different for the time t_2 . The Poincaré are reported in Fig.4.26 for the $(1, -7)$ mode only (left) and for all the $m = 1$ (black). The island is clearly smaller than the previous case and is mainly concentrated on the left hand side of the poloidal cross section. The corresponding complete Poincaré on the right shows the presence of a small sticky structure. The

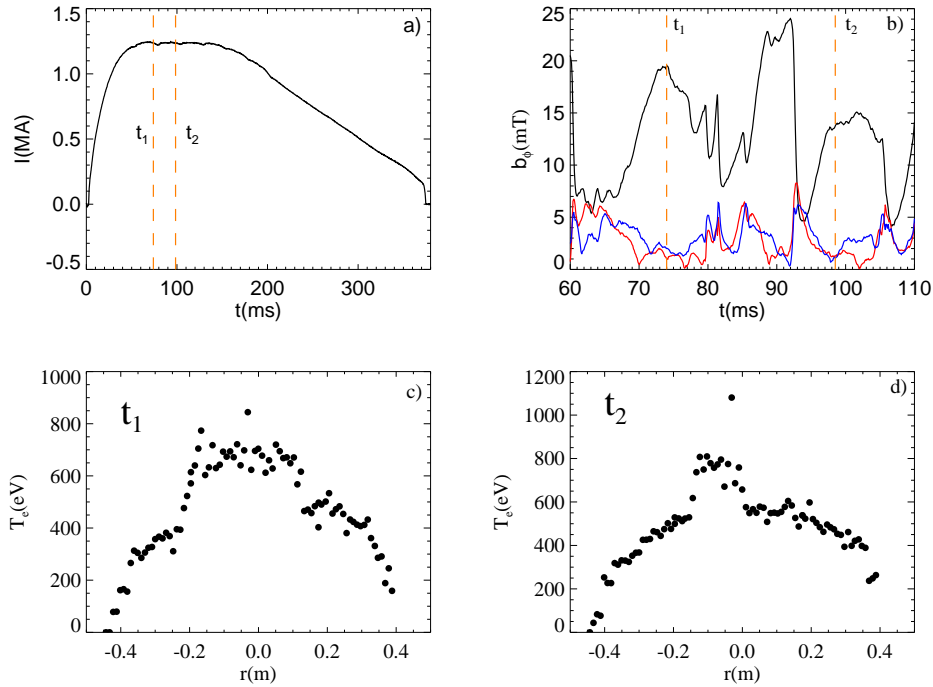


Figure 4.24: High current plasmas shot in RFX-mod. a) Waveform of the plasma current I_p ; b) tearing instabilities $m = 1, n = -7$ (black), $m = 1, n = -8$ (red), $m = 1, n = -9$ (blue). (c)-(d) are electron temperatures profiles by Thomson scattering at the times marked in (a)-(b) by shaped orange lines. Shot: 22222.

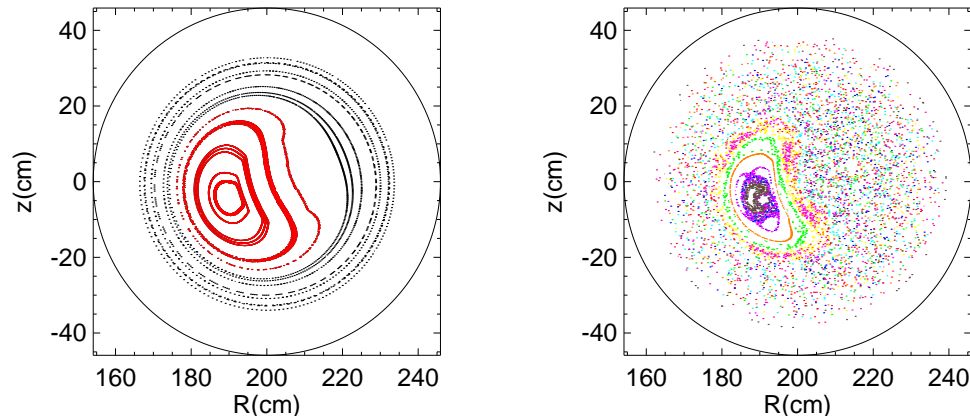


Figure 4.25: On the left: Poincaré plot for the $m = 1, n = -7$ mode at the time $t_1 = 74ms$ for the shot 22222. On the right: Poincaré plot at the same time but for all the modes $m = 1$.

peak of electron temperature in 4.24-(d) is related to this small region.

From a topological point of view we can conclude that the wider thermal structure is associated to a Poincaré plot with a wide stickiness region, while conserved surfaces are almost absent. The other case, in which the dominant mode is slightly lower, the sticky region is smaller. In order to perform a more quantitative comparison, maps of loss time have been performed.

About 20 electrons are deposited on a grid of (ψ_p, θ) in the central region on the plasma with a random pitch. The time required by half this population to reach an axisymmetric loss surface at $r/a \sim 0.65$ is recorded. This analysis has been performed for both the times t_1 and t_2 discussed in this section. The final contour of the loss time is reported in Fig.4.27 on the top at $t_1 = 74ms$ and on the bottom at $t_2 = 99ms$. The main difference in the two case can be seen while looking at the color bar which shows a maximum of $26ms$ for the first case, while only of $2.42ms$ in the latter. Thus, the good properties of the conserved surfaces extending for a large size of the plasma, shown in Fig.4.25, mean a strong increase of the time required by the electrons to escape from a given region (red dashed line in figure 4.27). For the two cases, in the transport simulations, we have used exactly the same electron temperature of the background and the same collisions, thus the only difference is just the magnetic topology. Note also that the structure at t_1 is more poloidally extended, while that at t_2 is concentrated around its maximum in red. Anyway, no clear increase of the high loss time region is ob-

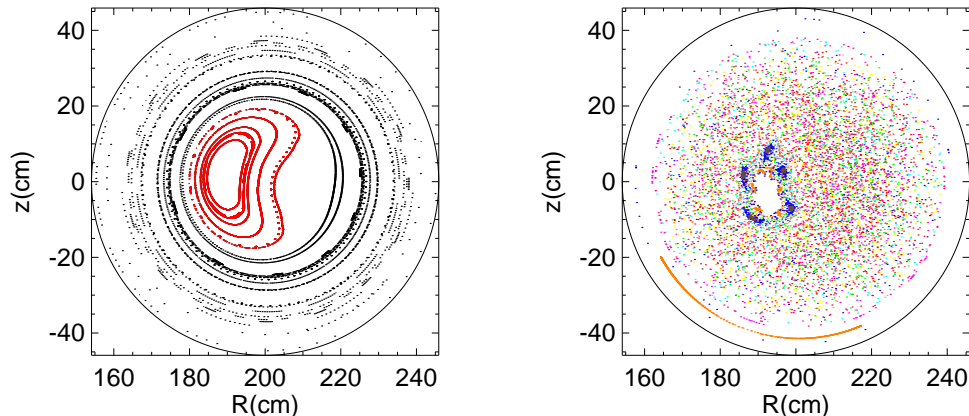


Figure 4.26: On the left: Poincaré plot for the $m = 1, n = -7$ mode at the time $t_2 = 99ms$ for the shot 22222. On the right: Poincaré plot at the same time but for all the modes $m = 1$.

served, therefore the difference may be probably due to an interplay between transport and power deposition. Finally, let us mention that an explanation of the difference between these two patterns has been recently proposed. In fact, it has been found that cases with flat electron temperature profiles and higher loss times occur when the separatrix of the island is expelled.

Let us conclude this section by highlighting the limitations of the conclusions performed so far. When such large magnetic islands are present, the equilibrium is not axisymmetric any more and the magnetic instabilities are so high that the perturbative approach may fail. Moreover, even if the particles were poloidally localized, for the evaluation of the loss time, the loss surface was axi-symmetric. Concerning the latter limitation, we developed a method to estimate transport coefficients in helical configuration, that will be described in the next Chapter. We shall consider a simplified situation, with one mode of small amplitude. In the magnetic island generated by this mode we consider ions and electrons transport with the aim to estimate a non axisymmetric loss time. Even if the analysis concern only a small SH configuration, we do not expect important differences in bigger island and in Quasi Single Helicity configuration near the island O-Point and inside the helical conserved flux surface. The method used is general and can be applied also to different problems.

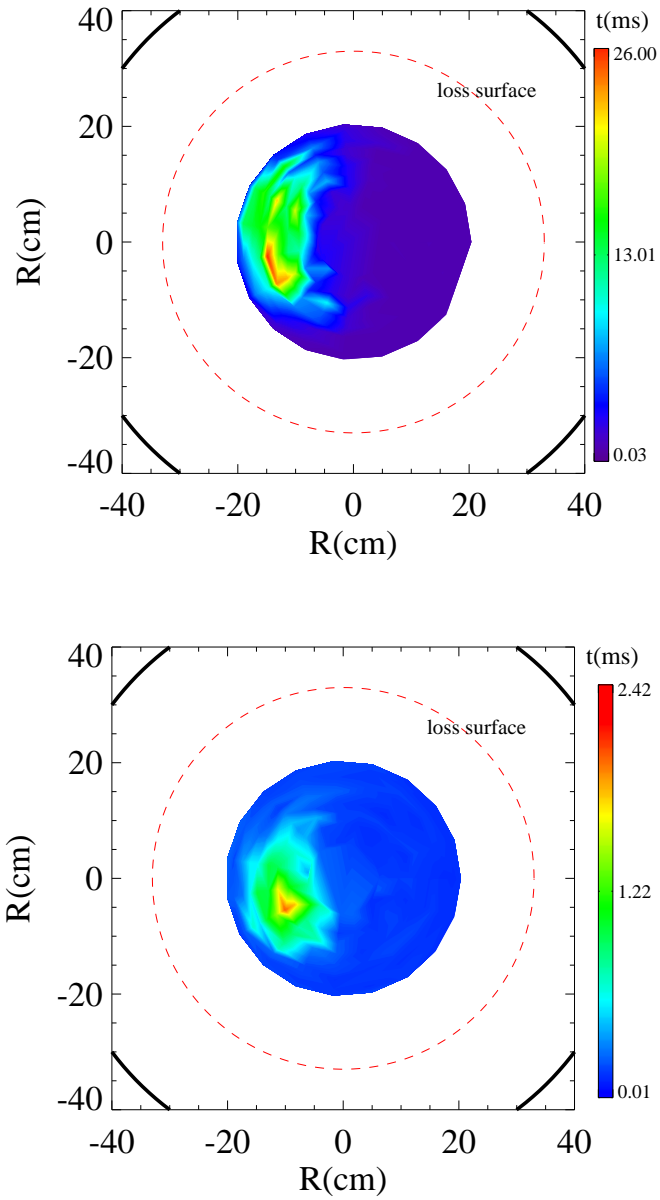


Figure 4.27: Transport simulation in RFX-mod. Electrons are deposited inside the plasma and the time they require for half of them to reach the red dashed line are recorded (loss times). On the top: contour of the loss time at $t_1 = 74ms$ of the shot 22222. On the bottom: contour of the loss time at $t_2 = 99ms$ of the same shot.

CHAPTER 5

Thermal particle transport in Single Helicity regimes

This Chapter is dedicated to the description of a method to estimate local test particle diffusion coefficients in helical toroidal geometry, as occurring in SH and QSH regimes (published in [57]). This method has been applied to Single Helicity states that are not experimentally observed, but it can be extended to configurations where the magnetic flux surfaces exist, such as the Quasi Single Helicity regimes. In the first part, a review of theoretical SH results is given, while in the second part the method to represent the helical surfaces of the magnetic island is presented. Finally, the results of numerical transport simulations are reported for different geometry helicities of the magnetic island. Scaling with collisionality, for the RFP relevant values, is discussed.

5.1 Single Helicity

Reports about Single Helicity have been first obtained in 2D numerical simulations [59] [60] [61]. More recent accurate 3D simulations shed light on the transition from the standard Multiple Helicity to SH [62] [63]. SH states are characterized by helically distorted magnetic flux surfaces, as displayed in Fig. 5.1. The helical shape of the SH field is due to a single resistive kink mode and its harmonics. This mode represents a sort of hybrid instability,

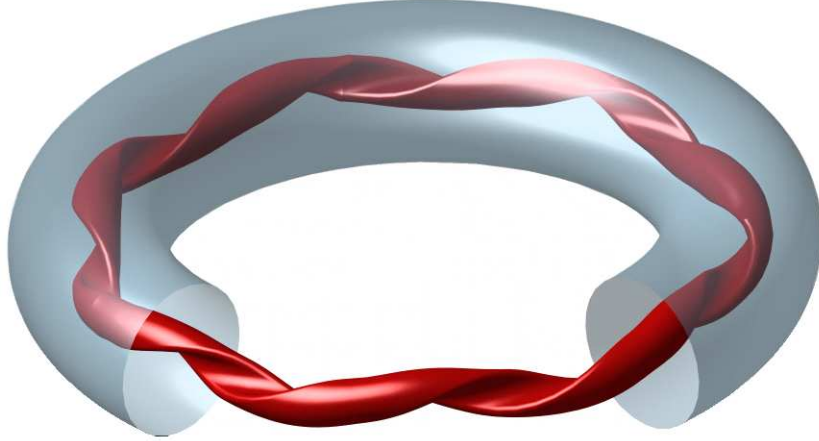


Figure 5.1: Artist's view of a helical state obtained in the RFX device (taken from [58]).

between the tearing mode (characterizing the MH axi-symmetric configuration) and the kink mode. Such an instability develops and saturates towards a stable equilibrium: this has been explained in terms of a simple model, that will be described in the following.

5.1.1 The wire model of the RFP dynamo

Let us consider a current-carrying wire on the axis of a cylindrical flux conserver, as represented in Fig. 5.2-a. A small constant axial magnetic field \mathbf{B}_T is also present, generated by an azimuthal current I_{shell} flowing in the shell. This represents the simplest approximation of a pinch experiment. It is well known that this wire is unstable to kink perturbations and we assume, for simplicity, that only two opposite pitches are possible in this system. If the kinked current of the wire I_θ has the same orientation as I_{shell} then the kink perturbation is unstable. In fact, the two currents attract each other and any initial perturbation is amplified.

The axial magnetic field B inside the kinked wire increases due to the solenoidal effect while the presence of a flux conserver decreases the field outside B' , as indicated in Fig. 5.2-b. This process continues until the growth of B in the center forces B' to reverse its sign. At this point, I_{shell} reverses

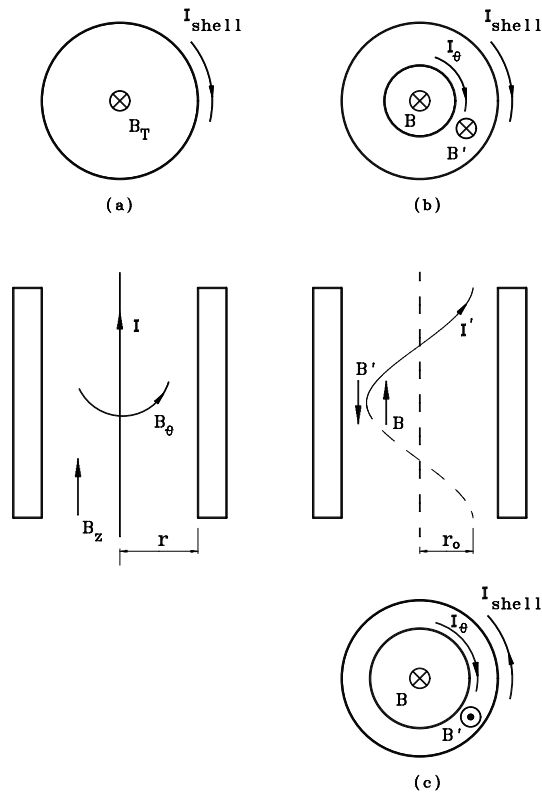


Figure 5.2: The wire model of the RFP: (a) a current-carrying wire in a cylindrical flux conserver, plus a magnetic field \mathbf{B}_T generated by the azimuthal current I_{shell} ; (b) development of a kink instability of the wire; (c) non-linear saturation of the kink instability through the reversal of the axial magnetic field (taken from [64]).

too and the instability starts to quench, because I_{shell} and I_θ have opposite signs and thus repel each other, as shown in Fig. 5.2-c. The wire reaches a stable helical equilibrium when the reversal of the axial magnetic field is high enough, provided that some dissipation mechanism of its mechanical energy is present.

This model shows intuitively how a self-organized magnetic system can spontaneously reach an equilibrium state thanks to the loss of cylindrical symmetry. This model shares many common features with the RFP. As shown in Chapter 1, in pinch devices like the tokamak and the RFP, a toroidal current is driven in a plasma embedded in a pre-existing toroidal magnetic field. In a tokamak, the toroidal magnetic field is very strong, and the plasma current is limited in order not to violate the Kruskal-Shafranov (KS) limit [16], i.e. $q(a) \simeq 1$, where a kink instability would develop and cause strong

sawtooth activity or even current disruptions. On the other hand, the current in the RFP is driven well above the KS limit and resistive kink-tearing modes develop. Nonetheless, current disruptions do not occur in the RFP, because the combined action of toroidal coils, used as a toroidal flux conserver, and of high magnetic shear tend to stabilize the helical modes.

5.1.2 MH-SH transition

One of the most difficult tasks is to understand when a transition MH-SH occurs. This has been studied in past years by the code Specyl which solves the visco-resistive compressible nonlinear MHD model in a periodic cylinder with axial periodicity $2\pi R_0$ under the constant-pressure and constant-density approximation [65],[66].

The numerical simulations have shown that the transition is determined by the plasma viscosity ν and the resistivity η [66], combined in the Hartmann number $H = (\eta\nu)^{-1/2}$ and in the magnetic Prandtl number $P = \nu/\eta$. The numerical analysis in [66] reveals that the Prandtl number $P = \nu/\eta$ acts only through the inertia term in the MHD equations. In particular, intermittent or stationary QSH regimes are found for simulations at values of H between MH and SH. The Quasi Single Helicity states are of particular interest because they have been observed in the experiments. Even though a dominant mode exists in the system with a stationary amplitude during QSH, a finite low level of magnetic and flow velocity turbulence still exists.

Energy of $m = 0$ modes is strongly correlated to the magnetic spectrum, assuming different values in SH and MH. Therefore the transition MH-SH can be represented by showing the dependence of the $m = 0$ modes energy to the H parameter. An example of bifurcation MH-SH is shown in Fig. 5.3-(a)-(b) where the time averaged energies $E_{m=0}^M$ of the spectral component $m = 0$ are plotted as function of the Hartmann number, for two different values of the Θ parameter. The transition between MH and SH occurs in the interval $H \in [2000, 3000]$; above this critical interval the system is in MH state; below the interval the system enters a SH laminar regime.

QSH states correspond to the transition interval of Fig. 5.3. The experimental absence, up to now, of a pure SH state could be due to a decrease of the viscosity as the magnetic chaos decreases. This might force the plasma to remain in QSH and not to reach the stable SH configuration. The consequence of the coexistence of chaos and helical conserved flux surfaces is that the dynamo is provided by a hybrid turbulent-laminar mechanism.

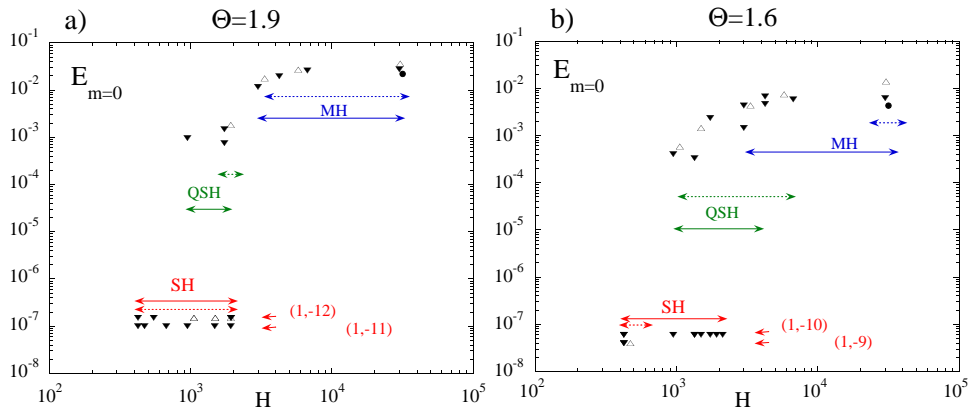


Figure 5.3: The time averaged magnetic energy of the $m = 0$ modes as a function of the Hartmann number for SpeCyl simulations at two values of the pinch parameter, (a) $\Theta = 1.9$ and (b) $\Theta = 1.6$. For a convenient representation in the log-scale plot, the vanishing SH $m = 0$ mode energy is set at a finite conventional value with different offsets associated with the two preferred helicities developed in the system (figure taken from [68]).

5.1.3 Electrostatic nature of the dynamo

Detailed analysis of the SH SpeCyl results have recently pointed out that the RFP is sustained in pure helical states by a laminar dynamo mechanism. In fact, in a stationary SH state, the poloidal electric field needed to maintain the magnetic configuration against resistive diffusion is continuously generated by the helical deformation of the magnetic flux surfaces. This dynamo mechanism relies on the modulation of the current density along the helically distorted magnetic field lines [67]. Associated to this modulation, there is an electric field along field lines, which drives a charge separation to balance it. As a result, an electrostatic potential Φ^{es} builds up, which drives to its turn a drift velocity \mathbf{u} , which has the same helicity as the kink perturbation:

$$\mathbf{u} = \frac{-\nabla\Phi^{es} \times \mathbf{B}}{B^2}. \quad (5.1)$$

The SH RFP dynamo is thus sustained by a global helical flow with laminar characteristics, in contrast to turbulent dynamos acting in other laboratory and natural cases.

5.1.4 Numerical study of transport in helical states: a summary

Single Helicity has a strong impact on the particles and energy transport. In fact the presence of conserved flux surfaces allows to avoid the typical chaotic field and the anomalous transport which is peculiar of the MH configuration. We present here a numerical study about this topic performed by using the ORBIT code. The diffusion coefficients inside a magnetic island will be computed by applying the Fick law. In fact, in stationary conditions and if transport is local, the flux of particles per unit area, Γ , across a helical surface inside the helical magnetic structure is given by the Fick's equation:

$$\Gamma = -D^\perp \nabla n \quad (5.2)$$

where D^\perp is the diffusion coefficient perpendicular to a particular magnetic surface and ∇n is the density gradient across that surface. As a consequence of Eq. 5.2, if D^\perp is constant inside the island and a stationary source of particles is positioned in the O-point, the density of test particles is a linearly decreasing function. By estimating both Γ and ∇n with a simulation, D^\perp is determined.

The estimate of Γ and ∇n would be easy if an helical equilibrium was available. Attempts to obtain helical SH equilibria have not been successful so far. If the helical geometry is only obtained through field line tracing, such an estimate is not possible unless an approximate representation of helical surfaces and a numerical computation of the perturbed magnetic flux enclosed by these surfaces is performed. We present in sections 5.5 – 5.6 the algorithm to represent the island's surfaces. The others paragraphs will describe the remaining steps required to evaluate Γ and ∇n : the considered equilibrium magnetic field and perturbation radial profile and the simulations with the test particles.

5.2 Equilibrium and Perturbations

Our study of particles transport in SH regimes is based on the RFX-mod geometry with an equilibrium characterized by the following parameters: plasma current $I_p = 600kA$, magnetic field on axis $B_0 = 0.6T$, reversal parameter (at the minor radius a) $F = B_\phi(a) / \langle B_\phi \rangle = -0.2$ and pinch parameter $\Theta = B_\theta(a) / \langle B_\phi \rangle = 1.5$.

As a SH perturbation we have considered both an $m = 1, n = -7$ mode with edge value of the magnetic fluctuation amplitude $b_\phi^{1,-7}(a) = 1.3mT$ and an $m = 1, n = -8$ mode with $b_\phi^{1,-8}(a) = 2.5mT$, corresponding respectively

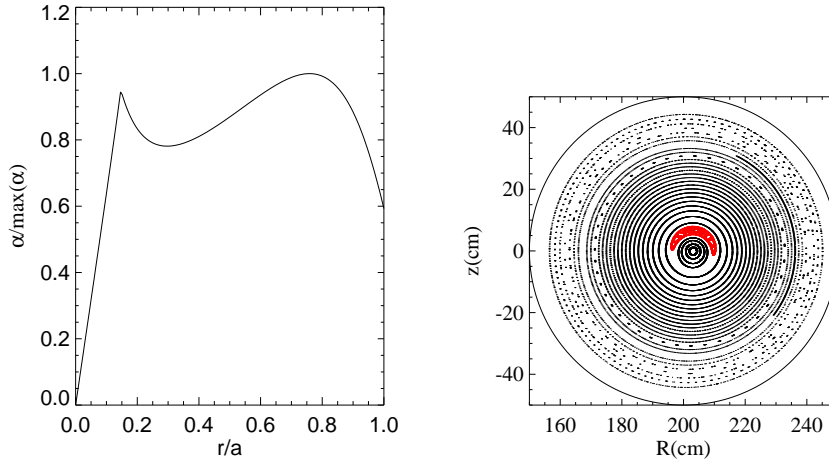


Figure 5.4: Left-hand-side : α profile for the magnetic perturbation which generates the $(1, -7)$ island in RFX-mod. Right-hand-side: poloidal Poincaré for the magnetic perturbation on the l.h.s.

to 0.3% and 0.6% of the field on axis. These modes are usually the innermost resonant ones in the RFX-mod plasmas; one of them is typically dominant with respect to the others in the QSH regime, as we have pointed out in the previous Chapter. The helical magnetic structures which are generated by these mode amplitudes are small in comparison with the total plasma volume (less than $1/10$) and our analysis and results are concerning only this region. Anyway, in RFX-mod larger islands have often been observed (as shown in section 4.5), with values of the SH perturbation at the edge also greater than $10mT$ (resulting in an island with a size of $20cm$). Moreover, a small helical structure simplifies the computational work and the main results are not affected by this limitation, as far as we are interested in particle transport near the O-point region.

The radial profile of the perturbations $b_r^{mn}(r)$ are reconstructed solving the Newcomb equation as shown in paragraph 4.4 from the measured edge magnetic fluctuations $b_\phi^{mn}(a)$ and $b_r^{mn}(a)$. We are considering a cylindrical approximation for the eigenfunction of the mode which generates the island. Figure 5.4 shows the α profile for the island considered in our study on the left-hand-side; on the right-hand-side a Poincaré reconstruction at a fixed toroidal angle gives an idea of the island size.

In Fig. 5.5 we have reported zooms of the poloidal Poincaré of the same island shown in red in Fig.5.4 but at four different toroidal angles. Field line tracing by ORBIT of the island magnetic surfaces is a crucial point to reconstruct the three-dimensional topology of the SH island. This is why a

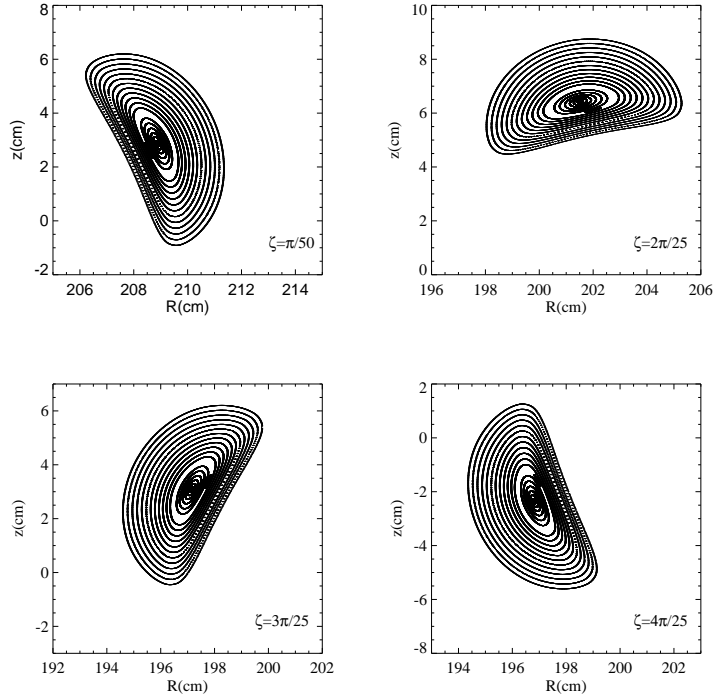


Figure 5.5: Poloidal Poincaré for the magnetic island on different toroidal sections.

new routine has been implemented in ORBIT which computes the field line tracing on a given number of poloidal section (in our case we use about 100 values of the toroidal angle ζ). At every point of the Poincaré also the corresponding equilibrium quantities are recorded. For example if (ψ_p, θ) is a Poincaré point on a poloidal surface at a given toroidal angle ζ_k , the code records: $X(\psi_p, \theta), Z(\psi_p, \theta), g(\psi_p), I(\psi_p), B^2(\psi_p, \theta), \psi(\psi_p, \theta)$. Also the value of the $\alpha(\psi_p, \theta, \zeta_k)$ perturbation at the considered point is saved. All these quantities are necessary to parametrize the helical surface of the island, as explained in the next section.

5.3 Perturbed flux ψ^M computation

In order to apply the Fick law we need to compute the perturbed magnetic flux associated with a set of nested helical surfaces inside the magnetic island. For each surface, the flux may be computed by integrating:

$$\psi^M = \int_C \mathbf{A} dl \quad (5.3)$$

where \mathbf{A} is the vector potential of the magnetic field (equilibrium and perturbation) and $d\mathbf{l}$ is an infinitesimal vector tangent to the curve C which encloses the magnetic island's surface at a given toroidal angle. The vector potential is related to the equilibrium and to the magnetic perturbation. The equilibrium magnetic field is expressed in Boozer Coordinates in terms of the poloidal magnetic flux ψ_p , and of the poloidal and toroidal Boozer angles θ and ζ , as shown in Chapter 2:

$$\mathbf{B}_0 = I\nabla\theta + g\nabla\zeta + \delta\nabla\psi_p. \quad (5.4)$$

We can compute the vector potential \mathbf{A} considering that:

$$\delta\mathbf{B} = \nabla \times (\alpha\mathbf{B}_0) = \nabla \times [\alpha g\nabla\zeta + \alpha g\nabla\zeta + \alpha\delta\nabla\psi_p] \quad (5.5)$$

and that the equilibrium magnetic field may be expressed in its contravariant form also by:

$$\mathbf{B}_0 = \nabla \times (\psi\nabla\theta - \psi_p\nabla\zeta). \quad (5.6)$$

The total magnetic field is:

$$\mathbf{B} = \mathbf{B}_0 + \delta\mathbf{B} = \nabla \times [\alpha g\nabla\zeta + \alpha g\nabla\zeta + \alpha\delta\nabla\psi_p + \psi\nabla\theta - \psi_p\nabla\zeta] \quad (5.7)$$

and therefore, from $\mathbf{B} = \nabla \times \mathbf{A}$, the vector potential is:

$$\mathbf{A} = \psi\nabla\theta - \psi_p\nabla\zeta + \alpha g\nabla\zeta + \alpha I\nabla\theta + \alpha\delta\nabla\psi_p. \quad (5.8)$$

where the small term with δ , related to the non-orthogonality of the coordinate system, has been neglected.

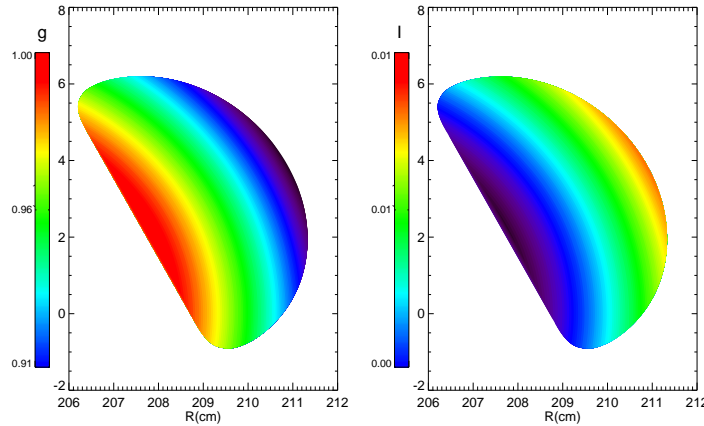


Figure 5.6: Example of the values assumed by I (l.h.s.) and g (r.h.s) inside the island on a poloidal section at a given toroidal angle.

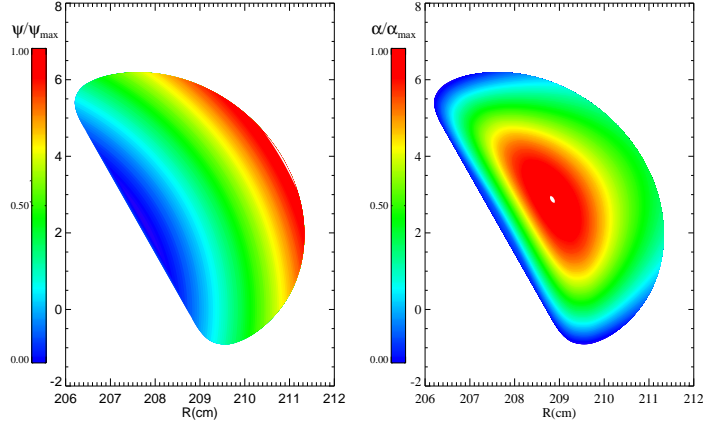


Figure 5.7: Example of the values assumed by the normalized toroidal flux $\psi/\max(\psi)$ (r.h.s.) and by the perturbation α (r.h.s.) on a poloidal section at a given toroidal angle.

As explained above, the term α contains the information about the radial profiles of the perturbations; we remind that $g(\psi_p)$ is proportional to the poloidal current outside ψ_p and $I(\psi_p)$ to the toroidal current inside ψ_p ; ψ is the toroidal flux. In figures 5.6 and 5.7 the contour of the quantities I, g, ψ and α are shown inside the island at a given toroidal angle. The contravariant representation of an infinitesimal length $d\mathbf{l}$ element on a $\zeta = \text{constant}$ surface is given by:

$$d\mathbf{l} = (d\mathbf{l} \cdot \nabla\theta) \frac{(\nabla\zeta \times \nabla\psi_p)}{J^{-1}} + (d\mathbf{l} \cdot \psi_p) \frac{(\nabla\theta \times \nabla\zeta)}{J^{-1}}. \quad (5.9)$$

Inserting 5.8 and 5.9 in 5.3 we obtain:

$$\psi^M = \int_C (\psi + \alpha I) dl_\theta \quad (5.10)$$

with $dl_\theta = d\mathbf{l} \cdot \nabla\theta$. In fact the terms in \mathbf{A} containing $\nabla\zeta$ have a zero cross product with the terms in $d\mathbf{l}$, because they are perpendicular to them.

Numerical integration of Eq. 5.10 requires the evaluation of the integrand on a set of points along a closed path C lying on a surface. This is performed when Poincaré sections are computed, but this information is not sufficient to integrate Eq. 5.10. An approximate determination of the curve C is also needed, as the set of points forming a Poincaré section is not ordered. While algorithms to order points for convex polygons are easy to implement, dealing with concave sections is not trivial: details of the method we developed are given in the following.

5.4 Helical surface reconstruction

Poincaré plots of nested magnetic surfaces have been performed at different toroidal locations ζ_k (typically $k = 1, 2, \dots, 100$). Consider now a poloidal Poincaré map at a given ζ_k , such as the one in Fig. 5.8(a). The intersection of a magnetic surface h with the ζ_k plane is an ensemble of points laying on a curve $C^{k,h}$. In Fig. 5.8(a) these are shown for different helical surfaces ($h = 1, 2$ for example). Integration of Eq. 5.10 along $C^{k,h}$ gives the enclosed total flux $\psi_{k,h}^M$ associated with the surface. The numerical integration of Eq. 5.10 requires to approximate the $C^{k,h}$ curve with a polygon $C_P^{k,h}$.

5.4.1 The polygon definition

An empirical algorithm have been developed in order to obtain such a polygon from the random set of points $x_i^{k,h}, z_i^{k,h}$ defining the Poincaré section. The algorithm assumes that the points describe a curve (not necessarily convex) and that the distance between neighboring points is much smaller than the dimensions of the Poincaré section. In our specific case (i.e. an $m = 1$ island), the relevant dimension is the radial extent of the island. In order to reconstruct the curve $C^{k,h}$, the randomly distributed points composing the Poincaré sections must be ordered according to the position along the curve. The algorithm consists in a series of estimates of a local tangent to the curve and projections of the section points along that tangent: once the neighbor is found a new estimate of the local tangent is performed and a new neighbor is determined.

The ordering procedure begins by selecting an initial point O belonging to the h -th Poincaré section in the toroidal section k for which we want to build an approximate representation of the curve $C^{k,h}$. Distance with all other points composing the Poincaré section is computed and the nearest N points are selected. In the example in Fig.5.8(b) we have used $N = 5$ and the initial point is represented by a triangle; the points closest to it are labelled by $P1, P2, \dots, P5$. The parameter N has been chosen so that the points allow a reliable determination of the local tangent. The tangent estimate is performed by a linear fit with Singular Value Decomposition (SVD, see for example Ref. [14]) of the $2 \times N$ matrix of chosen point coordinates. The eigenvector associated to the highest eigenvalue of the SVD represents the tangent vector. The initial N points are then ordered following their projections along that tangent.

Once N ordered points and a vector are defined, an iterative procedure is put in place, as follows: (i) project all remaining points along that vector;

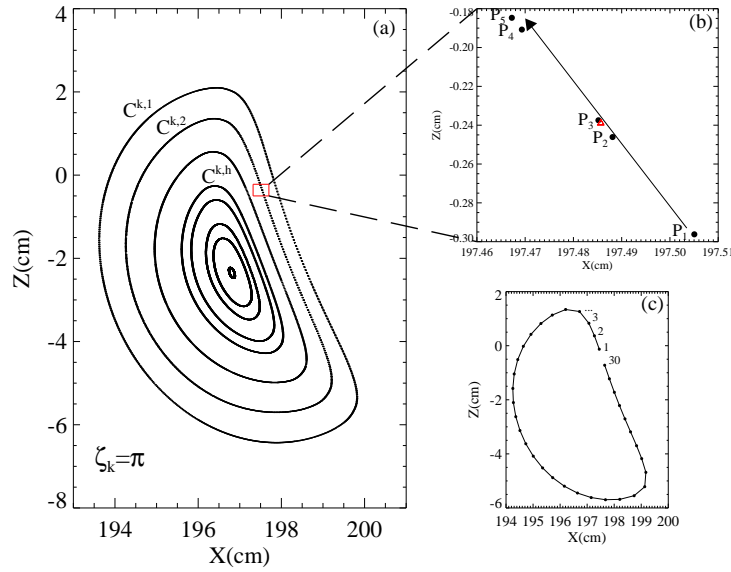


Figure 5.8: Helical surface reconstruction. (a) Poincaré maps of the island surfaces for a given value of the toroidal angle. (b) Re-ordering of the points for a selected surface of the Poincaré. Zoom of plot (a) in the selected region. (c) Re-ordered surface after the algorithm. X and Z are the usual Cartesian coordinates expressed in cm .

(*ii*) select the nearest one with positive projection; (*iii*) perform a new local tangent estimate with the new point and discard the most distant one; (*iv*) iterate the process until all points are ordered. The result does not depend on the choice of the parameter N for sufficiently regular curves. The ratio between the two eigenvalues of the SVD can be used as a figure of merit for the goodness of the choice of the parameter N : if the ratio is sufficiently high (significantly greater than 1) then the set of data is sufficiently elongated and the linear fit represents a good approximation of the local tangent. (For a discussion of SVD as a tool for total least squares fit see Ref. [69]).

A drawback of the numerical estimate of the tangent vector is that it may fail if the Poincaré section is characterized by sharp transitions (i.e. near the X-point). In order to refine this algorithm, an independent estimate of the

tangent vector would need to be performed: i.e. the projection of the magnetic field along the poloidal plane during the Poincaré plot computation should be stored. As we are considering regions around the O-point this is not an issue. Once the points of the Poincaré section are ordered, a polygon is defined by selecting 30 equally spaced points. This number has been chosen for practical reasons; we verified that increasing that number does not change significantly the numerical results. In Fig. 5.8 (c) the final result for an interpolated surface is shown.

The algorithm is then repeated for every polygon of ζ_k and at every ζ_k plane. Then, for each polygon $C_P^{h,k}$, the flux ψ^M has been computed by using Eq. 5.10. Our final goal is to obtain a numerical approximation of the $\psi^M(\psi_p, \theta)$ function. We verified, within numerical accuracy, that ψ^M is constant along the perturbed flux surface, i.e the $\psi^M(\psi_p, \theta)$ function is constant for $(\psi_p, \theta) \in C_P^{h,k}$. This corresponds to an irregular sampling of the ψ^M function on the (ψ_p, θ) space. The next step is to define a regular grid in (ψ_p, θ) and interpolate the function ψ_M on this new grid.

5.4.2 Triangulation and 2D interpolation

Up to now we have obtained a set of irregular distributed points in poloidal flux and poloidal angle for every angle ζ_k and the values assumed by the perturbed flux at these points. In order to obtain the function ψ^M splined on a regular grid we perform a triangulation procedure, followed by a 2D interpolation, using the IDL [70] routines TRIANGULATE and TRIGRID.

The TRIANGULATE procedure constructs a Delaunay triangulation of a planar set of points. We remind here that given a set V of $N \geq 0$ distinct and not all collinear points in the Euclidean space we can define a set E of $N(N-1)/2$ straightline segments (edges) between vertices in V . Two edges $e_1, e_2 \in E$, $e_1 \neq e_2$, are said to *properly intersect* if they intersect at a point other than their endpoints. A triangulation of V is a planar straight-line graph $G(V, E')$ for which E' is a maximal subset of E such that no two edges of E' properly intersect [71]. Any set of points can be triangulated and there are several ways to do it. In our case we use the *Delaunay triangulation*, which has the property that the circumcircle of any triangle in the triangulations contains no point of V in its interior. There are several efficient algorithms which are implemented in numerical codes to obtain a Delaunay triangulation for a given set of points. The code we have used follows the algorithm described in [72]. The result is a list that describes for each point the adjacent nodes in the Delaunay triangulation.

The output of the TRIANGULATE routine is given as input to perform the 2D interpolation on a new regular grid. The algorithm we have used

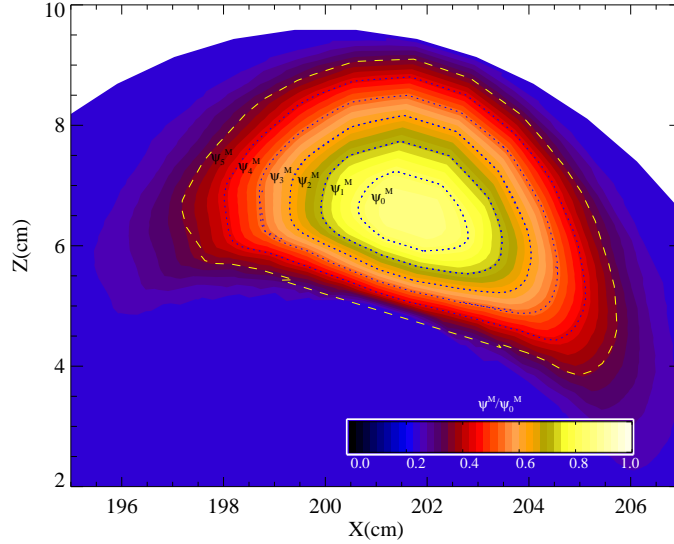


Figure 5.9: Reconstruction of the $m = 1, n = -7$ island after tracing field lines with ORBIT, triangulation and interpolation; (zoom in the island region). The island is the same as in Fig.5.8; it appears rotated because the reconstruction is performed on a different toroidal angle.

is described in [73] and implemented in the routine TRIGRID in the IDL program language. The value of the interpolated perturbed flux ψ_{int}^m at point (ψ_p, θ) in a triangle is interpolated by a bivariate fifth-degree polynomial in ψ_p and θ , i.e.:

$$\psi_{int}^M = \sum_{j=0}^5 \sum_{k=0}^{5-j} q_{jk} \psi_p^j \theta^k. \quad (5.11)$$

Note that there are 21 coefficients q_{jk} to be determined from:

- the values of the function ψ^M and its first and second order partial derivatives at each vertex of the triangle (18 independent conditions);
- the partial derivatives of the function ψ^M differentiated in the direction perpendicular to each side of the triangle which must be a polynomial of degree three, at most, in the variable measured in the direction of the side of the triangle (3 additional constraints). This last condition assures smoothness of interpolated values.

The final result is, for every poloidal section, an approximate representation of the 2D function $\psi^M(\psi_p, \theta)$ on a regularly spaced grid in ψ_p and θ ; this is represented on a section as a contour plot in Fig.5.9: constant colour lines closely correspond to the polygons $C_P^{h,k}$.

5.4.3 Linear 3D interpolation

The polygon representation is necessary for the transport simulation too: in order to determine whether a particle is inside or outside a given surface, the value of the $\psi^M(\psi_p, \theta)$ function needs in fact to be computed for an arbitrary particle coordinate flux in (ψ_p, θ, ζ) at every ζ angle. Since the mesh in the ζ variable is equally spaced by construction, a 3D-linear interpolation scheme is used. This is numerically efficient and has been implemented in the code for subsequent transport simulations, in order to determine the surface hit by a test particle at all time steps. For a given arbitrary value of the particle coordinates (ψ_p, θ, ζ) the nearest points in the regular grids are calculated $\psi_p^j, \theta^j, \zeta^j$ and the corresponding $\psi_j^M = \psi^M(\psi_p^j, \theta^j, \zeta^j)$. Once the following quantities are computed:

$$t = \frac{\psi_p - \psi_p^j}{\psi_p^{j+1} - \psi_p^j} \quad (5.12)$$

$$u = \frac{\theta - \theta^j}{\theta^{j+1} - \theta^j} \quad (5.13)$$

$$v = \frac{\zeta - \zeta^j}{\zeta^{j+1} - \zeta^j} \quad (5.14)$$

the interpolated value of the perturbed flux is given by:

$$\begin{aligned} \psi^M(\psi_p, \theta, \zeta) = & \psi^M(\psi_p^j, \theta^j, \zeta^j)(1-t)(1-u)(1-v) + \\ & \psi^M(\psi_p^{j+1}, \theta^j, \zeta^j)t(1-u)(1-v) + \psi^M(\psi_p^{j+1}, \theta^{j+1}, \zeta^j)tu(1-v) + \\ & \psi^M(\psi_p^j, \theta^{j+1}, \zeta^j)(1-t)u(1-v) + \psi^M(\psi_p^j, \theta^{j+1}, \zeta^{j+1})(1-t)uv + \\ & \psi^M(\psi_p^{j+1}, \theta^{j+1}, \zeta^{j+1})tuv + \psi^M(\psi_p^j, \theta^j, \zeta^{j+1})t(1-u)v + \\ & \psi^M(\psi_p^j, \theta^j, \zeta^{j+1})(1-t)(1-u)v. \end{aligned} \quad (5.15)$$

An example of the resulting final polyhedron that describes the helical surface inside a magnetic island is reported in Fig. 5.10 for a $(m = 1, n = -7)$ mode in RFX-mod.

5.5 Calculations of ion and electron diffusion coefficients

The knowledge of the ψ^M function is essential to study the diffusion properties of an ensemble of test particles, which are assumed to represent transport properties of the background plasma.

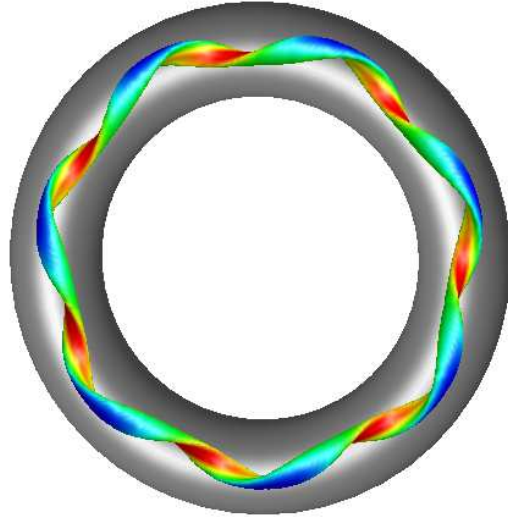


Figure 5.10: 3D reconstruction of a ($m = 1, n = -7$) helical polyhedron in RFX-mod (top-view). The colors are determined by the perturbed poloidal flux. Inner helical surfaces are red while the outer are blue.

A series of runs with 50 test particles have been performed: ions and electrons have been deposited at the island O-point with uniformly distributed pitch v_{\parallel}/v and with an energy $E_e = E_i = 250eV$. The particles are also subject to energy-conserving classical and pitch-angle collisions with a plasma background at the same temperature. For each run, the simulation was performed until stationary conditions are obtained: if a particle hits the outer boundary a new particle with random pitch is located in the island O-point. During the run, the distribution of the positions $\psi_M(\psi_{p_i}, \theta_i, \zeta_i)$ of particles is recorded and averaged with distributions recorded in previous time intervals. The simulation is stopped when the averaged test particle density distribution does not vary significantly compared to the previous step (the threshold variation is 5%).

For RFX-mod parameters the simulation time is typically 10ms for ions and 50ms for electrons. Changing the number of particles allows reducing the statistical fluctuations, and therefore the simulation time required to reach convergence condition, but it increases the CPU-time. We verified that the results do not change considerably if the number of particles is changed.

Pitch-angle and classical scattering are computed following the approach presented in section 3.8. For typical RFX-mod conditions the deflection col-

lision frequency ν_{\perp} of the test particles on a Maxwellian distribution of background particles is less than 0.3 collisions per toroidal transit.

Consider the particles flux Γ across the island; it is related to the time variation of the particle density for unit volume n_V by the continuity relation:

$$\nabla \cdot \Gamma = \frac{\partial n_V}{\partial t} \quad (5.16)$$

where no sinks and sources are present, because the total number of particles N is constant, i.e. $dN/dt = 0$. Integrate this equation over the volume V_{out} delimited by the helical surface S_{out} :

$$\int_{V_{out}} \nabla \cdot \Gamma dV = \int_{V_{out}} \frac{\partial n_V}{\partial t} dV \quad (5.17)$$

which can be written also as:

$$\int_{S_{out}} \Gamma dS_{out} = \frac{\partial}{\partial t} \int_V n_V dV. \quad (5.18)$$

by using the Gauss theorem. But the term on the righthand side is the number of total particles which leave the volume V_{out} over the time of the simulation Δt ; the left hand side of the equation can be simply written in terms of the mean flux $\langle \Gamma \rangle$. Eq. 5.18 becomes:

$$\langle \Gamma \rangle S_{out} \cong \frac{N_{lost}}{\Delta t}. \quad (5.19)$$

Now consider also the diffusion relation given by Eq. 5.2 and integrate it over the surface S_{out} which gives:

$$\langle \Gamma \rangle = -D^{\perp} \langle \nabla n_V \rangle \quad (5.20)$$

assuming a constant D^{\perp} inside the island. The stationary distributions of the number of particles $n(\psi^M)$ for the $m = 1, n = -7$ SH state, for ions with 0.2 collisions per toroidal transit, is shown in Fig. 5.11 (a): it decreases linearly from the O-point to zero in the external region of the island. Thus we can assume to model $n(\psi^M)$ in the island with the following dependence:

$$n = n_0 - \frac{n_0(\psi^M - \psi_0^M)}{(\psi_{out}^M - \psi_0^M)} \quad (5.21)$$

where ψ_0^M is the perturbed flux at the center of the island (where the number of particles is n_0) and ψ_{out}^M is the perturbed flux at the surface S_{out} (the loss surface, where we have $n = 0$ particles). Thus we have:

$$\langle \nabla n \rangle = -\frac{n_0}{(\psi_{out}^M - \psi_0^M)} \left\langle \frac{\partial \psi^M}{\partial r} \right\rangle \cong \frac{n_0}{r_{out}} \quad (5.22)$$

where r_{out} is the mean distance of the last helical surface S_{out} from the island O-point. The gradient of ∇n is related to ∇n_V by taking into account the volume of the different regions corresponding to the various beams of the distribution in Fig. 5.11-(a). In our case we have simply that:

$$\langle \nabla n_V \rangle \cong \frac{n_0}{S_0 r_0 r_{out}} \quad (5.23)$$

and $S_0 r_0$ is the volume of the first beam region with radius r_0 and helical surface of area S_0 .

The value of D^\perp can be found by using together Eq. 5.23 and Eq. 5.19:

$$D^\perp = -\frac{\langle \Gamma \rangle}{\nabla n_V} \cong \frac{N_{lost}}{S_{out} \Delta t} \frac{r_{out} r_0 S_0}{n_0} \quad (5.24)$$

which is a direct formula to compute the diffusion coefficients values in our simulations.

In this expression we can recognize a term $G = r_{out} \cdot S_0 \cdot r_0 / S_{out}$ which depends only on geometrical factors and a second $F_{run} = (\Phi / t n_0)$ dependent on the diffusion of the particles. In the cases considered here $G_{n=-7} = (1.4 \pm 0.3) \cdot 10^{-4} m^2$, while $G_{n=-8} = (2.6 \pm 0.6) \cdot 10^{-4} m^2$. Errors are mainly due to the approximations in the helical surface reconstruction.

5.6 Results: diffusion coefficients

The aforementioned technique has been applied to a series of runs with increasing collisionality. Estimates of the ion diffusion coefficient D_i^{isl} as a function of collisions per toroidal transit are shown in Fig. 5.11 (b)-(c) with a black line for the $m = 1, n = -7$ island. The numerical estimates of D_i^{isl} are comparable to the classical values calculated by the theoretical formula at high collisionality:

$$D_i^{th} = r_{Li}^2 \nu_d / 2 \quad (5.25)$$

with r_{Li} ion Larmor radius. In the RFX-mod scenario, about $0.2 coll/tran$, we find $D_i^{isl} \simeq 2 \div 7 m^2/s$ which exceeds the classical value $D_i^{th} \simeq 0.4 - 1 m^2/s$. These results hold for electrons too (Fig. 5.12). In the RFX-mod conditions $D_e^{isl} \simeq 0.01 \div 0.03 m^2/s$ slightly exceeds the classical value $D_e^{th} = 0.008 \div 0.012$. The increase of the D_i^{isl} values estimated by our simulation with respect to the classical ones given by Eq. 5.25 is a consequence of the neoclassical effects; while these are negligible in the standard axi-symmetric MH regime (as shown in Ref. [74] and [75]), they become important in the SH scenario because of the helical geometry of the system.

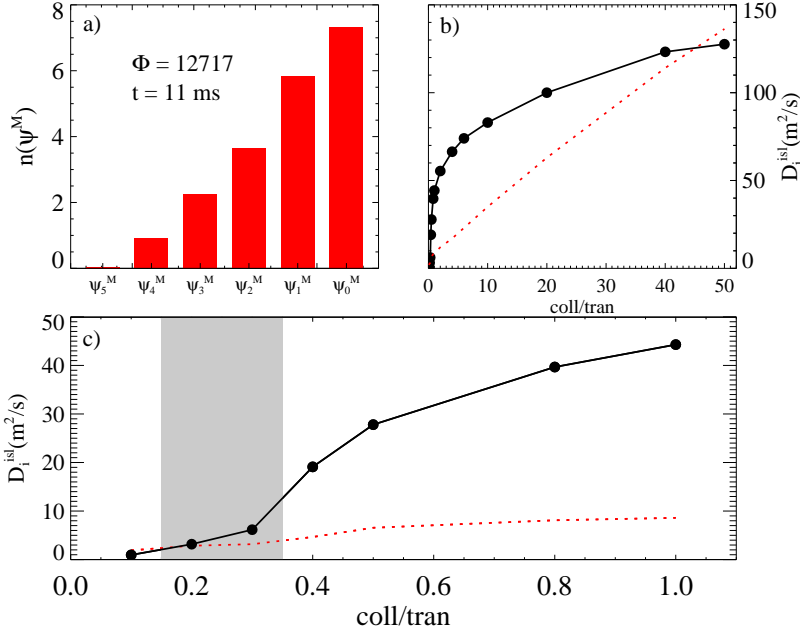


Figure 5.11: (a) Ions distribution $n(\psi^M)$ in the various ψ^M intervals for $n = -7$ mode with 0.2 collisions per toroidal transit. (b) Ion diffusion coefficient vs. collisions per toroidal transit. Smooth line: classical collisions and pitch angle scattering; dashed line: only classical collisions. (c) Zoom of plot b) in the interval between 0 and 1 collisions per toroidal transit. The shadow area represents the RFX-mod range of collisionality.

In fact, as discussed in Ref. [56], in SH regime the particles can be either poloidally or helically trapped. Poloidally trapped particles are characterized by thin banana orbits (with a radial excursion of less than 0.5 cm) and a simple toroidal drift across the island. The helically trapped particles encounter the mirror point along the helical surface after few poloidal turns and have a larger radial excursion, but remain inside the island itself. Old simulations performed by ORBIT show that for an unperturbed field the fraction of the trapped particles, initially with random pitch, is about the 30%. But when a perturbation is present, as for example in SH regime, the fraction of trapped particles almost doubles, i.e. it amounts to the 60%, a value which depends on the island width and on its helicity. In particular, the increased fraction of trapped particles is due to the helically trapped particles in a SH configuration. The number of poloidally trapped particles in fact is very close to that found in a MH axi-symmetric configuration.

In order to assess more deeply the effect of orbit topology on transport, we performed diffusion simulations with only classical scattering (dashed line in Fig. 5.11(b)-(c)), so that the pitch of particles, and therefore the orbit topology, was not changed due to collisions. We compared results with simulations with both classical and pitch angle scattering (black line). At large collision frequencies the black and the dashed curves are quite close, indicating that the pitch angle scattering becomes unimportant: in such regimes, in fact, the trajectories of ions between two collisions are so short that neoclassical effects become negligible. At low collision frequencies the pitch angle scattering significantly enhances the diffusion coefficient: this confirms the important role of neoclassical effects in the low collisionality regime for ions. As far as electrons are concerned, for all collisionality regimes considered in this scan (see Fig. 5.12) the diffusion coefficients with pitch angle scattering is almost identical to the one with classical collisions only; therefore neoclassical effects do not seem to play a significant role.

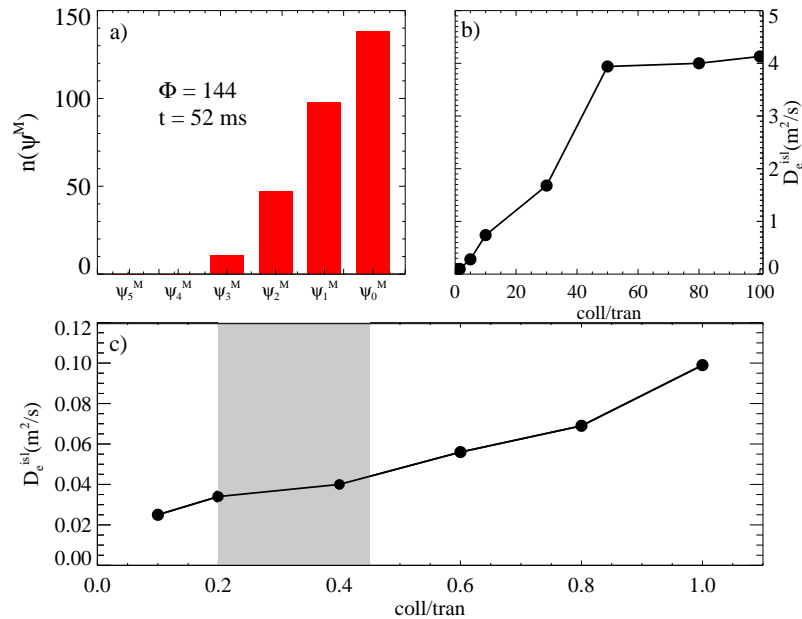


Figure 5.12: (a) Electron distribution $n(\psi^M)$ in the various ψ^M intervals for the $n = -7$ mode with 0.15 collisions per toroidal transit. (b) Electron diffusion coefficient vs collisions per toroidal transit. (c) Zoom of the plot (b) in the interval between 0 and 1 collisions per toroidal transit. The shadow area represents the RFX-mod range of collisionality.

In figure 5.13 we report the results of an analogous transport study with the magnetic island $m = 1, n = -8$; on the left-hand side the ion diffusion coefficient D_i^{isl} versus the number of collisions per toroidal transit (classical and pitch angle scattering) is shown; and on the right-hand side the electron diffusion coefficient D_e^{isl} . Focusing on RFX-mod collisionality range we find $D_i^{isl} \simeq 5 - 12m^2/s$ and $D_e^{isl} \simeq 0.1 - 0.17m^2/s$.

The study of ambipolar transport in this geometry requires the development of an approximate representation of the ambipolar potential: this requires defining a potential as a function of ψ^M and modifying the equations of motion in order to deal with such a $3D$ function. As theory predicts, we expect a value closer to the slowest species, electrons in our situation. A rough estimation of an ambipolar coefficient diffusion inside the island can be obtained by the geometric average:

$$D^{amb} = \sqrt{D_i^{isl} \cdot D_e^{isl}} \quad (5.26)$$

following the results of Ref. [56]. The final results are summarized in table 5.6 for the two islands with helicity $n = -7, -8$, in the standard RFX-mod collision range, with also the corresponding ambipolar coefficient. Note that the D^{amp} values are in the range $0.1 - 0.9m^2/s$ close to those typical of Stellarators configurations ($\simeq 0.1m^2/s$) [76] [77] with the correct scaling in collisionality. This is not surprising since the topology of the SH regime is very similar to that of a helical stellarator, even if with different length scale and plasma parameters; in both the situations the particle transport takes place in a helical structure.

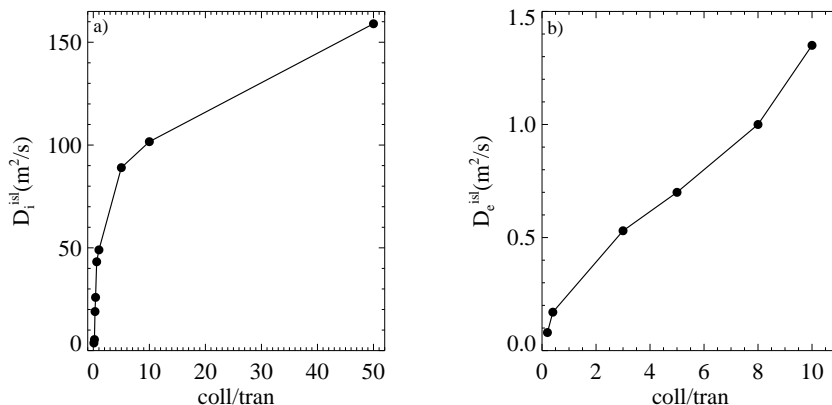


Figure 5.13: (a) Ion diffusion coefficient vs collisions per toroidal transit for the $n = -8$ mode. (b) Electron diffusion coefficient vs collisions per toroidal transit.

| | D_i^{isl} | D_e^{isl} | D^{amb} |
|----------------|------------------|-----------------------|---------------------|
| SH n=-7 | $2 \div 7m^2/s$ | $0.01 \div 0.03m^2/s$ | $0.1 \div 0.5m^2/s$ |
| SH n=-8 | $5 \div 12m^2/s$ | $0.1 \div 0.17m^2/s$ | $0.5 \div 0.9m^2/s$ |

Table 5.1: Final values of the diffusion coefficients from the ORBIT simulations in the collision range of RFX-mod. The estimate of the ambipolar transport is obtained by the geometric average of D_i^{isl} and D_e^{isl} .

Up to now the rotation of the modes has not been considered since RFX-mod is characterized by wall locked modes. It will be interesting taking into account the rotation of the modes for the other RFP experiments, even if frequencies are rather low (tens of kHz).

The cross field particle diffusion coefficients for ions and electrons $D_{i,e}^{isl}$ that we find in our simulations are at about one order of magnitude lower than the ones obtained in MH simulation in Ref. [56] and of those experimentally obtained by particle balance, $D \cong 30m^2/s$, during MH discharges in RFX, reported in Ref. [78]. It is then confirmed by our more detailed simulations that, within the magnetic islands in SH regime, transport is much lower.

The advantage of the algorithm and of the results shown in this paper is that they can be applied to QSH regimes too, for islands of similar size. In fact, near the island O-point, helical surfaces are conserved and the other modes are small in comparison with the dominant one: as the topology is very similar, also the cross field diffusion coefficient is expected to be comparable.

5.6.1 Comparison with previous studies

Even if the general difference between SH and MH remains, the more accurate results shown here differ in some aspects from the previous estimates ones reported in Ref. [56].

First of all, the former RFX experiment (described in Ref. [40]), was characterized by a different electron density. Moreover, results of the present paper more correctly estimate cross field diffusion coefficients. Electron density in RFX was about two times greater than the one typical of RFX-mod operations ($n_e \cong 2 - 3 \cdot 10^{19}m^{-3}$ for 600 – 800kA plasma currents); thus the interaction between the test particles and the background plasma (i.e. collisionality) was different. The collisionality regime, in fact, explains the difference between the estimates of the electron diffusion coefficients; by taking the same collisionality (1 collision per toroidal transit) of the previous RFX experiment we find: $D_e^{isl} = 0.1m^2/s$ to be compared with $0.09m^2/s$ in

Ref. [56].

As far as ions are concerned, the present estimate of the cross field diffusion coefficient at 1 collision per toroidal transit (i.e. the value typical of the old RFX) is $D_i^{isl} \sim 40m^2/s$, while the axi-symmetric rough estimate in Ref. [56] was $2m^2/s$: this discrepancy is due to the shape of the loss surface, which was toroidal in Ref. [56] while it is helical in the present study and to the topology of trapped ion orbits. We have, in fact, shown that in this collisionality regime, the estimate of the ion cross field diffusion coefficient is determined by pitch angle scattering. An important role may therefore be played by poloidally trapped ions: it was shown in Ref. [56] that these ions, describing thin banana orbits with negligible radial excursion, may drift out of the magnetic island in the toroidal direction. These ions, which contribute to perpendicular diffusion as they cross the magnetic island magnetic surfaces, never reach the axi-symmetric loss surface located outside the island as in Ref. [56]. Therefore the estimate in Ref. [56] neglected this class of particles, leading to a different estimate of the transport. In the present work the test particle flow is averaged over the perturbed flux surfaces and therefore it leads to a more local estimate of cross field diffusion.

CHAPTER 6

QSH regimes and fast ions in MST

In this Chapter we present magnetic topology and transport properties of thermal and fast particles in the Madison Symmetric Torus experiment for different kind of discharge operations. While the first results concern the confinement of thermal ions and electrons in QSH regimes, in the second section we shall give an explanation for the presence of fast electrons during $F \simeq 0$ shots. Finally, in the last section, we shall consider the properties of fast ions from NBI and their better confinement with respect to thermal ions in MST.

6.1 QSH regimes in the MST experiment

A picture of the experiment MST is given in Fig. 6.1. Its aspect ratio is $\simeq 3$ and its plasma current can reach values as high as $600kA$. The density of the filling gas (deuterium usually) is of the order of $\simeq 10^{19}m^{-3}$. MST is characterized by a close fitting aluminum conducting shell $5cm$ thick. The shell acts both as a vacuum chamber, magnetic flux conserver and single turn toroidal field winding. Current is driven in the shell through a transformer and a capacitor bank power supply. Toroidal and poloidal fluxes are applied through a toroidal and a poloidal gap respectively. The mechanical structure is thus much simpler than RFX-mod, the diagnostic access is easier and the magnetic field dishomogeneities are reduced.

The diagnostic system is about the same described also for RFX-mod. In



Figure 6.1: Picture of the MST experiment.

particular we shall be interested in the data from the Soft-X-Ray tomography and from the Hard-X-Ray detector. A detailed description of the Soft X-Ray tomography system in MST is available in [79].

The application of ORBIT in the MST experiment follows the same approach described in Chapter 4 for RFX-mod. The main difference is that the reconstruction of the magnetic mode profiles for MST uses the cylindrical model; moreover, due to the thickness of the shell, the radial perturbations are zero at the plasma edge.

In this section we shall discuss advanced regimes in which the magnetic chaos is reduced to low levels. This can happen in two different situations: when a QSH state appears, as the ones in RFX-mod, or when a particular method to perform the discharge is applied, called *Pulsed Poloidal Current Drive* or *PPCD*. The goal of the PPCD technique is to replace the dynamo mechanism, required in the RFP configuration. This reflects in a global reduction of the $m = 1$ instabilities which means a lower stochasticity in the magnetic field. Details on the PPCD applied to MST and its results are available in [80],[81],[82]. In the next section we give a brief description of a PPCD discharge and we shall focus on the magnetic properties of plasma in QSH and MH regimes both in standard and PPCD shots.

6.1.1 The Pulsed Poloidal Current Drive technique

In Fig. 6.2 we show three kind of discharges in MST: sustained (on the l.h.s.), decaying (central column), Pulsed Poloidal Current Drive (on the r.h.s.).

- *sustained discharge*: in this case, both the plasma current and the electron density waveforms are maintained almost constant during the flat-top phase of the shot, from 5 to 40ms. Typically quasi periodic discrete dynamo events are present in these discharges and are visible in many signals. The reversal parameter F and the pinch parameter Θ show a sawtooth-like temporal dynamic, which represents the rearrangement of the magnetic profiles during such dynamo events. The strong dynamo activity is associated to an increased level of magnetic fluctuations, as it is evident in the figure, which produces high thermal transport and a fast relaxation of the soft x-ray signal measured by a chord viewing the plasma core. While the sawtooth crash has always a turbulent MH spectrum, periods in between such discrete dynamo events can have both a MH or QSH spectrum.
 - *discharge decaying*: in these shots the current waveform is not sustained in time. The slope of the current decay can be controlled while keeping the electron density constant. During the current decay the need for dynamo is reduced, therefore the sawtooth events are almost suppressed. This produces a period in which the magnetic fluctuations don't exhibit the strong activity typical of sawtooth crashes.
 - *PPCD*: the decaying discharges are the most suitable for the application of PPCD, because the strong magnetic activity associated to sawtooth crashes doesn't interfere with its action. An example of a shot with PPCD is reported in the third column of Fig. 6.2. In MST five banks of capacitors are discharged in sequence, during the flat top of the shot (usually starting at $t = 10ms$), on the toroidal field circuit, which coincides in MST with the aluminum shell. The direction of the current pulses in the shell is such that a negative variation of the toroidal magnetic field flux is induced in the plasma. This increases the toroidal magnetic field reversal and inductively modifies the current density profile and therefore reduces the free-energy source for the tearing modes. The inductive modification of the magnetic profiles produced by the application of this technique is clearly visible in the F and Θ waveforms. Finally, the reduction of the magnetic fluctuations results in a strong transient increase of the confinement properties of
-

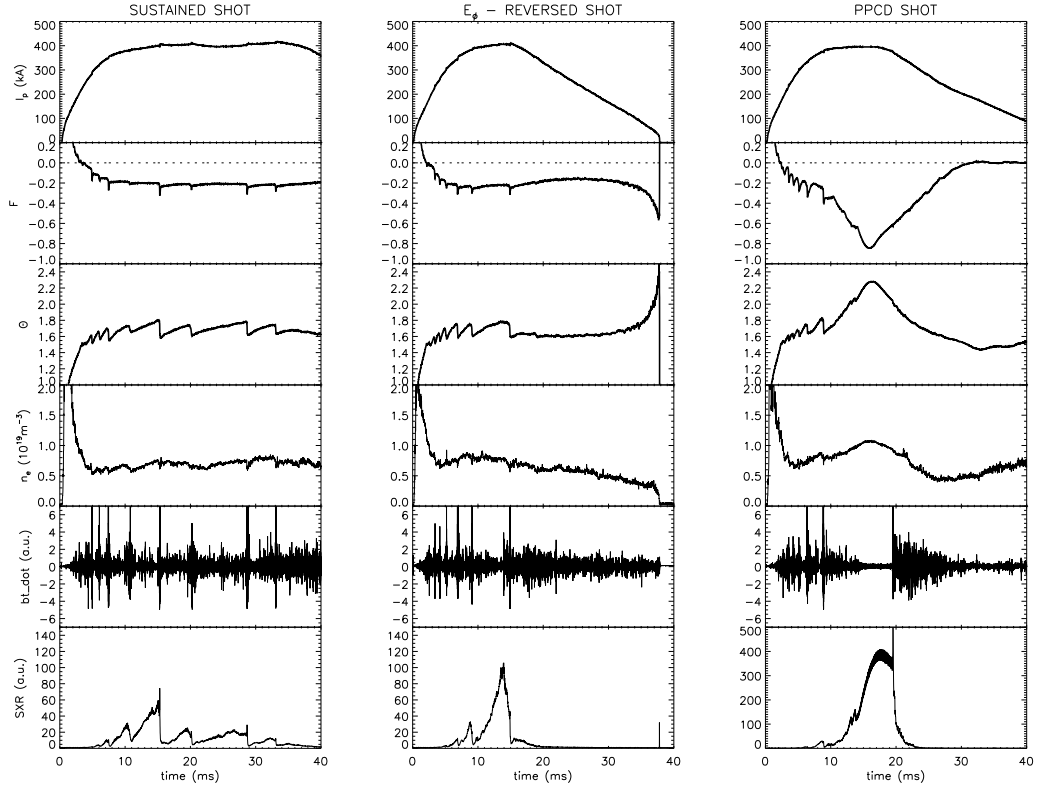


Figure 6.2: Waveforms of the plasma current I_p , reversal parameter F , pinch parameter Θ , core electron density n_e , time derivative of the toroidal magnetic field fluctuations \tilde{db}/dt , and soft x-ray brightness measured by a central chord for a sustained (first column), a decaying (second col.) and a PPCD discharges in MST (third col.).

the plasma. Electron temperatures as high as $1keV$ have been measured during these shots [83].

6.1.2 Magnetic topology in PPCD shots

By means of the ORBIT code a more quantitative analysis of the magnetic field topology during PPCD shots can be performed. In Fig. 6.3 typical safety factor profiles are shown for the MST experiment with $I_p \cong 400kA$. The black line refers to a standard shot. The first resonance from the center of the plasma is the $(1, 6)$ followed by $(1, 7)$ and $(1, 8)$ ¹; these are usually the

¹In MST a different sign convention is adopted, therefore internally resonant modes are indicated with positive toroidal number n .

highest modes in the plasma and their amplitude decreases with the toroidal number n . The red curve is the safety factor for a PPCD shot. As we have explained above, the reversal in PPCD plasma is deeper; this takes to a lower minimum also for q , which is proportional to the toroidal magnetic field.

When the PPCD is applied the magnetic spectrum may be both MH or QSH [84]. For MH PPCDs, all tearing fluctuations decay to such a low level that islands associated to more internally resonant modes are not overlapped. This is possible because lower values for the modes result in a lower width of the corresponding islands, still the size of the islands is such that they can be detected by tomography: an example is reported in the plot in Fig. 6.4. On the left-hand-side we report the tomographic inversion of the soft x-ray and on the right the reconstruction by ORBIT. The two visible islands correspond to the modes (1, 6) and (1, 7). Note that the flux surfaces around the island X-point are at least partly destroyed by a certain level of magnetic stochasticity due both to the other modes and to small overlap of the islands.

In PPCD with QSH spectrum only secondary modes decrease while the dominant grows. In these conditions a bigger (1, 6) island appears in the core of the plasma. In particular, the secondary modes reach very low amplitudes as low as $0.1mT$, almost near to the detection limit. A tomographic inversion of soft-x ray emissivity during QSH in a PPCD discharge is reported in Fig.6.5-(a), along with the ORBIT Poincaré section of the magnetic field lines at the same time instant (b). The helical non-stochastic flux surfaces are indicated with red points in the figure. Both the position, shape, dimensions

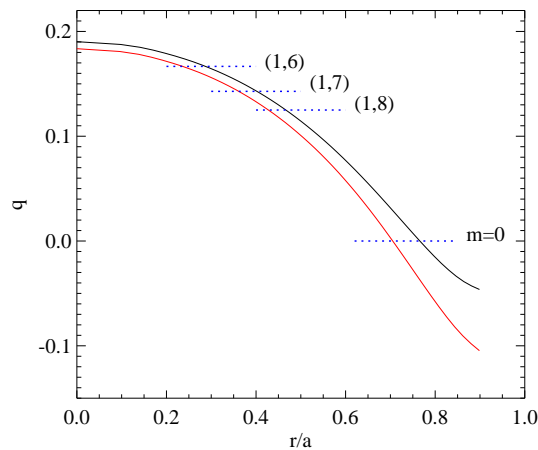


Figure 6.3: Safety factor profile in a standard (black) and in a PPCD (red) shot with the main resonance positions.

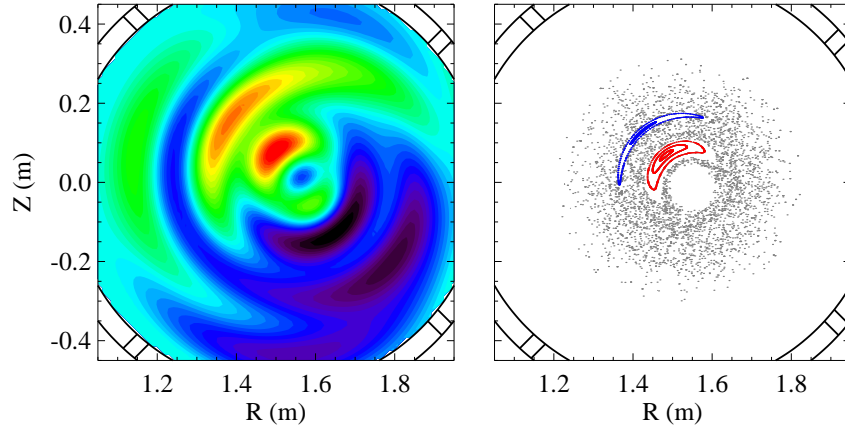


Figure 6.4: Example of an MH regime in the MST experiment where two distinct islands are visible both in the tomography inversion (l.h.s.) and on the Poincaré plot (r.h.s.).

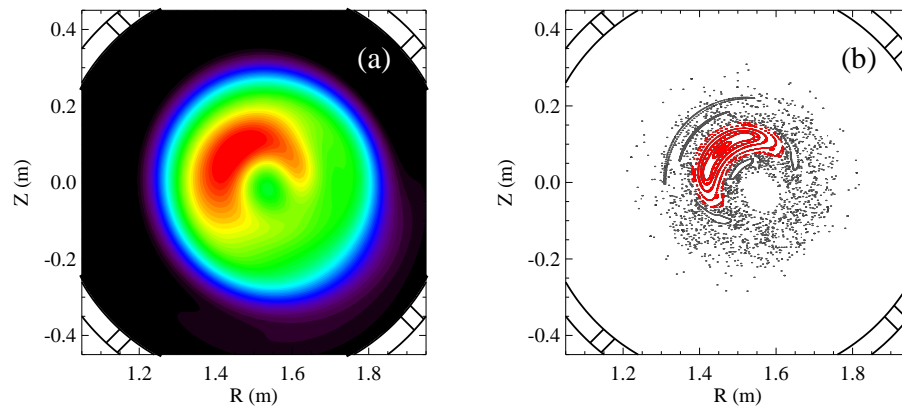


Figure 6.5: QSH regime in MST during a PPCD shot. In (a) the tomography inversion while in (b) the Poincaré plot performed by ORBIT.

of the soft x-ray island are well reproduced by the field line tracing. Magnetic chaos is present around the magnetic island, but, as for the previous MH case, the actual level of magnetic stochasticity in these plasmas is much lower than in standard conditions.

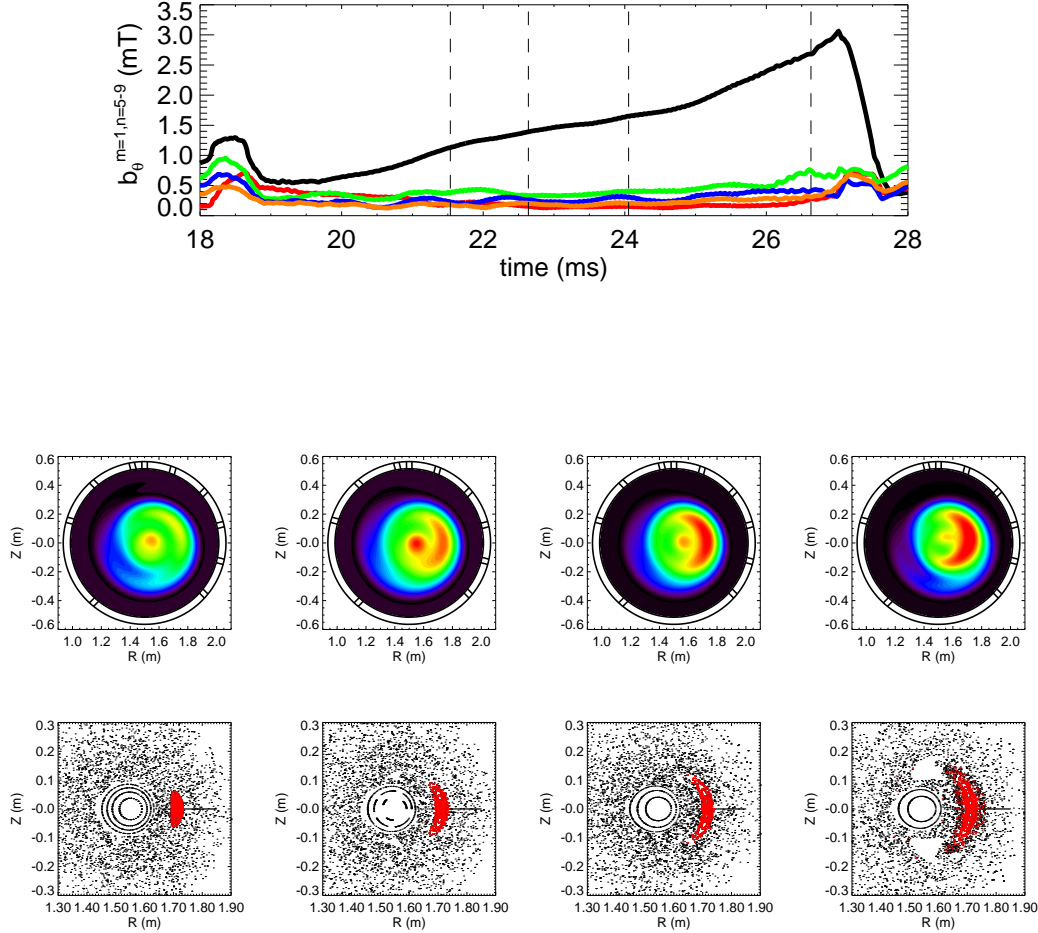


Figure 6.6: On the top: evolution of the tearing modes $m = 1, n = 6 \div 10$ during a standard discharge in QSH regime. In black the $n = 6$ mode, the others are colored. In the middle the tomographic inversions corresponding to the shaped lines of the previous plot ordered in the correct sequence increasing in time. On the bottom the Poincaré plots zoomed in a region near the island at the same times of the tomographic inversions.

6.1.3 Standard QSH in MST

Spontaneous quasi single helicity states have been observed also in standard discharges. Usually the QSH is not stationary but it grows up to the sawtooth crash. An example of time evolution is shown in Fig. 6.6. The plot on the

top shows the evolution of the modes $m = 1, n = 6$ (black), $n = 7 - 10$ (other colors) in a standard shot. From $t = 20ms$ the mode $n = 6$ starts to grow while all the others have low constant values. At the time $t = 27ms$ its amplitude is ten times bigger than the secondary modes. The shape of the magnetic structures is in good agreement with the corresponding SXR reconstructions (second and third line of Fig.6.6).

In the first temporal instant ($t \cong 21.6ms$) of the reconstructions a difference is present between the SXR inversion and the ORBIT Poincaré. The island appears in the magnetic space but not in the emission of SXR. This is probably due to the small dimensions of the magnetic island at this time, when the mode is still low .

6.1.4 Loss Times in QSH regimes

Magnetic field topology gives an incomplete view of transport. A more quantitative comparison of QSH in PPCD vs standard discharges can be performed by computing the loss time. In Fig. 6.7 on the top we report in the plane (r, θ) the magnetic island $(1, 6)$ during a PPCD shot on the left-hand-side, while on the right a QSH with the same helicity is reported for a standard discharge. In particular, the standard QSH is the same we have shown in Fig. 6.6 at the time $t = 22.7ms$.

About 30 test ions have been deposited along a fix radius at different values of the poloidal angle. In the PPCD case the deposition line was $r_{dep} \cong 12cm$ and for the standard shot $r_{dep} \cong 15cm$. Thus ions have been placed on a line passing through island O-points. For each position, when half of the ions reaches a loss surface located at $r \cong 25cm$ the ORBIT simulation is stopped and the physical run time is recorded. The same procedure is then repeated for each position. As a result we obtain a local estimates of the loss times at different coordinates of the poloidal angle θ , i.e. a qualitative estimate of the local particle transport. Final results are displayed in the same figure 6.7 on the bottom. On the left-hand-side the loss times versus the poloidal angle for the PPCD case is shown, while on the right-hand-side the same is reported for the standard QSH at different times of the shot.

These times are the ones of the reconstructions reported in Fig. 6.6: the black line corresponds to $t \cong 21.6ms$, the red to $t \cong 22.7ms$ and the green and blue respectively to $t \cong 24ms$ and $26.6ms$. It is interesting to observe that good confinement (i.e. high loss times) occurs only inside the structure. Moreover it is proportional to the island width: it varies from $\approx 1ms$ to about $3.8ms$ at the instant when the dominant mode is at its maximum. Anyway it is worth to note that the profile is very peaked around the island O-point and it decreases rapidly to low values. In fact, with the O-point centered at

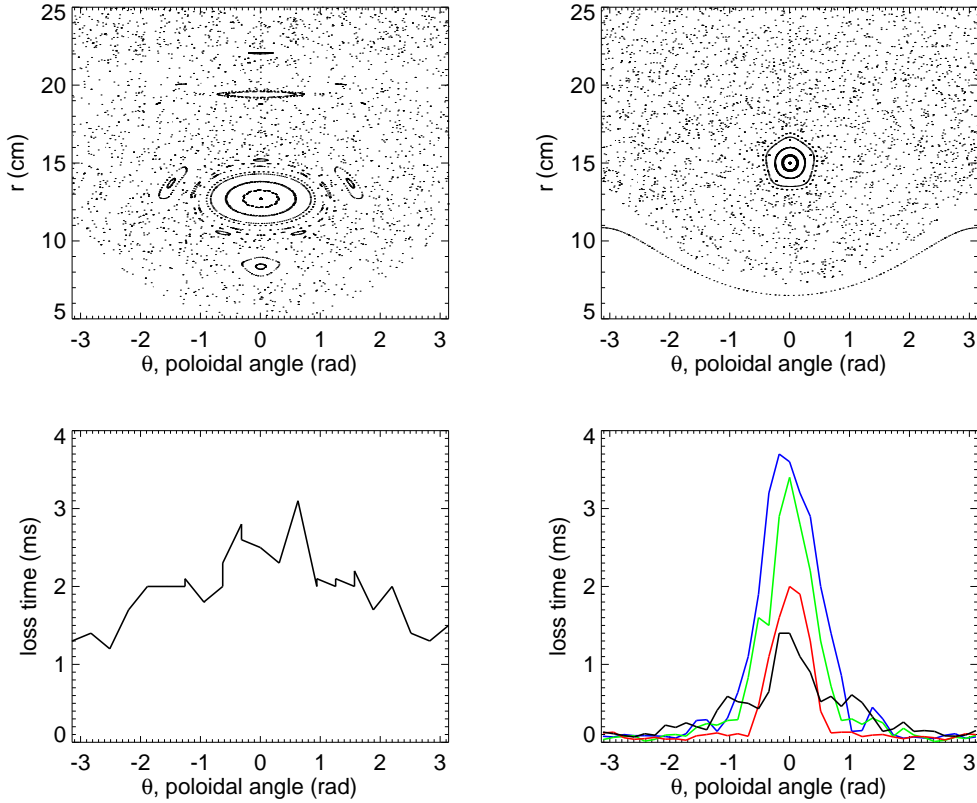


Figure 6.7: On the top: Poincaré for a QSH regime in the plane (r, θ) for a PPCD shot (l.h.s.) and for a standard discharge (r.h.s.). On the bottom the corresponding loss times profiles. The different colours of the loss times profile in the standard QSH are relative to the four instants marked in Fig. 6.6.

$\theta = 0$, a variation of $\Delta\theta \cong 1$ is enough to give a corresponding loss times ten time smaller. This is almost true for all the four times analyzed.

On the contrary, in QSH PPCD shots the loss time is rather high everywhere, even if it is higher around the O-point. In fact the loss time curve has along all the poloidal angle θ a value greater than $1ms$ and reaches a maximum in correspondence of the island O-Point. We can thus infer that a global decrease of the particles transport is present during the PPCD application. This is a direct consequence of the modes amplitude reduction due to the PPCD technique.

6.2 F=0 shot and Runaway electrons

A further proof of the enhancement confinement during PPCD shots is the detection of hard x ray (HXR) emitted by electrons with energy of hundreds of keV. This evidence suggests that *runaway electrons* are accelerated in regions of conserved flux surfaces for long times. The runaway electrons have been observed both in PPCD plasmas and in standard shots with QSH regimes. From an experimental point of view a correlation between times where a large magnetic island was present and the emission of hard-x-rays (x-rays with an energy of hundreds of keV) has been observed.

The detection of hard x-ray is performed by a multichord array of CdZnTe detectors implemented in MST sensitive to HXR in the range $10 - 300\text{keV}$ [85]. Most of the detectors are placed along a radial array of thin aluminum windows, and others on any available ports. The data is digitized at 10MHz and fitting routines are used to separate x-ray signals from noise. The processes data provides the time, the energy, the radial position of each x-ray detected with an excellent time and energy resolution.

We consider only standard shots with a QSH regime characterized by a reversal parameter F close to zero and a plasma current of $I_p \simeq 400\text{kA}$. In these plasmas the q profile is higher than usual and the first resonant mode is the $(1, 5)$. We report a typical case where the HXR have been detected in Fig. 6.8: the amplitudes b_ϕ of the tearing modes $(1, 5), (1, 6), (1, 7)$ at the wall have been plotted in black, red and blue respectively. The yellow bars on the figure correspond to periods in which hard-x-rays have been detected with the energy reported. It is worth noting that the HXR flux is measured when the mode $(1, 5)$ is much higher than the others, i.e. when a QSH state appears. The HXR flux is correlated to the presence of conserved flux surfaces, determined with the ORBIT code.

We report some examples of Poincaré reconstruction in Fig. 6.9. At the time $t = 31.5\text{ms}$ the mode $n = 5$ is higher than the secondary modes and HXRs are detected with an energy of about 10keV . The toroidal Poincaré at this time in the panel (a) shows that a conserved structure with $n = 5$ helicity is present. After few ms , at $t = 33.935\text{ms}$, the mode $(1, 5)$ decreases and the secondary modes are higher. No HXRs are detected at this time and the corresponding Poincaré in (b) shows that the magnetic topology is chaotic. The same behavior appears at $t = 41.6\text{ms}$ and $t = 45.2\text{ms}$: at this latter time the secondary modes increase and the emission of HXRs breaks down. The corresponding Poincaré in (c) and (d) shows this transition from QSH to MH. Note from the plot in 6.8 that higher energies of HXRs correspond to longer QSH periods between events when the secondary modes suddenly

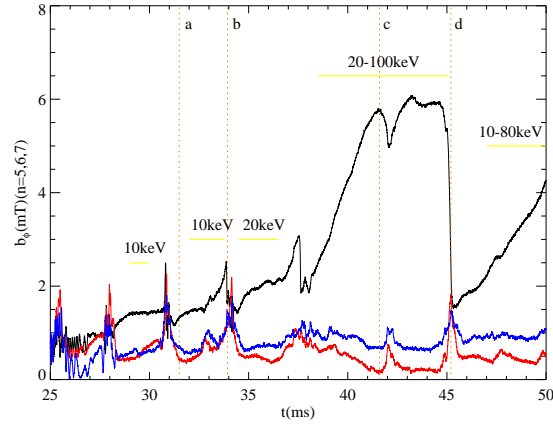


Figure 6.8: Evolution of the modes $m = 1, n = 5$ (black), $m = 1, n = 6$ (red) and $m = 1, n = 7$ (blue) during F=0 discharges where HXR have been detected. The periods where the HXR are emitted are marked with a horizontal yellow line with also their energy in keV. At the times (a),(b),(c),(d), marked with vertical orange lines, the Poincaré reconstructions have been performed and reported in Fig.6.9.

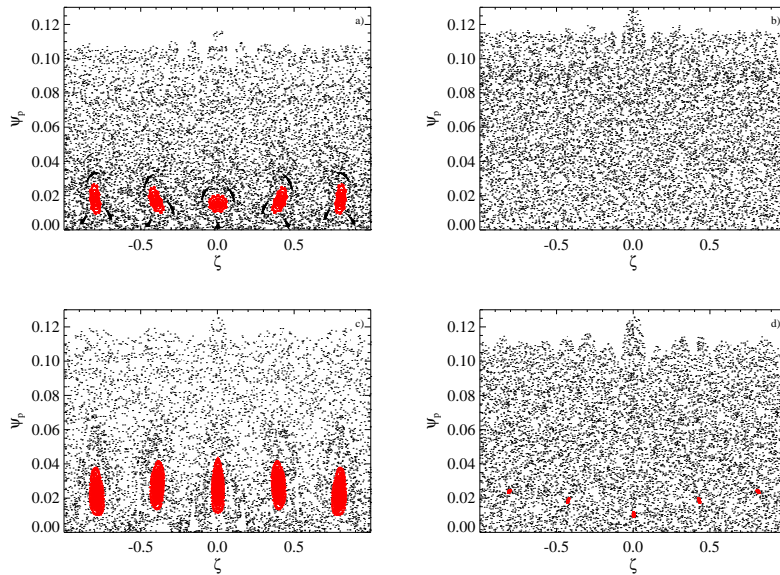


Figure 6.9: Reconstruction of the magnetic field at the times (a),(b),(c),(d) of figure 6.8.

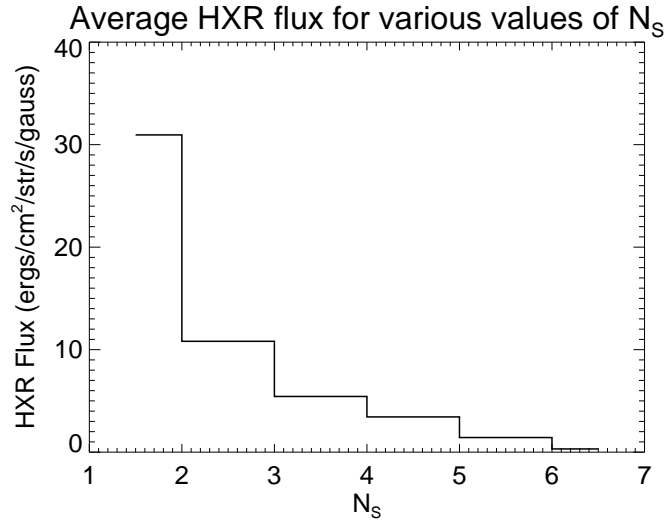


Figure 6.10: Average flux of HXRs versus the N_s parameter. QSH states correspond to lower values of N_s . We remind that low N_s corresponds to better QSH regimes (dominant \gg secondary modes).

grow. The same behavior holds also for the others times of the shot and for many discharges analyzed.

The correlation between the QSH regimes and the presence of HXR has been quantified experimentally by considering the HXR flux versus the N_s parameter. Fig. 6.10 clearly shows that the highest HXR fluxes are obtained at the lowest values of N_s , i.e. at the purest QSH. In summary, during QSH regime, conserved magnetic surfaces exist over which electrons can be accelerated for sufficient long times and reach the runaway energy. This means that these very fast electrons are generated in regions close to the island position.

6.2.1 The inductive electric field in ORBIT

To verify this hypothesis we have used the code ORBIT and performed transport simulations, as described in the following. In principles, a complete simulation of electron dynamics would require numerical simulations with a time-dependent equilibrium, the time evolution of magnetic modes and an inductive electric field. We simplify this situation by considering a fixed equilibrium and a constant spectrum of the tearing instabilities, but implementing in the equations of motion a term which represents an inductive potential.

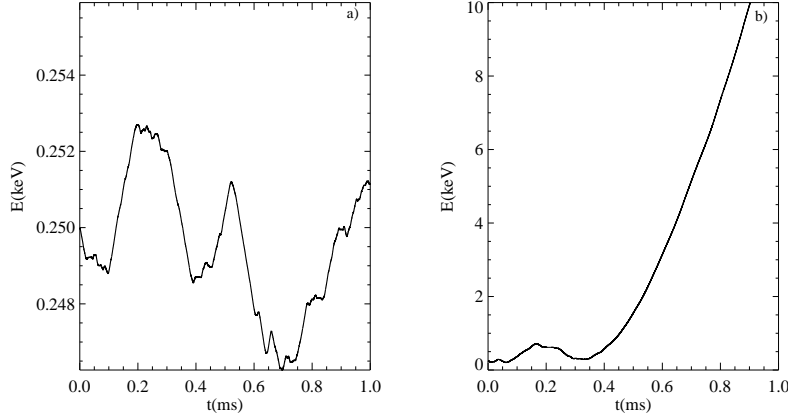


Figure 6.11: (a) Variation of the energy for a particle with a potential applied lower than the Dreicer electric field. (b) Increase of the energy when an high electric field is considered.

These assumptions are experimentally verified. In fact, consider the equilibrium of Fig. 6.9-(c) corresponding to a QSH scenario where HXR's are emitted. This is the Poincaré in a time during the period from 40ms to 45ms of Fig. 6.8: in this interval the equilibrium is almost unchanged and also the amplitude of the modes as it is clear from the plot.

Before modifying the code, a rough estimate of the minimum electric field necessary to have runaway electrons has been performed as follows. The problem was first discussed by Dreicer in [86] and [30]. It is shown that the acceleration of electrons to high energy is possible when the following relation between the plasma Debye length and the applied electric field E holds:

$$E \geq 0.214 \frac{e\Lambda}{4\pi\epsilon_0\lambda_D^2}; \quad (6.1)$$

Λ is the already mentioned Coulomb logarithm (for fusion plasma is of the order of $15 \div 17$) and λ_D is the Debye length which inversely depends on the background electron temperature T_e (see also section 1.3). For typical fusion plasmas the previous expression simplifies to:

$$E \geq \frac{700 \div 800}{T_e}. \quad (6.2)$$

Eq. 6.1 is inferred by the motion equation of an electron subjected to an external electric field and to a frictional force $F_{fr}^{e/i}$ due to collisions:

$$m \frac{dv_0}{dt} = eE + F_{fr}^{e/i} = e \left[E - \frac{e\Lambda G(\nu)}{\lambda_D^2} \right] \quad (6.3)$$

where G is the Chandrasekhar function (see [30] for details) which depends on the electron-background collision frequency and it is about 0.214 in our case. Given equation 6.2 and the MST loop voltage (about $1V/m$) we see that the induction voltage may be high enough to accelerate a sufficient number of electrons.

The implementation in the ORBIT equations of motion is obtained by adding a potential derivative term as follows:

$$\frac{\partial\Phi}{\partial\zeta} = \tilde{E} \neq 0, \quad \frac{\partial\Phi}{\partial\theta} = 0, \quad \frac{\partial\Phi}{\partial\psi_p} = 0. \quad (6.4)$$

By Eqs. 6.4 a non zero constant electric field is generated along ζ which simulates the inductive field applied that drives the plasma current. This modification of the equations of motion has an important consequence: energy is not conserved anymore and therefore the numeric scheme cannot rely on energy conservation for determining the integration time step. A simpler scheme with a time step inversely proportional to the velocity has been developed in order to keep the numerical accuracy. The value \tilde{E} to be given as input to Eq. 6.4 with the correct normalizations in the code is adjusted in such a way that the kinetic energy $K = \frac{1}{2}mv^2$ of a particle with mass m under only the applied electric field action E varies of a quantity $\Delta K = E \cdot 2\pi R_0$ after one toroidal transit. Thus a normalization constant \tilde{E}/E is found between the real electric field E and the ORBIT input \tilde{E} .

By varying the electric field in the code we have found the critical Dreicer electric field for different electron temperature background and thus different collision regimes. This is performed by finding the electric field necessary to accelerate without limit a large fraction of test electrons ($> 50\%$) in the MST magnetic equilibrium. An example of a runaway electron by ORBIT is shown in Fig. 6.11-(b). While in (a) the applied potential is not enough to win the frictional force of collisions, in (b), on the contrary, from $t = 0.2ms$ the energy monotonically increases. The collisions mechanisms are the ones described in section 3.8: pitch angle scattering and slowing down; we neglected the classical scattering being almost negligible in the interaction between fast particles and the plasma background. The number of collisions for toroidal transit versus the electron temperature is reported in Fig. 6.12-(a). In (b) the critical electric field E_c to obtain runaway electrons as function of the temperature T_e is shown, for the MST equilibrium considered, without perturbations. Note that this curve follows the relation:

$$E_c = \frac{783}{T_e^{1.12}} \quad (6.5)$$

in a good agreement with the theoretical formula 6.2. In the shots we are considering, the electron background temperature is of the order of $300eV$

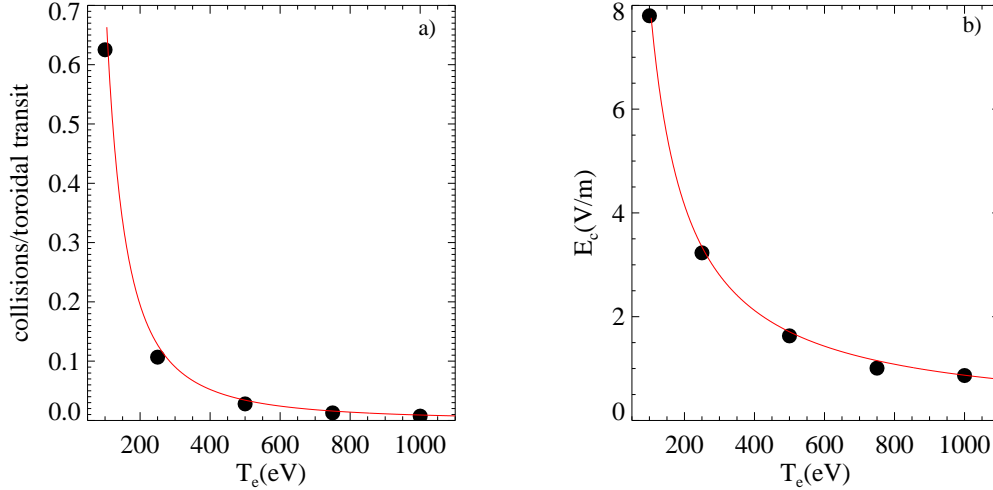


Figure 6.12: (a) Collision for toroidal transit as function of the electron temperature background. (b) Critical Dreicer electric field for the equilibrium of MST considered with $F = 0$ at several T_e .

which means a critical field of about $1.5 - 2V/m$ in MST. This value is just slightly higher than the inductive potential applied to the plasma (about $1V/m$). A consistent fraction of electrons can be accelerated if good surfaces are present in the plasma.

6.2.2 Numerical transport simulations by ORBIT

We have performed numerical simulation with a potential of $1V/m$ and an electron background temperature of $300eV$. Two thousand test electrons are initially deposited inside the magnetic island ($\psi_p/\psi_w \simeq 0.1$), almost uniformly in pitch angle and in the poloidal angle. Collisions are implemented with the correct frequency (about $\simeq 0.1$ collisions for toroidal transit). Collisions have both the effect to change the pitch of the test electrons and to decrease their energy. The effect of the applied electric field E instead is, on the contrary, to increase the energy of the electrons and to align their velocity with the field but in the opposite direction because of the electrons negative charge. The simulation lasts for $2ms$, a period of time comparable to the longer QSH period observed in the type of discharge reported in Fig.6.8.

In Fig. 6.13-(a) we show the final electron energy distribution: most of the electrons have an energy ranging up to $50keV$ but a long tail up to hundreds

of keV is clearly visible. Collisions and secondary modes remove part of the electrons out of the island, as it can be seen by the radial distribution shown in panel (b). In fact, the final distribution in poloidal flux shows a peak of electrons that are still near their initial position (i.e. $\psi_p/\psi_w \simeq 0.05 - 0.025$), but a significant fraction has diffused away. The electric field tends to align the final pitch angle distribution as shown in panel (c): most of the electrons have a velocity at 180° with respect to the magnetic field, which in the central region (where $B^\phi \gg B^\theta$) means in the toroidal direction but opposite to the applied field. The most energetic electrons are concentrated inside the island. This is shown in (d) where the angular positions, ζ and θ , of the final electrons are reported. The red colored points represent those electrons with

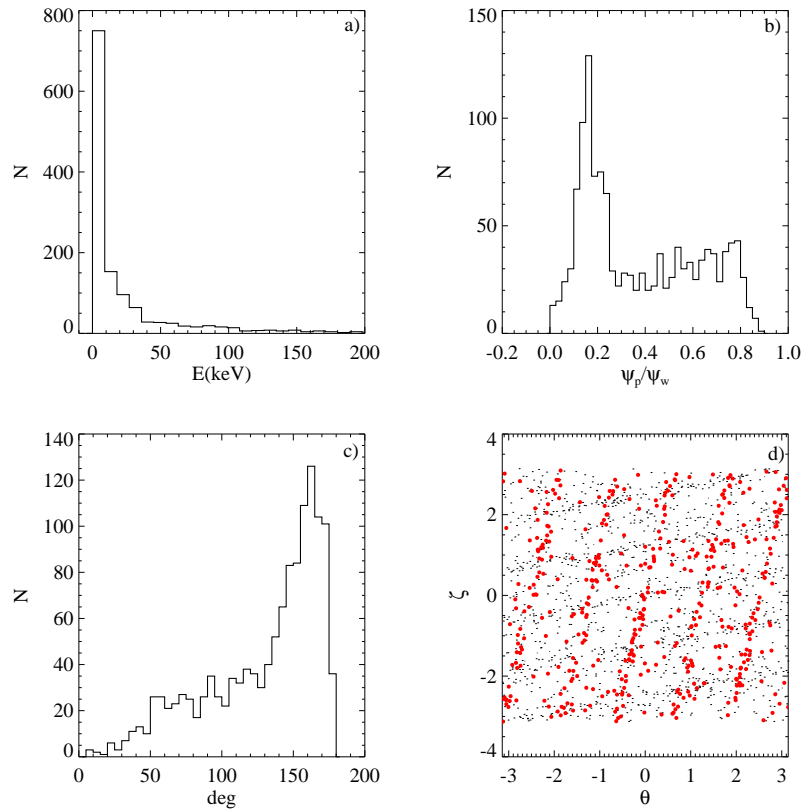


Figure 6.13: (a) Final distribution of electrons energy. (b) Final position of the electrons poloidal flux. A peak is located in the magnetic island region. (c) Final pitch angle in degrees distribution. (d) Final angular position of the electrons. In red: the electrons with higher energy (> 30 keV).

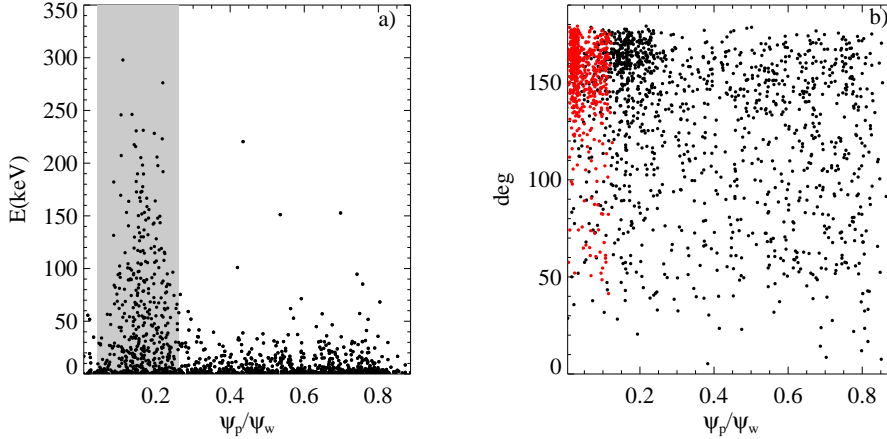


Figure 6.14: (a) Final energy versus final poloidal flux. The shaded area corresponds to the island extension in poloidal flux. (b) Final pitch angle versus poloidal flux. In red the electrons with energy greater than 30keV .

an energy greater than 30keV , which clearly shows a $n = 5$ character, i.e. they are inside the magnetic island. We conclude that the runaway electrons are mostly generated inside the good surfaces of the QSH regimes.

Such a result is confirmed by the plot in Fig. 6.14-(a) where the energy is reported as function of the poloidal flux position. The shaded region corresponds to the magnetic island. The correlation between high energy and the island position is clear. Few points with hundreds of keV lie also outside this area and represent electrons which have been pulled out from the island just before the end of the run. Panel (b) shows the correlation between the pitch angle in degrees and the electrons position: again, the most energetic electrons, in red, are those in the island region and with velocity in the toroidal direction.

When the same simulations are performed in MH, i.e. without conserved flux surfaces, the electrons are accelerated to energies not greater than few keV consistently with the observation that not HXR are observed.

6.3 Fast ions from NBI in MST: experiment and simulation by ORBIT

Fast ion studies have a great importance for fusion experiments. For example, the dynamic of the 3.5MeV α particles by fusion reactions will strongly

affect the confinement in the future reactors. But also in the tokamak devices exiting today, fast ions from NBI or RF heating lost from the plasma represent high outward energetic fluxes which may seriously damage the wall. Moreover, interaction between magnetic perturbations and an high energy ion population can lead to a significant fraction of losses in a very short time, which means a lower heating efficiency and confinement.

A different behavior has been observed from NBI in RFP experiments. In MST, in fact, fast ion confinement is measured via decay of deuterium-deuterium fusion $2.5MeV$ neutrons following a short pulse of an atomic deuterium beam injected into the deuterium plasma. This technique was successfully applied for fast ion confinement studies in tokamak [87], spherical tori [88], helical systems [89], and mirrors machines.

6.3.1 Experimental results

The RFP configuration introduces the new element of the magnetic stochasticity of the field. In fact, the measurements are performed in standard RFP plasmas, i.e. in a MH regime with a particle confinement time of about $1ms$ [90]. For these experiments the plasma current is $I_p = 400kA$, central plasma density $n_e = 1.2 \times 10^{19}m^{-3}$ and the central electron temperature $T_e = 400eV$.

The scheme of the NBI system for MST is displayed in Fig. 6.15. A short pulse ($1.3ms$) of deuterium atoms is injected at an energy of $20keV$ approximately at the equatorial plane, tangential to the magnetic axis, and parallel to the toroidal plasma current. The neutrons flux is measured with a plastic scintillator coupled with a photomultiplier tube, both shielded from hard x rays by 5cm thick lead, and placed near the MST vacuum vessel.

The flux of neutrons increases during beam injection, from the buildup of fast ions. This is shown in Fig. 6.16. Thereafter it slowly decays in several ms. The shaded area corresponds to the NBI duration. The confinement time has been computed in [92] assuming slowing down of ions by classical Coulomb collisions. The curve which fits the experimental neutron flux corresponds to a fast ions confinement time of $20ms$ well above the $1ms$ measured for thermal particles. This immunity of fast ions to field stochasticity agrees with the computation of particle orbits in RFP stochastic field as shown by the code RIO used in [92].

We performed similar simulations with ORBIT and we compared them with an analytical theory that will be described in Chapter 8. Following the method described in [92] we have performed Poincaré plots for the magnetic field line topology and for the fast ions motion.

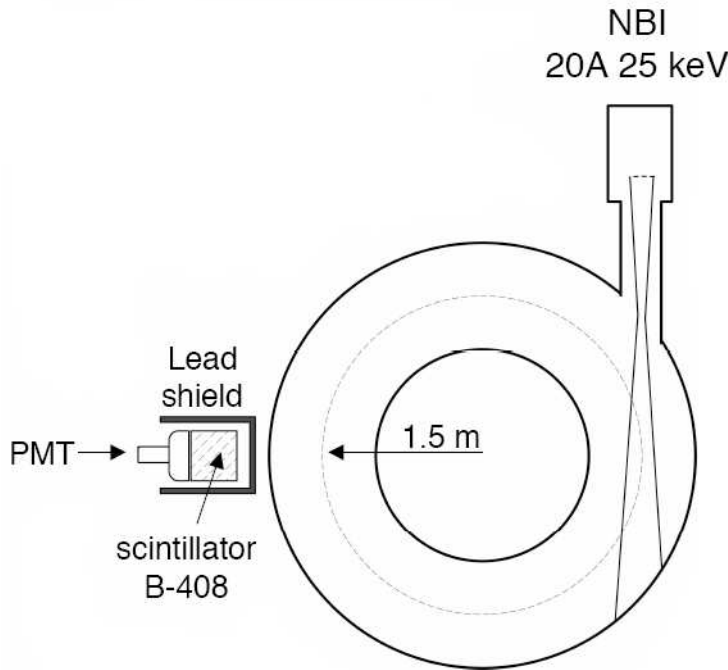


Figure 6.15: The NBI scheme in the MST configuration. On the left the diagnostic for the detection of the neutron from $d - d$ fusion reactions. Figure taken from [91].

6.3.2 Fast ion phase space

During the experiments the magnetic field topology is usually chaotic as it happens in MH states. This is reported in Fig. 6.17 on the left-hand-side. We have performed the same Poincaré by considering, instead of low energy particle with velocity parallel to the magnetic field, a population of fast ion with energy $20keV$ and pitch $\lambda = 1$. The motion of this class of particles is different with respect to magnetic field lines, because ions drift away from field lines. Due to the high energy the drift is particularly significant, as explained in general in Chapter 1 and in Chapter 3 for passing particles. The final Poincaré for $20keV$ deuterons is shown in Fig.6.17 on the right. We observe that in this fast ion phase space an island with helicity $(1, 5)$ appears with conserved surfaces (red points). A fast ion with pitch 1 deposited within these islands remains confined inside indefinitely in collisionless regimes. The phase space structure changes if different energies and pitches are considered. In the limit of zero energy, the phase space corresponds to magnetic field lines, as shown in Fig.6.17.

In order to understand the occurrence of the $n = 5$ structure, even if the field is not resonant, we computed the *effective field* safety factor profile $\tilde{q} = d\zeta/d\theta$. For low energy particles this is simple the safety factor q since they follow the wrapping of the magnetic field lines. We have thus performed single particle runs by ORBIT for fast ions initially placed at different position along the minor radius. During the simulation the coordinates (ζ, θ) of the particles are recorded and a mean value of \tilde{q} along the radius is calculated. We report these values in the plot of Fig.6.18 with a red curve. For a comparison we report also the standard safety factor for the magnetic field lines in black.

A similar computation was reported also in [92] where the quantity $(rv_\phi)/(R_0v_\theta)$ was calculated for the fast ion; v_ϕ and v_θ are the toroidal and poloidal velocity respectively of the guiding center fast ions. As $v_\phi = R_0\dot{\zeta}$ and $v_\theta = r\dot{\theta}$ this corresponds to \tilde{q} , i.e. the wrapping of the fast ion motion.

The increase of the safety factor for the fast ions is such that the resonance $(1, 5)$ appears (blue line in Fig. 6.18). This resonance is not present in the magnetic field space, where the safety factor is below 0.19. The appearance of this new resonance in the fast ion q profile is responsible of the formation of the island in the Poincaré of Fig. 6.17 on the right-hand-side and of the subsequent increase of the confinement time.

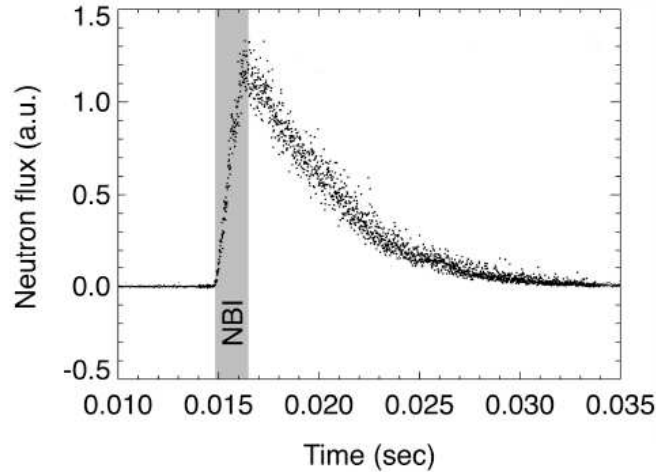


Figure 6.16: Neutron flux from MST after a short NBI pulse. The dashed zone corresponds to the NBI pulse duration. The decay of the signal lasts for a time proportional to the fast ion confinement. In the case of thermal particles the signal would have finished already at 0.016 s (on the x-axis). Figure taken from [91].

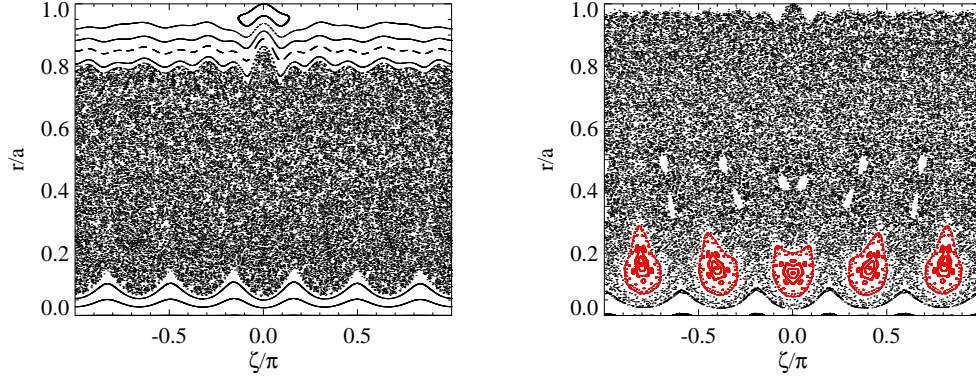


Figure 6.17: On the left-hand-side: Poincaré for the magnetic field in a MH scenario. On the right-hand-side: fast ion phase space, an island (1, 5) is visible (in red)

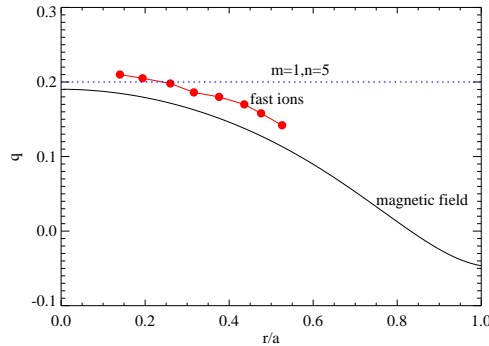


Figure 6.18: Standard safety factor q (in black) and fast ions effective \tilde{q} in red. The blue dashed line corresponds to the resonance (1, 5)

The computation of \tilde{q} and of the appearance of the resonance justifies the presence of the (1, 5) island, but it is always based on numerical simulations. We postpone the explanation of such a behavior in Chapter 8 where the drift effects of the non-uniformity and of the curvature of the magnetic field will be analytically described.

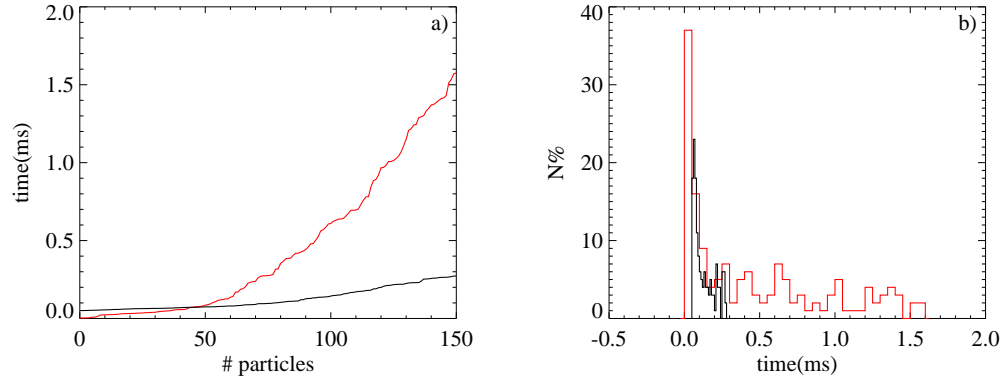


Figure 6.19: MH regime: (a) Loss times for the lost particles in a transport simulation: in red the curve related to the fast ions, in black that of the thermal ones. (b) Loss time distribution of thermal (black) and fast ions (red).

6.3.3 Thermal and fast ion loss times

While useful to understand the modified phase space topology in which fast ions move, analysis of pitch 1 particles does not give direct informations on transport, since ions from NBI has several values of pitch. Transport needs to be estimated by analyzing losses of a population of ions with a uniform pitch distribution. The fast ions have been deposited in a region near the core of the plasma with the beam energy $E = 20\text{keV}$. The poloidal and toroidal angles are random. When half of the test ions reach the loss flux surface placed at $r/a = 0.7$ the run is stopped. For each of the lost ions we record the time taken to reach the loss surface. Both pitch angle and classical scattering are included in the simulation with the correct collisions frequency reported in section 3.8. The results are shown in Fig.6.19. In (a) we have reported the loss time both for thermal (black line) and fast ions (red line). Half of the thermal particles are lost only after 0.3ms , while the fast ions run lasts for more than 1.5ms , i.e. more than a factor 5 higher. In (b) of the same figure we show also the loss time distribution for thermal (black) and fast (red) ions. While a peak of prompt losses occurs almost immediately, the fast ion distribution is characterized by a longer tail. We expect that when the modes have smaller amplitude, as in QSH cases, the fast ion confinement time increases. We do not have experimental data on this but predictions may be given by ORBIT simulation.

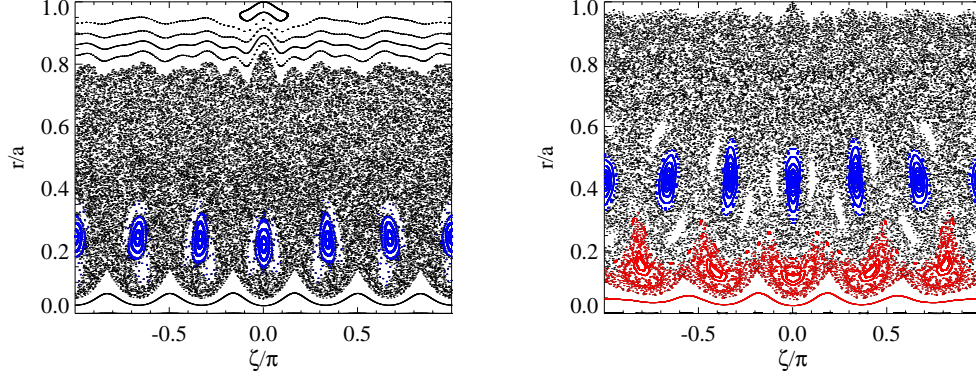


Figure 6.20: On the left: Poincaré for the magnetic field in a QSH scenario. In blue the magnetic island (1,6). On the right: fast ion phase space, both the island (1,5) and (1,6) are present.

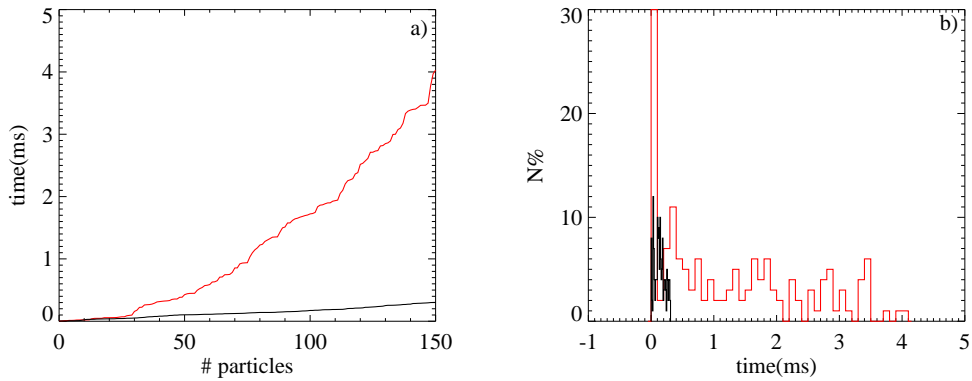


Figure 6.21: QSH regime: (a) Loss times for the lost particles in a transport simulation: in red the curve related to the fast ions, in black that of the thermal ones. (b) Loss time distribution of thermal (black) and fast ions (red).

6.3.4 Fast ion in QSH regime

We have considered the case of similar shots with $I_p = 400kA$ but in a QSH regime with a magnetic island (1,6). The Poincaré of the magnetic field is shown in the left-hand-side of Fig.6.20. In blue we have colored the

conserved surfaces for the island (1, 6). If the same plot is performed for fast $20keV$ ions as test particles with pitch 1 we find the Poincaré on the right of the figure. The island (1, 6) in the fast ion phase space is shifted outward, and the new island (1, 5) appears as in the MH case. The new position of the (1, 6) structures agrees with the fast ion safety factor reported in Fig. 6.18 in red. Since this curve is enhanced with respect to the q for the magnetic field (black) the position of the (1, 6) resonance is at a outer radial location.

The islands generated in the fast ion phase space contribute to create a wide region of lower stochasticity. Moreover in QSH the secondary are still of a reduced amplitudes with respect to standard RFP multiple helicity regimes. Performing the same transport simulations of the previous paragraph for the MH case we find a further improvement of the loss times. This is shown in Fig. 6.21-(a) and (b). The maximum loss time for the QSH situation is of $4ms$ (red curve) for fast ions and of $0.4ms$ for thermal particles (black curve).

CHAPTER 7

Fast Ions in ASDEX-Upgrade

In Tokamaks, fast ions dynamic is different compared to RFPs. In particular the role of magnetic perturbations is opposite: their presence actually increases losses. In this Chapter we describe recent measurements performed in ASDEX-Upgrade and we model the losses with a test particles approach. Even if only one perturbation is present, phase space orbits are stochastic, as will be illustrated in the following.

In section 7.1 an introduction to ASDEX-Upgrade [93], to its NBI system and to the detector which measures the fast ion losses, is given. The experimental data are discussed in section 7.2 while in 7.3 – 7.4 the results of numerical simulations in circular cross section approximation are presented (published in [94]). The ripple effect and the real D-shaped geometry of the plasma are taken into account in 7.5 – 7.6. Finally, in 7.7 – 7.8 we show how the amount of losses depends on the radial shape of the magnetic perturbation and on its rotation.

7.1 The experiment ASDEX-Upgrade

The tokamak fusion experiment ASDEX-Upgrade (AUG) is operated by the Max-Planck-Institut für Plasmaphysik in Garching, Germany. The ASDEX-Upgrade design is based on the successful operation of the Axial Symmetric Divertor EXperiment (ASDEX) and on conceptual studies for a next step

fusion reactor, in particular the need for an elongated plasma shape. This is an essential prerequisite for the contribution of AUG to the discussion of physical issues arising during the design of ITER.

AUG has divertor target plates which collect the impurities of the plasma. In ASDEX the divertor coils were inside the vacuum vessel close to the plasma but in AUG they have been adapted to meet the technical requirements of a fusion reactor. The poloidal magnetic field coils, which are a prerequisite to form the elongated plasma shape with an X-point, have to be outside the toroidal magnetic field coils in a fusion reactor. As a consequence the divertor chambers are no longer separated from the plasma vessel by narrow slits but are widely open. This results in an increase of the plasma volume, and in turn of the plasma current, by a factor of 3 with respect to ASDEX. In Fig.7.1 a scheme of the AUG poloidal cross section with the separatrix and the divertor plates is shown.

The major radius of AUG is $R_0 = 1.65m$ while the minor radii measure $0.8m$ and $0.5m$. The maximum value achievable for the plasma current is $I_p = 1.6MA$ and for the toroidal magnetic field $3.9T$. The typical discharges duration are less than 10s. Other details on AUG parameters and on its performance are available in [93].

7.1.1 The NBI system in ASDEX

The NBI system of AUG consists of two beam lines. Each beam line is equipped with four ion sources. The sources of the first beam line are operated at $55keV$ for hydrogen (H^0) and $60keV$ for deuterium (D^0) respectively. The sources of the second beam line operate at $70keV$ for hydrogen and $100keV$ for deuterium. A total power of $14MW$ H^0 and $20MW$ D^0 can be injected in the AUG torus. As we have reported at the end of Chapter 1, also in ASDEX, not only hydrogen or deuterium are created in the ion source, but the hydrogen or deuterium molecular ions too ($H_2^+, H_3^+, D_2^+, D_3^+$) with half and one third of the acceleration energy.

A top view scheme of the NBI system is shown in Fig. 7.2 where both injectors are depicted with the corresponding injection geometry of both the radial and the tangential beam lines. In the analysis performed in this Chapter we shall consider the fast deuterons with an energy of about $93keV$, i.e those coming from the NBI source 2. Their distribution in the plasma after the ionization is simulated by the code FAFNER [96] which provides the birth location, the energy and the pitch angle for a sample population of ions (typically $30000 \div 100000$). These are the initial conditions we will assume in our simulations. Plasma temperatures and densities are defined to be constant on flux surfaces and the interaction between the thermal

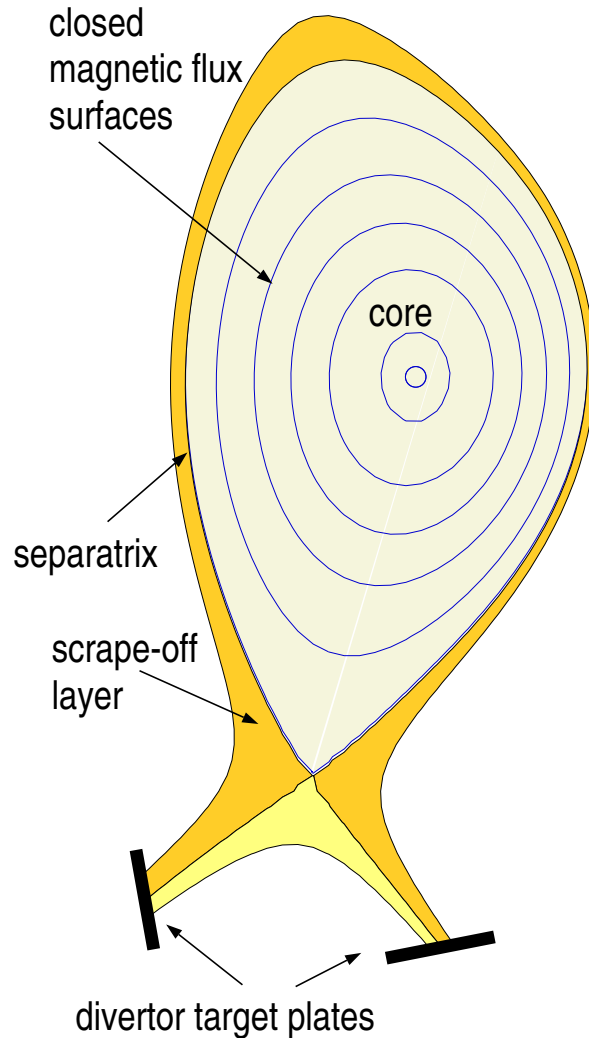


Figure 7.1: Scheme of the poloidal cross section of AUG. The position of the divertor plates and of the separatrix are shown.

background and the fast ions are the key elements which determine collisions and the ionization pattern.

These fast ions can escape the plasma in a very short time because of the high energy drift, the ripple and the collisions with the background. An increase of the losses is observed when a magnetic perturbation is present in the plasma [94] [97]. The amount of losses is correlated with the magnetic instability; moreover, the pitch distribution is not uniform.

The aim of additional heating is to transport the beam energy to the bulk plasma. Thus, losses that occur on time scales shorter than the slowing down are a limit in heating and current drive efficiency. Therefore the measure-

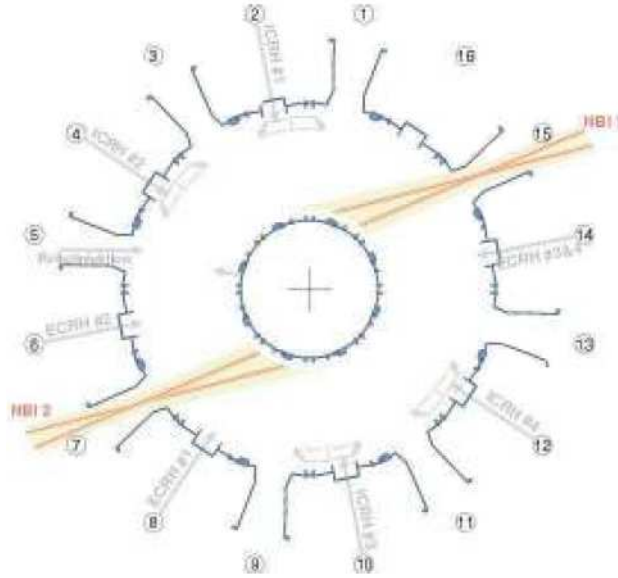


Figure 7.2: Toroidal position of the NBI system in ASDEX-Upgrade. Figure taken from [95].

ment and the modeling of such fast losses is important to understand and eventually to optimize the NBI physics. Recently a Fast Ion Loss Detector (FILD) has been installed and operated, as it will be described in the next section.

7.1.2 The FILD detector

The FILD acts as a magnetic spectrometer, dispersing the fast ions that reach the entrance slit onto a scintillator. The strike point depends on their gyroradius and pitch angle; in fact, as the detectors are located on different scintillator positions, only the flux of ions with selected pitch and energy is measured. The design is based on the concept α -particle detector used for the first time in TFTR [98] and more recently in W7-AS [99]. The detector head is composed by a 3-dimensional ion collimator, a stainless steel plate coated with the scintillator powder and a graphite cup.

A schematic view of the detector is shown in Fig. 7.3. The gyroradius of the particle orbit determines how far from the aperture the particle will strike the scintillator. On the other hand the displacement of the strike point in the orthogonal direction is determined by the pitch angle. The present geometry enables the detection of particles with gyroradius up to 120mm and angles between ions velocity and the magnetic field in the range $30^\circ < \theta < 87^\circ$. The first limit of this range corresponds to passing ions while the latter to deeply

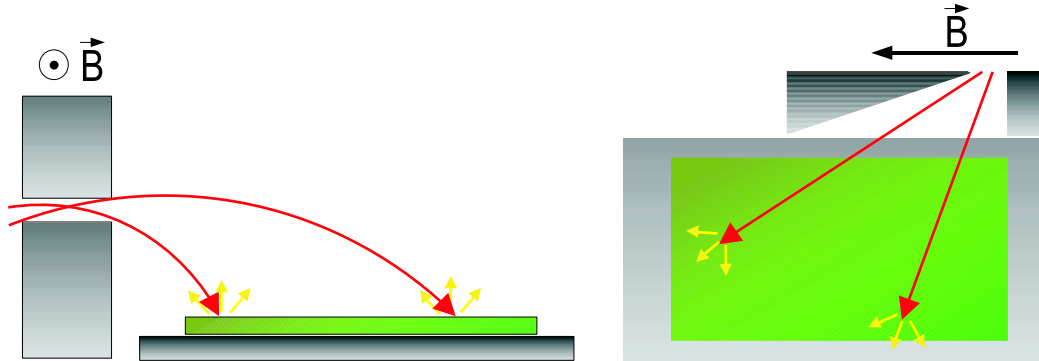


Figure 7.3: A scheme of the top and side view of collimator operation principle, including two fast ion orbits. The gyroradius of the particle determines how far from the aperture it will strike the scintillator. The pitch angle determines where the ions strike the scintillator along the orthogonal dimension. Figure taken from [95].

trapped particles.

The scintillator plate can be inserted by means of a movable manipulator up to a few mm behind the limiter slightly above the mid-plane. The scintillating surface, stroke by the fast ions entering the detector, is observed by a CCD camera, which provides a slow but highly spatially resolved image and by an array of 20 photomultipliers which are characterized by a bandwidth of $1MHz$ and therefore provide a very high time resolution.

The detector response has been modeled numerically using the codes GOURDON [100] and EfiDesign [101] allowing the generation of a mapping between locations on the scintillator and the gyroradius and pitch angles of particles that can hit there.

The experiments discussed here have been performed in plasmas with toroidal current $I_p = 0.8MA$, $B_t = 2T$, safety factor $q_{95} \simeq 4.5$ and NBI as heating particles source. Losses are always detected even when no perturbation is present. When magnetic instabilities are present losses increase but not at all energies and pitch angles. We shall show below some example of signals from the FILD. First, we present the type of instabilities we will consider, i.e. the Neoclassical Tearing Modes.

7.1.3 Neoclassical Tearing Modes

Neoclassical Tearing Modes or NTMs belong to the class of the tearing instabilities which arise in the plasma because of its non negligible resistivity. We have already introduced the main features of the general tearing modes in

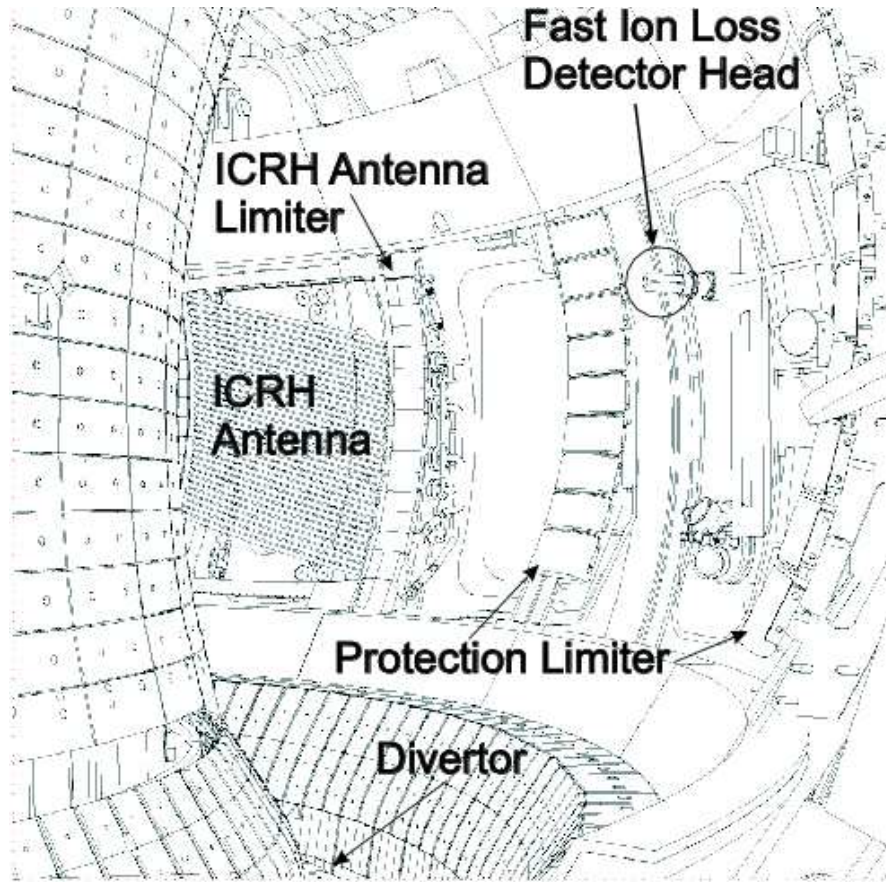


Figure 7.4: An internal view of ASDEX with the ICRH heating systems, the divertor, the protection limiter and the position of the FILD.

Chapter 1: the main effect is the formation of magnetic island with a center, called O-Point, and the point where the field lines cross, the X-point. Like in the RFP, these islands are generated at the resonance radii of the safety factor profile.

The term *neoclassical* refers to a type of tearing modes in which trapped particles play an important role for their destabilization. In fact, in a toroidally confined plasma, because of the density gradient, more trapped particles exist in the inner part than in the outer part of a banana orbit. In a poloidal cross section this results in a net current in the positive poloidal (counterclockwise) direction. However, the trapped particles have their main velocity component in the toroidal direction resulting in a nearly toroidal current, the so called *bootstrap current*, which is directly proportional to the total pressure gradient [19]. When the magnetic reconnection process of the tearing modes allows a local flattening of the pressure profile, a helical hole in the

bootstrap current arises. In these situations the modes are defined as NTMs.

Neoclassical Tearing Modes are the most common types of resistive instabilities in high β tokamak plasmas. They are responsible for confinement degradation of the plasma since they enhance the radial outward transport. Their mode structure is conventionally defined in terms of the dominant Fourier component of the island where m is the poloidal mode number and n is the toroidal mode number, like for the RFP in the previous Chapters. The typical helicity for these modes in AUG are $(m, n) = (2, 1)$ and $(m, n) = (3, 2)$ around the resonance surfaces $q = 2$ and $q = 1.5$ respectively. The $(3, 2)$ NTMs can lead to a confinement degradation of 10 – 30% while the $(2, 1)$ can lead to a confinement degradation of 40 – 50% and often even to disruptive termination of the discharge at low q_{95} .

7.2 Fast Ion Losses: experimental evidences

Time traces of the total NBI power and the magnetic fluctuations due to the $(2, 1)$ and the $(3, 2)$ NTM for a typical discharge (#21089) are shown in the middle of Fig.7.5. An NBI power ramp in the period 1 – 2s excites the $(2, 1)$ NTM which changes strongly in frequency and resonant location during the NBI modulation phase in the period 2 – 3s. Between $t = 3s$ and $t = 5s$ the mode reaches a plateau phase in which it maintains constant its main features i.e. frequency, resonant location and amplitude. This phase has been selected to study the properties of the $(2, 1)$ NTM induced fast ion loss and its dependence on the mode amplitude.

In order to identify the lost particles in phase space we analyze the loss pattern recorded by the CCD camera during the MHD activity. On top, Fig.7.5 shows a CCD frame for the discharge #21089 at $t = 4.03s$, when the NTM is present; $(2, 1)$ NTM induced fast ions together with the prompt losses generated by three different NBI sources are visible. The more radially injected ions (sources #3 and #5) appear in the region of higher pitch angle ($70 - 75^\circ$) while a tangential source (#7) produces losses in a lower pitch angle region ($50 - 60^\circ$). The pitch angle is defined here as $\text{acos}(\lambda)$ with $\lambda = \mathbf{v} \cdot \mathbf{B}/(vB)$, i.e. is the angle between the fast ion velocity \mathbf{v} and the magnetic field \mathbf{B} .

The $(2, 1)$ NTM contribution to the fast ion loss pattern shows a pitch angle selective character with two main components. First, a loss of fast ions appears only when the $(2, 1)$ NTM is present in the phase space region corresponding to pitch angles $35 - 45^\circ$ and to the NBI main injection energy, as reported in Fig.7.5. In addition, the prompt losses pattern due to the NBI sources #5 and #7 shows a broader energy distribution, when the NTM is

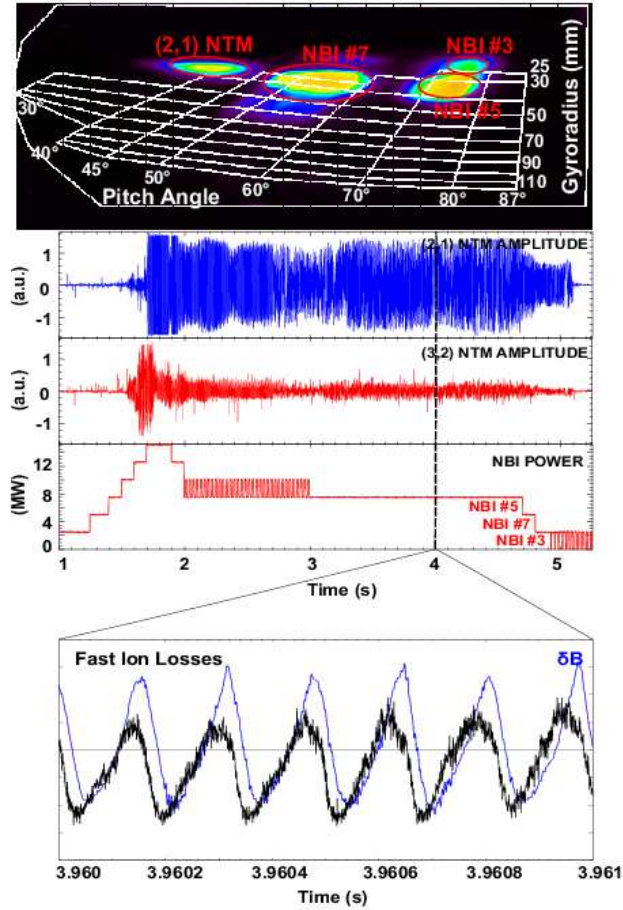


Figure 7.5: AUG discharge #21089: CCD showing the three spots produced by the first orbit losses from NBI sources #3,#5,#7 and (2,1) NTM induced fast ion losses. On the bottom: the magnetic activity is shown by the Odd-n and Even-n magnetic pick up coils signals together with the total NBI power. The lock-phase between the (2,1) magnetic perturbation amplitude $\delta B(t)$ and the signal from the FILD is also shown. Data from [95].

present, which ranges from the 93keV injection energy down to the minimum measurable energy (60keV).

Fig. 7.5 shows the magnetic activity present in the discharge by means of the Odd-N and Even-N magnetic signals together with the total NBI power. The figure shows that the oscillations of the magnetics and of the FILD channel are well correlated. To quantify the amount of lost particles due to the NTM magnetic perturbation and to separate those from the common NBI prompt losses, a Fast Fourier Transformation (FFT) was applied to the

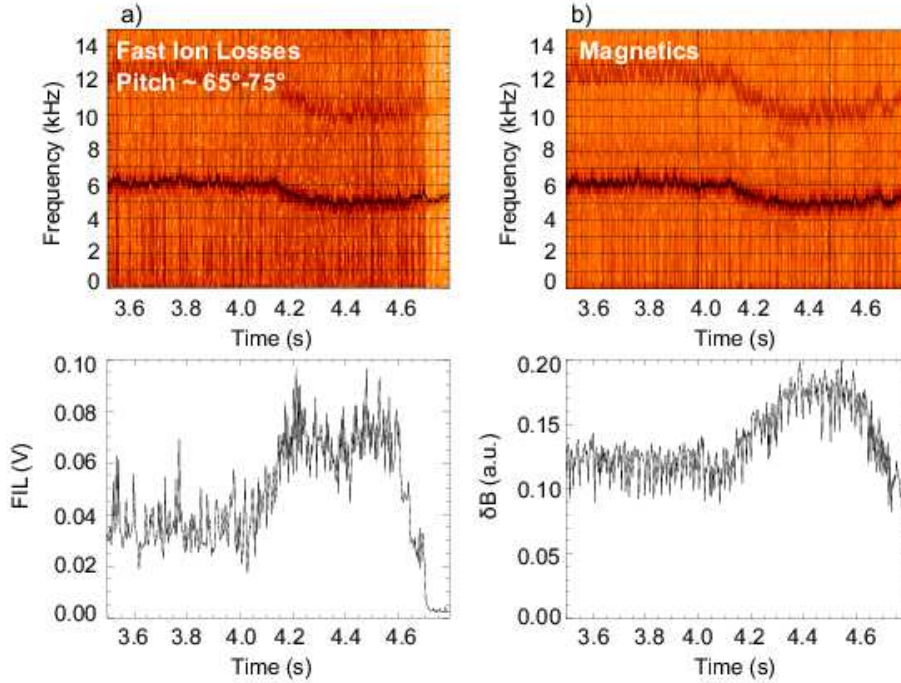


Figure 7.6: AUG discharge #21089: Amplitude analysis of the (2,1) magnetic perturbation $\delta B(t)$ and their corresponding fast ion losses at a pitch angle $65^\circ - 75^\circ$ and gyroradii of 40mm . Data from [95].

signal of the photomultipliers which cover the phase space regions where NTM induced losses are observed, Fig. 7.6-(a).

The same FFT was also applied to the magnetic perturbation recorded by the Mirnov coils, Fig.7.6-(b). We observe a correlation between the frequency and phase of the mode and those of the losses. Tracking the main frequency of magnetic perturbation and of the ion losses we find, in general, a strong correlation between the NTM amplitude and the energetic particle loss signal.

The intermittent operation of NBI sources, with a switch-on time shorter than $50\mu\text{s}$, has been used to provide a periodically changing source of fast particles which helps to study the loss time scales. In discharge #21168, the NBI source #8 (which is injecting rather radially deuterium ions at 93keV) has been modulated with square pulses of 2.5MW amplitude, on top of a constant background of 5MW . In this discharge, a large (2,1) magnetic island is the responsible for the fast ion losses. A detailed analysis of the loss time scales reveals a different behavior depending on the pitch angles of the lost ions. The losses of deuterons with energies $E \simeq 93\text{keV}$ and rather parallel velocities (i.e. pitch angles $\simeq 35 - 45^\circ$), injected by the modulated beam,

closely follow both the time evolution of their source and the mode evolution. Fig.7.7-(a) shows the spectrogram of the FILD channel #7 corresponding to $E \simeq 93keV$ and pitch angle $\simeq 35 - 45^\circ$.

Besides the slow trend following the frequency evolution of the mode and of its harmonics, the scintillator displays a signal in other locations. The intensity of the signal in such spots is modulated. As shown in bottom of Fig.7.7-(b), the amplitude of the losses at the dominant mode frequency (black curve) is modulated according to the NBI evolution (red curve) and its envelope follows the amplitude of the magnetic mode (blue curve). Looking more closely into an individual NBI square pulse, Fig. 7.7-(b), we observe that the losses recorded by the FILD channel #7 promptly decay as soon as the modulated source is switched-off, thus indicating a time scale for these losses not larger than a few tens of μs . The FILD channel #9, which corresponds to lost particles with $E \simeq 93keV$ and pitch angles $\simeq 70 - 75^\circ$ shows different features. While the modulation pattern is still recognizable, after the beam switch-off there is a tail in the loss signal, corresponding to a time scale of the order of few ms for this kind of particles. Both signals show a strong correlation between the amount of fast ion losses and the amplitude of the magnetic perturbation.

The absolute amount of lost ions has been estimated taking into account the photomultiplier signals and the number of photons produced by each incident ion in the scintillator plate (ionoluminescence). The typical lost ion flux varies from $4 \cdot 10^{13} Ions/(cm^2s)$ for the NTM prompt losses up to $10^{14} Ions/(cm^2s)$ for the lost ions with higher pitch angle. Both signals are of the same order as the maximal NBI prompt loss signal, $4 \cdot 10^{14} Ions/(cm^2s)$.

7.3 Orbits stochasticity as mechanism for losses

The experimental findings of the previous section are discussed in the framework of a mechanism which involves drift islands in the fast ion orbit space [102]. In this and the next section we present an interpretation of the experimental results in a approximated circular version of AUG.

A single magnetic perturbation like the (2, 1) NTM produces an island chain in the magnetic field. These magnetic islands do not cause significant ergodicity of magnetic field lines for the amplitudes observed here. The situation for fast particles is different: the coupling between the fast particles guiding center motion in the perturbed magnetic field and the orbit shift, due to the high energy drifts (which have a (1, 0) character), results in a several chain of drift islands with helicities (2, 1), (1, 1), (3, 1), (4, 1) in fast particle phase space. Depending on the shape of the q profile, on the energy of the

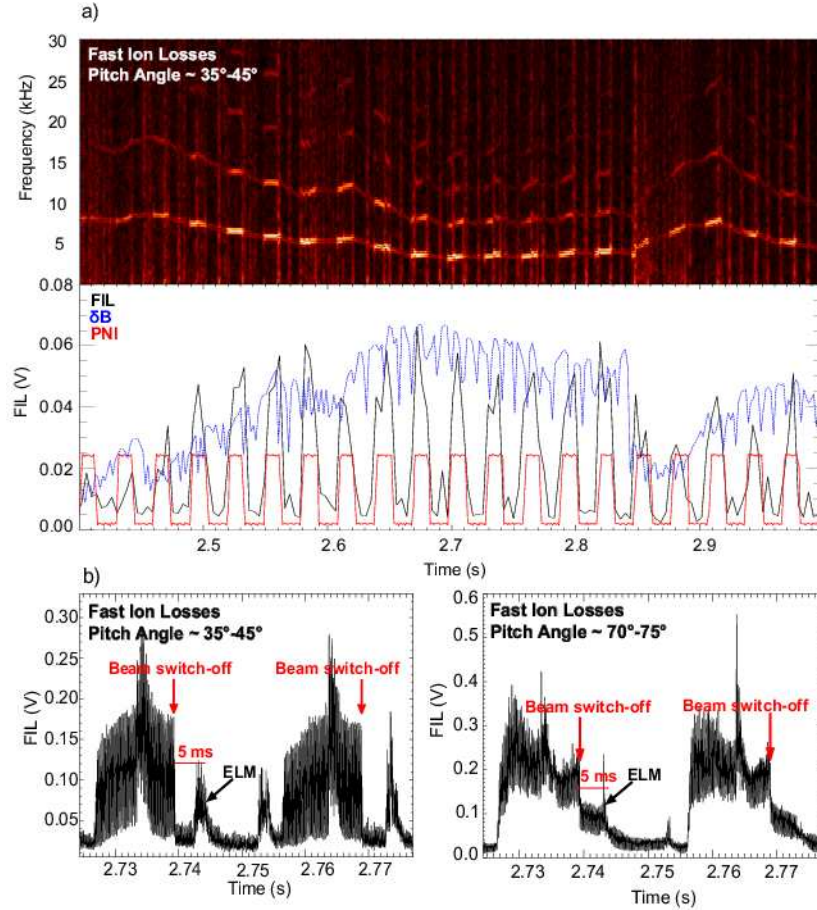


Figure 7.7: AUG discharge 21168: (a) Amplitude analysis of fast ion losses during the (2, 1) magnetic island activity. The blue line depicts the amplitude of the magnetic perturbation. The NBI modulation is drawn by a red line. (b) Two FILD channels are presented, i.e. two pitch angle regions, showing different temporal behavior. Data from [95].

fast ions and on the amplitude of the magnetic perturbations, these islands may or not overlap but in both cases they may drive fast particle losses. If there is overlapping a stochastic region is created in the fast particle orbit space, which originates significant losses. This problem has been studied by computing the trajectories of fast ions injected by NBI in a tokamak magnetic equilibrium perturbed by a (2, 1) mode by the code ORBIT which was used also in [103] and in [104].

We begin by studying a circular geometry of ASDEX with the same major radius $R_0 = 165\text{cm}$ but a minor radius given by the average of the two semi-axis of the original D-shaped device: $a = 63\text{cm}$. We use Boozer coordinates

with the equilibrium reconstructed as shown in Chapter 2. The q profile is taken from the experimental data and is reported in Fig.7.8-(a) with the resonance $(2, 1)$ and $(3, 2)$ positions. The magnetic field on axis is equal to $2T$ like in the experiment and its profile is reported in Fig. 7.8-(b) as a function of the major radius coordinate.

The perturbation considered for the $(2, 1)$ NTM is stationary and is implemented in the code in terms of α with the following eigenfunction:

$$\alpha(\psi_p, \theta, \zeta) = \alpha_0 r(\psi_p)^m (\psi_p - \psi_w) \sin(n\zeta - m\theta + \phi_0) \quad (7.1)$$

where (m, n) is the helicity of the mode and $r(\psi_p)$ the normalized radius as function of the poloidal flux; ψ_w is the poloidal flux at the wall and ϕ

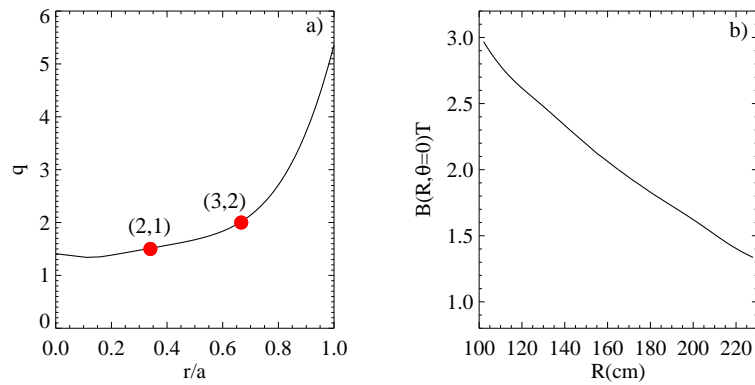


Figure 7.8: (a) Safety factor profile from the experimental data used as input in the ORBIT simulations. (b) Toroidal magnetic field profile versus the major radius coordinate.

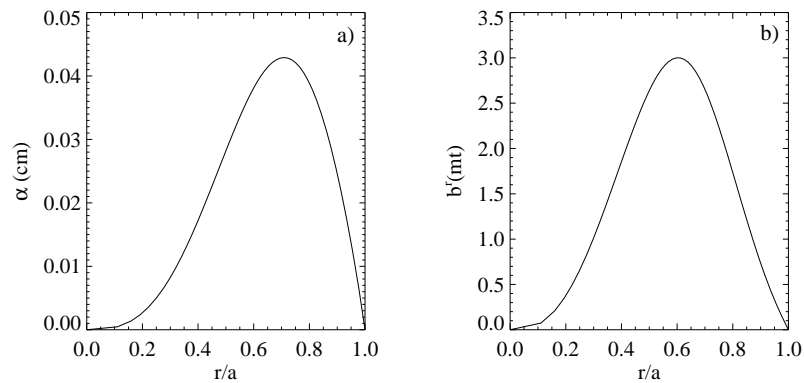


Figure 7.9: (a) α profile of the magnetic perturbation of Eq. 7.1. (b) Corresponding b^r magnetic perturbation.

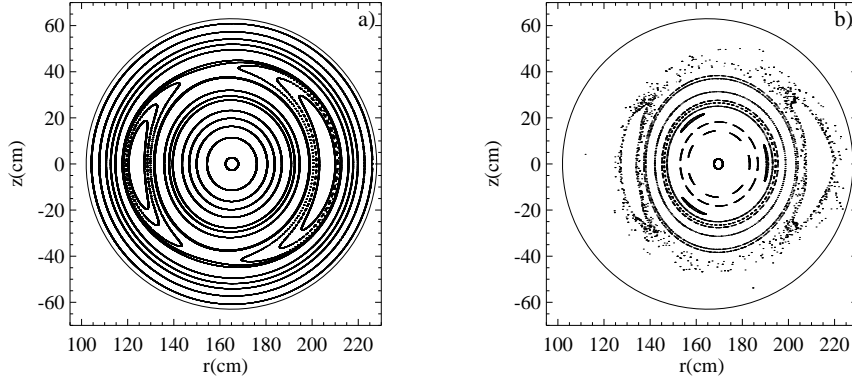


Figure 7.10: (a) Magnetic field topology on a poloidal cross section. (b) Fast ions phase space with an energy of 93keV on a poloidal plane.

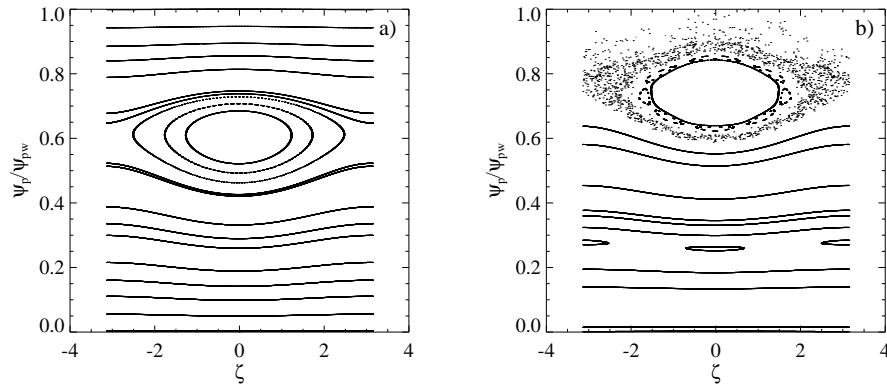


Figure 7.11: (a) Magnetic field topology on a toroidal cross section. (b) Fast ions phase space with an energy of 93Kev on a toroidal plane.

the mode phase. The radial magnetic eigenfunction b^r is related to α by the relation $b^r = [\nabla \times (\alpha \mathbf{B}_0)]^r$. As the modeling of the equilibrium is rather rude, no sensitivity study of the dependence of simulated losses on the detail of the perturbation profile is performed here. Such a study is postponed to the next section where a more realistic D-shaped geometry is used. In Fig.7.9-(a) we have reported the profile given by Eq. 7.1. Its maximum is determined by the constant α_0 and is adjusted empirically to have on the low field side the same island width of the experiment, i.e. $10 - 12\text{cm}$. The corresponding perturbation in b^r is shown in Fig.7.9-(b).

Before studying the fast ions transport we have performed Poincaré plots to analyze the topology of the magnetic field and of the fast ion phase space. This is done with the same methods of the previous Chapters. In Fig. 7.10-(a)

the magnetic field on a poloidal section is displayed, i.e. low energy particles with no drifts and following the magnetic field lines are considered. The result is a set of conserved flux surfaces with a $m = 2$ island. The $n = 1$ character is visible in the corresponding toroidal Poincaré in Fig.7.11-(a).

We observe a very different scenario for the fast ions $93keV$ phase space. The coupling between the fast ions drift and the perturbation $(2, 1)$ creates a region of stochasticity around the island. Surfaces are not conserved anymore and fast ion orbits are stochastic. This is shown both in Fig.7.10-(b) for the poloidal section and in Fig.7.10-(b) for the toroidal one. Ions with high energy can thus be lost from the plasma and reach the wall by stochastic diffusion.

It is worth highlighting that the test ions phase space in RFP and Tokamaks in presence of magnetic perturbations have opposite characteristics. While in RFPs, despite the chaotic magnetic field, structures in phase space are present, in the tokamaks with conserved magnetic surfaces, orbits are stochastic. Both phenomena are explained by the same physical mechanism, i.e. orbit drifts: this will be shown in the next Chapter.

7.4 Results of the transport simulation by ORBIT

Phase space analysis allowed us to identify the mechanism responsible of fast ion losses, but transport simulations are required to perform more quantitative comparison with experimental data. The transport simulations have been performed with an ensemble of 90000 deuterons with $93keV$ energy simulated by the FAFNER code. As this code consider the D-shaped geometry, a re-mapping onto the circular version used in ORBIT has been necessary. The toroidal angle ζ and the pitch angle λ are unchanged but the poloidal angle θ has been re-defined as $\arctan(z/(x - x_0))$ where x, z are the coordinates computed by FAFNER, and x_0 is the axis coordinate. As far as the radial coordinate is concerned, a linear relation between the poloidal flux ψ_p and the numbering of the magnetic conserved surfaces, output of FAFNER, is assumed.

The result of the re-mapping is reported in Fig. 7.12. Different colors refer to different pitch λ values. The remapping procedure introduces a distortion of the radial distribution. In fact, the number of the ions in the center is underestimated, on the contrary those on the outer regions are over-estimated and thus also the losses. D-shaped simulations will be more accurate.

The radial distribution of the initial position of the fast ions is also shown in Fig.7.13-(a). From this plot it is clear that the distribution is moved toward

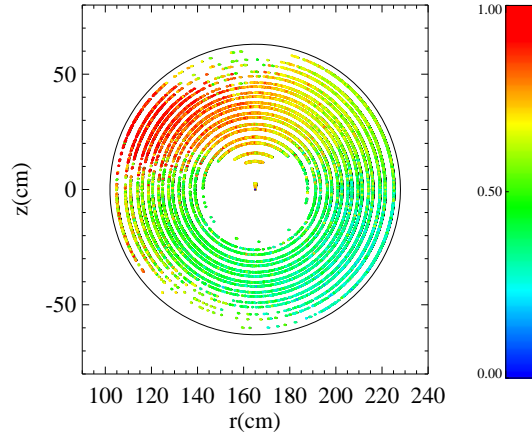


Figure 7.12: Initial position of the fast ions after the re-mapping from the code FAFNER outputs. The colors refer to the values of the pitch angle.

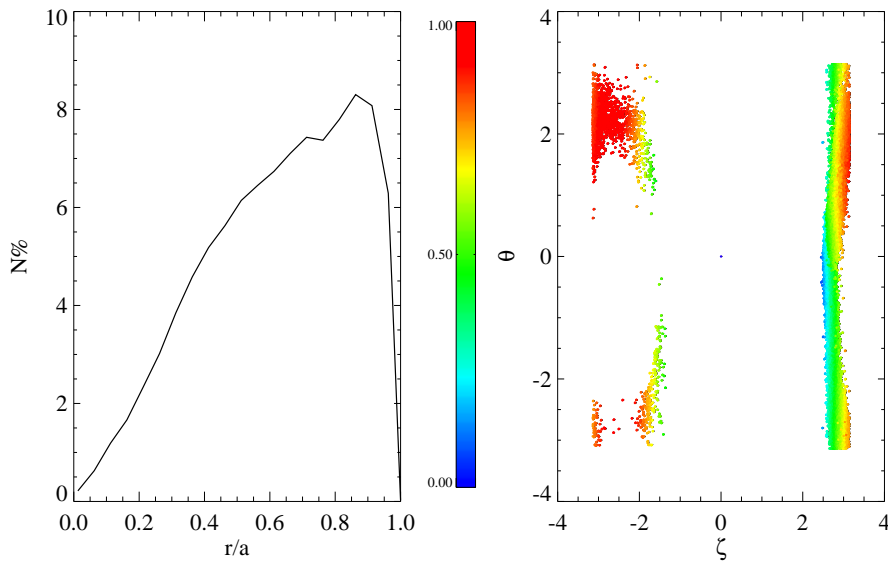


Figure 7.13: (a) Initial radial distribution of fast ions. (b) θ - ζ diagram for the initial positions of the fast ions used in the numerical simulation. Colors refer to the pitch angle values.

the higher values of the normalized radius. In (b) instead we have reported the θ versus ζ initial coordinates with informations on the pitch angle by the color scale. Two tracks are clearly visible which correspond to the two *NBI* sources with energy over 90keV located at different toroidal position.

The trajectories of a set of fast particles all starting at $t = 0$ are integrated over time and all informations about particles that reach the wall are recorded. Interactions of fast ions with the background plasma, i.e. pitch angle scattering [31] and slowing down [30] have been included in the simulations (see also section 3.8). While the first have only the effect to change the velocity direction of the ions, the latter are responsible for their thermalization with the bulk of the plasma.

By comparing results of simulations with and without a stationary perturbation, several differences occur. The mode causes a significant enhancement of the fraction of simulated fast particles reaching the wall, mostly concentrated in a toroidally localized region (which, as we will see in Fig.7.15-(a), is a signature of the $n = 1$ character of the losses) and close to the equatorial mid plane. Given the perturbation parameterization that we have chosen, the 10% of the injected fast ion population is lost within a few ms. Let us recall that the model here, both for the equilibrium and the radial perturbation, is rather crude: the main aim is in fact to investigate if experimental losses can be qualitatively reproduced.

In Fig.7.14 we show the distribution of the pitches of lost ions. For this figure, we have considered only the particles lost within a limited region in toroidal and poloidal angles, around the location of the FILD detector (see Fig.7.15). The energy of these particles is very close to their birth energy, as they are lost on time scales much shorter than the slowing down. For comparison the distribution of the losses without the mode is also shown (red curve); the two peaks in the distribution without the mode correspond

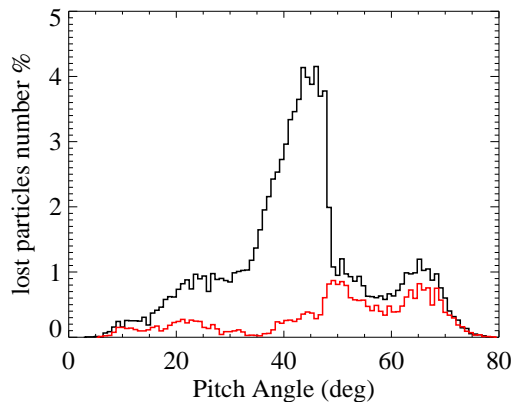


Figure 7.14: Histograms of the pitch angle of the particles lost during the ORBIT simulation with perturbation (black line) and without it (red line).

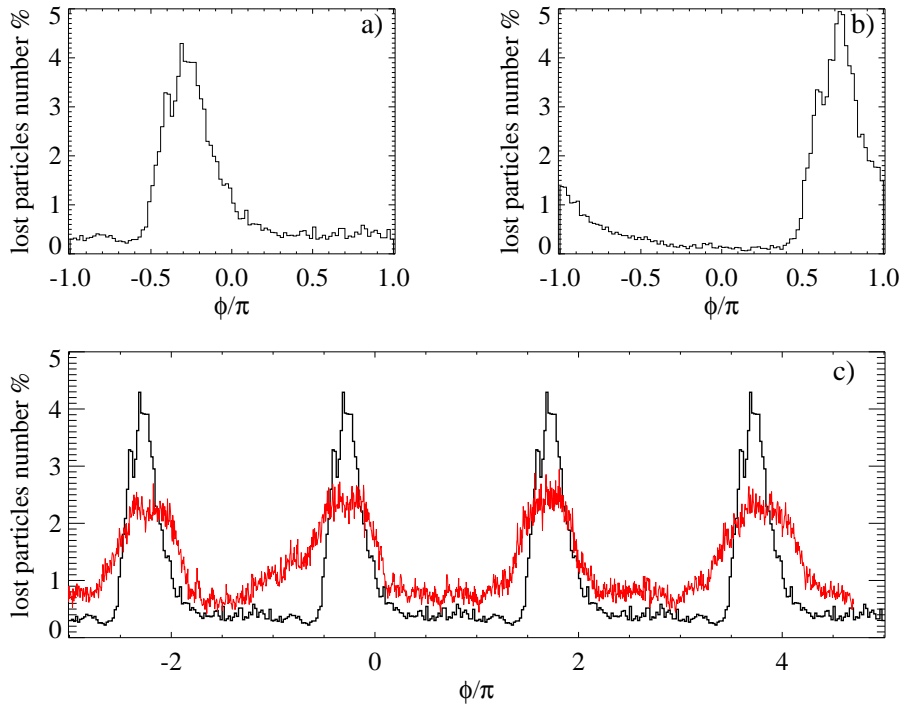


Figure 7.15: Toroidal angle distribution as a function of the toroidal angle ϕ . The two panels (a) and (b) show histograms for two choices of the phase of the (2,1) mode, differing by π . In (c) a comparison between the simulation (red line) and the experimental data (black line) is shown.

to first orbit losses for the two 93 keV beams used in this simulation. The increase of losses is different for particles of different pitch: in particular a large increase is observed around 45° . This peak has interesting analogies with the experimental observations. At this pitch angle, in fact, a spot is found in the CCD image (that labeled (2,1) NTM in Fig.7.5). The experimental losses corresponding to that spot appear only when the mode is present, a fact, which is consistent with the simulated peak in Fig.7.14.

A peak in the numerical losses is observed also around 70° , which is consistent with the corresponding experimental spot due to NBI source #3 (see Fig.7.5). The increase of losses in the simulation due to the mode is much smaller than for the pitch region around 45° , corresponding to trapped particles. In fact, the dominant loss mechanism for this class of ions is ripple, that was not included in the simulations performed so far.

The peak around $50 - 55^\circ$, corresponding to the NBI source #7, is not evident in the simulation, though losses slightly increase in that region. Likely we have a merging with the adjacent peak, possibly due to the limits of the model. Moreover, for computational reasons, statistically significant results are obtained integrating losses over a range of toroidal angle, while the measurement is toroidally localized. It is worth noting that the simulation also shows losses at pitch angles $< 35^\circ$, which can not be detected by the FILD.

In order to study the correlation of the modulation of the FILD measurements with the mode phase, simulations have been performed with different mode phases. The distribution of the toroidal loss angles for particles with a pitch $\simeq 45^\circ$ (corresponding to the peak of losses in presence of the NTM) is shown in Fig. 7.15-(a): it is characterized by a single peak, reflecting the $n = 1$ nature of the losses. The location of the peak is correlated to the phase of the magnetic perturbation: Fig.7.15-(b) shows the histogram of the losses for a simulation where the phase of the $(m = 2, n = 1)$ perturbation was displaced by π . This is in agreement with the experimentally observed modulation of the losses at the frequency of the NTM (Fig.7.6).

Even if ORBIT simulations are not time dependent, a comparison with the experimental time trace is performed by mapping the toroidal angle into time (assuming that losses occur on a time scale much faster than a rotation period). The result is shown in Fig.7.15-(c) where a few periods of the FILD

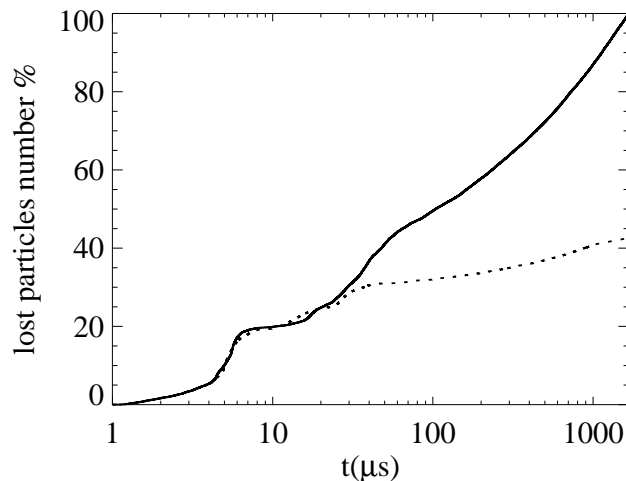


Figure 7.16: Integral probability distribution of the lost ions with an energy $> 90keV$ in the presence of the perturbation (black line) and without it (dashed line). Both the distributions are normalized to the number of $E > 90keV$ particles lost in the simulation with the NTM.

signal have been superimposed to the simulated toroidal distribution (replicated several times) by assuming a rotation with constant angular velocity and adjusting the initial phase to match the maximum. The amplitude of the signal is multiplied only by a constant without any change in the offset. The agreement with the experiment is qualitatively good.

Finally we considered the distribution of the times at which simulated particles were lost. The integral probability distribution of loss times for the lost particles described in Fig.7.14 is reported in Fig.7.16, for the case with NTM (solid curve) and without (dashed curve). For a given value in the x-axis, the curve provides the number of particles lost, which leave the plasma within that time. Particles with energy close to their birth value ($93keV$), which are those experimentally recorded, are typically lost within that time range. The plot shows that particles are lost in a broad range of time scales: while the first are promptly lost after $\simeq 10\mu s$ (to be compared with the toroidal transit time for 100 keV deuterons equal to $5\mu s$) a fraction of the population takes a longer time before escaping. This phenomenology is similar to the experimental observation of ions being lost on a slow time scale (Fig. 7.7 lower right frame). In fact, the particles with the shortest loss times are those deposited by the NBI system on the high field side well inside the separatrix, and cross readily on the low field side due to the torus drift displacement of their orbits.

The modulation with the island frequency can be explained by the drift islands with (3,1) and (4,1) helicities. Particle losses after longer times (hundreds of μs till ms time scale) are those more influenced by the stochastic diffusion. The comparison between the model and the experiment as far as loss times are concerned needs anyway to be considered as qualitative, because of the before mentioned limits of the model.

7.5 A D-shaped version of ASDEX in straight field line coordinates

In order to obtain more quantitative results, we have used a D-shaped geometry reproducing the AUG device. Initial attempts with Boozer coordinates were unsuccessful, due to a divergence of the coordinates near the separatrix. In order to avoid that problem, ORBIT equations were modified to deal with generic straight field line equilibria, as it has been described in Chapter 3. The equilibrium obtained with VMEC has been adopted to ORBIT following the procedure described in Chapter 2.

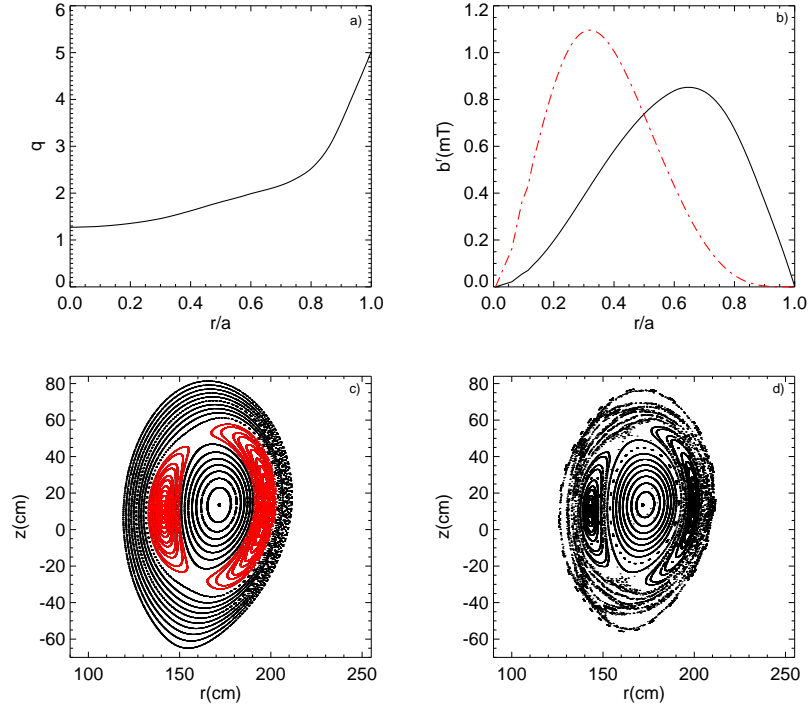


Figure 7.17: (a) Profile of the safety factor q for the AUG discharge 21089. (b) Two different parametrizations of the radial component of the magnetic field perturbation for the $(2,1)$ mode: the black refers to Eq.7.1 and the red to Eq.7.2. (c) Poincaré map of a poloidal section by field line tracing with ORBIT. (d) Representation of fast ion $93keV$ space phase.

7.5.1 Phase space properties

To obtain more precise simulations, a sensitive study for the detailed perturbation profile was necessary. It has been found, by comparing different parameterizations, that even if the radial extent of a $(2,1)$ island, as measured by ECE, is reproduced, the location of the O-point may vary by $2cm$. Moreover, even the value of the perturbation at the edge, where the drift islands occur, can be different. Unfortunately no diagnostics are available to determine precisely the shape of the perturbation. We will show in the following that very small variations in the island position may lead to important differences in the final results of the simulations.

The measured safety factor q profile is again reported in Fig. 7.17-(a); the resonant position for the mode $(2,1)$ is at the radius $r/a \simeq 0.6$. In the same figure in (b) the black curve is the profile of the radial component b^r

of the $\alpha(\psi_p)$ given by Eq.7.1. Such an eigenfunction superimposed to the equilibrium magnetic field generates the poloidal section Poincaré displayed in (c); this is performed, as usual, with ORBIT field line tracing. It is clear from the plot that these islands do not cause significant ergodicity of the magnetic field lines; thus, no chaos is present in the configuration and there are no sources for anomalous transport to the wall of thermal particles.

Like in the circular cross section case, fast ions behave in a very different way because of the drifts. This is clearly visible in Fig. 7.17-(d) for fast ions with $93keV$ energy. While magnetic surfaces in 7.17-(c) exist, a chaotic fast particle phase space is created and losses can occur.

7.5.2 The initial fast ion distribution in the D-shaped geometry

For the D-shaped case the fast ions initial distribution computed with FAFNER is given as input without remapping. We have used for each simulation about 30000 ions, less than the circular case, because in the D-shaped equilibrium the motion equation integration requires more CPU-time.

A map of the initial ions deposition is reported in Fig.7.18 where the colored points represent particles which are lost within $3ms$. The different colours correspond to different initial pitch angle λ . Few of these ions are close to the wall and are lost in a short time (less than $10\mu s$), because of the shift due to their high energy. The fraction of these ions is about the 0.03% of the initial total population. From Fig. 7.18 we can see also the two tracks of the beams while crossing the plasma.

The radial profile of the initial fast ions distribution, vs the poloidal flux, is reported in Fig. 7.19 (a) together with the pitch angle distribution profile (b). The initial ions position is distributed almost uniformly as function of the radial coordinate, with a peaking near the center of the plasma.

The fast ions guiding center trajectories have been computed for a time of $3ms$ taking into account also their collisions with the background as in the circular case. The simulations have been performed with the (2, 1) NTM mode just shown in the Poincaré of Fig. 7.17-(c)-(d). The phase of the mode has been changed to different values in order to verify the experimental behavior i.e. to check if the particles losses are in phase with the mode.

7.5.3 Transport numerical simulations with a fixed mode

At the end of the simulation all the informations about the final position, pitch and energy of the fast ions are recorded. The same is done for the fast

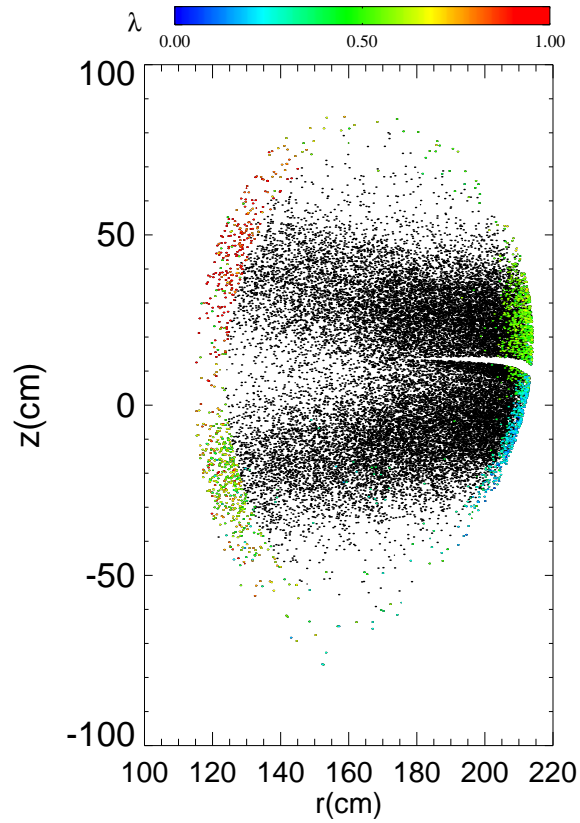


Figure 7.18: Map of the initial position of the particles from NBI projected on the poloidal cross section.

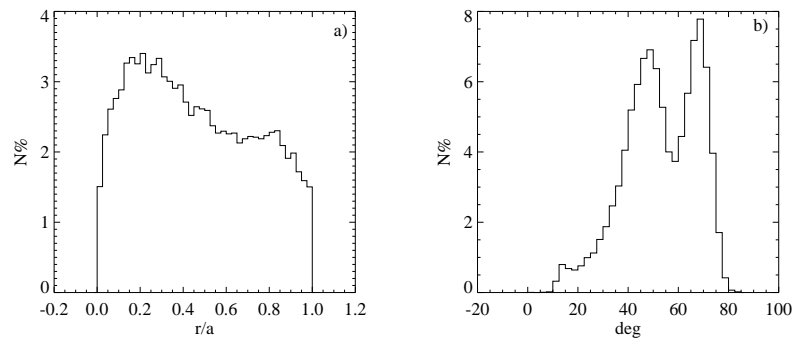


Figure 7.19: a) Initial distribution of the fast ions 93keV deposited from NBI. b) Initial pitch angle distribution.

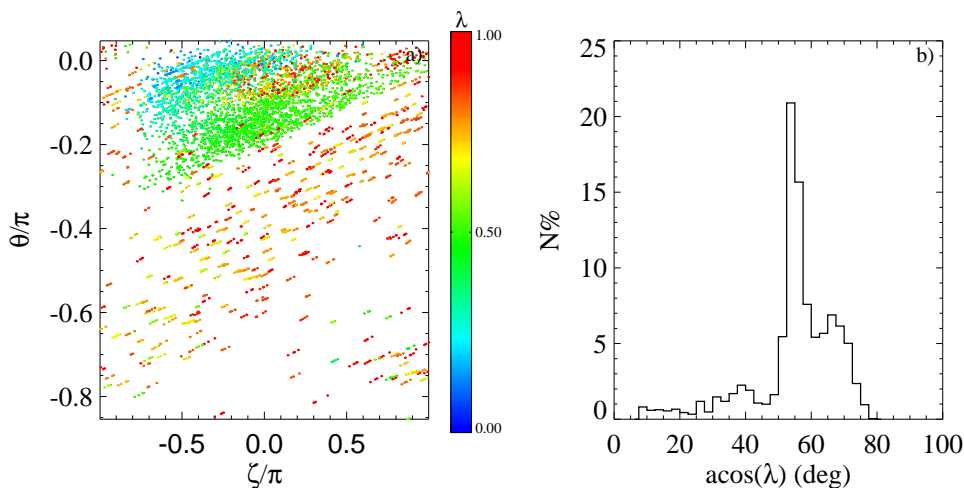


Figure 7.20: (a) Final ζ and θ position of lost fast ions. The color refers to the pitch angle. (b) Final pitch angle distribution of the lost ions around the plane $\theta = 0$.

ions which reach the wall before the end of the simulation. The particles lost after $3ms$ are about the 5.44% of the fast ions initially deposited, while when no perturbation is present losses decrease to 2.8%. This value, as we shall show in the following, is dependent on the amplitude of the mode.

The final distribution of toroidal and poloidal angles of the lost ions are plotted in Fig. 7.20-(b). The different colors refer to the final pitch angle λ of the particles. The green spot corresponds to fast ions losses triggered by the mode (2,1). It is worth noting that these losses are localized toroidally and are concentrated near the poloidal plane $\theta = 0$. This is the region where the FILD detector lies.

The pitch angle distribution of lost ions is in a good agreement with experimental observations. This is reported in Fig. 7.20-(a) as function of $\text{acos}(\lambda)$ for lost ions around the plane $\theta = 0$ ($-20^\circ < \theta < +20^\circ$ to be consistent with the data from the FILD which is placed at this poloidal position). The y-axis represents the fraction of lost particles on a given range of pitch angle with respect to the total loss particles. The three peaks at different values of pitch are clearly visible in this figure. The first on the right refers to deeply trapped ions which have left the plasma with an angle of about 90° with the magnetic field. The second peak is centered at about 55° and is higher than the first one. These two class of ions are lost in a smaller fraction also without the mode. The peak centered at about $40^\circ - 45^\circ$ is entirely due to the NTM action, and is related almost to passing ions. This

figure shows also the presence of an other maximum for deeply passing ions ($\text{acos}(\lambda) < 20^\circ$) which cannot be resolved by the FILD.

Similarly to the circular case, the toroidal distribution of losses is correlated with the phase of the mode. This has been verified for many phases and an example is reported in Fig. 7.21-(a)-(b) which shows the final toroidal angle distribution for the fast ions with $\text{acos}(\lambda) \simeq 40^\circ - 50^\circ$, i.e. the losses induced by the NTM. The phase of the mode for the distribution in *b*) is displaced by an angle of π with respect to the case of *a*); this reflects in a shift of the maximum of the distribution by the same factor. The presence of a single peak in the final toroidal distribution reflects the character $(2, 1)$ of the mode. Similar analysis for a mode $(3, 2)$ are in fact characterized by two maxima, which, also in this case, move with the phase of the mode.

The integral probability distribution of loss times is reported in Fig. 7.22-(a). As in the previous plots the 100% is referred to the total fast ion lost from the plasma in $3ms$. This plot shows that ions are lost in a broad range of time scales. The first in fact are promptly lost after only $10\mu s$; this corresponds to ions which have covered a very small distance, being the time required to complete a poloidal turn of the device about $5\mu s$. Another part of the population takes a longer time before escaping from the plasma. This phenomenology is similar to the experimental observation of ions lost on a slow time scale. These particles are those more influenced by the slow stochastic diffusion.

Another point which is consistent with the experiment is the final energy of the lost ions. The distribution is reported in Fig. 7.22-(b). Most of the losses have a final energy around $93keV$ like in the experiment, for the fastest losses. Only a small fraction, about the 1% is under $90keV$.

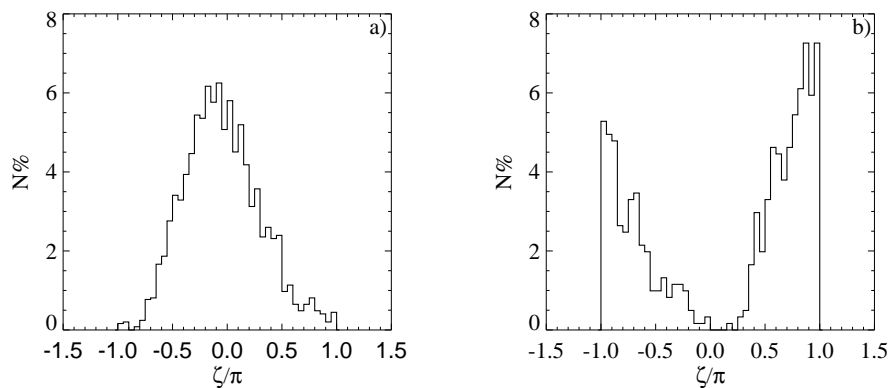


Figure 7.21: The toroidal localization of the losses depend on the phase of the mode. In (a) and (b) the phases were shifted of π .

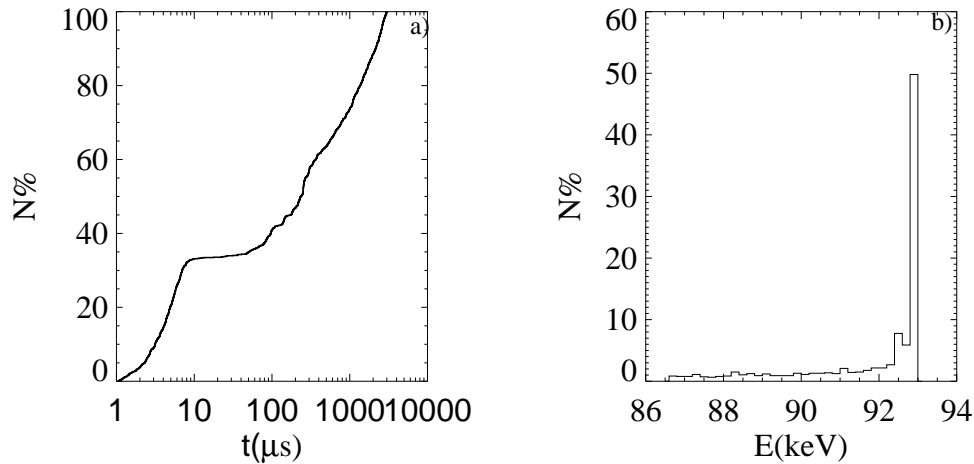


Figure 7.22: (a) Losses as function of time in the first 3ms of the simulation. (b) Final energy distribution of lost ions (within 3ms).

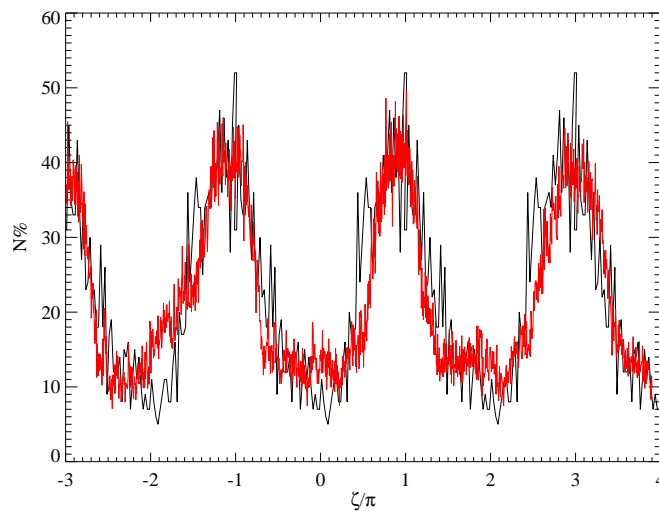


Figure 7.23: Experimental (black) and simulation (red) signal of the losses.

Many of the results shown in this section confirm those for a circular version of AUG: the toroidal localization of the losses, the fast and slow time scales are visible also in an approximated geometry. Details on the pitch angle distribution in a D-shaped are more in agreement with the experiment. In fact the three peaks could not be resolved in the circular geometry, but

only two were visible. The peaks centered at 45° and 55° formed a one-only maximum in the circular geometry approximation.

The reproduction of the experimental data is improved by superimposing the signal of the losses with the final toroidal distribution obtained by the simulation and reproduced for few periods, as in Fig. 7.15-(c). As for the circular case, the amplitude of the signal is multiplied only by a constant, without any change in the offset. The result is reported in Fig. 7.23: in black the signal and in red the simulation by ORBIT.

7.6 Effect of the ripple implementation

The reproduction of losses of trapped particle was not particularly good, due to the lack of ripple in the model. We added this effect and repeated simulations. Ripple increases the no-perturbative losses from 2.8% to 6.9%. The pitch angle distribution for this case is reported in Fig. 7.24 with the red histogram for particles lost around the $\theta = 0$ plane. The ripple mostly affects deeply trapped particles but a peak is also present at $\text{acos}(\lambda)$ close to 55° . This is in a very good agreement with the experimental results where the mode is not present.

When the $(2, 1)$ perturbation is added, a third peak at 40° appears, as displayed in Fig. 7.24 by the black histogram. Another good agreement with the experiment is that the mode increases also the losses of the second peak, the one centered at 55° . Like in the situation without the ripple, the mode

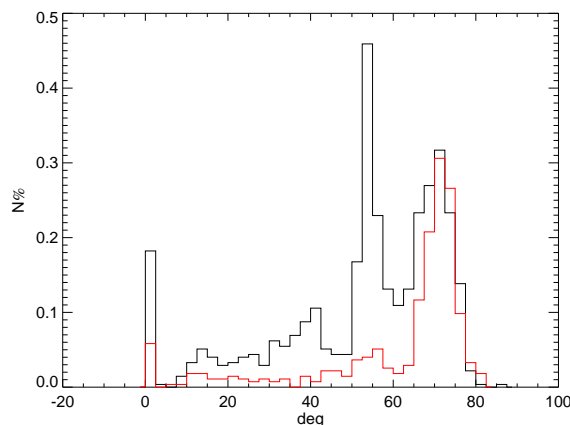


Figure 7.24: Final pitch angle distribution when the ripple is taken into account in a equilibrium simulation (red) and when a fixed mode $(2, 1)$ is present.

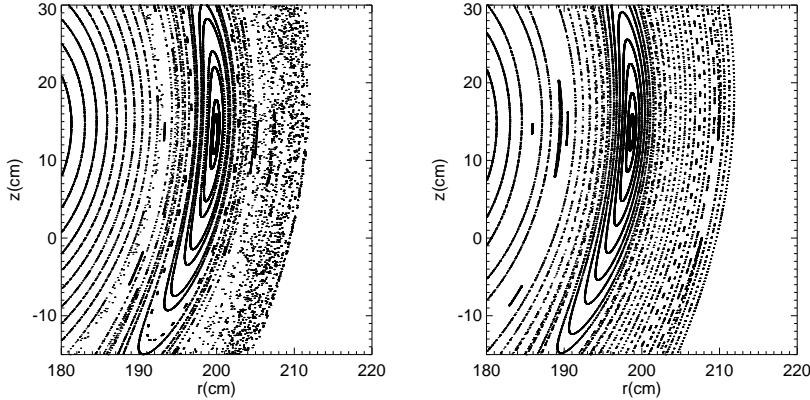


Figure 7.25: R.h.s: zoom of the magnetic island obtained by a perturbation of the form Eq. 7.2. L.h.s: zoom of the magnetic island by Eq. 7.1.

induces ion losses also at pitch angles lower than 30° which can't be resolved by the FILD detector. A bar of the histograms is visible on the left of the figure for particles with a velocity parallel to the magnetic field. These ions are those lost in few μs , i.e. in less than one toroidal transit.

The toroidal angle and energy distribution are very similar to the ones shown in the previous section without the ripple. An important difference is given by the total amount of particles lost when both the ripple and the $(2, 1)$ mode are present. In fact, the fraction of fast ion which leave the plasma in this case is about the 10.40% of the initial $93keV$ particles population from the NBI system. If the ripple is considered the mode $(2, 1)$ is thus responsible of an increase of the losses of the 3.5%.

7.7 Sensitivity of the losses amount on the radial perturbation profile

Due to the uncertainty in the radial profile of the perturbation, we tried to estimate how a different shape can change the loss estimates. In particular, our results partially differ from other simulations that use slightly different parameterizations [105] and where stochasticity is not the main mechanism responsible of the losses.

In Fig. 7.29 we have reported a zoom of the Poincaré plots in the fast ion space generated by the perturbation of Eq. 7.1 (b) and by a different profile of the form:

$$\alpha(r, \theta, \zeta) = \alpha_0 \left(\frac{r(\psi_p)^m}{x_0} \right) \left(\frac{1-r}{1-x_0} \right)^{m(x_0^{-1}-1)} \sin(m\theta - n\zeta + \phi_0) \quad (7.2)$$

where the free parameter x_0 has been adjusted in order to have an O-Point position nearer to the magnetic axis by about $2cm$ respect to the one given by Eq. 7.1. The profile of this eigenfunction is reported in terms of the magnetic field perturbation b^r in the plot of Fig. 7.17-(b) with the red curve. Even though the displacement is rather small, the phase stochasticity is significantly reduced, and consequently losses strongly decrease. For example for an island extending for a width of $11cm$ the different parametrization and O-Point position shows an increase of the losses due to the mode only up to the 7.5%, just the 0.6% more than in the equilibrium case.

Changing the amplitude of the maximum for α is equivalent to consider islands with different width. A scan has been performed for both the types of eigenfunctions just discussed and the results are reported in Fig. 7.26. The red curve corresponds to profile for α described by Eq. 7.2 and the black to our standard perturbation 7.1. The dependence of losses on the amplitude is different for the two kind of radial profiles: while the red curve seem to saturate at 20%, the black one is significantly higher.

The explanation of such a different behavior lies in the stochasticity of the fast ion space. Such a stochasticity, in fact, is due to the (2, 1) NTM, the (1, 0) shift and the islands chain generated by their coupling. When the first

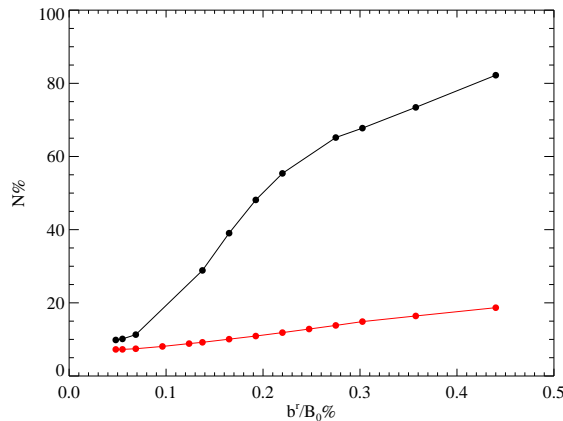


Figure 7.26: Percentage of losses as function of the magnetic perturbation amplitude for Eq. 7.2 (red) and Eq. 7.1 (black).

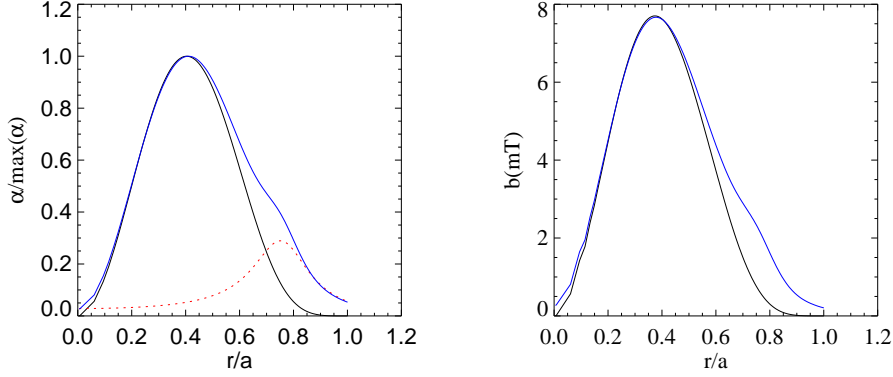


Figure 7.27: On the left: α function profile of Eq. 7.2 in black; in red the dumb of Eq. 7.3 at the resonance (3, 1). The final profile obtained adding Eq. 7.3 and Eq. 7.2 in blue. On the right: the corresponding profiles for the magnetic perturbations.

eigenfunction (Eq. 7.1) is considered the corresponding Poincaré reported in Fig. 7.17-(d) shows the presence of an island (3, 1). The dimensions of the island depend mainly on the value of the (2, 1) eigenfunction at the position of the resonance (3, 1) and on its radial derivative. The (3, 1) resonance is about at $r/a \approx 0.8$. At this point both the value of the eigenfunction 7.1 and its derivative are non zero, as shown in the black curve in Fig. 7.17-(b). The situation is very different for the profile 7.2 reported in red in figure 7.17-(b). In fact, at $r/a \approx 0.8$ the eigenfunction (2, 1) is very close to zero, and this results in a (3, 1) island of very small size. In order to control the size of the (3, 1) island independently, we further modified the radial profile locally. We have added to the α eigenfunction 7.2 a bump of magnetic perturbation centered close to this resonance position expressed as:

$$\delta\alpha(r) = \frac{\alpha_1}{1 + \gamma(|r - r_1|/a)^2} \quad (7.3)$$

where α_1 is the amplitude of the bump at $r = r_1$, and γ determines its width. A plot of $\delta\alpha$ is reported in Fig. 7.28-(a) in red, which, summed with the profile of the basic eigenfunction (black) α of Eq. 7.2, gives the blue curve. We have chosen as r_1 a radial position a little before of the resonance (3, 1), so as to have a non-zero derivative of $\delta\alpha$ at $r/a \simeq 0.8$. The corresponding eigenfunction for the magnetic perturbation b^r is reported in Fig. 7.28-(b). Performing the simulations with this small correction of the (2, 1) eigenfunction takes to a fast ion losses percentage of 9%, i.e 1% more than the one obtained by using Eq. 7.2.

It is worth noting that, while the absolute value of losses critically depends on the details of the eigenfunctions, the final toroidal angle and pitch angle distributions have the same features and are similar to those described for the case discussed in the previous section. We have also summed up all the fast ion lost in the first 3ms of the simulations with pitch angle in the range $30^\circ < \text{acos}\lambda < 45^\circ$ where a peak appears only when the NTM is present. If we consider the eigenfunction of the form 7.1 we observe a 110% increase of the losses with respect to a simulation without perturbations. On the contrary the eigenfunction 7.2 increases the losses of less than the 12%. Finally, a small variation of the magnetic perturbation value at the resonance (3, 1) added to Eq. 7.2 can lead to a 30% increase of lost ions.

This last study shows how the entire profile of the eigenfunction may affect the final result of the simulation. Using eigenfunction 7.1 means that stochasticity of the fast ion space is the mechanism at work. On the contrary only the drift islands are responsible of the losses if we consider the eigenfunction 7.2 since it does not create chaotic regions in fast ion space. Table 7.7 summarizes the fraction of fast ions lost during the first 3ms of the several simulations both with and without perturbation.

In [105] the data from the FILD have been studied by numerical simulations with the GOURDON code [100]. In this case, a significant stochasticisation of the drift islands is not observed. The main loss mechanisms are thus: the prompt passing particle losses, NTM-induced passing particles losses caused by drift islands formation, ripple losses of trapped particles. The results obtained in this study are very similar and compatible with ours if we use the parametrization of the eigenfunction given by Eq.7.2. In fact, the Gourdon code deals with a form of the perturbation which is much closer to Eq.7.2 than to Eq.7.1. As we have shown above in Fig.7.29, this means a strong reduction of the drift islands overlap and hence of stochasticity.

| scenario | % equilibrium | % perturbation |
|-----------|---------------|----------------|
| no ripple | 2.8 | 5.44 |
| ripple | 6.9 | 10.40 |
| Eq. 7.2 | 6.9 | 7.5 |
| Eq. 7.3 | 6.9 | 9 |

Table 7.1: Final losses percentage with several simulations: without and with the ripple and by using different parameterizations of the magnetic perturbation.

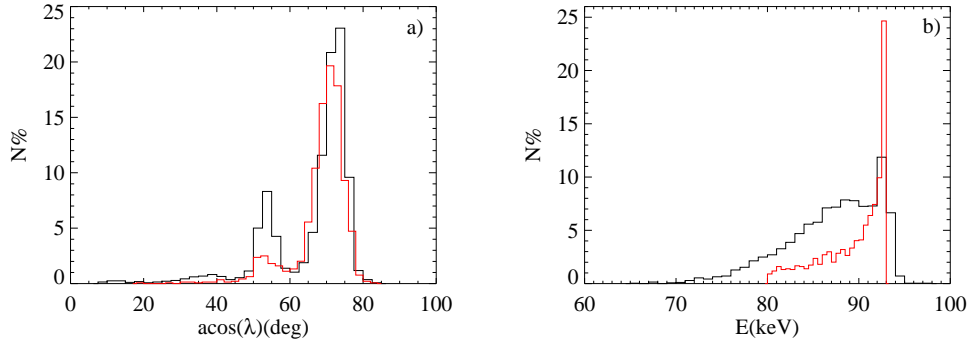


Figure 7.28: (a) In black the final distribution of the losses around the $\theta = 0$ plane when a rotating perturbation $5kHz$ is present, compared with equilibrium final distribution (red). (b) Corresponding final energy distributions.

7.8 Steady-state with rotating modes

So far the perturbation was assumed stationary. This assumption is correct as long as losses occur on a faster time scale than the rotation period. As we observed also a fraction of particles lost on longer time scales, a series of simulations have been performed where we have considered a rotating mode with the same frequency observed in the experiment, $\omega \simeq 5kHz$. Such a simulation requires a modification of the potential, to take into account the fast dynamics of background electrons, as explained in Chapter 3.

We have performed a run in a steady state scenario, i.e. in a modified version of the code where the number of particles is kept constant in time. Every time a fast ion is lost, a new one, belonging to the particles distribution generated by the code FAFNER, is reintroduced in the plasma. The run lasts for about $7ms$ with an island of the same width considered before, i.e. $11cm$ on the low field side.

At the end of the run we have plotted in Fig. 7.28-(a) the final distribution of pitch angles to check if the results found with a non-rotating mode still hold also for this new more complete simulation. On the y-axis we have reported the fraction of lost ions, within a pitch-angle interval, with respect to the constant number of ions in the plasma (i.e. 30000). In red the distribution without the mode but for a longer time run than that of section 6, lasting only $3ms$, is shown. The two peaks at 55° and 70° are clearly visible. When the rotating mode is present, the black curve shows the increase at 40° of the losses. Also at 55° the ion losses increase with the rotating mode, about the

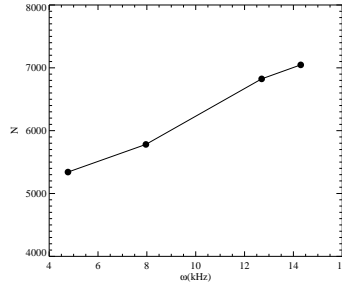


Figure 7.29: Dependence of the losses on the frequency in run with the same duration of $7ms$.

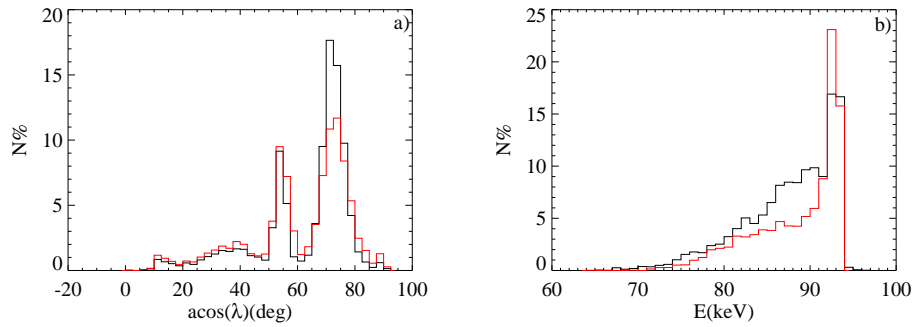


Figure 7.30: (a) Final distribution of all the lost ions with two different mode rotating frequencies: $8kHz$ (red), $14kHz$ (black). (b) Corresponding final energy distribution.

double with respect of the equilibrium. In (b) the final energy distribution of the losses is reported for a case with only the equilibrium magnetic field (red) and with the rotating perturbation (black). In $7ms$ the slowing down collisions decrease the energy to $80keV$ for a large fraction of ions. The presence of the rotating mode further contributes to the energy spread because of the associated rotating potential. This explains the broader distribution at lower energies.

The results with the rotating perturbations thus confirm the behavior already observed with a fixed mode, and others analysis are still in progress. It has also been observed, by performing several runs, a slightly increase of the losses with the increasing mode's frequency. This is shown in the plot of Fig.7.29. All these simulations have been performed with the same duration of the run ($7ms$). The final pitch and energy distributions are about the same for different frequencies if we consider the ions lost around the plane $\theta = 0$ and are similar to that plotted in Fig.7.28-(a). If we study all the losses at every angle, thus including particles lost in regions far away from the

FILD detector we observe that higher frequencies of the mode affect mainly the losses of trapped particles (peak at 70°) while the others are mainly unchanged. This can be seen in Fig. 7.30-(a). The red curve corresponds to a frequency of $8kHz$ and the black to $14kHz$. These new losses may be due to new resonances between banana orbits of deeply trapped ions and the mode. In (b) for the same frequencies we represent the final energy distribution for all the particles. The black curve, corresponding to the higher frequencies, is broader than the red one. This is a behavior observed also for different ω values: the highest ω , the broadest is the final energy distribution.

Further studies with the rotating perturbation are still in progress and also new experimental data analysis will be performed in the future on this topic.

CHAPTER 8

Fast ions in Tokamak and RFP

In this Chapter we give an analytical description of the results exposed in Chapters 6-7, concerning the dynamic of fast ions in the RFP and the Tokamak configurations. We will derive, from the guiding center motion equations, the ‘kinetic’ safety factor \tilde{q} , i.e. the mean helicity of a passing particle moving with a given kinetic energy and magnetic moment. This point had also been hinted in [106] for alpha particle motion in a tokamak. We present here a generalization for axisymmetric pinch equilibria and in particular we consider the strong consequences on RFP fast ion confinement.

8.1 An analytic approach: the kinetic safety factor

We briefly recall here the fundamental features of the standard equilibria in RFP and Tokamak experiments. They both have a magnetic field with toroidal (B_ζ) and poloidal (B_θ) components, although in the tokamak $B_\zeta \gg B_\theta$, while in the RFP $B_\zeta \approx B_\theta$, an ordering which results in a different safety factor q profile, defined as the helicity of a magnetic field line $\langle \frac{d\zeta}{d\theta} \rangle$ where the brackets indicate an average around a poloidal transit and $d\zeta, d\theta$ are the infinitesimal differential elements along the toroidal and the poloidal coordinates, respectively. In a circular device q is given by the well-known expression: $q(r) = \frac{rB_\zeta}{R_0B_\theta}$ where r is the radial position along the minor radius

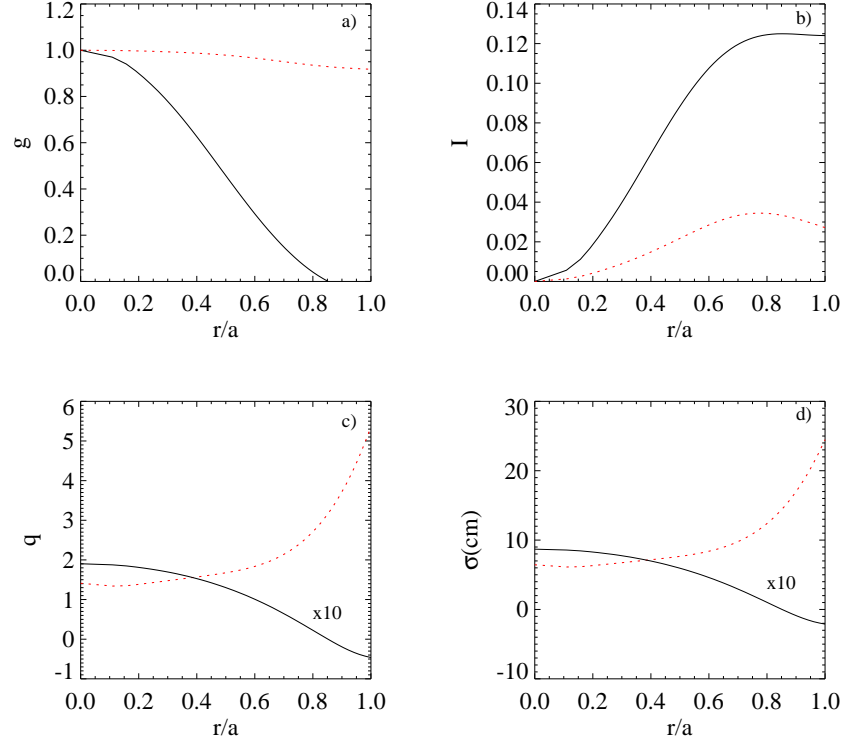


Figure 8.1: Typical profile for a circular Tokamak (red) and a RFP (black) of g , I , q and the shift σ .

a and R_0 is the major radius.

We use Boozer coordinates with the normalizations used in ORBIT, presented in Chapter 2. Examples of the poloidal and toroidal current g, I and q profiles for an RFP and a Tokamak, of the same size ($a = 0.5m$, $R_0 = 1.5m$) and the same magnetic field on axis ($B_0 = 1T$), are shown in Fig. 8.1-(a)-(b)-(c). Note that g is almost constant and close to 1 for the Tokamak while I is slightly greater than zero. For an RFP g decreases from 1 to 0 and I is significantly greater than 0.

Consider a passing particle with a velocity v and kinetic energy E in a magnetized plasma without collisions, where only the equilibrium magnetic field $\mathbf{B}(\psi_p, \theta) = \mathbf{B}_\zeta + \mathbf{B}_\theta$ is present. The equations of guiding center (g.c.) motion for such a particle were derived in Chapter 3, by writing the expression of $\dot{\psi}_p$, $\dot{\theta}$, $\dot{\zeta}$ and $\dot{\rho}_\parallel$ in terms of partial derivatives of the Hamiltonian $H = \rho_\parallel^2 B^2 / 2 + \mu B$; μ is the particle magnetic moment and $\rho_\parallel = \mathbf{v} \cdot \mathbf{B} / B^2 = \sqrt{2(E - \mu B)} / B$. These equations describe in a sophisticated coordinate system the drift \mathbf{v}_D of a particle, due to the magnetic field

curvature and inhomogeneity:

$$\mathbf{v}_D = \frac{v_{\parallel}^2}{B^2} \frac{\mathbf{R}_C \times \mathbf{B}}{R_C^2} + \frac{v_{\perp}^2}{B^2} \nabla B \times \mathbf{B} \quad (8.1)$$

where \mathbf{R}_C is the curvature radius of \mathbf{B} and v_{\parallel}, v_{\perp} are the parallel and perpendicular velocity of the particles respectively. In a device with both a toroidal $B_{\zeta} \mathbf{e}_{\zeta}$ and poloidal $B_{\theta} \mathbf{e}_{\theta}$ magnetic field, this drift can be decomposed along two different directions.

The combination of \mathbf{B}_{ζ} gradient and curvature generates a total drift of the orbits in the vertical direction. In the presence of a poloidal magnetic field an outward shift of the g.c. orbits, proportional to the particle energy, is added. The motion of the particle has been described in section 3.7 with a displacement of the orbit given by Eq.3.81: $\sigma = \frac{v|q(r)}{\omega_c}$ for a circular geometry and a generalization of this quantity for a D-shaped device can be found iteratively by solving Eq. 3.74. This shift is shown for typical Tokamak and RFP equilibria in Fig. 8.1-(d) (with pitch $\lambda = \frac{\mathbf{v} \cdot \mathbf{B}}{vB} = 1$, energy $E = 100keV$, same magnetic field $B_0 = 1T$): while in a Tokamak the orbit shift can be of several cm , in the RFP it's less than $1cm$.

As we want to compute the effective safety factor, at first we need an approximate orbit representation. This is obtained, for a passing ion in a circular device, by expanding ρ_{\parallel} in the terms of the inverse aspect ratio r/R to give the location of the ion orbit to lowest order (Eq. 3.82) that we write here below again:

$$\psi_p^I(\psi_{p0}, \theta) \cong \psi_{p0} + \sigma \cos(\theta), \quad (8.2)$$

where σ is the shift in poloidal flux units. For $\lambda < 0$ the shift σ becomes negative. At $\theta = \pm\pi/2$: $\psi_p^I(\psi_{p0}, \pm\pi/2) = \psi_{p0}$.

The poloidal magnetic field is also responsible, because of Eq. 8.1, for an additional component of the velocity drift in the toroidal direction \mathbf{e}_{ζ} . We rewrite here a simplified form of guiding center motion equations in the Boozer case with no perturbations and potential $\Phi = 0$:

$$\dot{\theta} = \frac{\rho_{\parallel} B^2}{D} (1 - \rho_{\parallel} \partial_{\psi_p} g) + \frac{g}{D} \left[(\mu + \rho_{\parallel}^2 B) \frac{\partial B}{\partial \psi_p} \right] \quad (8.3)$$

$$\dot{\zeta} = \frac{\rho_{\parallel} B^2}{D} (q + \rho_{\parallel} \partial_{\psi_p} I) - \frac{I}{D} \left[(\mu + \rho_{\parallel}^2 B) \frac{\partial B}{\partial \psi_p} \right]. \quad (8.4)$$

It is worth noting that because of the shift effects explained above the coordinate ψ_p in these equations must be replaced with $\psi_p^I(\theta)$ which describes the projection on the poloidal cross section of the real motion of the particle.

Taking the ratio of equations 8.4 and 8.3 we define a kinetic safety factor as:

$$\tilde{q}(\psi_p^I, \theta) = \frac{d\zeta}{d\theta} = \frac{q + \rho_{\parallel} I' - \eta I}{1 - \rho_{\parallel} g' + g\eta}, \quad (8.5)$$

where $q(\psi_p)$ is the usual magnetic field safety factor. All the primes indicate derivatives with respect to the poloidal flux ψ_p^I and $\eta(\psi_p^I, \theta) = B'(\mu + \rho_{\parallel}^2 B)/(\rho_{\parallel} B^2)$. The shift effect of Eq. 8.2 is included in Eq. 8.5 by evaluating the latter along the actual path of the test particle g.c. , i.e. for $\psi_p = \psi_p^I$. When $E \rightarrow 0$, and thus $v \rightarrow 0$ too, $\eta \rightarrow 0$ and Eq. 8.5 becomes the usual safety factor q for the magnetic field lines, since the particle follows the magnetic field line.

Resonance occurs when an orbit closes on itself after a finite number of toroidal and poloidal turns. In order to obtain the new resonance position in the fast ion phase space, for a given (m, n) helicity, we impose that the average kinetic \tilde{q} value is equal to m/n , thus:

$$\langle \tilde{q} \rangle_{\theta} = \frac{m}{n} \quad (8.6)$$

where $\langle \dots \rangle_{\theta}$ is the average over the poloidal angle θ . By solving Eq. 8.6 in ψ_p for a given (m, n) mode the new resonant position in the fast ion space is found. Let $\xi_{m,n}$ be the mean radial displacement of the location of a given (m, n) fast ion resonance for the orbit of an ion g.c. This shift is very different in a tokamak and an RFP. The magnetic resonance occurs at $q = m/n$. But because of the drifts the kinetic \tilde{q} value is typically larger than q . Thus the position of the fast ion resonance occurs in a region of smaller q .

For a Tokamak, such region is located at smaller minor radius close to the magnetic resonance surface, due to the high $dq/d\psi_p$ (shear factor). For an RFP, the ion resonance is quite far from the magnetic surface and at higher minor radius, due to the low negative shear. More precisely, a first order approximation for $\xi_{m,n}$ may be estimated by the relation:

$$\xi_{m,n} \cong \frac{\langle \tilde{q} \rangle_{\theta} - q}{\frac{d\langle \tilde{q} \rangle_{\theta}}{d\psi_p}}. \quad (8.7)$$

In particular, for $\lambda = 1$ the $\langle \tilde{q} \rangle_{\theta}$ profile is greater than the usual safety factor profile and thus the resonances are moved inward (if $q'(\psi_p) > 0$, Tokamak) or outward (if $q'(\psi_p) < 0$, RFP) by a quantity $\xi_{m,n}$. Taking into account also the local shift in θ (Eq. 8.2) the final position $\psi_{p;m,n}^I$ for an (m, n) resonance at a given θ is :

$$\psi_{p;m,n}^I \cong \psi_{p0;m,n} + \sigma \cos\theta + \xi_{m,n}. \quad (8.8)$$

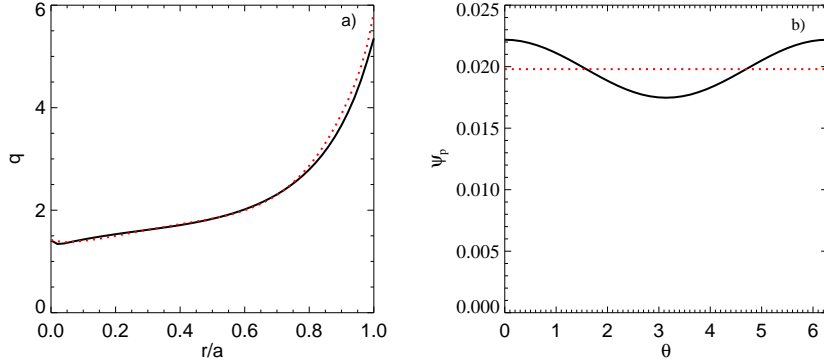


Figure 8.2: (a) Comparison between the kinetic (red-dashed) and the standard (black) q profile in a Tokamak configuration. (b) ψ_p^I vs θ for an ion with low energy (black) and for $E = 100 \text{ keV}$ (red-dashed) in a Tokamak.

8.2 The kinetic safety factor in a Tokamak

We now apply equations 8.5 and 8.6 to a Tokamak configuration for a $\lambda = 1$ passing ion and we assume that $\rho_{\parallel} \ll 1$, the gyro-radius being small compared to the major radius. In a Tokamak $g \sim 1$ and $I \sim 0$; thus, keeping only the first order in ρ_{\parallel} we obtain from Eqs. 8.5 and 8.6:

$$\langle \tilde{q} \rangle_{\theta} \cong \left\langle \left[q \left(1 - v \frac{1}{B^2} \frac{dB}{d\psi_p} \right) \right] \Big|_{\psi_p^I} \right\rangle_{\theta} = \frac{m}{n}. \quad (8.9)$$

Note that in a Tokamak the drift term qvB'/B^2 is much smaller than q unless very high values of energy are reached. To lowest order we have that $\langle \tilde{q} \rangle_{\theta} = \langle q|_{\psi_p^I} \rangle_{\theta}$.

Now we write the safety factor q as a power series in ψ_p :

$$q(\psi_p) = \sum_k a_k \psi_p^k \quad (8.10)$$

and we evaluate the expression along the fast ion orbit by the substitution $\psi_p \rightarrow \psi_p^I = \psi_p + \sigma \cos \theta$ to calculate $q|_{\psi_p^I}$. If $\epsilon = \sigma(\psi_p)/\psi_p \ll 1$ then $(\psi_p^I)^k \cong \psi_p^k (1 + \epsilon k \cos \theta)$, keeping only first order in ϵ . Averaging over a full poloidal circumference $\Delta \theta = 2\pi$ to compute $\langle q|_{\psi_p^I} \rangle_{\theta}$, we obtain $\langle \tilde{q} \rangle_{\theta} = q$. Thus, there is no difference between the magnetic field q profile and $\langle \tilde{q} \rangle_{\theta}$ to lowest order. The ‘mean’ resonance radii for the fast ions are nearly the same as would be found for the magnetic field.

This does not mean that locally the resonances in fast ion space are in the same radial position as the resonances in the magnetic field space. At every θ , particle g.c. orbits are locally shifted according to Eq. 8.2, which means that resonances are radially shifted by the same quantity, outward for $\theta = 0$ and inward for $\theta = \pi$ when $\lambda = 1$ (the opposite happens when $\lambda = -1$). At $\theta = \pi/2$ no shift is observed. Thus the resonance position for a given θ is given by Eq. 8.8 with $\xi_{m,n} = 0$. When the term qvB'/B^2 becomes of the same order of q the complete formula 8.9 must be used and the local positions of the resonances are given by Eq. 8.8, including also a finite non-zero $\xi_{m,n}$.

As an example of application of the previous results, we consider a circular tokamak experimental situation similar to the circular ASDEX described in Chapter 7 ($R_0 = 1.72m$, $a = 0.63m$). The results are shown in Fig. 8.2. The mean positions of the resonances in fast ion space are nearly unchanged (see the q profiles in (a)), but, as it is clear from the fast ion motion in (b), the islands on the low field side are moved outward and inward on the HFS. Their coupling with the fast ions motion, with a shift $(1, 0)$, are responsible of generating new secondary islands and thus stochasticity in the fast ion phase space. The mean resonances position modifications may be visible only for higher q -values. For example the $(2, 1)$ island, in the fast ion orbit space, 'sees' about the same mean q profile and is subject mainly to the orbit shift (Eq. 8.2).

8.3 The kinetic safety factor in a RFP

In a RFP configuration the correct expression for \tilde{q} is always Eq. 8.5. Unless very high energy values are considered ($\gtrsim 1MeV$) this expression can be directly computed using the $v \rightarrow 0$ orbits, i.e. for $\psi_p^I = \psi_p$, because the shift σ is almost negligible. Note that g in the RFP varies from 1 to zero and I is comparable to gq and can not be neglected.

The resonance condition is given to the first order in $\rho_{||}$, for an ion with $\lambda = 1$, by:

$$\langle \tilde{q} \rangle_{\theta} \cong \left\langle \left[q - v(gq + I) \frac{1}{B^2} \frac{dB}{d\psi_p} \right] \Big|_{\psi_p^I} \right\rangle_{\theta} = m/n. \quad (8.11)$$

In the RFP the main effect is a strong difference between q and \tilde{q} due to the drift: thus, a new pattern of resonances appears in the \tilde{q} profile, which can be beneficial for fast ion confinement.

In Fig. 8.3-(a) a profile for the fast ions q (red), computed by Eq. 8.11 with $E = 20keV$, is compared with the magnetic field q (black) for the conditions of the MST experiment reported in [92] ($R_0 = 1.5m, a = 0.52m$). The \tilde{q}

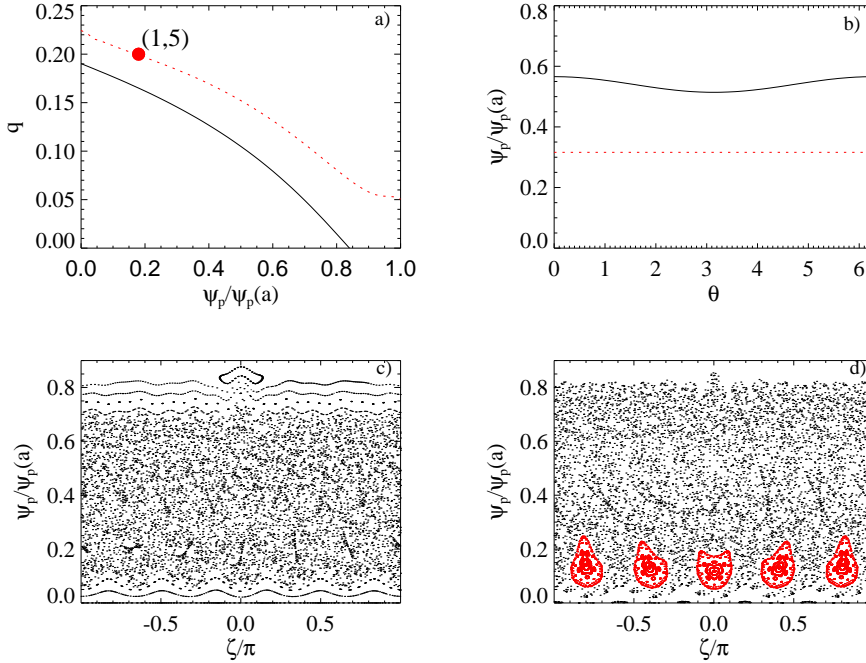


Figure 8.3: (a) Magnetic q profile and $\langle \tilde{q} \rangle_\theta$ for fast ions (dashed) for a RFP (MST) with $20keV$ and $B_0 = 0.5T$. (b) ψ_p^I vs θ for an ion with low energy (black) and for $E = 20keV$ (dashed) in a RFP. (c) Toroidal Poincaré for the magnetic field in the MST device and (d) in fast ion phase space.

profile is larger than q and the resonance $(1, 5)$ appears in the fast ion space while it is not present in the q profile. This result was obtained numerically in Chapter 6 and reported in [92].

The shift term has a very small effect compared with $\xi_{m,n}$ (from Eq.8.7) in this case. Fig. 8.3-(b) shows (solid line) the initial orbit for a low energy particle and also a fast ion orbit (dashed line); the poloidal flux is plotted vs θ . There is a large change in the mean poloidal flux position due to the drift term and a small modulation proportional to $\cos\theta$ due to the shift effect.

In the bottom of Fig.8.3 we report again the field line tracing with the ORBIT code. No islands are present and the field is mainly chaotic, but fast ions feel a new resonance and an island $(1, 5)$ appears, as shown in Fig. 8.3-(d). The position of the new island is in agreement with the prediction of Eq. 8.11.

In the fast ion orbit space there is therefore a healing of stochasticity near the plasma core, and a single helicity coherent structure appears, which is reminiscent of the analogous one which can be present in the magnetic field

and also leads to enhanced confinement of thermal particles.

8.3.1 A simple model of the toroidal drift

The different behavior of fast ions in a Tokamak and an RFP is a consequence of the predominant shift effect in the former and of the toroidal drift in the latter. Even in a Tokamak of the size of ITER [12], the toroidal drift experienced by a $1MeV$ from NBI shall produce a mean variation of \tilde{q} less than approximately the 5% respect to the magnetic q . This means that the displacement of the resonance positions is almost entirely due to the the shift effect which can reach an amplitude of $20cm$, inward on the HFS and outward on the LFS.

The toroidal drift, as we have already pointed out, is a consequence of the curvature and of the non-uniformity of the poloidal magnetic field, which produces a new velocity component v_D in the toroidal direction. Its effect for a particle moving with a parallel velocity v on a magnetic field helix with n poloidal turns in m toroidal transits can be easily visualized with a simple model. Such an (m, n) helix can be represented in space in a simplified cylindrical geometry by the parametric time (t) equation:

$$x(t) = r_s \cos(\omega t) \quad y(t) = r_s \sin(\omega t) \quad z(t) = \frac{m}{n} R_0 \omega t \quad (8.12)$$

where $z = R_0 \zeta$ refers to the toroidal direction, r_s is the mode resonant radius and $\omega = v/(r_s^2 + (mR_0/n)^2)^{1/2}$ is determined by the condition that $\sqrt{\dot{x}^2 + \dot{y}^2 + \dot{z}^2} = v$.

As long as the particle moves with its guiding velocity parallel to the magnetic field, its trajectory has obviously the same geometrical helicity (m, n) as that of \mathbf{B} . But this is not exactly the case if we consider the effect of the poloidal magnetic field which introduces a new component v_D of the velocity in the toroidal direction.

The final trajectory of the particle can be obtained by adding to $z(t)$ the term $v_D t$. Depending on the sign of \mathbf{v}_D with respect to \mathbf{B} , the fast ion trajectory is an ‘elongated’ (\mathbf{v} parallel to \mathbf{B} , Fig. 8.4) or ‘compressed’ (\mathbf{v} antiparallel to \mathbf{B}) helix. Thus, the number of poloidal turns in one toroidal transit is changed; the new q is then given by $m/n \pm |\Delta q|$. This variation in Δq is about of the same order for Tokamak and RFP, but it is negligible compared to the equilibrium q , while in the latter can reach 20 – 40% of the magnetic field q . This is why the toroidal drift effect in the RFP is much more important with respect to the Tokamak, where it is often negligible.

An approximate estimate of the toroidal drift velocity v_D may be derived in a cylindrical geometry where we consider only the effect of a poloidal

magnetic field $B_\theta(r)$ depending on the radial coordinate r . We consider a passing particle with velocity components v_θ/B_θ and $v_\phi \perp B_\theta$. It is subject to two different drift effects since the magnetic field is both curved and non uniform. For a particle with mass m and charge e the curvature drift in SI units is given by:

$$v_{D,1} = \frac{mv_\theta^2 \mathbf{R}_c \times \mathbf{B}}{eB^2 R_c^2} \simeq \frac{mv_\theta^2}{eB_\theta r} \quad (8.13)$$

in the toroidal direction, i.e. along the angle ϕ in a cylindrical geometry. The ∇B drift is also toroidal but its magnitude is given by:

$$v_{D,2} = \frac{mv_\phi^2}{2eB^3} \mathbf{B} \times \nabla B \simeq \frac{mv_\phi^2}{2eB_\theta^2} \frac{\partial B_\theta}{\partial r}. \quad (8.14)$$

The total toroidal drift is thus $v_D = v_{D,1} + v_{D,2}$ which we can insert in equation 8.12 for z , i.e. $z(t) = R_0\phi = \frac{m}{n}R_0\omega t + v_D t$. To have a variation of $\Delta\phi = 2\pi$ the variation in t is given by:

$$\Delta t = \frac{2\pi}{\frac{m}{n}\omega + \frac{v_D}{R_0}} \quad (8.15)$$

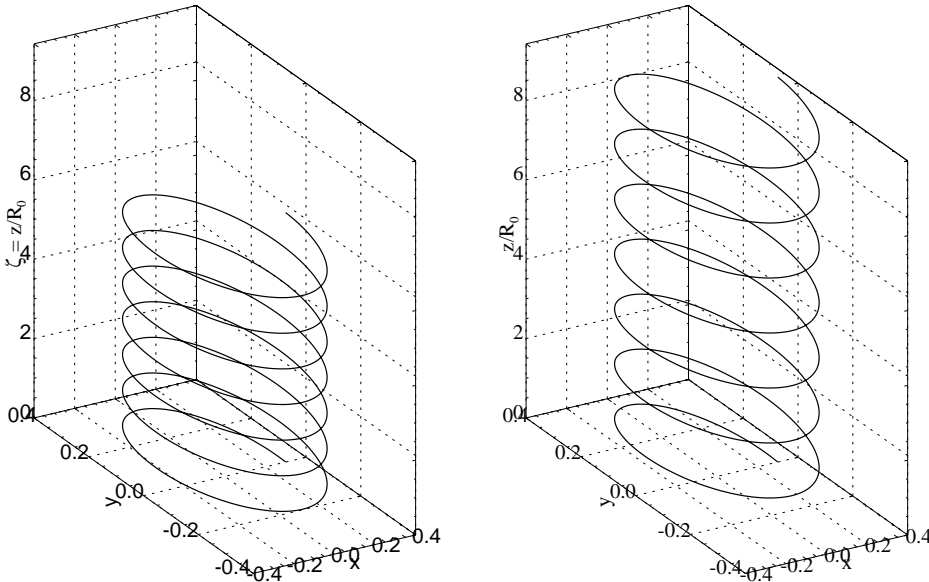


Figure 8.4: Left-hand-side: model of the helical wrapping of the magnetic field line along the toroidal direction; right-hand-side: orbit of a pitch 1 fast ion, obtained by adding the drift velocity v_D . The number of poloidal transits to cover the same toroidal distance is different in the two cases.

which means a variation in θ of:

$$\Delta\theta = \frac{2\pi\omega}{\frac{m}{n}\omega + \frac{v_D}{R_0}}. \quad (8.16)$$

The number of poloidal turns for one poloidal transit is thus:

$$\tilde{q} = \frac{\Delta\phi}{\Delta\theta} = \frac{m}{n} + \frac{v_D}{\omega R_0} \quad (8.17)$$

which clearly shows the increase of the standard safety factor by a term proportional to the drift velocity v_D . Using also the correct expression of ω we have for \tilde{q} :

$$\tilde{q} \simeq q + q \frac{m}{ve} \frac{1}{B_\theta} \left(\frac{v_\theta^2}{r} + \frac{v_\phi^2}{B_\theta} \frac{\partial B_\theta}{\partial r} \right) \quad (8.18)$$

where we have used the standard safety factor definition: $m/n = rB_\phi/(R_0B_\theta)$.

Thus the variation in q is given by $\Delta q \simeq q \frac{m}{ve} \frac{1}{B_\theta} \left(\frac{v_\theta^2}{r} + \frac{v_\phi^2}{B_\theta} \frac{\partial B_\theta}{\partial r} \right)$.

In RFP devices B_θ and B_ϕ are of the same order. But if we consider a region near the center then $B_\theta \simeq 0$, and the velocity of a passing particle is mostly in the toroidal direction, i.e. $v_\theta \simeq 0$ and $v_\phi \simeq v$. Thus Eq. 8.18 can be simplified in:

$$\tilde{q} \simeq q \left[1 + \frac{mv}{eB_\theta^2} \frac{\partial B_\theta}{\partial r} \right]. \quad (8.19)$$

Deuterons with $25keV$ energy have $v_D \simeq 2.2 \cdot 10^6 m/s$ and $\Delta q \simeq 0.05$. They generate new resonances in the fast ions space, since in the RFP $q \simeq 0.15$ near the center. The relative variation is thus $\Delta q/q \simeq 20 - 30\%$. In Tokamak near the center $\Delta q \simeq 0.1 - 0.2$ which is a variation of the same order of the RFP case but it is less than the 5% of a typical tokamak q profile which is usually greater than 1 and is much lower than the orbit shift effect.

8.3.2 Application to fast ions in RFX-mod

As a final example we apply Eq.8.11 to predict the fast ion confinement in the RFX-mod experiment for $25keV$ fast ions, the same energy used in the TPE-RX beam [107].

We consider first a standard $800kA$ discharge with a MH spectrum (magnetic perturbations are about 1% of $B_0 \approx 0.8T$). The corresponding safety factor is shown in Fig. 8.5 in black. The magnetic field has a stochastic region (Fig.8.6-l.h.s.), similar to the MST situation in Fig. 8.3, and the nearest resonance to the axis is the ($m = 1, n = -7$).

Eq. 8.11 is used to predict the $\langle \tilde{q} \rangle_\theta$ profile for the fast ions: they feel a new resonance ($1, -6$) near the axis, which is not present for the low

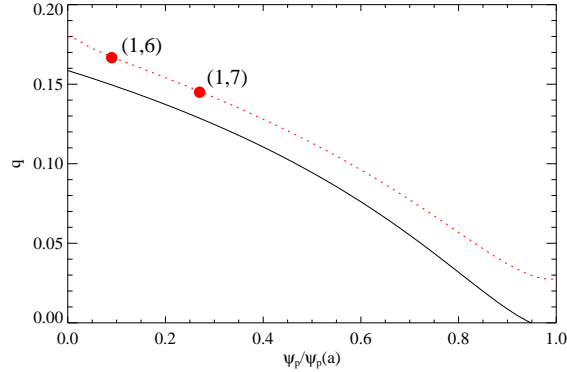


Figure 8.5: (a) Magnetic q profile and $\langle \tilde{q} \rangle_\theta$ for fast ions (red-dashed) in RFX-mod with $E = 25keV$ and $B_0 = 0.8T$.

energy particles. The plot of the kinetic q is shown in Fig. 8.5-(a) with a red dashed line. We have performed particle transport simulations in axisymmetric geometry, both for thermal ($\sim 300eV$) and fast ions ($\sim 25keV$) with random pitch initially deposited in a region ($\psi_p/\psi_p(a) \approx 0.1$) including the new resonant position $(1, -6)$. Classical and pitch angle collisions have been included too. Estimates of loss time have been performed with a loss surface placed at $\psi_p/\psi_p(a) \cong 0.5$. In our simulations, the loss time is $\tau_{TH} \cong 0.8ms$ for the thermal deuterons, to be compared with that of the $25keV$ ions of $\tau_{F,MH} \cong 3.8ms$.

A significant improvement is achieved if a $(1, -7)$ Quasi Single Helicity magnetic fluctuation spectrum is considered. The corresponding Poincaré for the magnetic field is shown in Fig. 8.7-l.h.s.; blue dots represent field lines forming the $(1, -7)$ island. On the right of this figure the Poincaré for the fast ions phase space: the magnetic island $(1, -7)$ is shifted outward while a new island $(1, -6)$ appears near the core. The reduced magnetic chaos in phase space corresponds to a loss time for fast ions, $\tau_{F,QSH}$, of $5.4ms$. As a QSH field is present, also thermal particles loss time is higher than MH, i.e. $\tau_{TH} \sim 1.3ms$.

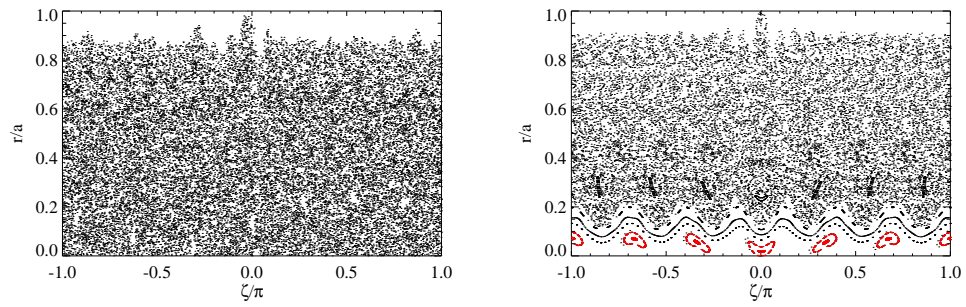


Figure 8.6: Left-hand-side: Poincaré in MH regime for a standard discharge of RFX-mod. Right-hand-side: fast ions 25keV phase space for the same discharge. An island $(1, -6)$ is visible near the core in red.

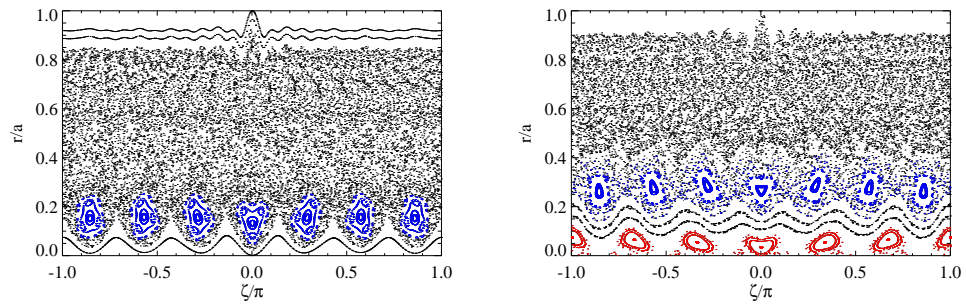


Figure 8.7: Left-hand-side: Poincaré in QSH regime for a standard discharge of RFX-mod. In blue the magnetic island $(1, -7)$. Right-hand-side: fast ions 25keV phase space for the same discharge. An island $(1, -6)$ is visible near the core in red together with the magnetic island $(1, -7)$ shifted outward.

Summary & Conclusions

Quasi Single Helicity regimes in the RFPs.

The simulations described in this Thesis allow to better understand the confinement improvement that can be obtained in QSH. Investigation was performed by analyzing both the magnetic field lines topology and the diffusion properties of test particles.

To study the QSH regimes in RFX-mod we have implemented in the ORBIT code the radial eigenfunctions profiles of the perturbations by solving the Newcomb equation in the real toroidal geometry. For high plasma current ($\geq 800kA$) magnetic islands of important size have been detected and their dimensions have also been confirmed by the tomographic diagnostics. In such scenario around the conserved helical magnetic surfaces a wide region of sticky magnetic field lines is present, which is still beneficial for the confinement of particles and energy.

For the MST device we have analyzed the effects on the magnetic topology when the Pulsed Poloidal Current Drive (PPCD) technique is applied. By ORBIT simulations we have found that there are interesting differences between the QSH regimes during standard and PPCD discharges. The computation of the loss time, in fact, shows that when the QSH appears in PPCD shots, a large portion of space is characterized by a higher loss time, even if the islands are of comparable size. This is mainly due to the consistent decrease of the secondary modes amplitudes when PPCD is applied which reduces the level of chaos also outside the island conserved surfaces.

Another phenomenon which shows the appearing of well-conserved he-

lical flux surfaces during QSH regimes is the emission of hard-x-ray with hundreds of keV due to the collisions between thermal ions and high energy electrons. Experimental data show the correlation between the emission of this radiation and the presence of QSH states in MST plasma with reversal parameter $F \sim 0$. The simulations by ORBIT have confirmed this behavior. The toroidal electric field amplitude is close to the so-called *Dreicer* limit over which electrons can be accelerated without limit. If electrons are deposited in the island region, ORBIT shows that a fraction of them can reach very high energy before escaping because of collisions or magnetic perturbations. The final spatial distribution of electrons clearly evidences that those more energetic ($\geq 30keV$) are distributed in the ζ and θ plane with the (m, n) helicity of the magnetic island.

Estimate of transport coefficients in SH regime

To quantify the improvement of the particle confinement in helical geometry we have performed transport simulations in a simplified geometry. A Single Helicity state (SH) has been considered: only one tearing mode is present while all the secondary modes are equal to zero. By ORBIT we have developed a sophisticated algorithm to reconstruct the real 3-D helical geometry of the magnetic island. Thermal ions and electrons have been deposited in the island O-Point and diffuse subjected to the pitch angle and classical collisions in the geometry of RFX-mod for a low plasma current equilibrium ($I_p \sim 600kA$).

With a steady state condition, i.e. a constant particle number in the island domain, we have calculated the ions and electrons perpendicular diffusion coefficients for several collision frequencies. In the RFX-mod scenario we find that $D_i^{isl} \sim 5m^2/s$ and $D_e^{isl} \sim 0.05m^2/s$ with a spread of the 30% depending also on the helicity of the island. An estimate of the ambipolar value by a geometric mean gives $D \sim 0.3m^2/s$, close to the values found in stellarator devices, with the correct scaling of equilibrium parameters and collisionality. This value must be compared with those typically measured in chaotic plasmas which are two order of magnitude greater ($\sim 30m^2/s$). A Single Helicity regime, thus, strongly affects positively the particles diffusion inside the islands. Even if indications of this behavior have been already suggested by previous analysis, it's the first time that numerical simulations have been performed in the real non axi-symmetric helical geometry.

Fast ions improved confinement in MST

Experiments in the MST device have shown that $20keV$ fast ions from NBI are characterized by a longer confinement time respect to those thermal. Simulations by ORBIT show that in fast ions phase space a magnetic island appears near the core. Even if the magnetic field of the plasma is in a multiple helicity regime, the fast ions see a QSH topology and thus are affected by its typical improved confinement properties. A totally different behavior has been observed in the Tokamak configuration: when instabilities are present, fast ions confinement is reduced; on the contrary, thermal particles are still well confined. We have studied this phenomenon in the Asdex-Upgrade Tokamak (AUG).

Fast ion losses in Asdex-Upgrade.

In the tokamak experiment AUG the interaction between Neoclassical Tearing Modes (NTM) and fast ions ($E \sim 90keV$) is responsible of the stochasticity in the fast ions space phase. In fact, the magnetic island generated by a NTM couples with the displacement of the fast ion (helicity $(1, 0)$). As a result many secondary islands appear in the fast ions phase space whose overlap may lead to stochasticity.

The loss of fast ions has been studied numerically by ORBIT both in a circular and D-shaped geometry of AUG. A better agreement has been found with simulations performed in the more realistic D-shaped geometry, which has required a modification of the code in order to deal with straight field line coordinates. An increase of the lost ions when an NTM is present has been observed, but even without the modes a fraction of ions is lost because of the drift due to their high energy or to collisions and ripple effects. Complete simulations in the D-shaped geometry with ripple and slowing down collisions, lasting for about $3ms$, show that the fraction of lost fast ions is about the 10% when the mode $(2, 1)$ is present, the 3% more than the equilibrium case. Final pitch angle distribution and toroidal localization are in a very good agreement with the experimental signals.

A parametrization study has been performed with different profile of the magnetic perturbation $\alpha(r)$. In fact, small variations of the perturbation profile can mean a different position for the O-Point of the magnetic island and thus a greater or lower level of chaos in the fast ion phase space. Also the rotation of the modes have been implemented in the code. Simulations with rotating modes confirm the results obtained with a fixed mode and show a slight dependence of the losses amount versus the mode frequency.

The simulations performed in this context for fast ions and NTM can

be easily adapted also for the analysis of other perturbations. An on going analysis is dedicated for example to the interaction between Toroidal Alfvén Eigenmodes (TAE) and fast ions from radio wave heating (ICRH).

The kinetic safety factor.

The different behavior of fast ions in Tokamak and RFP experiments has been explained in terms of guiding center drifts: the modifications of orbits caused by resonances with magnetic field perturbations are derived analytically for both configurations. The kinetic safety factor \tilde{q} profile felt by fast ion guiding centers, which controls the resonant interaction with perturbations, has been calculated.

The poloidal magnetic field introduces a drift in the toroidal direction for fast ions which is the cause of the modification of the standard q . While in tokamak the variation of \tilde{q} is of few % respect to the magnetic field q , in RFPs it can be also of the 30%. New resonances can thus appear that affect the fast ion orbits. The main consequence is the generation of a QSH state in the fast ion phase space. Simulations by ORBIT show that, if the magnetic field is in a QSH regime, the confinement time is still increased.

These results may be very useful in predicting the behavior of fast ions injection in the RFX-mod experiment. Estimation of the current drive and on the effects of different injection angles are still in progress.

APPENDIX A

Flux Coordinates

A.1 Reciprocal sets of vectors

The concept of reciprocal sets of vectors is a crucial building block for the description of vectors in curvilinear coordinates. We recall that the vectors $\mathbf{A}, \mathbf{B}, \mathbf{C}$ and $\mathbf{a}, \mathbf{b}, \mathbf{c}$ are called *reciprocal sets of vectors* if:

$$\mathbf{A} \cdot \mathbf{a} = \mathbf{B} \cdot \mathbf{b} = \mathbf{C} \cdot \mathbf{c} = 1$$

$$\mathbf{A} \cdot \mathbf{b} = \mathbf{A} \cdot \mathbf{c} = \mathbf{B} \cdot \mathbf{a} = \mathbf{B} \cdot \mathbf{c} = \mathbf{C} \cdot \mathbf{a} = \mathbf{C} \cdot \mathbf{b} = 0 \quad (\text{A.1})$$

Each vector of one set is orthogonal to two vectors of the other set, and produces a dot product of unity with the remaining vector of the other set. These relations are satisfied only if the two sets are each comprised of linearly independent vectors (non coplanar, nor parallel). This implies that their respective triple product $\mathbf{a} \cdot (\mathbf{b} \times \mathbf{c})$ and $\mathbf{A} \cdot (\mathbf{B} \times \mathbf{C})$ are non zero. From the relations A.1 we can calculate the set $\{\mathbf{a}, \mathbf{b}, \mathbf{c}\}$ from its reciprocal set $\{\mathbf{A}, \mathbf{B}, \mathbf{C}\}$:

$$\mathbf{a} = \frac{\mathbf{B} \times \mathbf{C}}{\mathbf{A} \cdot (\mathbf{B} \times \mathbf{C})}, \quad \mathbf{b} = \frac{\mathbf{C} \times \mathbf{A}}{\mathbf{B} \cdot (\mathbf{C} \times \mathbf{A})}, \quad \mathbf{c} = \frac{\mathbf{A} \times \mathbf{B}}{\mathbf{C} \cdot (\mathbf{A} \times \mathbf{B})}. \quad (\text{A.2})$$

It's easy to check that this choice for $\{\mathbf{a}, \mathbf{b}, \mathbf{c}\}$ satisfies relations A.1. Each set of vectors can be used to express any 3-D vector as a linear combination

of them; hence the two sets qualify as legitimate basis vector in 3-D space. Indeed, any vector \mathbf{W} can be written as:

$$\mathbf{W} = (\mathbf{W} \cdot \mathbf{a})\mathbf{A} + (\mathbf{W} \cdot \mathbf{b})\mathbf{B} + (\mathbf{W} \cdot \mathbf{c})\mathbf{C} \quad (\text{A.3})$$

or

$$\mathbf{W} = (\mathbf{W} \cdot \mathbf{A})\mathbf{a} + (\mathbf{W} \cdot \mathbf{B})\mathbf{b} + (\mathbf{W} \cdot \mathbf{C})\mathbf{c} \quad (\text{A.4})$$

Specializing to Cartesian coordinate system, the set of unit basis vector is reciprocal to itself.

Now consider a transformation $\mathbf{R}(\mathbf{u}^1, \mathbf{u}^2, \mathbf{u}^3)$ by means of which any point, determined by the position vector \mathbf{R} of 3-D space, is expressed as a function of three parameters u^1, u^2, u^3 . By expanding \mathbf{R} in its components x, y, z in a Cartesian coordinate system, we can rewrite this transformation as

$$x = x(u^1, u^2, u^3) \quad y = y(u^1, u^2, u^3) \quad z = z(u^1, u^2, u^3). \quad (\text{A.5})$$

If the transformation is one-to-one, it can be inverted:

$$u^1 = u^1(x, y, z) \quad u^2 = u^2(x, y, z) \quad u^3 = u^3(x, y, z). \quad (\text{A.6})$$

For the transformation to be invertible, the functions x, y, z must have continuous partial derivatives with respect to u^1, u^2, u^3 and the determinant made up by the nine partial derivatives $\partial x/\partial u^1, \partial x/\partial u^2, \partial x/\partial u^3, \partial y/\partial u^1, \dots$ must be no zero. Below we shall call this determinant the Jacobian J of the transformation. Equation A.4 shows that a certain point with Cartesian coordinates (x, y, z) can be described uniquely by the independent parameters (u^1, u^2, u^3) , so they are coordinates as well (we'll call them *curvilinear* as a generalization of *rectilinear*). In the curvilinear system there are three naturally occurring families of *coordinate surfaces* obtained when one coordinate u^i is held fixed while the other two are varied continuously. The equations for these surfaces are:

$$\begin{aligned} u^1 &= c^1 && (u^2, u^3 \text{ variable, } c^1 \text{ arbitrary constant}) \\ u^2 &= c^2 && (u^1, u^3 \text{ variable, } c^2 \text{ arbitrary constant}) \\ u^3 &= c^3 && (u^2, u^1 \text{ variable, } c^3 \text{ arbitrary constant}) \end{aligned}$$

Analogously, three families of *coordinate curves* are produced when one coordinate u^i is allowed to vary while the other two u^j, u^k are held fixed. The equations are:

$$\begin{aligned} u^2 &= c^2, & u^3 &= c^3 & (u^1 \text{ variable}) \\ u^3 &= c^3, & u^1 &= c^1 & (u^2 \text{ variable}) \\ u^1 &= c^1, & u^2 &= c^2 & (u^3 \text{ variable}) \end{aligned}$$

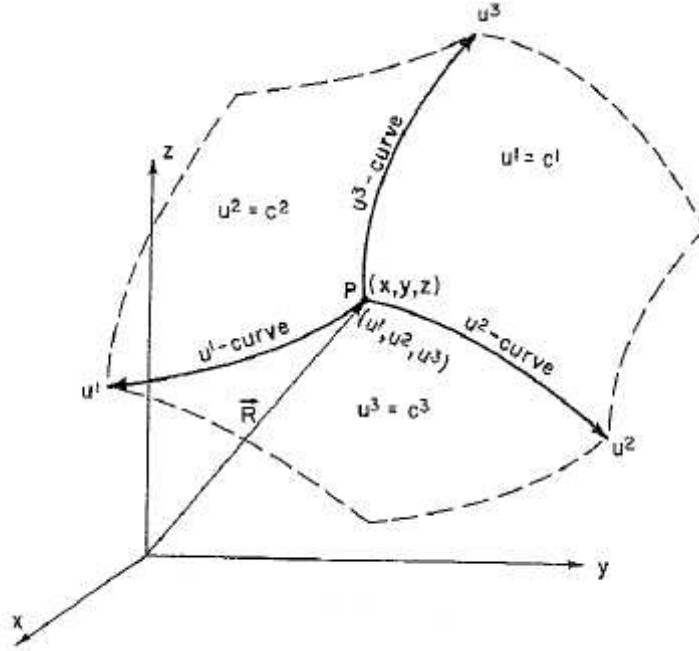


Figure A.1: General curvilinear system with coordinates (u^1, u^2, u^3) . The coordinates curves and coordinate surfaces are represented with respect to a Cartesian system with coordinates (x, y, z) .

The direction in which a variable point of the curve moves as u^i is increased is taken to be the positive direction along that coordinate curve. The general coordinate system is summarized in Fig. A.1. If the coordinate curves intersect at right angles, then the curvilinear system is called *orthogonal*. Examples of simple curvilinear coordinate systems are the familiar cylindrical and spherical systems. These are orthogonal.

Consider the system of generalized coordinates u^1, u^2, u^3 shown in Fig. A.1. We define a basis at a point P , determined by the position of the vector R , as any set of vectors $\mathbf{e}_1, \mathbf{e}_2, \mathbf{e}_3$ of fixed length pointing in the positive direction of the coordinate curves. The *basis vectors* $\mathbf{e}_1, \mathbf{e}_2, \mathbf{e}_3$ are tangent vectors of the coordinate curves at the point P . Simple differential geometry shows that we can choose as basis vectors:

$$\mathbf{e}_1 = \frac{\partial \mathbf{R}}{\partial u^1}; \quad \mathbf{e}_2 = \frac{\partial \mathbf{R}}{\partial u^2}; \quad \mathbf{e}_3 = \frac{\partial \mathbf{R}}{\partial u^3}; \quad (\text{A.7})$$

This definitions is consistent with the requirement that a set of basis vectors must be linearly independent. This basis is also *local* in the sense that it varies from point to point. Note that the tangent basis vector \mathbf{e}_i has a subscript but the coordinates u^i are represented with a superscript. Also, in

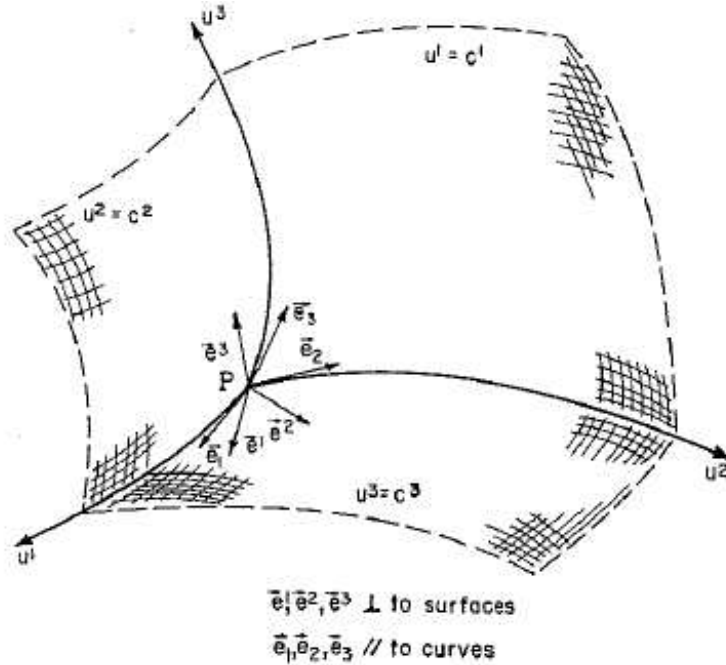


Figure A.2: Basis vector \mathbf{e}^i and \mathbf{e}_j at point P . The contravariant basis vector are perpendicular to the constant coordinate surfaces; the covariant basis are parallel to the coordinate curves.

general, these basis vectors are neither orthogonal nor of unit length, nor even dimensionless. Only in coordinate systems with straight lines as coordinate *curves*, i.e. with rectangular and oblique coordinate lines, do the basis vectors not vary from point to point.

It has now to be defined the reciprocal basis vectors. In order to do this we must recall that the gradient $\nabla\phi$ of a scalar function ϕ is defined so that the differential $d\phi$ is given by $d\phi = \nabla\phi \cdot d\mathbf{R}$. Let $\phi = u^i$, we obtain:

$$du^i = \nabla u^i \cdot d\mathbf{R}. \quad (\text{A.8})$$

If we consider the position vector R as a function of u^i we find from the chain rule that:

$$d\mathbf{R} = \frac{\partial \mathbf{R}}{\partial u^j} du^j = \mathbf{e}_j du^j \quad (\text{A.9})$$

where we have used the definition of \mathbf{e}_j given in A.7 (Einstein's convention used hereafter). Substitution of $d\mathbf{R}$ given by A.9 in A.8 leads to:

$$du^i = \nabla u^i \cdot \mathbf{e}_j du^j, \quad (\text{A.10})$$

which can hold only if:

$$\nabla u^i \cdot \mathbf{e}_j = \delta_j^i. \quad (\text{A.11})$$

\mathbf{e}_j form a reciprocal set of vectors as defined in A.1. Therefore, we define the set ∇u^i as the reciprocal-basis vectors:

$$\mathbf{e}^i = \nabla u^i. \quad (\text{A.12})$$

It's important to note that while the basis vectors \mathbf{e}_i are tangent to the u^i coordinate curves, the reciprocal basis vectors \mathbf{e}^i are *perpendicular to the coordinate surfaces* $u^i = c^i$. The two sets of basis vectors we have found have been recognized as reciprocal sets of vectors and allow to calculate each vector of one set if the three vectors of the other set are known. Thus we have:

$$\nabla u^i = \frac{\mathbf{e}_j \times \mathbf{e}_k}{\mathbf{e}_i \cdot (\mathbf{e}_j \times \mathbf{e}_k)} = \mathbf{e}^i \quad (\text{A.13})$$

and:

$$\frac{\partial \mathbf{R}}{\partial u^i} = \frac{\mathbf{e}^j \times \mathbf{e}^k}{\mathbf{e}^i \cdot (\mathbf{e}^j \times \mathbf{e}^k)} = \mathbf{e}_i. \quad (\text{A.14})$$

According to our earlier discussions, a vector can be written as a linear combination of the vectors from either of the (reciprocal) sets of basis vectors. From A.3 and A.4 for any vector \mathbf{D} we can write:

$$\mathbf{D} = (\mathbf{D} \cdot \mathbf{e}_i) \mathbf{e}^i = (\mathbf{D} \cdot \mathbf{e}^i) \mathbf{e}_i \quad (\text{A.15})$$

The terms $(\mathbf{D} \cdot \mathbf{e}_i) = D_i$ are called the *covariant components* of the vector D while the $(\mathbf{D} \cdot \mathbf{e}^i) = D^i$ are called *contravariant components*. Any vector in 3-D space can always be defined by its contravariant or its covariant components.

The vector $d\mathbf{R}$ connecting the two positions defined by \mathbf{R} and $\mathbf{R} + d\mathbf{R}$ is represented naturally by its contravariant components du^i , as obtained by the chain rule in Eq.A.9. But it can also be written by its covariant components:

$$(d\mathbf{R})_i = (d\mathbf{R} \cdot \mathbf{e}_i) = du^j \frac{\partial \mathbf{R}}{\partial u^j} \cdot \mathbf{e}_i = \mathbf{e}_i \cdot \mathbf{e}_j du^j = g_{ij} du^j \quad (\text{A.16})$$

where we have introduced the *metric tensor* g_{ij} given by the dot product of the basis vector \mathbf{e}_i and \mathbf{e}_j .

The normal way to decompose the gradient is by its covariant components. In fact you have:

$$\nabla \phi = \frac{\partial \phi}{\partial u^i} \nabla u^i = \frac{\partial \phi}{\partial u^i} \mathbf{e}^i \quad (\text{A.17})$$

but we can write it also in the contravariant components as shown below:

$$(\nabla \phi)_i = \nabla \phi \cdot \mathbf{e}^i = \frac{\partial \phi}{\partial u^j} \nabla u^j \cdot \mathbf{e}^i = \mathbf{e}^i \cdot \mathbf{e}^j \frac{\partial \phi}{\partial u^j} = g^{ij} \frac{\partial \phi}{\partial u^j} \quad (\text{A.18})$$

where $g^{ij} = \mathbf{e}^i \cdot \mathbf{e}^j$. The Metric Coefficients g^{ij} and g_{ij} form the backbone of the general curvilinear coordinate systems. They determine the differential arc length along a curve, they allow us to switch back and forth between the covariant and contravariant components of a vector, and they will provide us with a mean to calculate the dot and cross products of two vectors.

It is common practice to call the tangent vector \mathbf{e}_i the covariant-basis vectors, and the reciprocal vector \mathbf{e}^i the contravariant-basis vectors. (But it's only a convenience, each vector can always be written in terms both of covariant and contravariant components, and so the basis too).

In analogy with a general relativistic treatment we can also introduce the concepts of triads; they are important to find the relations between the coordinate quantities and the ones measured by a physical observer. For this latter it is natural and convenient to use a local system of Cartesian coordinate axes, which provide him with an instantaneous inertial frame. The result of measurement can be compared with the invariant projection on these axes of the vector which characterizes the phenomenon under consideration. In our case a triad is a simple orthonormal system of three vectors, $\mathbf{e}_{\hat{a}}$, which satisfy the condition:

$$\mathbf{e}_{\hat{a}} \cdot \mathbf{e}_{\hat{b}} = g_{\alpha\beta} e_{\hat{a}}^{\alpha} e_{\hat{b}}^{\beta} = \delta_{ab}. \quad (\text{A.19})$$

A dual triad can be defined naturally as

$$\mathbf{e}^{\hat{a}} = \delta^{ab} \mathbf{e}_{\hat{b}}. \quad (\text{A.20})$$

Below, the Jacobian definition and some important relationship between contravariant and covariant components are reported which could be useful in the following sections and in the Thesis. More details about the vectorial operations to obtain these results are available in [108].

A.1.1 Metric Coefficients and their properties

1. Square of the arc length:

$$dl^2 = g_{ij} du^i du^j \quad (\text{A.21})$$

2. Change of components:

$$D_i = D^j g_{ij} \quad D^i = D_j g^{ij} \quad (\text{A.22})$$

3. Determinant:

$$g = \det[g_{ij}] \quad g^{-1} = \det[g^{ij}] \quad (\text{A.23})$$

4. Dot product:

$$\mathbf{A} \cdot \mathbf{B} = g_{ij} A^i B^j = g^{ij} A_i B_j \quad (\text{A.24})$$

5. Cross product:

$$(\mathbf{A} \times \mathbf{B})_k = \varepsilon_{ijk} \sqrt{g} A^i B^j \quad (\text{A.25})$$

and:

$$(\mathbf{A} \times \mathbf{B})^k = \frac{\varepsilon_{ijk}}{\sqrt{g}} A_i B_j \quad (\text{A.26})$$

6. Divergence:

$$\nabla \cdot \mathbf{A} = \frac{1}{J} \frac{\partial}{\partial u^i} (J A^i) \quad (\text{A.27})$$

7. Curl:

$$\nabla \times \mathbf{A} = \frac{\epsilon^{ijk}}{J} \frac{\partial A_j}{\partial u^i} \mathbf{e}_k \quad (\text{A.28})$$

A.1.2 The Jacobian

1. Definition:

$$J = \frac{\partial \mathbf{R}}{\partial u^1} \cdot \frac{\partial \mathbf{R}}{\partial u^2} \times \frac{\partial \mathbf{R}}{\partial u^3} \quad (\text{A.29})$$

2. Inverse transformation:

$$J^* = \nabla u^1 \cdot \nabla u^2 \times \nabla u^3 \quad (\text{A.30})$$

3. Main properties:

$$J^* = J^{-1} \quad (\text{A.31})$$

$$e^i = \frac{1}{J} (e_j \times e_k) \quad (\text{A.32})$$

$$e_i = J (e^j \times e^k) \quad (\text{A.33})$$

$$g = (J)^2 \quad (\text{A.34})$$

A.1.3 Differential elements

1. Arc Length along a coordinate curve u^i :

$$dl(i) = \sqrt{g_{ii}} du^i \quad \text{no Einstein's summation} \quad (\text{A.35})$$

2. Area Element in the coordinate surface u^i :

$$dS(i) = \sqrt{g_{jj}g_{kk} - g_{jk}^2} du^j du^k \quad \text{no summation over } j \text{ or } k \quad (\text{A.36})$$

3. Volume Element

$$dS(i) = \sqrt{g} du^1 du^2 du^3 \quad (\text{A.37})$$

A.2 Magnetic Field Structure

A magnetic field line is by definition a curve whose tangent at any point is parallel to the magnetic field vector \mathbf{B} . This property can be translated into mathematical terms as follows:

$$\mathbf{B} \propto d\mathbf{R} \quad \text{or} \quad \mathbf{B} = cd\mathbf{R} \quad (\text{A.38})$$

where c is a proportionality constant and $d\mathbf{R}$ is a differential vector tangent to the field line. Equivalently we can write:

$$\mathbf{B} \times d\mathbf{R} = 0 \quad (\text{A.39})$$

Using the contravariant components of $\mathbf{B}(B^1, B^2, B^3)$ and $d\mathbf{R}(du^1, du^2, du^3)$, either of the above equations leads to:

$$\frac{B^1}{du^1} = \frac{B^2}{du^2} = \frac{B^3}{du^3} = c. \quad (\text{A.40})$$

Noting that $B^i = \mathbf{B} \cdot \nabla u^i$ we can also write:

$$\frac{\mathbf{B} \cdot \nabla u^1}{du^1} = \frac{\mathbf{B} \cdot \nabla u^2}{du^2} = \frac{\mathbf{B} \cdot \nabla u^3}{du^3} \quad . \quad (\text{A.41})$$

If we parametrize the field line by the arc length l , the tangent vector $d\mathbf{R}/dl$ is a unit vector, usually denoted by \mathbf{B}/B or by $\hat{\mathbf{t}}$:

$$\frac{\mathbf{B}}{B} = \frac{d\mathbf{R}}{dl} \quad \text{derivation along } \mathbf{B} \quad . \quad (\text{A.42})$$

From relation A.38 we see that the constant c is equal to B/dl , so that the *equation of a magnetic field line* is, in its component form:

$$\frac{B}{dl} = \frac{B^1}{du^1} = \frac{B^2}{du^2} = \frac{B^3}{du^3}, \quad (\text{A.43})$$

or

$$\frac{B}{dl} = \frac{\mathbf{B} \cdot \nabla u^1}{du^1} = \frac{\mathbf{B} \cdot \nabla u^2}{du^2} = \frac{\mathbf{B} \cdot \nabla u^3}{du^3} \quad . \quad (\text{A.44})$$

Any surface that is traced out by a series of magnetic field lines is called a *magnetic surface*. In practice, however, the name is referred for *closed* surfaces of a cylindrical or toroidal type. In that context a magnetic surface is also called a flux surface.

In a toroidal system, a magnetic surface is a surface which is ergodically covered by non-closing magnetic field lines. Between these surfaces we can

define other surfaces that contain field lines that close upon themselves after one or several transit around the machine. Such surfaces are called *rational surfaces*, because the ratio of the number of poloidal transits to the number of toroidal transits of a field line is a rational number. The other surfaces are called *irrational surfaces*. Since the set of real number is dense, a rational surface can be approximated very accurately by a nearby irrational surface. Suitable magnetic surfaces are usually taken to be a requirement for adequate plasma equilibrium as described by the MHD equation:

$$\mathbf{j} \times \mathbf{B} = \nabla p \quad . \quad (\text{A.45})$$

These magnetic surfaces are constant pressure surfaces, since $\mathbf{B} \cdot \nabla p = 0$ and the current-density lines lie on these surfaces because $\mathbf{j} \cdot \nabla p = 0$. Violation of these conditions leads to the formation of an island-chain configuration and possibility to ergodic behavior of field lines in a volume in the vicinity of the rational surfaces.

It is questionable whether the simple MHD equilibrium model is not a too crude approximation or about the existence of the magnetic surfaces; from a pragmatcal point of view we assume that a suitable set of nested toroidal magnetic surfaces is present, whose cross-section in a poloidal plane forms a set of smooth closed curves. The degenerate magnetic surface with the limiting zero values is called the *magnetic axis*.

A.3 The Elementary Toroidal Coordinates

We have seen that in 3-D space to locate a point uniquely a coordinate system consists of three suitable families of surfaces such that a point is defined by the intersection of three surfaces, one for each family. The coordinate curves are the intersection lines of two coordinate surfaces (see fig A.1 for an example).

The best known coordinate system is the *pseudo-toroidal* or elementary toroidal coordinate system. This is essentially a *toroidalized* cylindrical system with coordinates (R, ϕ, z) as shown in Fig. A.3. The cylindrical angle is measured from the x -axis towards the y -axis. The *toroidalization* is done by replacing R and z by (r, θ) . Since, conventionally, θ and ζ are taken as the second and third coordinates respectively, whereas $\phi = \zeta_c$ is the second in the cylindrical system, the angle ζ is measured in the positive sense from the y -axis towards the x -axis (i.e. $\zeta = \pi/2 - \phi$).

The relations between the Cartesian coordinates (x, y, z) and the ones of the elementary system (r, θ, ζ) are:

$$x = (R_0 + r \cos \theta) \sin \zeta \quad (\text{A.46})$$

$$y = (R_0 + r \cos \theta) \cos \zeta \quad (\text{A.47})$$

$$z = r \sin \theta \quad (\text{A.48})$$

with R_0 being the major radius.

In theoretical fusion-plasma physics, it is customary to choose as the first family of coordinate surfaces the magnetic surfaces, regardless of their shape. We label these magnetic surfaces by a parameter ϱ which is constant on them (toroidal flux, poloidal flux, pressure etc...). Thus, on every magnetic surface, $u^1 = \varrho = \text{constant}$. The other coordinates are $u^2 = \theta$ and $u^3 = \zeta$. The $u^2 = \text{constant}$ surfaces are based on the magnetic axis and in general are partial-cone like surfaces. These surfaces can be thought of as being produced by bending, stretching or squeezing the partial cones of the elementary toroidal coordinate system in Fig. A.3 (where θ here is the usual poloidal angle) provided that each surface crosses the toroidal magnetic surface only once.

Likewise, the $u^3 = \text{constant}$ are a generalized version of the usual toroidal angle in the elementary system (see also fig A.3). Coordinate curves for θ and ζ are constructed as usual via intersections of coordinate surfaces. With the coordinate surfaces constructed as explained above, we obtain *closed curves* for the coordinate curves as shown in Fig. A.4. We require that the functions $\theta(x, y, z)$ and $\zeta(x, y, z)$ of the transformation from x, y and z to θ and ζ , have continuous first derivatives, implying that the tangents to the curves and the gradients to the surfaces are continuous vector fields. It should be noted that for place positioning it is sufficient to isolate a $\varrho = \text{constant}$ surface and lay out a grid of θ and ζ curves. However this is not enough for a proper description of vectors. With the grid of contours, the covariant (tangent) basis are determined at every point, but the contravariant (reciprocal) basis vector ∇u^i can only be found if the $u^2 = \text{constant}$ and $u^3 = \text{constant}$ surfaces are known.

A.4 Flux Coordinates

We can always construct a suitable set of new angle functions $\tilde{\theta} = \tilde{\theta}(\mathbf{R})$ and $\tilde{\zeta} = \tilde{\zeta}(\mathbf{R})$ by adding functions which are periodic with a period of 2π to the original θ and ζ :

$$\tilde{\theta} = \theta + f(\varrho, \theta, \zeta) \quad (\text{A.49})$$

$$\tilde{\zeta} = \zeta + g(\varrho, \theta, \zeta). \quad (\text{A.50})$$

The periodicity of f and g in both θ and ζ is equivalent to stating that f and g are single valued in (θ, ζ) . Because of this single valuedness the (θ, ζ) coordinate curves are deformed in such a way that the new coordinates $(\tilde{\theta}, \tilde{\zeta})$ have

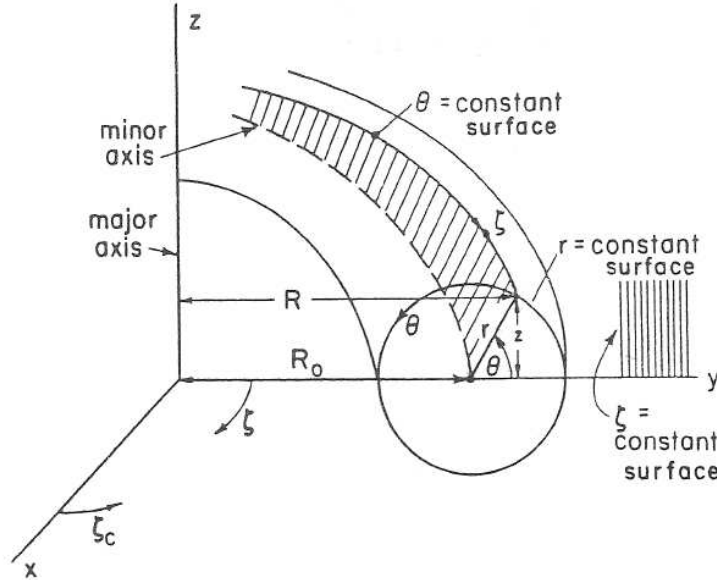


Figure A.3: Coordinate curves and surfaces of the elementary cylindrical-toroidal system.

proper curves as well, making them acceptable coordinates. The reason for working in these coordinate systems is straightforward. To perform analytic calculations, it is convenient to choose a *natural* coordinate system, such that in that coordinate system the geometry of the problem under consideration becomes simple. In theoretical plasma physics computations, it is very helpful to choose the $\theta(x, y, z)$ and the $\zeta(x, y, z)$ functions so as the magnetic field lines (which oscillate in the elementary toroidal coordinate system) appear as *straight lines*. This means that along a field line, $d\theta/d\zeta$ is a constant (precisely a flux function), for that choice of θ and ζ functions. It's customary to call coordinates in which the magnetic field is straight *magnetic coordinates* or *flux coordinates*.

A convenient way to label the magnetic surfaces is by means of magnetic flux. There are several magnetic fluxes which label a flux surface in a toroidal device uniquely. Assume that an arbitrary $(\theta(x, y, z), \zeta(x, y, z))$ coordinate system has been established for the angular variables. First, there is the *toroidal flux*:

$$\Psi_{tor} = \int_{S_{tor}} \mathbf{B} \cdot d\mathbf{S} \quad (\text{A.51})$$

where S_{tor} is the surface produced by cutting the flux surface with a poloidal surface $\zeta = \text{constant}$. Next, the poloidal flux inside and outside a flux surface

may be used. The poloidal flux inside the flux surface S_{pol}^r , e.g. through a ribbon at constant θ between the magnetic axis and the surface, is given by:

$$\Psi_{pol}^r = \int_{S_{pol}^r} \mathbf{B} \cdot d\mathbf{S} \quad (\text{A.52})$$

where the superscript r refers to the *ribbon*. S_{pol}^r is the part of a θ =constant surface that lies within the flux surface under consideration. The poloidal flux outside the flux surface is obtained by integrating \mathbf{B} over a disk-like surface that is tangent to the flux surface everywhere, and is bounded by a ζ coordinate curve on the flux surface S_{pol} :

$$\Psi_{pol}^d = \int_{S_{pol}^d} \mathbf{B} \cdot d\mathbf{S}. \quad (\text{A.53})$$

Note that:

$$d\Psi_{pol}^r = -d\Psi_{pol}^d. \quad (\text{A.54})$$

It's often used also the q factor (average number of poloidal transit for one toroidal transit) which is equal also to:

$$q = \frac{\delta\Psi_{tor}}{\delta\Psi_{pol}^r} = \frac{\nabla\Psi_{tor} \cdot d\mathbf{R}}{\nabla\Psi_{pol}^r \cdot d\mathbf{R}} \quad (\text{A.55})$$

where \mathbf{R} is an arbitrary position vector. If \mathbf{B} is straight in (θ, ζ) , it follows from the definition of q :

$$\frac{d\zeta}{d\theta} = q(\varrho) \quad . \quad (\text{A.56})$$

The equation of field lines A.44 requires that we always have:

$$\frac{d\theta}{d\zeta} = \frac{B^\theta}{B^\zeta} = \frac{\mathbf{B} \cdot \nabla\theta}{\mathbf{B} \cdot \nabla\zeta}. \quad (\text{A.57})$$

Using equations A.57 and A.56 it's possible to prove the validity of the following relation (see [108]):

$$q = \frac{\dot{\Psi}_{tor}}{\dot{\Psi}_{pol}} \quad (\text{A.58})$$

where the dot represents the derivative with respect to the chosen flux surface label ϱ .

The well-known expression for the safety factor q :

$$q = \frac{rB_T}{RB_p} \quad (\text{A.59})$$

is a lowest order approximation. It's rigorously correct only in an axisymmetric tokamak with circular cross section flux-surfaces where r is measured from the center of the circular flux surface, R is the distance from the major axis to a point on the surface, $B_T = (\mathbf{B} \cdot \hat{\zeta}_e)$, $B_P = (\mathbf{B} \cdot \hat{\theta}_e)$ where θ_e and ζ_e are the elementary angles based on the center of the surface.

A.5 Straight Field Line Coordinates

We have defined above the toroidal flux coordinates as a set of poloidal and toroidal angles θ_f and ζ_f chosen such that the equation of a field line is that of a straight line in those coordinates. In this paragraph we'll give more details about the way to define these coordinates. To construct the function $\theta_f(\mathbf{R})$ and $\zeta_f(\mathbf{R})$ we suppose the magnetic field \mathbf{B} is known completely and that θ and ζ are arbitrary angle coordinates. The first coordinate of the system will be the flux-surface label ϱ , which stands for any flux-surface function and can be replaced anywhere by a quantity such as the poloidal or the toroidal flux. The angles θ and ζ on the surface are defined by *multiple-valued functions*, in the sense that a point on the flux surface has (θ, ζ) coordinates equal to $(\theta + 2\pi m, \zeta + 2\pi n)$ with (m, n) integer. Their gradients must be single valued, however.

We write the magnetic field in terms of its contravariant components:

$$\mathbf{B} = B^\varrho \mathbf{e}_\varrho + B^\theta \mathbf{e}_\theta + B^\zeta \mathbf{e}_\zeta \quad (\text{A.60})$$

but B^ϱ is zero from the definition of a flux surface, so from the relation A.14 and A.34 we can write:

$$\mathbf{B} = B^\theta J(\nabla\zeta \times \nabla\varrho) + B^\zeta J(\nabla\varrho \times \nabla\theta) \quad (\text{A.61})$$

The two components B^θ, B^ζ are not independent because of the zero divergence of \mathbf{B} . The $\nabla \cdot \mathbf{B} = 0$ relation suggests that B^θ, B^ζ are derived from a single function $\nu(\theta, \varrho, \zeta)$ as follows:

$$B^\theta = -\frac{1}{J} \frac{\partial \nu}{\partial \zeta}, \quad B^\zeta = \frac{1}{J} \frac{\partial \nu}{\partial \theta}. \quad (\text{A.62})$$

Inserting this expression in A.61 we obtain:

$$\mathbf{B} = \nabla\varrho \times \left(\frac{\partial \nu}{\partial \zeta} \nabla\zeta + \frac{\partial \nu}{\partial \theta} \nabla\theta \right) \quad (\text{A.63})$$

Adding a term proportional to $\nabla\varrho$ in the brackets leaves \mathbf{B} unchanged because $\nabla\varrho \times \nabla\varrho = 0$; thus we can use $\nabla\nu = (\partial\nu/\partial\varrho)\nabla\varrho + (\partial\nu/\partial\theta)\nabla\theta +$

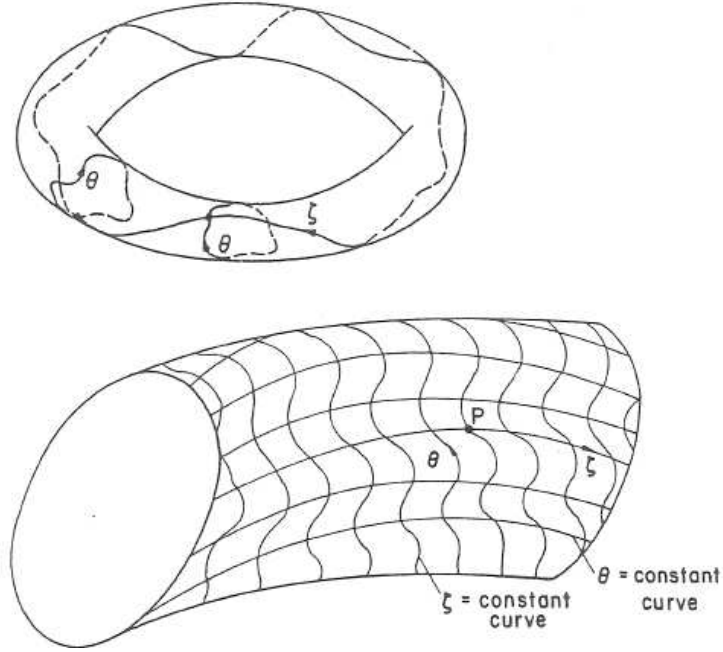


Figure A.4: Position location on a toroidal surface based on a grid constructed for generalized angles θ and ζ .

$(\partial\nu/\partial\zeta)\nabla\zeta$ and then write simply:

$$\mathbf{B} = \nabla\varrho \times \nabla\nu \quad (\text{A.64})$$

which is also called Clebsh form of the magnetic field. (Remember this is a contravariant form!). This equation states that the \mathbf{B} lines lie on constant ν surfaces. If we substitute A.62 in the equation A.43 then: $d\nu = 0$ on a flux surface. Hence the equation of a field line lying on a flux surface $\varrho = \varrho_0$ is

$$\nu(\varrho_0, \theta, \zeta) = \text{constant} \quad (\text{A.65})$$

From the expression in A.64 we can infer what form the function ν must have. \mathbf{B} in fact is a physical quantity and is thus single valued, i.e., its components must be periodic in (θ, ζ) . We need not to require the gradient of ν to be single valued but $\nabla\varrho \times \nabla\nu$ must be. This can be possible if the ν function has only the first order in θ and ζ in a polynomial series expansion and thus:

$$\nu(\varrho_0, \theta, \zeta) = B(\varrho)\theta + C(\varrho)\zeta + \tilde{\nu}(\varrho_0, \theta, \zeta). \quad (\text{A.66})$$

The terms $B(\varrho)$ and $C(\varrho)$ are determined from equations A.62 and the definitions of the toroidal A.51 and poloidal magnetic flux A.52-A.53, as shown

with details in [108]: $B(\varrho) = \dot{\Psi}_{tor}/2\pi$, $C(\varrho) = -\dot{\Psi}_{pol}^r/2\pi$. $\tilde{\nu}(\varrho_0, \theta, \zeta)$ is a periodic function in θ, ζ . Thus we can write:

$$\nu(\varrho_0, \theta, \zeta) = \frac{1}{2\pi}(\dot{\Psi}_{tor}\theta - \dot{\Psi}_{pol}^r\zeta) + \tilde{\nu}(\varrho_0, \theta, \zeta) \quad (\text{A.67})$$

If $\tilde{\nu}$ happens to be zero or a flux surface function then the θ, ζ coordinates we started from are already flux coordinates. Indeed, because the field lines lie on constant ν surfaces we have:

$$\frac{1}{2\pi}(\dot{\Psi}_{tor}\theta - \dot{\Psi}_{pol}^r\zeta) = \text{constant} \quad (\text{A.68})$$

which is the equation of a straight line in (θ, ζ) coordinates. If $\tilde{\nu}$ is a function of θ and ζ we perform a change of variables in order to eliminate $\tilde{\nu}$:

$$\theta_f = \theta \quad \zeta_f = \zeta - 2\pi \frac{\tilde{\nu}}{\dot{\Psi}_{pol}^r} \quad (\text{A.69})$$

or

$$\zeta_f = \zeta \quad \theta_f = \theta - 2\pi \frac{\tilde{\nu}}{\dot{\Psi}_{tor}} \quad (\text{A.70})$$

and the function ν becomes:

$$\nu(\varrho, \theta_f, \zeta_f) = \frac{1}{2\pi}(\dot{\Psi}_{tor}\theta_f - \dot{\Psi}_{pol}^r\zeta_f). \quad (\text{A.71})$$

The contravariant components of \mathbf{B} now have the following form:

$$B^{\varrho} = 0, \quad (\text{A.72})$$

$$B^{\theta_f} = -\frac{1}{J} \frac{\partial \nu}{\partial \zeta} = -\frac{C(\varrho)}{J} = \frac{1}{2\pi J} \dot{\Psi}_{pol}^r, \quad (\text{A.73})$$

$$B^{\zeta_f} = \frac{1}{J} \frac{\partial \nu}{\partial \theta} = \frac{B(\varrho)}{J} = \frac{1}{2\pi J} \dot{\Psi}_{tor} \quad (\text{A.74})$$

and \mathbf{B} in the Clebsch form:

$$\mathbf{B} = \nabla \varrho \times \nabla \left(\frac{\dot{\Psi}_{tor}}{2\pi} \theta_f - \frac{\dot{\Psi}_{pol}^r}{2\pi} \zeta_f \right) \quad (\text{A.75})$$

or, from the q definition and with $\varrho = \Psi_{pol}^r$:

$$\mathbf{B} = \frac{1}{2\pi} \nabla \Psi_{pol}^r \times \nabla (q\theta_f - \zeta_f). \quad (\text{A.76})$$

The general Clebsch form can be written as the sum of two term:

$$\mathbf{B} = \frac{\dot{\Psi}_{pol}^r}{2\pi}(\nabla\zeta_f \times \nabla\varrho) + \frac{\dot{\Psi}_{tor}}{2\pi}(\nabla\varrho \times \nabla\theta_f) = \mathbf{B}_P + \mathbf{B}_T \quad (\text{A.77})$$

and \mathbf{B}_P is called the poloidal field and \mathbf{B}_T the toroidal field. The covariant components of \mathbf{B} can be found from those contravariant by using the metric coefficients as shown in A.22. To summarize, if the magnetic field \mathbf{B} is known everywhere, we try to find suitable poloidal (θ_f) and toroidal (ζ_f) coordinates that make \mathbf{B} straight in (θ_f, ζ_f) . One can start with an acceptable grid of θ and ζ curves as a function of which the magnetic field is known (the *elementary system* for example) and deform the coordinate system until it possesses the desired properties.

In the following and in the ORBIT code we shall use as surface label coordinate ϱ the poloidal flux normalized to 2π :

$$\psi_p = \frac{\Psi_{pol}^r}{2\pi} \quad (\text{A.78})$$

and the same we do for the toroidal flux, so we define:

$$\psi = \frac{\Psi_{tor}}{2\pi}. \quad (\text{A.79})$$

By these definitions, equation A.77 for the contravariant magnetic field becomes in general coordinates:

$$\mathbf{B} = \nabla\zeta \times \nabla\psi_p + \nabla\psi \times \nabla\theta + \nabla\psi_p \times \tilde{\nu} \quad (\text{A.80})$$

while in straight field lines, where $\tilde{\nu} = 0$:

$$\mathbf{B} = (\nabla\zeta_f \times \nabla\psi_p) + (\nabla\psi \times \nabla\theta_f). \quad (\text{A.81})$$

In Chapter two, and generally in the Thesis, for simplicity we shall indicate only with ϕ the general geometric toroidal angle and with ζ the corresponding straight field line coordinate.

A.5.1 The vector potential.

We can give a physical meaning to the function ν . It acts as a potential function for the magnetic field as suggested by Eq. A.62. The formula for the curl relates covariant and contravariant components as follows:

$$(\nabla \times \mathbf{A}^*)^i = \frac{1}{\sqrt{g}} \left(\frac{\partial A_k^*}{\partial u^j} - \frac{\partial A_j^*}{\partial u^k} \right) \quad (\text{A.82})$$

If we identify \mathbf{A}^* with the vector potential, relation A.82 links the contravariant \mathbf{B} components with the covariant \mathbf{A}^* ones. From Eq. A.62 and Eq. A.82 we can write:

$$A_i^* = (-\nu, 0, 0) = \frac{1}{2\pi}(-\dot{\Psi}_{tor}\theta_f + \dot{\Psi}_{pol}^r\zeta_f, 0, 0) \quad (\text{A.83})$$

Thus ν is a potential function in the sense that it is the only component of a vector potential \mathbf{A}^* . Although \mathbf{A}^* and ν produce the correct magnetic field \mathbf{B} , in general they are not acceptable as physical quantities because of their non-periodicity, i.e. non single valuedness in θ_f and ζ_f . This problem can be solved considering that every vector potential is only defined up to an additive term which is the gradient of any arbitrary function f . Thus we define the correct potential vector \mathbf{A} as:

$$\mathbf{A} = \mathbf{A}^* + \nabla f \quad (\text{A.84})$$

choosing f in such a way that \mathbf{A} has the correct periodicity. If we split f in two parts, one periodic \tilde{f} and one secular f' , we can impose that $\nabla f'$ cancels the linear terms in θ_f and ζ_f of \mathbf{A}^* . We report here the final result for \mathbf{A} :

$$\mathbf{A} = (a + \frac{\Psi_{tor}}{2\pi})\nabla\theta_f + (b - \frac{\Psi_{pol}}{2\pi})\nabla\zeta_f + \nabla\tilde{f} \quad (\text{A.85})$$

where \tilde{f} is an arbitrary periodic function and a, b constants independent of ϱ .

A.6 General Current Representation

The current density \mathbf{j} satisfies two important relationship:

$$\mathbf{j} \cdot \nabla\varrho = 0 \quad (\text{A.86})$$

$$\nabla \cdot \mathbf{j} = 0. \quad (\text{A.87})$$

As we have already seen similar equations are obeyed by the magnetic field \mathbf{B} . This means that we can use the same procedure for the current \mathbf{j} as we did for \mathbf{B} . In particular from equation A.87 we have:

$$\frac{\partial}{\partial\theta}(\sqrt{g}j^\theta) + \frac{\partial}{\partial\zeta}(\sqrt{g}j^\zeta) = 0 \quad (\text{A.88})$$

and we can write j^θ and j^ζ as derivatives of a Clebsch function $\eta(\varrho, \theta, \zeta)$:

$$j^\theta = -\frac{1}{\sqrt{g}}\frac{\partial\eta}{\partial\zeta} \quad (\text{A.89})$$

$$j^\zeta = \frac{1}{\sqrt{g}} \frac{\partial \eta}{\partial \theta}. \quad (\text{A.90})$$

This means that \mathbf{j} is expressible in Clebsch form:

$$\mathbf{j} = \nabla \varrho \times \nabla \eta \quad (\text{A.91})$$

such that the current density lines on a flux surface ($\varrho = \text{constant}$) are defined by the equation

$$\eta(\varrho, \theta, \zeta) = \text{constant}. \quad (\text{A.92})$$

As we did with the function ν for the magnetic field, it can be proved that η has the following expression:

$$\eta(\varrho, \theta, \zeta) = \frac{1}{2\pi} \dot{I}_{tor}(\varrho) \theta - \frac{1}{2\pi} \dot{I}_{pol}^r(\varrho) \zeta + \tilde{\eta}(\varrho, \theta, \zeta) \quad (\text{A.93})$$

with $\dot{I}_{tor}(\varrho) = dI_{tor}/d\varrho$ where $I_{tor}(\varrho)$ represents the total toroidal current flowing within the volume enclosed by the flux surface ϱ and $\dot{I}_{pol}^r = dI_{pol}^r/d\varrho$ where $I_{pol}^r(\varrho)$ is the poloidal current flowing within the flux surface ϱ . The function $\tilde{\eta}$ in Eq. A.93 is a periodic function in θ and ζ . New angular coordinates can be defined to obtain current-lines straight and to eliminate $\tilde{\eta}$, with the same procedure used for the magnetic field.

We consider now some aspects of Ampere's law:

$$\mu_0 \mathbf{j} = \nabla \times \mathbf{B} \quad (\text{A.94})$$

which represents an inhomogeneous vector differential equation for the magnetic field with a source term equal to $\mu_0 \mathbf{j}$. According to the theory of differential equation, if \mathbf{j} is given, the equation is linear and the solution consist of two parts, \mathbf{B}_0 , the solution of the homogeneous equation and \mathbf{B}_j , a particular solution of the inhomogeneous equation. Thus we have:

$$\nabla \times \mathbf{B}_0 = 0 \implies \mathbf{B}_0 = \nabla \Phi \quad (\text{A.95})$$

$$\nabla \times \mathbf{B}_j = \mu_0 \mathbf{j} \quad (\text{A.96})$$

$$\mathbf{B} = \mathbf{B}_0 + \mathbf{B}_j. \quad (\text{A.97})$$

We suppose to be already in magnetic field straight lines conditions, and thus we use the coordinate $(\varrho, \theta_f, \zeta_f)$. To find the relation between the covariant magnetic field components and the contravariant current components we use the Ampere law:

$$j^i = \frac{1}{\mu_0} (\nabla \times \mathbf{B}_j) = \frac{1}{\mu_0} \frac{1}{\sqrt{g}} \left(\frac{\partial B_k}{\partial u^j} - \frac{\partial B_j}{\partial u^k} \right). \quad (\text{A.98})$$

Writing the contravariant components of \mathbf{j} in function of η (Eq. A.93) Eq. A.98 becomes:

$$j^\varrho = \left(\frac{\partial B_{J\zeta_f}}{\partial \theta_f} - \frac{\partial B_{J\theta_f}}{\partial \zeta_f} \right) = 0 \quad (\text{A.99})$$

$$j^{\theta_f} = \frac{1}{\sqrt{g}} \left[\frac{1}{2\pi} \frac{\partial I_{pol}^r}{\partial \varrho} - \frac{\partial \tilde{\eta}}{\partial \zeta_f} \right] = \frac{1}{\mu_0} \frac{1}{\sqrt{g}} \left(\frac{\partial B_{J\varrho}}{\partial \zeta_f} - \frac{\partial B_{J\zeta_f}}{\partial \varrho} \right) \quad (\text{A.100})$$

$$j^{\zeta_f} = \frac{1}{\sqrt{g}} \left[\frac{1}{2\pi} \frac{\partial I_{tor}}{\partial \varrho} - \frac{\partial \tilde{\eta}}{\partial \theta_f} \right] = \frac{1}{\mu_0} \frac{1}{\sqrt{g}} \left(\frac{\partial B_{J\theta_f}}{\partial \varrho} - \frac{\partial B_{J\varrho}}{\partial \theta_f} \right). \quad (\text{A.101})$$

Solutions for these equations are given by:

$$B_{j\varrho} = -\mu_0 \tilde{\eta}(\varrho, \theta_f, \zeta_f) \quad (\text{A.102})$$

$$B_{j\theta_f} = \frac{\mu_0}{2\pi} I_{tor}(\varrho) \quad (\text{A.103})$$

$$B_{j\zeta_f} = -\frac{\mu_0}{2\pi} I_{pol}^r(\varrho) \quad (\text{A.104})$$

as it can be proved by direct substitution in Eq. A.99- A.101. Eq. A.104 has a physical meaning if we add to the toroidal component of \mathbf{B} in its covariant form a constant i.e. the total poloidal plasma current $\mu_0 I_{pol}^{plas}$; in this way the circuitation of B_{ζ_f} along a ζ_f curve is equal to the plasma current outside the flux surface $\varrho = \text{constant}$.

The structure of the vacuum scalar potential Φ is related to the external coils currents $\sum I_{coils}$ so we can write:

$$\Phi = \frac{\mu_0}{2\pi} \sum I_{coils} + \tilde{\Phi}(\varrho, \theta_f, \zeta_f) \quad (\text{A.105})$$

where $\tilde{\Phi}$ is a periodic potential. We define the total poloidal current crossing a disk touching the magnetic axis as $I_{pol}^{tot} = I_{pol}^{plas} + \sum I_{coils}$ and the poloidal current outside a flux surface as $I_{pol}^d(\varrho) = I_{pol}^{tot} - I_{pol}^r(\varrho)$. Using this new definition, the potential Φ and equation A.97 we finally have for the covariant components of the magnetic field in straight field lines:

$$B_\varrho = -\mu_0 \tilde{\eta}(\varrho, \theta_f, \zeta_f) + \frac{\partial \tilde{\Phi}}{\partial \varrho} = \mu_0 \delta(\varrho, \theta_f, \zeta_f) \quad (\text{A.106})$$

$$B_{\theta_f} = \frac{\mu_0}{2\pi} I_{tor}(\varrho) + \frac{\partial \tilde{\Phi}}{\partial \theta_f} = \mu_0 I(\varrho, \theta_f, \zeta_f) \quad (\text{A.107})$$

$$B_{\zeta_f} = \frac{\mu_0}{2\pi} I_{pol}^d(\varrho) + \frac{\partial \tilde{\Phi}}{\partial \zeta_f} = \mu_0 g(\varrho, \theta_f, \zeta_f). \quad (\text{A.108})$$

where we have defined $\delta(\varrho, \theta_f, \zeta_f) = -\mu_0 \tilde{\eta}(\varrho, \theta_f, \zeta_f) + \partial \tilde{\phi} / \partial \varrho$, $I(\varrho, \theta_f, \zeta_f) = \frac{1}{2\pi} I_{tor}(\varrho) + \frac{1}{\mu_0} \partial \tilde{\phi} / \partial \theta_f$ and $g(\varrho, \theta_f, \zeta_f) = \frac{1}{2\pi} I_{pol}^d(\varrho)$. Note that for a general equilibrium, from equations A.107-A.108, you have:

$$\frac{\partial I}{\partial \zeta} = \frac{\partial g}{\partial \theta} = \frac{\partial^2 \tilde{\Phi}}{\partial \theta \partial \zeta}. \quad (\text{A.109})$$

In particular we are interested in the axi-symmetric case i.e. where $\partial_{\zeta_f} = 0$. If this happens then g, I, δ are only functions of the ϱ and θ_f coordinates. Note that from Eq. A.108 g is a function only of ϱ .

A.7 Boozer Coordinates

Flux coordinates for straight magnetic field lines are not unique. In other words, there is more than one pair of angle functions $\theta_f(\mathbf{R})$ and $\zeta_f(\mathbf{R})$ in which the magnetic field is straight. For example **Hamada** coordinates [109] are obtained by choosing the Jacobian J to be a function of ϱ alone. Some codes, like PEST (Princeton Equilibrium and Stability,[110]) consider $J \sim X^2$ and ζ is chosen equal to the geometric toroidal angle ϕ . We are interested in a particular form of Hamada coordinates, developed by **Boozer**, where $J \sim \frac{1}{B^2}$ which simplify the representations for \mathbf{B} and \mathbf{j} .

In the following we'll suppose to be already in straight field lines and we'll suppress the pedix f for the angular coordinates. Our straight field line coordinates are thus (ϱ, θ, ζ) . The covariant equations for the magnetic field are given by equations A.106-A.108. We assume also axi-symmetry so that there is no dependence of any function from ζ .

Boozer Coordinates are defined by choosing the potential $\tilde{\phi} = 0$. Consider the contravariant and covariant expression for the magnetic field in straight field lines:

$$\mathbf{B} = \frac{\dot{\Psi}_{tor}}{2\pi} \nabla \varrho \times \nabla \theta - \frac{\dot{\Psi}_{pol}^r}{2\pi} \nabla \varrho \times \nabla \zeta \quad (\text{A.110})$$

and

$$\mathbf{B} = \left(-\mu_0 \tilde{\eta} + \frac{\partial \tilde{\phi}}{\partial \varrho}\right) \nabla \varrho + \left(\frac{\mu_0}{2\pi} I_{tor} + \frac{\partial \tilde{\phi}}{\partial \theta}\right) \nabla \theta + \left(\frac{\mu_0}{2\pi} I_{pol}^d + \frac{\partial \tilde{\phi}}{\partial \zeta}\right) \nabla \zeta. \quad (\text{A.111})$$

Since $\mathbf{B} \cdot \mathbf{B} = (B^i B_i) = B^2$ we obtain from the dot product of Eq. A.110 and Eq. A.111:

$$B^2 = \frac{1}{\sqrt{g}} \frac{\mu_0}{4\pi^2} (\dot{\Psi}_{pol}^r I_{tor} + \dot{\Psi}_{tor} I_{pol}^d) + \mathbf{B} \cdot \nabla \tilde{\phi} \quad (\text{A.112})$$

and then the Jacobian is given by:

$$\sqrt{g_B} = \frac{\mu_0}{4\pi^2} \frac{\dot{\Psi}_{tor} I_{pol}^d + \dot{\Psi}_{pol}^r I_{tor}}{B^2 - \mathbf{B} \cdot \nabla \tilde{\phi}}. \quad (\text{A.113})$$

Boozer takes $\tilde{\phi} = 0$; therefore Boozer Jacobian $\sqrt{g_B}$ is:

$$\sqrt{g_B} = \frac{\mu_0}{4\pi^2} \frac{\dot{\Psi}_{tor} I_{pol}^d + \dot{\Psi}_{pol}^d I_{tor}}{B^2}. \quad (\text{A.114})$$

By using the poloidal flux ψ_p as parameter for ϱ in Boozer coordinates and ψ for the toroidal flux, so that $d\psi/d\psi_p = q$, and using the definition of g and I for the current representation, the Jacobian becomes simply:

$$\sqrt{g_B} = \mu_0 \frac{qg + I}{B^2}. \quad (\text{A.115})$$

Taking $\tilde{\phi} = 0$ means from equations A.106-A.108 that even I is a function only of the poloidal flux and is not depending on θ as in general straight field lines geometry.

Bibliography

- [1] J.Reece Roth. Introduction to Fusion Energy. Ibis Publishing, Charlottesville, Virginia, 1986.
 - [2] Roger A. Hinrichs. Energy Its Use And The Enviroment. Sanders College Publishing, 1996.
 - [3] G.Marland, T.Boden, and R.J. Andres. A Compendium of Data in Global Change. Carbon Dioxide Information Analysis Center Oak Ridge National Laboratory U.S., 2005.
 - [4] M. K. Hubbert. Nuclear Energy and the Fossil Fuels, volume in Spring Meeting of the Southern District, American Petroleum Institute, Sant' Antonio, Texas. 1956.
 - [5] IPCC. Climate change 2001: the scientific basis. 2001.
 - [6] R.J. Goldston and P.H. Rutherford. Introduction to Plasma Physics. Institute of Physics Publishing, 1995.
 - [7] K.Miyamoto. Plasma Physics for Nuclear Fusion. the MIT press, Cambridge, Mass., 1989.
 - [8] W.K.Hogan. Nucl.Fusion, 44, 2004.
 - [9] J.D. Lawson. Proc. Phys.Soc., B70:6, 1957.
 - [10] K.M. McGuire and al. Phys. Plasmas, 2:2176, 1995.
-

-
- [11] A.Gibson and al. Phys. Plasmas, 5:1839, 1998.
- [12] ITER Physics Expert Groups. Nucl. Fusion, 39:2137, 1999.
- [13] D.J. Campbell. Phys. Plasmas, 8:2041, 2001.
- [14] ITER Documentation. Design Description Document 1.7, G 17.
- [15] T.J.M Boyd and J.J. Sanderson. The physics of plasmas. Cambridge University Press, 2003.
- [16] J.P.Freidberg. MHD Instabilities. Cambridge, Mass, MIT Press, 1978.
- [17] G.Bateman. MHD Instabilities. New York, Plenum Press, 1978.
- [18] H.P.Furth, J.Killen, and M.N. Rosenbluth. Phys. Fluids, 6:459, 1963.
- [19] J.Wesson. Tokamaks. Claredon Press, Oxford 1987.
- [20] S.Ortolani and D.D.Schnack. Magnetohydrodynamics of Plasma relaxation. Singapore,World Scientific, 1993.
- [21] Nuhremberg and al. Overview of Weldenstein 7-X Theory, Proc. 6th Int. Conf. on Plasma Physics and Controlled Fusion (Tokyo 1994), page 71, 1995.
- [22] G.Grieger. Plasma Phys. Control. Fusion, 3:525, 1991.
- [23] Roscoe B. White and Leonid E. Zakharov. Phys. Plasmas, 10:573–576, 2003.
- [24] W.D.Shafranov. Reviews of Plasma Physics, 2:103, 1966.
- [25] J.M.Greene, J.L.Johnson, and K.E.Weimer. Phys.Fluids, 14:67, 1971.
- [26] Roscoe B. White. The theory of Toroidally confined plasmas. Imperial College Press, London, 2001.
- [27] J.B.Taylor. Phys.Rev.Lett., 33:1139, 1974.
- [28] W.Shen and J.C.Sprott. Phys.Fluids B, 3:1225–1231, 1991.
- [29] S.P.Hirshman and S.Betancourt. J.Comput. Phys, 96:99, 1991.
- [30] B.A.Trubnikov. Review of plasma physics, 1:105, 1965.
- [31] A.H.Boozer and G. Kuo-Petravich. Phys. Fluids, 24:851, 1981.
-

-
- [32] R.Carruthers. Plasma Phys. Control. Fusion, 20:1993–2000, 1988.
- [33] A.B.Rechester and M.N.Rosenbluth. Phys. Rev. Lett., 40:38, 1978.
- [34] S.Cappello and D.Biskamp. Nucl. Fusion, 36:571, 1996.
- [35] Piovesan and al. Phys. Rev. Lett., 93:235001, 2004.
- [36] L.Marrelli and al. Plasma Phys. Control. Fusion, 49:B359–B369, 2007.
- [37] M.Rubel and al. Fusion Eng. Des., 49:323, 2000.
- [38] R.N.Dexter and al. Fusion Technol., 19:131, 1991.
- [39] P.Sonato, G.Chitarin, P.Zaccaria, and al. Fusion Engineering and Design, 66:161, 2003.
- [40] G. Rostagni. Fusion Eng. Des., 25:301, 1995.
- [41] C.M. Bishop. Plasma Phys. Control. Fusion, 31:1179, 1989.
- [42] L.Marrelli and al. Plasma Phys. Control. Fusion, 49:B349–B359, 2007.
- [43] Paolo Zanca and al. Nucl. Fusion, 47:1425–1436, 2007.
- [44] P.Franz, L.Marrelli, A.Murari, G.Spizzo, and P.Martin. Nucl. Fusion, 41:695, 2001.
- [45] A.M.Cormark. J.App.Phys., 34, 1963.
- [46] A.Alfier and R.Pasqualotto. Rev. Sci. Instrum., 78:013505, 2007.
- [47] P.Innocente and S.Martini. Rev. Sci. Instrum., 63:4996, 1992.
- [48] L.Carraro, M.E.Puiatti, P.Scarin, and M.Valisa. Rev. Sci. Instrum., 63:5188, 1992.
- [49] T.Bolzonella, N.Pomaro, G.Serianni, and D.Marcuzzi. Rev. Sci. Instrum., 74:1554, 2003.
- [50] A.Murari and al. Rev. Sci. Instrum., 70:581, 1999.
- [51] Newcomb W.A. Ann. Phys., 10:232, 1960.
- [52] Robinson D.C. Plasma Phys., 13:430, 1970.
- [53] P.Zanca and D. Terranova. Plasma Phys. Control. Fusion, 46:1115–1141, 2004.
-

-
- [54] P.Martin, L.Marrelli, A. Alfier, and al. Plasma Phys. Control. Fusion, 49:A177, 2007.
- [55] Italo Predebon. Magnetic Field Topology and Particle Transport in Reversed Field Pinch. PHD Thesis, 2003.
- [56] I.Predebon, L.Marrelli, P.Martin, and R.B.White. Phys. Rev. Lett., 93:145001, 2004.
- [57] M.Gobbin and al. Phys. Plasmas, 14:072305, 2007.
- [58] D.Escande, P.Martin, and S.Ortolani. Phys. Rev. Lett., 85:2169, 2000.
- [59] Caramana E.J., Nebel R.A., and Schnack D.D. Phys. of Fluids, 26:1305, 1983.
- [60] Kusano K. and Sato T. Nucl.Fusion, 26:1051, 1986.
- [61] Schnack D.D. and al. Phys. of Fluids, 28:321, 1985.
- [62] Cappello S. and Paccagnella R. Phys. Fluids, B4:611, 1992.
- [63] Finn J.M., Nebel R.A., and Bathke C.C. Phys. Fluids, B4:1262, 1992.
- [64] D.F.Escande and al. Plasma Phys. Control. Fusion, 42:B243, 2000.
- [65] S.Cappello and D.Biskamp. Nucl. Fusion, 36:571, 1996.
- [66] S.Cappello and D.F. Escande. Phys. Rev. Lett., 85:3838, 2000.
- [67] D.Bonfiglio, S.Cappello, and D.F.Escande. Phys. Rev. Lett., 94:145001, 2005.
- [68] S.Cappello. Plasma Phys. Control. Fusion, 46:B313, 2004.
- [69] Branham R. Scientific Data Analysis: An introduction to overdetermined systems. Springer Verlag, New York, 1990.
- [70] ITT Visual Informations Solution. The Interactive Data Language. 4990 Boulder CO, USA,<http://www.ittvis.com/idl/>.
- [71] E.L. Loyd. Technical Report MIT LCS TM 88, Laboratory for Computer Science, Massachusetts Institute of Technology, 1977.
- [72] D.T. Lee and B.J. Schachter. Int. J. of Computer and Information Sci., 9:219–242, 1980.
-

-
- [73] H.Akima. ACM Transactions on Mathematical Software, 4:148–159, 1978.
- [74] M.Wakatani and R.Itatani. J. Phys. Soc. Jpn., 34:181, 1973.
- [75] T.S.Chen, Akiyoshi Nagata, Koichi Sato, Hisao Ashida, and Tsuneo Amano. J. Phys. Soc. Jpn., 61:530, 1992.
- [76] V.Tribaldos. Phys. Plasmas, 8:1229, 2001.
- [77] T. Estrada, Sanchez, B.Ph. van Milligen, L. Cupido, V.Zhuravlev, A. Silva, and M.S.Manso. Proceedings of Workshop, Camberra, Paper no.PIIA4, 2001.
- [78] D.Gregoratto, L.Garzotti, P.Innocente, S.Martini, and A.Canton. Nucl. Fusion, 38:1199, 1998.
- [79] P.Franz, G.Gadani, and al. Rev. Sci. Instrum., 74:3, 2003.
- [80] B.E.Chapman et al. Phys. Plasmas, 9:5, 2002.
- [81] B.E.Chapman et al. Phys. Plasmas, 5:1848, 1998.
- [82] R. O’Connel and al. Phys.Rev.Lett, 91, 2003.
- [83] J.S.Sarff et all. Phys.Rev.Lett, 72, 1997.
- [84] P.Franz and all. Phys. Rev. Lett., 92:12, 2004.
- [85] D.J.Clayton and al. 48th Annual Meeting of The Division on Plasma Physics,October 30- November 3, Philadelphia (USA), 2006.
- [86] H.Dreicher. Proceedings of the 2nd International Conference on the Peaceful Uses of Atomic Energy, Geneva, 31:57, 1958.
- [87] W.W.Heidbrink and G.J.Sadler. Nucl. Fusion, 34:535, 1994.
- [88] W.W.Heidbrink, M.Miah, D.Darrow, B.LeBlanc, S.S. Medley, A.L.Roquemore, and F.E.Cecil. Nucl. Fusion, 43:883, 2003.
- [89] M.Isobe, M.Sasao, M.Osakabe, M.Fujita, S.Okamura, R.Kumazawa, and T.Minami. Nucl. Fusion, 68:532, 1997.
- [90] T.M.Biewer, C.B. Forest, J.K. Anderson, G.Fiksel, B.Hudson, S.C.Prager, J.S.Sarff, and J.C.Wright. Phys.Rev.Lett, 91:045004, 2003.
- [91] G. Fiksel. 47th APS DPP Meeting, Denver,CO,October 24-28,2005.
-

-
- [92] G.Fiksel, B.Hudson, D.J.Dan Hartog, and al. Phys.Rev.Lett, 95:125001, 2005.
- [93] A.Herrmann. Fusion Science and Technology, 44:569, 2003.
- [94] M.G. Munoz and al. Nucl. Fusion, 47:L10–15, 2007.
- [95] Manuel Garcia Munoz. Fast Response Scintillator Based Detector for MHD Induced Energetic Ions Losses in ASDEX Upgrade. PHD Thesis, 2006.
- [96] G.G. Lister. Tech. Rep. Max Planck Institut Fuer Plasmaphysik, IPP 4:222, 1985.
- [97] M.G. Munoz. accepted for publication in Phys. Rev. Lett., 2007.
- [98] D.Darrow. Rev.Sci.Instrum., 66:476, 1995.
- [99] A.Weller A.Werner. Rev.Sci.Instrum., 72:780, 2001.
- [100] C.Gourdon. Programme optimise de calculs numeriques dans les configurations magnetiques, centre d’etudes nuclearires de Fontenay aux Roses, 1970.
- [101] S.Baeumel. Rev.Sci.instrum, 75:3563, 2004.
- [102] H.E:Mynick. Phys.Fluids, B5:1471, 1993.
- [103] S.J.Zweben et al. Nuc. Fusion, 39:1097, 1999.
- [104] E.M. Carolipio and al. Nucl.Fusion, 42:853, 2002.
- [105] Erika Strumberger and al. submitted to New Journal of Physics, 2007.
- [106] S.V. Putvinskii. Rev. Plasma Phys., 18:239, 1993.
- [107] Y.Yagi and al. Fusion Eng. Des., 45:409, 1999.
- [108] W.D.D’haeseleer, W.N.G Hitchon, J.D. Callen, and J.L. Shoet. Flux Coordinates and Magnetic Field Structure. Springer Verlag, Germany, 1991.
- [109] S.Hamada. Nucl.Fusion, 2:23, 1962.
- [110] R.C.Grimm, J.M.Greene, and J.L.Johnson. Methods in Computational Physics, volume 16. Academic,New York, 1976.
-

Acknowledgments

In the three years of this research work, I benefited from the knowledge, encouragement and support of several people. At this stage I would like to express my gratitude.

First of all, I would like to thank **Prof. Piero Martin** who has been my group leader and has given me the opportunity to perform this challenging work under his supervision. In particular I wish to thank him for giving me the opportunity to work in collaboration with the ASDEX-Upgrade team in order to study the physics of fast particles.

I do not have words to express my gratitude to **Dr. Lionello Marrelli**. The work presented in this Thesis would not have been possible without his outstanding support and his personal and professional advice. He has invested a tremendous amount of time in introducing me into the fascinating world of numerical simulations of plasma physics phenomena. I'm very grateful to him for helping me to solve my daily problems.

I'm specially grateful to **Prof. Roscoe B. White** of the Princeton Plasma Physics Laboratory. His enthusiasm for physics is contagious. The period we have passed working together has been extremely fruitful. His experience in theoretical physics and programming has allowed us to obtain important and useful results. Moreover, it has been a pleasure to work with such a friendly and cordial person.

I want to thank all the members of the **FD group**; their collaboration has been essential for the comparison of the numerical results with the experimental data. I wish to thank in particular Dr. Federica Bonomo for the tomographic reconstructions which have been included in this Thesis. A spe-

cial thank also to all the the RFX-mod team: physicists, engineers, the administrative staff and technicians.

I'm thankful to **Dr. S.Günter**, **E. Strumberger** and **V.Igochine** for the fruitful discussions on fast ions losses in ASDEX-Upgrade. A particular thanks to **Manuel G. Munoz** for the collaboration and for the experimental data analysis performed.

I'm incredibly fortunate to have had such friendly workmates and PHD colleagues: **Magostini**, **Fedona**, **Lukano**, **Takkone**, **Fulbio**, **Sbrombiz**, **Spiss**, **Pizzi**, **Rituz**, **Piove**. It is not possible to forget the break time at the coffee machine, the lunch at the *boschetto* three days a week, the *RFX trips*, the political and religious discussions. I thank every one of them for their wonderful friendship! And sorry for my foot which can't stop from pounding on the floor nervously.

I want to thank my long-term friends which have always supported me. A special thank to **Filippo**, **Cristiana**, **Marco**, **Skagge**, **Bea**, **Giulia**, **Alex**, **Alessio**, **Lucy**, **Fasu**, **Lora**, **Serena**. You all have been very patient with me!

During my PHD years I have had the great opportunity of spending about 6 months in the United States of America. This has been not only a great work collaboration but has given me the effort to discover the beauty and the greatness of this Country. I'll never forget the wonderful people I have met: **Ellen**, **Nicola**, **Laura**, **Rob**, **Hervé**, **Bryan**, **Mirko**, **Sana**. But I will never forget also the amazing places where I have been: Manhattan, Boston, Philadelphia, Washington D.C., the Niagara Falls. A special thank to Starbucks and Dunkin' Donuts. Thank You, **America**, for everything you gave me and see You soon. God Bless You.

Finally the greater acknowledgment is dedicated to my parents, **Gobbin Armando** and **Stella Cardin** for making possible my physics studies and therefore this work. Their moral support in many difficult moments has been very important. A special thought to **Minou** and **Theo**, recently disappeared.
